# *Shear Strength and Strength Degradation of Concrete Bridge Decks with GFRP Top Mat Reinforcement*

By

Ross D. Amico

Thesis submitted to the faculty of the Virginia Polytechnic Institute and State University
in partial fulfillment of the requirements for the degree of

Master of Science

In

Civil Engineering

APPROVED:

Carin Roberts-Wollmann, Chairperson

Thomas E. Cousins

John J. Lesko

May 31, 2005

Blacksburg, VA

Keywords: fiber reinforced polymer (FRP) bars, shear strength, bridge decks, reinforced concrete

# *Shear Strength and Strength Degradation of Concrete Bridge Decks with GFRP Top Mat Reinforcement*

By

Ross D. Amico

(ABSTRACT)

The primary objective of this research was to investigate the shear strength of concrete bridge decks with GFRP top-mat reinforcement. Several models currently exist to predict the shear strength during the design process; however, previous research at Virginia Tech indicates that the existing equations are overly conservative. For this research, a series of concrete decks with varying lengths were tested in a laboratory environment in a two-span continuous configuration, during which data was collected on deflections, rebar strain, crack widths, and ultimate load. It was concluded that the existing equations, particularly the guidelines of ACI 440, are grossly over-conservative for GFRP-reinforced concrete bridge decks continuous over multiple supports. It was suggested that this is due to multiple factors, including additional support provided by the typically-neglected steel reinforcement in the bottom mat and a higher shear strength of the uncracked portion of concrete due to higher compressive stresses in the section as a result of the continuous deck configuration.

The second objective of this research was to investigate the effects of environmental exposure on the composite deck and the individual GFRP rebar. Three deck specimens were subjected to differing environmental conditions, including one that was placed into service at an interstate weigh station. All three decks were tested in the same manner as those in the shear investigation. Additionally, live load tests were conducted on the weigh station deck during the time it was in place and tensile tests were conducted on rebar that were extracted from the concrete decks. In the live load testing, the GFRP strains increased by more than 200% over the period of service, which was likely due to a combination of a reduction in GFRP stiffness and a greater amount of cracking. During the laboratory tests on the decks, no clear correlation between conditioning and deflections or cracking was found. The ultimate strength actually increased with conditioning, with the weigh station specimen exhibiting the highest shear strength. Finally, the results of the rebar tensile tests suggested a decrease in both modulus of elasticity and ultimate tensile strength of the GFRP with environmental exposure when compared to unconditioned bars.

## *Acknowledgements*

First, I want to express my deepest appreciation for Dr. Carin Roberts-Wollmann for her wisdom, expertise, and guidance throughout my undergraduate and graduate years. Her motivation, love of engineering, and genuine concern for her students helped make my research a very positive experience. I would also like to thank Dr. Tommy Cousins and Dr. Jack Lesko who served on my committee. Dr. Cousins provided considerable guidance during the live load testing and coordinated installation efforts at the weigh station.

A tremendous amount of assistance also came from my fellow graduate students who were there to help during all phases of this research, including construction, installation, testing, and demolition. In particular, I want to thank Matt Harlan, Tim Banta, Bernie Kassner, Chris Link, and Kim Phillips. Additionally, none of this work could have been completed without the involvement of Brett Farmer and Dennis Huffman who were always happy to help with the test setups in the Structures Lab.

I also want to thank my family and friends for their constant support, especially my parents who have always been there for me. Finally, I want to thank my loving wife, Angela, who continually fills my life with joy, encouragement, and inspiration. Her patience and support were highly instrumental in completing this work.

# Table of Contents

# List of Figures

# List of Tables

# *Chapter 1 – Introduction*

## 1.1 Background

At an average cost of between $75 and $100 per square foot for initial construction (Weyers 2001), there is no argument that bridges are typically the most expensive elements on a per unit basis of any roadway system. Although bridges are usually designed for 50-70 years of service, bridge decks usually require significant rehabilitation after only 20-25 years (Ralls 2005), greatly increasing the life-cycle cost of the structure. According to data in the 2004 FHWA National Bridge Inventory (NBI), 77,613 of the 593,065 bridges in the United States have been identified as structurally deficient. In Virginia alone, 1,186 of the Commonwealth's 13,160 bridges in the NBI are structurally deficient. More than one-third of these bridges needing rehabilitation are deficient because of damage to the bridge deck (Everett 2002). Deterioration of steel-reinforced concrete bridge decks can be caused by freeze thaw cycles, traffic loading, results of poor design or construction, or inadequate maintenance; but the primary factor reducing the life of most steel-reinforced concrete bridge decks is corrosion of the steel reinforcement. Given that steel corrosion can increase the volume of the bar by up to seven-fold, expansive tensile stresses are developed in the concrete around the bars leading to further cracking and spalling of the deck. The chlorides causing this corrosion are introduced to the structure through either marine exposure or the application of deicing salts for snow and ice removal.

Three general options are available to counter this chloride attack: preventing the chlorides from reaching the reinforcement with a physical barrier, blocking chloride penetration into the concrete with certain inhibitors or admixtures, or by using rebar that is resistant to corrosion. Although the specification of thicker concrete cover and the use of epoxy-coated rebar have been specified in attempts to increase the service life of bridges, the porous nature of concrete, the development of cracks, and the deterioration of bar coatings still allow for the corrosion of the steel. Therefore, much research has been devoted to finding suitable alternative materials to typical mild steel reinforcement.

Fiber-reinforced polymer (FRP) bars are widely being considered as one alternative. Although several material options are available for the fiber portion of the composite bar

including carbon and aramid, glass fibers are most common in structural applications because of their relatively low cost. Advantages of glass fiber reinforced polymer (GFRP) bars over typical steel reinforcement include the material's lighter weight and ease of installation, magnetic invisibility, and, most importantly in the case of bridge decks, it's resistance to corrosion. However, despite the numerous advantages, there are several factors that designers must consider when designing with GFRP. First, GFRP bars do not exhibit a yield plateau as steel does and are linear-elastic to failure on a stress-strain plot. Although the bars have a higher tensile strength than regular steel reinforcement, the lack of a yield plateau requires reconsideration of the typical design methodologies which plan for the steel to yield prior crushing of the concrete to allow for a visual warning of impending failure. Additionally, compared to steel, GFRP has a lower modulus of elasticity, requiring a larger cross-sectional area or reinforcement in order to limit crack widths to acceptable levels. Crack control is still considered necessary despite the fact that the bars will not corrode in order to limit the potential for chlorides to reach the steel which is typically still used in the bottom reinforcing mat. Crack widths must also be minimized to allow for sufficient aggregate interlock necessary to maintain concrete shear strength and for peace of mind for users of the bridge. One other detracting characteristic of the material is that GFRP is known to lose strength over time due to loading and environmental exposure.

Due to the differences in material properties, the shear strength of GFRP reinforced concrete elements will likely be different than similar elements reinforced with steel. The lower modulus of elasticity of GFRP relative to that of steel causes larger crack widths, which reduces the shear strength attributed to aggregate interlock. Further, no shear strength of an FRP-reinforced section is considered to be contributed by dowel action involving the FRP rebar.

The current method of investigating the shear strength of concrete bridge decks involves using the equivalent strip method outlined in the AASHTO LRFD Bridge Design Specification (2002) with the shear strength described by ACI based on the type of reinforcement used. Traditionally, one-way shear of bridge decks is not checked because it is not a critical case for common steel-reinforced decks. GFRP-reinforced decks should be checked due to the lower shear strength described above. However, several attempts have been made to model the shear behavior of GFRP-reinforced decks, but the resulting equations have typically been overly conservative.

## 1.2 Objectives

### 3.1.1 Investigation of one-way shear strength

The primary objective of this research was to investigate the shear strength of GFRP-reinforced bridge decks. This was accomplished through the construction and testing of six prototype decks of various sizes and known dimensions. These decks were built and tested at the Virginia Tech Structures and Materials Laboratory. Four of the decks were built with the same thickness, but with varying lengths in the direction of traffic travel, and were tested soon after the concrete attained the design strength. The other two decks were built for installation in a test bed in the northbound lane of the Troutville Weigh Station at milepost 149 on Interstate 81 in Virginia. Only one, however, was installed in the weigh station to endure the elements and the loadings of the passing trucks for a little more than one year. The other was stored in the lab where it was protected from the environment. The results from the tests, including failure mode and maximum load, were compared to predictions developed from existing design models. Additionally, the research considered the cracking load, deck deflections, and crack widths in comparison with anticipated behavior, as well as deck performance at service loads.

### 3.1.2 Investigation of the reduction of slab strength and stiffness

The secondary objective of this research was to examine the reduction of the composite slab performance after long-term vehicular loading and exposure to the elements. As noted above, GFRP reinforcing bars are known to lose strength and stiffness over time as a result of repeated loadings and environmental effects such as temperature and alkalinity.

Of the six decks discussed in the previous section, three are of approximately the same size and were used to investigate strength loss. Two decks were built and allowed to age for more than a year prior to testing. Of these two, as noted above, one was protected from the elements and the other was exposed to significant truck traffic and the weather. The third was tested shortly after the concrete attained its design strength. This variety allowed for the investigation of strength loss due to time alone as well as time combined with the effects of loading and environmental factors. No additional data collection was necessary beyond that already described in the previous section.

## 1.3 Thesis Organization

This thesis is organized into five chapters including this introduction. Chapter 2 presents a review of previous research and literature pertaining to the use of GFRP rebar. Methods and materials used to achieve the objectives stated in Section 1.2 are presented in Chapter 3. Results and related discussion are presented in Chapter 4. Finally, Chapter 5 summarizes the conclusions of the research and provides recommendations for further research.

# Chapter 2 - Literature Review

## 2.1 Introduction

FRP rebar consists of thousands of continuous hairline fibers oriented longitudinally with respect to the bar and bound together with a polymer matrix (Bradberry 2001). The fibers are aramid (AFRP), carbon (CFRP), glass (GFRP), or a combination thereof and comprise approximately 70% of the reinforcing bar (Brown 1993). The polymer matrix makes up the other 30% and is typically an epoxy resin, polyester resin, vinyl ester resin, or a combination. This resin serves to bind the fibers together and distribute the load across the cross-section to attain the composite properties of the material. Additionally, it acts as protective coating against environmental factors (Bradberry 2001).

Of the three fiber types mentioned above, glass is the most typically used as concrete reinforcement due to its relatively low cost. Within this glass category two types are most common, E-glass and S-glass. Although S-glass is stronger and has a greater stiffness, E-glass is used more often in concrete structures due to its resistance to alkaline environments.

These two primary components of FRP rebar, the continuous fibers and resin matrix, are combined by pultrusion. In this process, the fibers are drawn through the resin bath, aligned, and pulled through a heated steel die that sets the diameter of the rebar. Typically, a helical band is wound around the bar to create physical deformations to improve the bond between the bar and the concrete it reinforces (Brown 1993). It should be noted, however, that some research has shown that this helical wrap may damage the fibers underneath it when the bar is subjected to cyclic tensile loading. This is because it imposes a repeated lateral force on the fibers beneath it and may in some circumstances lead to premature failure of the bar (Katz 1998). In addition to the helical band, FRP rebar is often impregnated with sand, which gives it a rougher surface to increase the physical bond with the concrete. These imposed bar deformations do not, however, meet the specification of ASTM A615 and there is currently no standard for deformations of FRP rebar (Brown 1993).

## 2.2 GFRP Material Properties

Although FRP is being touted as an alternative to steel for concrete reinforcement, particularly in bridge decks, its properties are significantly different. Further, the lack of industry standards in the manufacturing of FRP components results in a wide range of characteristics and properties, which differs from steel where the properties are generally well known for a given material grade. This makes it difficult for engineers to specify FRP without limiting themselves to a narrow range of manufacturers or producing uneconomical designs (Bradberry 2001).

The range of material properties varies depending on the information source, but Table 2.1 presents the typical tensile properties for GFRP and a comparison with steel as published by the ACI 440 committee (ACI 2003).

***Table 2.1 – Comparison of GFRP and Steel Properties***

| Property | GFRP | Steel |
|---|---|---|
| Tensile Strength | 70 to 230 ksi | 70 to 100 ksi |
| Modulus of Elasticity | 5100 to 7400 ksi | 29000 ksi |
| Rupture Strain | 0.012 to 0.031 | 0.060 to 0.120 |

As seen in Table 2.1, the tensile strength of GFRP generally exceeds that of steel bars, but the modulus of elasticity is significantly lower. This directly influences the service performance of the structure by increasing the deflections and crack widths of a member relative to a similarly reinforced section with steel rebar. In order to counteract this negative characteristic, more GFRP bars must be used (Brown 1993).

Another significant difference from steel is in the stress-strain behavior of FRP. The material is linearly elastic to failure, which means that the bars do not experience any sort of yield plateau. This can be addressed to some extent through the use of hybrid FRP bars, which exhibit a multisloped stress-strain curve, but there is still no actual yield point. Therefore, the use of GFRP rebar in a structure requires a new approach to the design of reinforced concrete as the typical mode of reinforcement-yielding is not possible. Reliance on the standard method used for steel would lead to a sudden, catastrophic failure of the section as the brittle GFRP rebar ruptures. A better approach is for the engineer to design an overreinforced section in which the concrete crushes first which, although not preferred in steel-reinforced members, provides greater warning of failure in GFRP-reinforced structures. Thus, the ductility of a GFRP-reinforced member is significantly reduced over a steel-reinforced counterpart. However,

significant ductility is not necessary for bridge deck application since the typical failure mode of a deck slab is punching shear, except in the overhangs where a plastic hinge is not statically permissible anyway (Bradberry 2001).

Several other factors, both positive and negative, affect the engineer's decision for using this material. In addition to its high tensile strength, GFRP has a low density (approximately 20 to 25% that of steel), leading to a high strength-to-weight ratio. Unfortunately, some of the benefits of the low density of the material are negated by the greater bar requirement necessitated by the low modulus of elasticity; on the other hand, individual bar handling is unquestionably easier during construction. GFRP is also nonmagnetic, which makes it ideal for use around equipment sensitive to electromagnetic fields, and has a low thermal and electric conductivity (ACI 2003). The most significant merit of this material, however, is its electrochemical inertness. GFRP produces no expansive corrosion product that would accelerate deterioration of the structure (Bradberry 2001), which is particularly important in highly corrosive environments such as marine structures and bridge decks treated with deicing salts (ACI 2003).

Nevertheless, several characteristics must be weighed against these merits. As previously mentioned, there is no yield point prior to brittle failure in tension and GFRP has a low modulus of elasticity. Additionally, the material is anisotropic, so it has very low shear strength and low strength at fabricated bar bends. Further, while the longitudinal coefficient of thermal expansion is similar to concrete, the transverse coefficient is significantly higher than the concrete, which may lead to radial cracking from large increases in temperature (TTI 2000) and raises the question of some loss of bond strength with large drops in temperature since bond strength is typically developed mechanically. The low ultimate tensile strain limit and durability concerns of the glass fibers in moist and alkaline environments have also been raised (Bradberry 2001, ACI 2003). The major resistance to its expanded use, however, stems from its higher initial cost and a lack of experience with the material. Yet, as research continues to advance our understanding of the material and the number of successful implementations increase, these last two aspects will dissipate.

In a document intended to help describe the future of bridge engineering, the Transportation Research Board's Committee on General Structures identifies FRP as an area that will experience revolutionary changes over the next 20 to 30 years (TRB 2001). At the same time, it admits to the material's innate problems in "deflection, material ductility, creep,

reactivity with concrete and steel, and performance under long-term exposure to ultraviolet light and other environmental factors such as moisture, freeze-thaw, humidity, and external chemical attack." However, it proclaims that new design methods and testing standards will be developed to resolve these issues and extensive research will help make FRP a common, dependable material for bridge construction.

## 2.3 Shear Strength of GFRP-Reinforced Members

The current common method for the design of concrete bridge decks is presented in the AASHTO LRFD Bridge Design Specification (2002) and the AASHTO Standard Specifications for Highway Bridges (2002). The method involves analyzing the deck as a series of equivalent strips, the width of which are determined based on the type of deck and the direction of the primary reinforcement relative to the direction of traffic. The strips are treated as beams continuous over rigid pinned supports that represent the girders and the applied load per unit width of slab is found by dividing the factored wheel load by the strip width. Shear and moment envelopes are then developed for the worst-case positioning of truck loads and the critical location for negative moment and shear are found based on flange width and girder type. Shear resistance is calculated with one of the methods discussed later in this section, typically the ACI 440 equations in the case of GFRP-reinforced slabs. However, the specific guidelines in AASHTO LRFD regarding the equivalent strips for shear are vague, but it is assumed that the negative moment strip width is appropriate for shear near the girders.

Traditionally, one-way shear is not a case that is checked for common steel-reinforced concrete slabs. The commentary in AASHTO LRFD section C4.6.2.1.6 states:

> "Past practice has been to not check shear in typical decks. A design section for shear is provided for use in nontraditional situations. It is not the intent to investigate shear in every deck."

Additionally, Section 3.24.4 of the AASHTO Standard Specifications states:

> "Slabs designed for bending moment in accordance with Article 3.24.3 shall be considered satisfactory in bond and shear."

Although one-way shear of steel-reinforced concrete decks may not have been a concern, it should be checked for FRP-reinforced decks because of the lower modulus of elasticity of the reinforcement.

Extensive research has been conducted regarding the flexural behavior of FRP-reinforced concrete members, but less of an effort has been put towards the investigation of shear strength of such structural components. The transfer of shear within a member is managed through four mechanisms: shear strength of the uncracked concrete, aggregate interlock, dowel action, and residual tensile stresses across an inclined crack (Tureyen 2002). ACI prescribes the empirical equation shown as equation 2.1, which was developed for steel-reinforced concrete members.

$$V_c = 2\sqrt{f_c'}\, b_w d \qquad \text{(Eqn. 2.1)}$$

Where: $V_c$ = nominal concrete shear strength, lbs
$f_c$ = compressive strength of concrete, psi
$b_w$ = width of the member, in.
$d$ = effective depth, in.

The lower stiffness of GFRP rebar causes a member reinforced with this material to have a smaller depth to the neutral axis when compared to a similar steel-reinforced section. This results in larger crack widths that therefore penetrate deeper into the section, leaving a smaller region of concrete in compression. These wider cracks significantly reduce the contribution of aggregate interlock and residual tensile stresses and the smaller compression region results in lower shear resistance from the uncracked concrete. Further, the lower stiffness and transverse strength of the GFRP rebar leads to the assertion that the strength component attributed to dowel action is also reduced (ACI 2003, Tureyen 2002). This assembly of factors detrimental to the shear strength of the section leads to the general agreement that the concrete shear strength, $V_c$, of GFRP-reinforced members is considerably lower than the general lower bound of shear strength for steel-reinforced members shown in Equation 2.1.

In an attempt to study the behavior of GFRP-reinforced concrete decks in flexure, Michaluk, et al. (1998) tested eight one-way concrete slabs, five of which were reinforced with GFRP. Two of the other three were reinforced with steel and one with CFRP as control specimens. The intent was to observe the three classical modes of failure relating to under-reinforced, balanced, and over-reinforced conditions (rupture of reinforcement, simultaneous rupture of the reinforcement and crushing of the concrete, and crushing of the concrete, respectively). The specimens were 11.5 ft long and 3.28 ft wide and had a clear span of 10 ft. Two different slab thicknesses were used: 6 in. and 8 in. with a concrete cover of 1.5 in. The adjustment of the reinforcement ratios was handled with a combination of differing numbers of

bars and differing bar sizes. As a side note, this use of multiple bar diameters introduces the variable of interlaminar shear lag, which theoretically varies the effectiveness of the fibers within a GFRP rebar allowing those towards the outer edges to experience higher stresses than the fibers at the core.

The under-reinforced sections in this investigation failed as intended with rupture of the GFRP rebar. Both over-reinforced sections, however, failed in shear as opposed to the predicted crushing of the concrete. The researchers observed in both cases that cracks grew to extreme widths, significantly reducing the area of the compression zone in the concrete that could resist shear and virtually eliminating any contribution from aggregate interlock. The specimens failed at 8.4 kips and 17.7 kips, which were significantly lower than the predictions based on the Canadian Design Code of 37.9 kips and 56.1 kips, respectively. In response to this outcome, the researchers proposed adding a factor of the ratio of the FRP modulus of elasticity to that of steel to the ACI equation for shear strength of nonprestressed members with normal weight concrete and subject only to shear and flexure (ACI Eqn. 11-3, ACI 11.3.1.1). The proposed equation is presented as Equation 2.2 (modified to US Customary Units).

$$V_c = \frac{E_f}{E_s}\left(2\sqrt{f_c^{'}}b_w d\right) \qquad \text{(Eqn. 2.2)}$$

Where: $V_c$ = nominal concrete shear strength, lbs
$E_f$ = modulus of elasticity of concrete, psi
$E_s$ = modulus of elasticity of steel, psi
$f_c^{'}$ = compressive strength of concrete, psi
$b_w$ = width of the member, in.
$d$ = effective depth, in.

According to the authors, the prediction from this proposed equation is approximately 70% greater than the experimental results.

A study was performed by Deitz, et al. (1999) to further explore the possibility of using GFRP as a replacement for epoxy-coated steel rebar in bridge decks. A total of twelve reinforced deck panels were constructed for three reinforcement systems: all GFRP, all epoxy-coated steel, and GFRP top mat with epoxy-coated steel bottom mat.

The panels were tested in one-way flexure with span lengths of 7 ft and 9 ft. The GFRP-reinforced panels experienced a shear diagonal tension failure, which occurred well above the

strength predicted by Equation 2.2. Therefore, the researchers proposed modification of the equation by a multiplier of 3, as shown in Equation 2.3.

$$V_c = 3\frac{E_f}{E_s}\left(2\sqrt{f_c'}b_w d\right) \qquad \text{(Eqn. 2.3)}$$

According to Yost, et al. (2001), significant research regarding the shear strength of GFRP-reinforced concrete members was conducted in Japan with the same outcome: the shear strength of concrete members with GFRP as the longitudinal reinforcement is lower than members with steel longitudinal reinforcement. To provide further experimental data on this matter, Yost tested 18 GFRP-reinforced concrete beams without shear reinforcement. Six different reinforcement ratios were investigated, all over-reinforced, and three beams were tested for each level of reinforcement. The specimens were tested as simply-supported with span lengths of 7 ft. The specimen cross-sections and test setup are shown in Figure 2.1.

The failure mechanisms for all 18 beams were identical. The first observed cracks were flexural crack located between the load points where the moment was constant and the shear was zero. As the load increased, flexural cracks developed between the supports and the load points. Further increases in the load caused the cracks to incline more towards the load points. The flexural cracks furthest from the load points, where the shear would be the highest, developed into a shear crack in each specimen and led to the consistent diagonal-tension shear failure.

None of the GFRP-reinforced specimens reached the lower-bound ACI shear prediction calculated from Equation 2.1. Further, all specimens greatly exceeded the shear strength predictions obtained from the equation proposed by Michaluk et al. (Equation 2.2). The average specimen shear strength however, exceeded Equation 2.3, proposed by Deitz, by an average of 25%, which is conservative, but not grossly

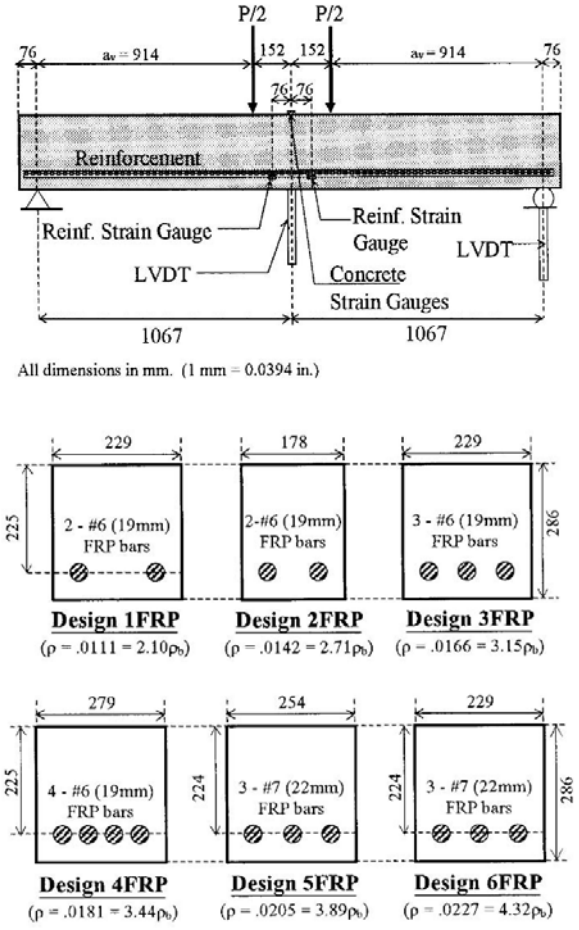


**Figure 2.1 - Specimen details and test setup for shear research conducted by Yost, et al. (Yost 2001, Reproduced by permission of ASCE)**

so. The excess in shear strengths of the specimens with respect to this model ranged from 6% to 56%, making this appear to be an acceptable model of the shear strength in this study.

Additionally, the authors pointed out that there was no evident correlation between shear strength and the reinforcement ratio. In steel-reinforced members, previous research has shown a decrease in shear strength for lightly reinforced sections, which was mostly attributed to the loss of aggregate interlock. The lower values for the modulus of elasticity of GFRP already affect the contribution of aggregate interlock through the allowance of wider cracks, so lighter reinforcement ratios had no apparent additional effect.

To specifically investigate the effect of the lower modulus of elasticity of GFRP rebar on the shear strength of reinforced concrete beams, Tureyen and Frosch (2002) conducted tests on nine concrete beams with differing types and ratios of reinforcement. Reinforcement ratios considered were approximately 1% and 2% and within each of these two series three FRP-reinforced beams (2 GFRP and 1 AFRP) and one steel-reinforced beam were considered. The specimens were 13 ft long, 18 in. wide, and 16 in. deep with effective depths of 14-3/16 in. The ninth beam tested was a steel-reinforced beam with a reinforcement ratio of only 0.36% to try to match the overall axial stiffness of the steel reinforcement with the FRP counterparts. Figure 2.2 shows the details of the specimen cross-sections and the test setup.

With regards to deflection, the study showed no significant difference between the different reinforcement types and ratios while the beams were uncracked. After the beams were fully cracked however, the stiffness differences between the specimens were found to be of approximately the same ratio as the ratio of the axial stiffness of the reinforcement between the specimens. In other words, the two GFRP-reinforced specimens and the low-reinforcement ratio steel section of the second series showed

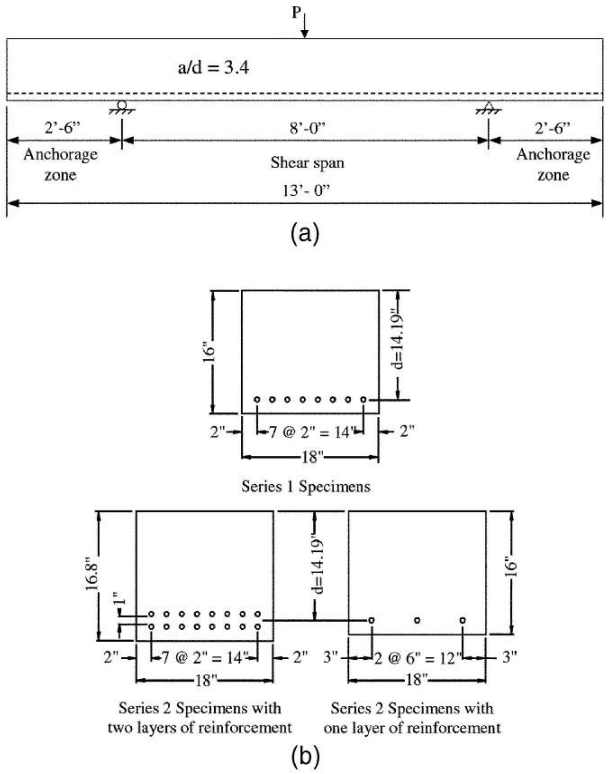


**Figure 2.2 - Specimen details and test setup for shear research conducted by Tureyen and Frosch (Tureyen 2002, Reproduced with permission of ACI)**

similar load-deflection curve stiffness. The ratio of stiffness of the 2.0% steel reinforced section to the similar GFRP-reinforced sections, however, was about 4.0, which was also the ratio of the steel modulus of elasticity to the FRP modulus of elasticity.

With regards to shear, the study found a relationship between the axial stiffness of the overall reinforcement and the shear strength of the section. For instance, the lightly-steel-reinforced section in the second series exhibited shear strength similar to that of the 2% GFRP-reinforced sections which had the same overall reinforcement stiffness. This led to the suggestion that members reinforced with either GFRP or steel would have the same shear strength if both members had the same effective reinforcement ratio, which is defined in Equation 2.4.

$$\rho_{eff} = \rho \frac{E_{rein}}{E_{steel}} \qquad \text{(Eqn. 2.4)}$$

Where: $\rho_{eff}$ = Effective reinforcement ratio
$\rho$ = Actual reinforcement ratio
$E_{rein}$ = Modulus of elasticity of reinforcement
$E_s$ = Modulus of elasticity of steel (29000 ksi)

Otherwise, the shear strength between the lesser and greater reinforced sections did increase with the greater reinforcement ratio, but not at the same multiplicative factor. The average increase in GFRP-reinforced shear strength from reinforcement ratios of 1% to 2% was 44%; whereas the shear strength increase for the steel-reinforced specimens in this situation was only 13%. The increase in shear strength for the 2% reinforced steel section over the lightly reinforced steel section, which is approximately a 500% increase in reinforcement ratio, was 56%.

The results were then compared to the ACI 440 recommended equation for shear strength of FRP-reinforced members shown in Equation 2.5.

$$V_{c,f} = \frac{\rho_f E_f}{\rho_s E_s} V_c \qquad \text{(Eqn. 2.5)}$$

Where: $V_{c,f}$ = nominal shear capacity of an FRP-reinforced concrete member
$\rho_f$ = FRP reinforcement ratio
$\rho_s$ = steel reinforcement ratio of equivalent section
$V_c$ = nominal shear capacity of a steel-reinforced concrete member

In Equation 2.5, the steel reinforcement ratio, $\rho_s$, is the ratio of the area of tensile reinforcement to the area of the gross cross section of a hypothetical steel-reinforced section with a flexural strength identical to the GFRP-reinforced section.

It was found that the ACI equation was quite conservative. The ultimate shear strength of the FRP-reinforced specimens were on average more than 400% higher for the 1% reinforcement ratio series and 300% higher for the 2% reinforcement ratio series. It was also noted that the FRP-reinforced members followed the same trends as the steel-reinforced members and incorporation of an effective reinforcement ratio was encouraged.

A later publication by the same authors, Tureyen and Frosch (2003), continued with the development of a model for shear strength that could be used for both GFRP- and steel-reinforced concrete beams. The model originated by using Mohr's circle to find the principle stresses on the concrete in compression and equating it to the tensile strength of concrete. The equation for the maximum shear stress and the flexural stress at the middepth of the compression zone were substituted into an expression developed from Mohr's circle that equated the principle tensile stress to the concrete tensile strength. The result is presented as Equation 2.6.

$$V_c = \frac{2}{3} b_w c \sqrt{f_t^2 + f_t \frac{\sigma_m}{2}} \qquad \text{(Eqn. 2.6)}$$

Where: $V_c$ = nominal concrete shear strength

$b_w$ = width of beam

$c$ = depth of compression zone

$f_t$ = tensile strength of concrete $\left(6\sqrt{f_c'}\right)$

$\sigma_m$ = flexural stress at middepth of compression zone

This model was compared to the results of 26 studies, which involved 370 shear tests including 44 FRP-reinforced specimens. The ratio of the measured to calculated shear strengths for each specimen was plotted against the effective reinforcement ratio to show general agreement with the model over the entire range of $\rho_{eff}$ with an average ratio of 1.18 and standard deviation of 0.15. The equation was then simplified to Equation 2.7.

$$V_c = K\sqrt{f_c'} b_w c \qquad \text{(Eqn. 2.7)}$$

Where: $K = \sqrt{16 + \frac{4\sigma_m}{3\sqrt{f_c'}}}$

The value of K was found to be relative constant at 5.5 for $\rho_{eff} > 0.8\%$ and subsequent consideration led to setting the variable to 5 in the model to provide conservative estimates of the shear strength and to simplify the model for the design process. The final proposed model is shown as Equation 2.8.

$$V_c = 5\sqrt{f_c'}b_w c \qquad \text{(Eqn. 2.8)}$$

Where: $V_c$ = nominal shear strength

$f_c'$ = specified compressive strength of concrete, psi

$b_w$ = beam width, in.

$c$ = cracked transformed section neutral axis depth, in.

$$c = kd$$

$$k = \sqrt{2\rho n + (\rho n)^2} - \rho n$$

$\rho$ = reinforcement ratio

$n$ = modular ratio

Research conducted by Cawrse (2002) at Virginia Tech on a bridge deck prototype again found the ACI 440 equation for shear (shown here as Equation 2.5) to be overly conservative. Cawrse tested a bridge deck measuring 17 ft 4 in. long and 24 ft wide with overhangs at each end. The deck was supported on three steel girders at spaced at 6 ft 6 in. on center and had overhangs of 2 ft 2 in. The intent was to validate the deck design prior to construction of the Route 668 Bridge over Gills Creek in Franklin County, Virginia, which was designed with GFRP reinforcement as top mat reinforcement in one of the three spans.

The low strength prediction by the ACI 440 equation led to the predicted failure mode during cantilever testing of the overhangs to be one-way shear. However, both overhangs failed in two-way (punching) shear at loads of 86 kips and 78 kips, which is much greater than the ACI 440 predicted one-way shear strength of 10.3 kips. Although the one-way shear strength was not discovered, the extremely higher than expected failure loads and alternate mode of failure suggest excessive conservatism of the ACI 440 equation.

## 2.4 Strength Degradation of GFRP Reinforcement

One of the significant reasons currently preventing the widespread use of GFRP as reinforcement for concrete structures is that the long term effects of environmental factors and service loadings on the material's durability are not fully understood (Micelli 2004). Substantial

research has been conducted to address this concern, but the majority has been focused on aerospace applications where the material would be installed in an industrial process. Civil engineering projects, however, would place the material under the harsher conditions of an outdoor construction site. Although strength degradation can be caused by a number of factors, particular concern is focused on loss caused by moisture retention, the high pH of pore water during hydration of the concrete, and severe long-term loading conditions.

Research conducted by Laio, et al. (1998) specifically focused on the details related to civil engineering applications. The researchers conducted four-point flexural and tensile tests on pultruded GFRP coupons. The specimens were cut from GFRP plates with alternating layers of unidirectional fibers.

For this thesis the tensile tests performed in this study are of particular interest. The researchers aged the specimens in de-ionized water for 9120 hours at room temperature. It was found that the GFRP coupons experienced a 23% decrease in tensile modulus and 29% decrease in tensile strength when compared to unaged specimens.

Research conducted by Bhise (2002) at Virginia Tech investigated the effects of the concrete environment on the material properties of GFRP rebar, specifically considering the higher temperatures and alkalinity. The specimens were encased in cement mortar and soaked in one of three calcium hydroxide solutions maintained at temperatures of 30, 45, or 57 ˚C.

Tensile tests were conducted on five specimens per batch after 10, 30, 60, 90, and 180 days to track the strength loss and compare it to strength degradation models. After 180 days of exposure in this harsh environment, the bars maintained at 57 ˚C experienced a 43% loss of tensile strength 18% reduction of the modulus of elasticity.

Micelli (2004) conducted research on several different types of FRP bars to observe the effect of alkaline pore water conditions and an accelerated aging procedure using freeze-thaw, high relative humidity, high temperature, and high ultraviolet radiation cycles. Two types of GFRP bars and three types of carbon FRP (CFRP) bars were considered, each with different resin matrices. The bars were conditioned with the environmental cycling procedure and different lengths of alkaline exposure. Changes in the longitudinal and transverse properties were investigated with tensile tests and short beam tests, respectively.

It was found that the type of resin matrix used greatly effects the ability of the bar to resist environmental attack. The study showed that GFRP specimens with a polyester resin

matrix experienced a loss in ultimate strength of 40% after being exposed to the alkaline solution for 42 days, which was the simulated time for 28 years. GFRP bars with a thermoplastic matrix experienced no strength loss under the same conditions. Additionally, neither specimen type experienced any appreciable loss of strength due solely to the accelerated aging procedure nor was the modulus of elasticity greatly affected under any of the conditions for any of the bars.

A scanning electron microscope (SEM) was used to observe the damage to the bars caused by the alkaline exposure. The E-glass fibers at the edge of the bars containing the thermoplastic matrix showed signs of damage including complete fiber breakages, but the fibers in the core of the bar were substantially intact. In the other bar type, however, the polyester resin was found to be extensively cracked, which allowed deeper penetration of the alkaline solution and subsequent damage to the E-glass fibers within the core of the bar.

With regards to GFRP rebar, this research showed the importance of the matrix in protecting the glass fibers from environmental attack and that the high alkalinity of concrete pore water can adversely affect the ultimate tensile strength. To limit this strength loss, the researchers recommended the use of a thermoplastic resin matrix as opposed to a polyester resin matrix.

## 2.5 Conclusions

It is evident from the results of the previous research efforts detailed in this chapter that there is a need for better methods to predict the shear strength of concrete members with GFRP rebar as the primary longitudinal reinforcement. The majority of research that has been conducted in this area of study has been on reinforced concrete beams rather than reinforced concrete decks. Bridge decks, with shallower effective depths and wider widths, may experience different mechanisms than their beam counterparts, which may be leading to some of the discrepancies between the studies. Additionally, all research leading to the development of equations for shear strength prediction was conducted on simply-supported specimens. However, bridge decks are typically continuous elements over several girders.

The high level of interest in the use of this material, particularly in the reinforcement of bridge decks due to its corrosion resistance, requires that a better understanding of its characteristics be developed. Further research and development in order to more fully understand or offset GFRP strength loss due to environmental factors will ease concerns of

engineers and administrators and lead to the expanded use and lower cost of the material, ultimately resulting in the increased service life of the bridges in which it is used.

# *Chapter 3 - Experimental Methods*

## 3.2 Shear Strength

### 3.2.1 Introduction

The evaluation of the shear strength of concrete decks reinforced with GFRP was performed by constructing and subsequently testing four specimens of differing widths. The design of the experimental decks was intended to mimic the characteristics of a recently constructed bridge on Route 668 over Gills Creek in Franklin County, Virginia. One span of this three-span structure utilized GRFP as the top mat deck reinforcement and was the subject of a constructability study and field performance evaluation conducted at Virginia Tech (Harlan 2004). Additionally, the general design also matched the decks used for the strength degradation research discussed in Section 3.2 of this document. Therefore, the specimens could be used for the study of both shear strength and strength degradation.

The specimens were each tested as a two-span continuous deck on three parallel supports with loads on either side of the center support. The intent of this phase of the research was to evaluate the shear failure load and failure type and to analyze the stress distribution in the rebar along the width of the deck throughout the loading plan. Testing was conducted at the Structures and Materials Laboratory at Virginia Tech.

### 3.2.2 Specimen Materials and Construction

For the shear strength investigation four slabs were constructed. These specimens were 15.25 ft wide (transverse to the direction of traffic) and were 1 ft, 2 ft, 3.5 ft, or 5 ft long (in the direction of traffic). The top mat reinforcement consisted of GFRP rebar and the bottom mat was made up of steel rebar.

The top mat reinforcement for the decks was comprised of No. 6 GFRP rebar in both directions obtained from Hughes Brothers, Inc. The bars were helically wrapped and had a mild level of sand impregnation to increase the quality of the bond between the concrete and the rebar. The makeup of the bars was 73% E-glass fibers and 27% vinyl ester resin by volume. The ultimate strength and modulus of elasticity of the bars were determined through tensile tests conducted at the end of experimentation. The average ultimate strength and modulus were found

to be 94 ksi (14 specimens) and 6200 ksi (29 specimens), respectively, for unused rebar. Details of these tests are presented in the discussion of the strength degradation portion of the research.

The bottom mat reinforcement consisted of No. 6 black steel rebar ($f_y$ = 60 ksi) in the transverse (long) direction and with No. 4 black steel rebar in the longitudinal (short) direction.

Forms were made using ¾ in. plyform sheets, which are plywood sheets with no knots on the concrete side and are precoated with form release oil. Support for the plyform was provided by standard 2x4 lumber on the sides and 4x4 lumber on the floor as shown in Figure 3.1.

**Figure 3.1 - Construction of 1 ft and 2 ft decks**

Prior to placing the mats, strain gages were applied to selected longitudinal bars of both the top and bottom mats. Gages were placed only in negative moment locations (i.e. over the edges of the center support) on the GFRP bars and in both negative and positive moment regions for the steel bars. The gage layout for each of the decks is presented in Appendix B of this report. The gage application and waterproofing processes are detailed in Appendix C of this report.

The steel bars were placed and tied to form the bottom mat with a clear cover of 2 in. and 8 in. center-to-center spacing of the transverse bars. The center-to-center spacing of the steel longitudinal bars in the 2 ft, 3.5 ft, and 5 ft decks was 5 ¾ in. between the positions of the supports. An additional three bars were placed evenly in each overhang of the decks. No bottom mat longitudinal bars were placed over the locations of the supports. The purpose of this layout was to match the rebar layout in the strength degradation decks discussed later to allow direct comparison of specimens. Figure 3.2 illustrates this spacing for one of the strength degradation decks. Steel bar chairs with a height of 2 in. were used beneath the transverse steel rebar to ensure the correct bottom concrete cover.

The GFRP bars were next placed and tied to form the top mat reinforcement with a clear cover of 1-5/8 in., 4 in. center-to-center spacing of the transverse bars, and typical 6 in. center-to-center spacing of the longitudinal bars. Epoxy-coated steel rebar chairs with a height of 4.5 in. were used beneath the longitudinal bars to correctly position the top mat reinforcement to meet the required top concrete cover. Both the steel and GFRP bars were tied together using epoxy coated "pigtail-type" rebar ties. The bar placement details for each deck are presented in Appendix D.

**Figure 3.2 - Bottom mat bar spacing**

The strain gage wires were run along the bars to a single exit slot in the form on one of the long sides of the specimen and wires were attached to the bars using plastic zip ties. Prior to pouring the concrete, hooks made of No. 3 steel rebar were installed to facilitate handling of the decks after the concrete had cured. Additionally, the GFRP top mat was tied with plastic zip ties to the steel bottom mat to prevent the top mat from floating off the chairs during concrete placement. Short lengths (less than 4 in.) of excess GFRP rebar were tied to both ends of two transverse GFRP bars at the corners of the mat so that they contacted the short side forms to ensure that the mat would not shift. This is shown in Figure 3.3 for one end of the 1 ft wide specimen

**Figure 3.3 - End of the 1 ft wide specimen**

The concrete used for the specimens was a VDOT A4 mix obtained from Marshall Concrete of Christiansburg, Virginia. The mix has a maximum aggregate size of ¾ in., a specified compressive strength of 4000 psi, a water-cement ratio of 0.45, typical slump of 2 in. to

4 in., and an air content of 6.5% ± 1.5%. Concrete was placed using a ¾ $yd^3$ bucket lifted by the overhead lab crane. The concrete was thoroughly vibrated to remove any voids and prevent honeycombing. A vibrating screed was used to strike off the concrete to the level of the top of the formwork and the surface was finished with a smooth float. Fourteen 4 in. diameter concrete cylinder specimens were also made to monitor the strength gain of the concrete as it cured and to determine the strength at the start and end of the testing period.

The decks were covered with burlap, watered daily, and covered with thick plastic sheeting for seven days. The cylinders were cured in the same manner as the deck and the concrete compressive strength data is shown in Table 3.1.

***Table 3.1 - Shear Deck Concrete Strength Values***

| Age | Compressive Strength | Average Compressive Strength |
|---|---|---|
| 7 days | 4417 psi<br>4616 psi | 4520 psi |
| 14 days | 5809 psi<br>6128 psi | 5970 psi |
| 28 days | 6167 psi<br>5809 psi | 5990 psi |
| 58 days | 6645 psi<br>6685 psi | 6670 psi |

Concrete strength gain curves are shown in Appendix A. All side forms were stripped after seven days and bottom forms were removed when the specimens were moved for testing.

### 3.2.3 Experimental Setup Details

The experimental setup was consistent throughout all phases of this research involving the decks. Figure 3.4 is a photograph of the setup for the 1 ft shear specimen. A more general diagram is presented in Figure 3.5. The slabs were placed across three supports, which were W27x94 steel sections, spaced at 6 ft-6 in. center-to-center. This section was chosen because the flange width was similar to the supports in the weigh station

**Figure 3.4 - Lab setup with the 1 ft deck**

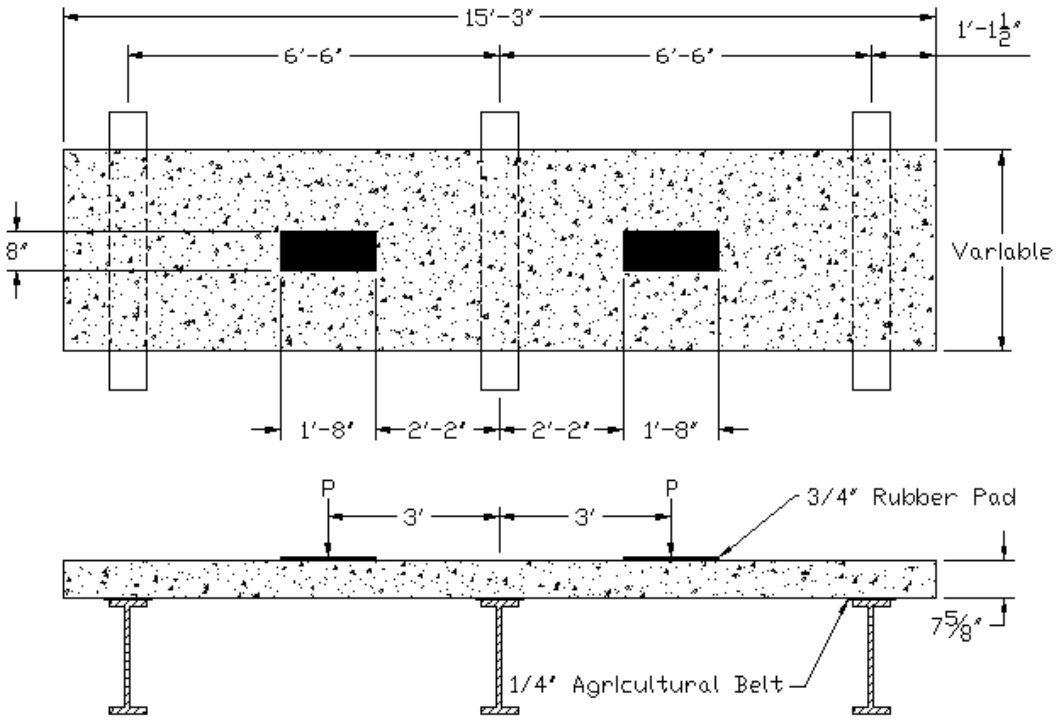


**Figure 3.5 - General shear specimen design**

. Each support had a piece of ¼ in. thick textured rubber agricultural belt placed on the top flange. The deck rested on the belts, which minimized stress concentrations. A load frame constructed of A36 steel members suspended a 500 kip hydraulic ram over the center support. A spreader beam was used to distribute the load from the ram to two load points spaced 6 ft apart center to center, centered across the middle support to model the standard AASHTO truck axle configuration. The size of the spreader beam varied as necessary to meet load expectations for each deck. Depending on the depth of the spreader beam used, the load was transferred to the deck at the load points through either a prefabricated steel transfer tower, shown in Figure 3.6, or a stack of steel plates, shown in Figure 3.7. In tests where steel plates were used to transfer the load, the plates were stacked so that the spreader beam was high enough above the deck to allow

**Figure 3.6 - Point load setup for the 1 ft deck**

**Figure 3.7 - Point load setup for the 5ft deck**

cracks to be seen at the center of the deck. Further, they were stacked to allow the load to spread, assuming a 45˚ angle, to the entire length of the tire patch. The load was ultimately transferred to the deck by 1 in. thick rubber pads designed to resemble a truck tire patch. The dimensions were calculated in accordance with the AASHTO LRFD Specification (2002) as shown in Equations 3.1 and 3.2.

$$\text{Tire Width} = \frac{P}{0.8} \qquad \text{(Eqn. 3.1)}$$

$$\text{Tire Length} = 6.4 \times \gamma \times \left(1 + \frac{IM}{100}\right) \qquad \text{(Eqn. 3.2)}$$

Where: P = Wheel load (kips)

$\gamma$ = Load factor

IM = Impact factor, %

Given a standard wheel load of 16 kips, a load factor of 1.0, and an impact factor of 30%, the wheel patch width was calculated as 20 in. and the wheel patch length was calculated to be 8.3 in. The tire patch used was a 20 in. × 8 in. neoprene pad.

## 3.2.4 Shear Strength Test

### *3.2.4.1 Introduction*

The testing process was designed to simulate a worst case negative live load moment over the center support using an AASHTO truck tire spacing. During the test, records were made of the strain in the GFRP and steel rebar, the deflections of the spans, the applied load, the widths of cracks, and the strain in the top of the deck.

### *3.2.4.2 Shear Strength Test Instrumentation*

As noted in section 3.1.2, each deck specimen was instrumented with strain gages at predetermined locations on both the GFRP and steel rebar to measure bar strain. After determining the modulus of elasticity from the GFRP rebar tensile tests, the stress in each bar could be calculated from Equation 3.3.

$$\sigma = E \times \varepsilon \qquad \text{(Eqn. 3.3)}$$

The gage layout and gage properties are shown in Appendix B.

The procedure used to apply the strain gages to the rebar and the gage waterproofing process are detailed in Appendix C. Standard strain gage wire was used for the connection between the gages and the data acquisition system. Figure 3.8 shows a strain gage applied to a GFRP bar with strain gage wire soldered to the tabs prior to waterproofing.

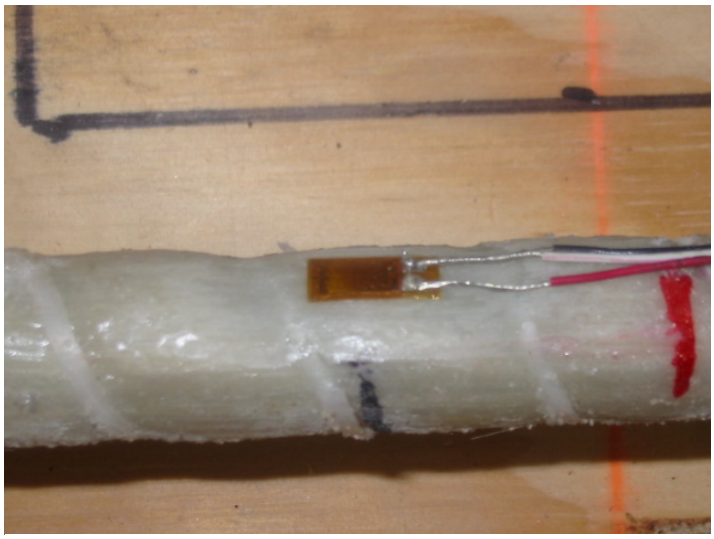

**Figure 3.8 - Typical GFRP strain gage prior to waterproofing**

Since the resistance read by the data acquisition system included the resistance of the wires, which is dependent on the length of the wire, and because the wires for each strain gage were of different lengths, the gage factor input into the data acquisition system for each strain gage was modified to account for the resistance of the wires. To determine the resistance in each individual wire, the resistance of the shorted pair of wires for the specific gage was found with an ohmmeter just before the gages were connected to the system and divided by two. The equation used to adjust the gage factors was provided in documentation from the gage manufacturer, MicroMeasurements, and is shown here as Equation 3.4.

$$GF_{mod} = GF_{original} \times \frac{R_{gage}}{R_{gage} + R_{wire}} \qquad \text{(Eqn. 3.4)}$$

A listing of individual gage factors used for each gage follows the diagrams and gage properties in Appendix B. The typical difference was insignificant at approximately 0.3%. However, the adjustment was made anyway since the error of the gage itself was only 0.5%.

Displacement measurements of each span were recorded with ST-type wirepots. These devices were connected to the slab below the center of the load points with a screw twisted into a plastic anchor in the bottom of the deck. The wirepots were carefully placed directly below the anchor using a plumb bob as a guide. One wirepot was used for each span of each test.

Applied load was measured with a 500 kip load cell placed between the top of the hydraulic ram and horizontal beam of the load frame. The load cell was calibrated through a compression test in the SATEC machine in the lab. The load applied throughout the test was

displayed on the computer monitor to allow for manual notations of loads corresponding to crack formation and widths.

Crack widths were measured at various points during the testing process using a combination of a crack microscope and a crack card. The card was typically used either when cracks were not in an area of particular emphasis (positive moment regions of the deck) or when the cracks became significantly wide. The measured crack widths were then compared with the results of the Gergely-Lutz crack width equation.

A demountable mechanical strain gage, or DEMEC gage, was used to measure the strain in the top of the deck over the center support. Prior to the start of the test, DEMEC points, which are small, flat pieces of metal with an indentation in the middle, were applied to the deck with epoxy. The points were placed using a spacing bar that came with the gage to set them at an approximately equal gage length of 8 in. In addition to providing strain of the top surface of the uncracked deck during the first portion of the test, the DEMEC measurements also served to provide indications of the formation of a crack within the particular gage length. After initial cracking, but prior to significant crack growth, the DEMEC gage also provided an additional method to measure crack widths. After the application of further, more substantial loads, however, the formation of multiple cracks between the same two DEMEC points made it impossible to determine individual crack width to any level of accuracy through this method. DEMEC data is tabulated in Appendix E.

#### *3.2.4.3 Shear Strength Testing Procedure*

Values from the strain gages, load cell, and wirepots were collected using a computer-based data acquisition system. The System 6000 was used for all decks except the 2 ft wide specimen, which was monitored by the System 4000. The Strain Smart software was used to record and manage data during the tests. This software provided instantaneous on-screen displays of various values including the applied load so that the load could be recorded with the manual DEMEC and crack width measurements.

The load was applied through the hydraulic ram using a two-speed hand pump for the 1 ft and 2 ft wide decks to allow for more careful control of the loading, particularly at lower values. A power hydraulic pump was used for the 3.5 ft and 5 ft wide decks because their failure load exceeded the capacity of the hand pump.

Just prior to zeroing all inputs on the data acquisition system, a settling load of 2 to 5 kips was applied and subsequently removed from each deck. All channels on the data acquisition system were then zeroed and the load was applied in small increments until the first crack in the deck was detected. DEMEC measurements were taken at each pause in this loading process to measure the strain in the top of the deck prior to cracking and also to serve as an indicator of probable crack formation.

Once the cracking load was determined, each deck was unloaded and reloaded to its calculated service load. This cycle was repeated three times and for each cycle the decks were brought directly to service load, DEMEC and crack measurements were taken, and the load was subsequently reduced directly to zero. The appropriate service load per patch per foot length of deck was calculated for each specimen by dividing the product of an AASHTO truck tandem wheel load (16 kips) and an impact factor of 1.33 by an effective width. The effective width, which was determined to be 5 ft-7 ½ in., was calculated from Table 4.6.2.1.3-1 of the AASHTO LRFD Bridge Design Specifications (1994) and the equation is presented here as Equation 3.5. This was then multiplied by the actual deck width to find the service load per patch as shown in Equation 3.6.

$$b_{eff} = 48 \text{ in.} + 0.25S \qquad \text{(Eqn. 3.5)}$$

Where: $b_{eff}$ = Effective Width for shear in negative moment region, in.

$S$ = Spacing of supports, in.

$$P_{service} = \frac{P \times IM}{b_{eff}} \times b_{act} \qquad \text{(Eqn. 3.6)}$$

Where: $P_{service}$ = Service load per patch

P = Tire load (16 kips)

IM = Impact factor (1.33)

$b_{eff}$ = Effective width of deck (5 ft-5/8 in.)

$b_{act}$ = Actual width of specimen

After the third time that the service load was reached during the cycling, the load was increased in intervals until failure of the deck. At each interval, the deck was inspected for the formation of new cracks and measurements of crack widths and DEMEC readings were recorded.

Unfortunately, both the 3.5 ft and 5 ft tests were stopped prematurely and restarted. In the case of the 3.5 ft deck, the spreader beam used was believed to be of 50 ksi steel, but was found to be 36 ksi steel after the beam yielded and had to be replaced with a larger beam. In the case of the 5 ft deck, the failure load of the deck exceeded the capacity of the hand pump being used. In both cases, it was determined that the unintended "cycling" of the experiment had negligible effect on the results and in each case the second "cycle" skipped the service load portion of the procedure and went directly to the failure load in increments.

## 3.3 GFRP Strength Degradation

### 3.3.1 Introduction

The strength degradation of the GFRP bars was investigated through three types of tests: a field-based performance test of a GFRP-reinforced concrete deck subjected to high truck loadings, a lab-based test of three decks, each treated differently between construction and testing, and a series of tensile tests on the GFRP rebar extracted from the different decks.

As noted previously, the general design for the two additional decks built for this portion of the research matched the shear deck design so that direct comparison of the specimens was possible.

The intent of this phase of the research was to evaluate the loss of strength and stiffness of the GFRP rebar due to a variety of factors. Field tests were conducted at the I-81 truck weigh station in Troutville, Virginia, and lab tests were conducted at the Structures and Materials Laboratory at Virginia Tech.

### 3.3.2 Reinforced Concrete Deck Tests

This portion of the research involved two identical decks reinforced with GFRP rebar in the top mat and steel rebar in the bottom mat. The first deck was installed in the I-81 truck weigh station in Troutville, Virginia, where it was exposed to a severe level of truck loadings and environmental factors such as weather and deicing chemicals. The deck was in place in the weigh station for approximately fourteen months. The second deck was stored in the Structures and Materials Laboratory at Virginia Tech for the same period of time. The lab specimen was maintained in a climate-controlled environment and was not subjected to significant loadings.

This portion of research was conducted in two major phases. First, tests were conducted on the weigh station deck with live truck traffic during which rebar strain data and truck weights

were recorded. Second, the weigh station deck, after being in service, and the lab deck were both tested to failure in the same manner as the shear decks discussed in Section 3.1.

#### *3.3.2.1 Specimen Materials and Construction*

The two decks used for the strength degradation portion of the research were designed similarly to the shear decks discussed previously. The primary difference in the design was that the thickness of these decks was adjusted to match, as closely as possible, the grade of the roadway around the test bed at the weigh station. The beams in the test bed, which is discussed in more detail in Section 3.2.2.2, experienced differential settlement during previous projects prior to this research. As a result, in order to match the grade at the site, the thickness of the decks was modified so that the completed deck was non-prismatic. Although grade matching was not an issue for the lab deck, the same thickness adjustments were made to it as well so that a direct comparison between the two decks could be made. The final measurements of the decks are presented in Figure 3.9. The clear cover for the top mat was 2-1/8 in. and for the bottom mat was 1-1/2 in.

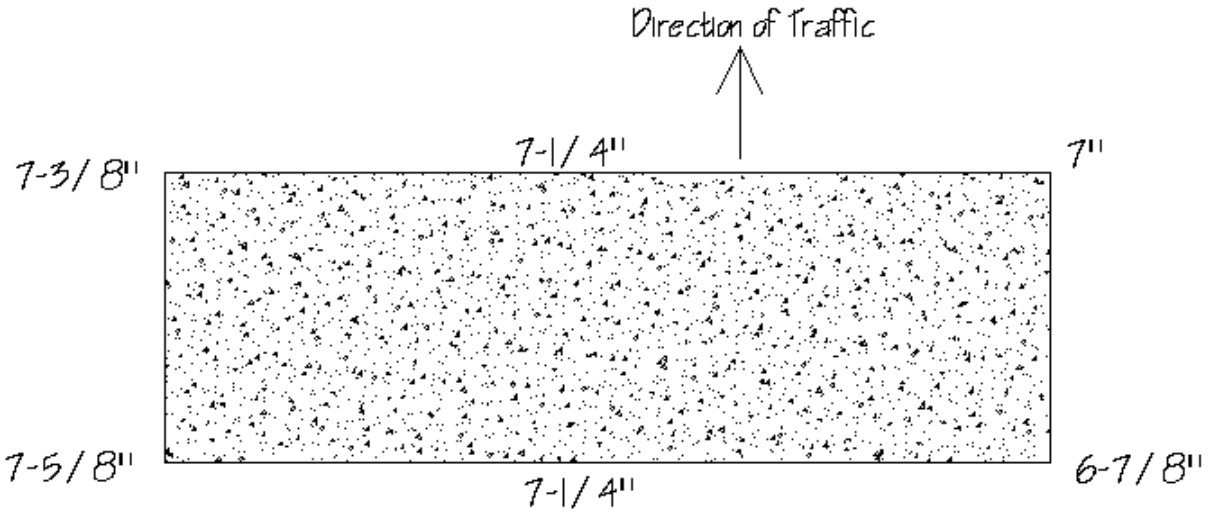


**Figure 3.9 - Final deck thicknesses of weigh station specimen**

The general construction process for these two decks was, for the most part, identical to the shear decks and, for brevity, will not be repeated here. One primary difference between the two processes, however, was in the procedure used for waterproofing the strain gages. Specifically, flux solvent was applied to the gage terminals to remove excess flux from the soldering process and the waterproofing procedure followed the instructions outlined in instruction bulletin B-147-5 of Vishay Micro-Measurements Division (Vishay 2002). In accordance with these guidelines, Teflon tape was used in place of the acrylic coating to protect

the gage and the terminals in order to insulate "against electrical leakage, and minimize gage resistance shifts during the cure cycle." The lead wires were primed with a 50:50 mixture of MEK (methylethyl ketone) and M-Coat B (nitrile rubber) to form a good bonding surface and allowed to dry overnight. M-Coat J, a two-part polysulfide liquid polymer compound, from an M-Coat J-1 kit was applied to the gage and lead wires. Care was taken to thoroughly coat the prepared area as well as underneath the lead wires. It should be noted that the percentage of gages that survived casting with this waterproofing process was much lower than that used for the shear decks. However, the specific factor leading to this success rate difference between the two application methods is not clear. It is believed that the use of the flux solvent may have inadvertently reduced the quality of the solder connection between the lead wires and the gage terminals. However, a failure of the Teflon tape protection layer could also be easily argued. An example of gages protected with the M-Coat J environmental protection coating is shown in Figure 3.10. Gage layouts and properties for the strength slabs are presented in Appendix B.

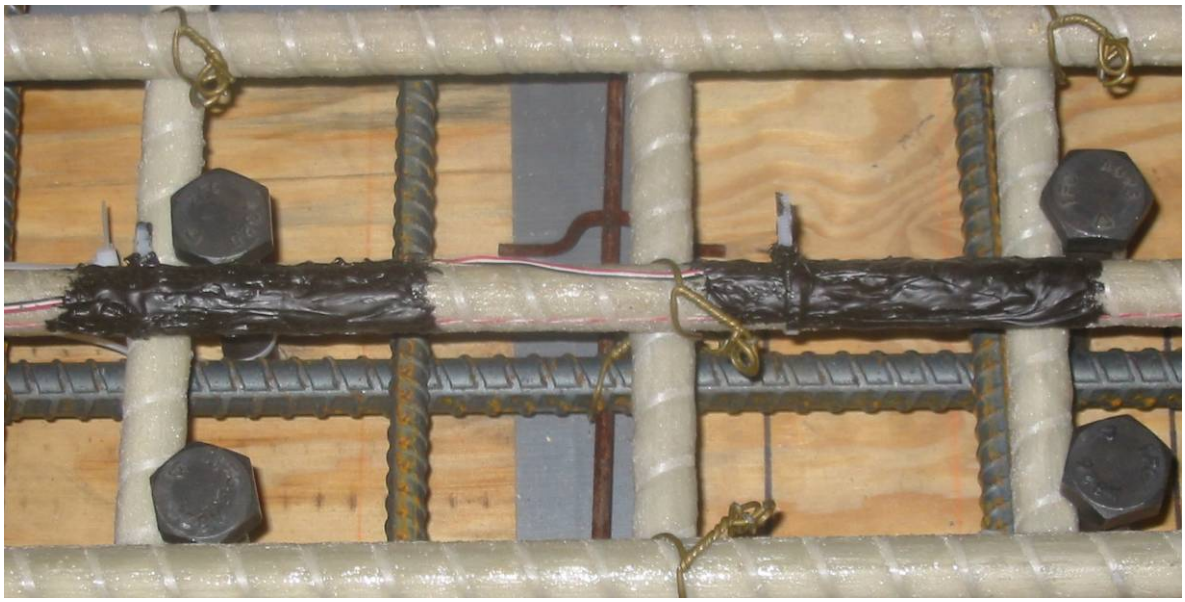

**Figure 3.10 - Strain gages in the lab deck protected with B-147-5 waterproofing method**

To connect the weigh station deck to the steel beams in the test bed at the weigh station, ½ in. diameter A325 bolts were positioned in the formwork and stabilized by tying them to the reinforcement mats with plastic zip ties. Each connection consisted of four bolts, two on each side of the beam flange, and two 6 in. x 6 in. x ½ in. steel plates, one on each side of the flange. Each plate was held by a pair of bolts, was spaced from the underside of the deck with washers,

and fixed with nuts so as to pinch the top flange of the beams in the weigh station test bed. This connection is illustrated in Figure 3.11.

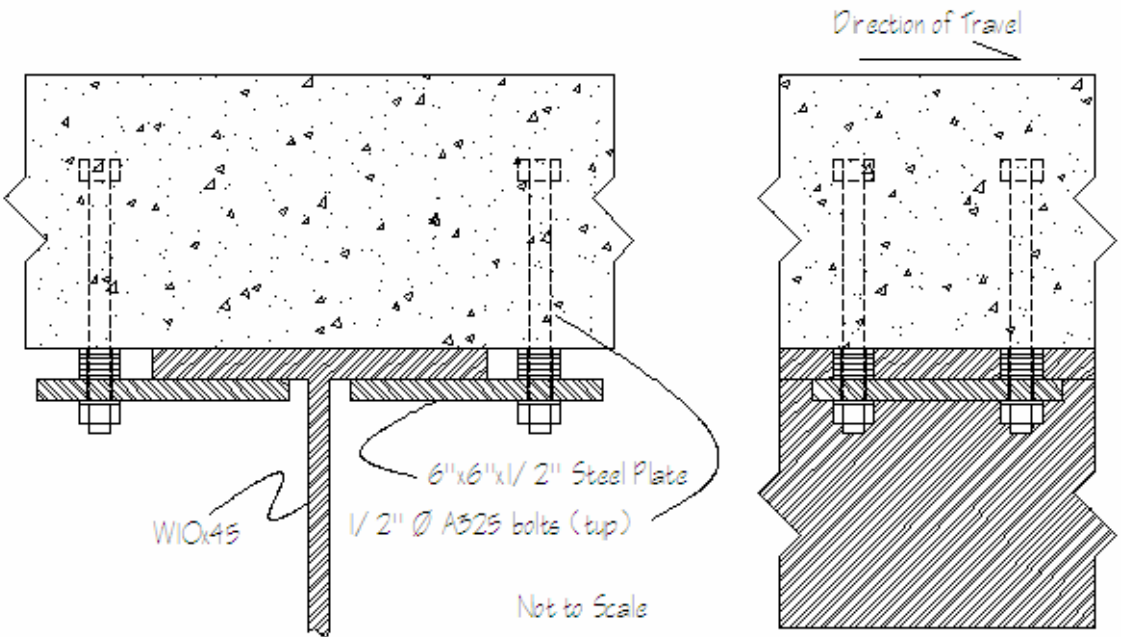


**Figure 3.11 - Diagram of deck connection in test bed. Left image is in direction of traffic. Right image is perpendicular to traffic.**

### *3.3.2.2 Weigh Station Test Bed Details and Installation*

In the fall of 1999, researchers at Virginia Tech worked to design and construct a site for testing composite bridge decks at a weigh station on I-81 in Troutville, Virginia. This test bed, which is located in the approach lane to the northbound weigh station scale, allowed for a low risk research site with a high volume of traffic. In June 2005, weigh station records showed that an average of 252,000 trucks passed through the weigh station (1,455,000 from January 1 to June 23, 2005); of this traffic, the personnel at the weigh station estimated that 60% went across the northbound scales, which would also require them to pass over the test bed.

The test bed was constructed in November, 1999, and consists of three W10x45 steel beams, spaced at 6 ft-6 in., resting on a reinforced concrete slab, all below the roadway grade. Steel access panels were installed in front of and behind the specimen location to allow easier installation of decks. The bed was designed for a specimen length (in the direction of traffic) of 5 ft and width of 15 ft-3 in. A drain located in the test bed prevents water from ponding beneath the specimen and two conduits extend below grade from the test bed to the roadway shoulder to carry wires for sensors to a data collection system. A general plan view of the test bed is shown in Figure 3.12, but a more detailed explanation of the design and construction of the site can be

found in Temeles (2001). The test bed is shown during installation of the weigh station specimen on December 10, 2002, before placement of the steel access panels in Figure 3.13 and during panel placement in Figure 3.14.

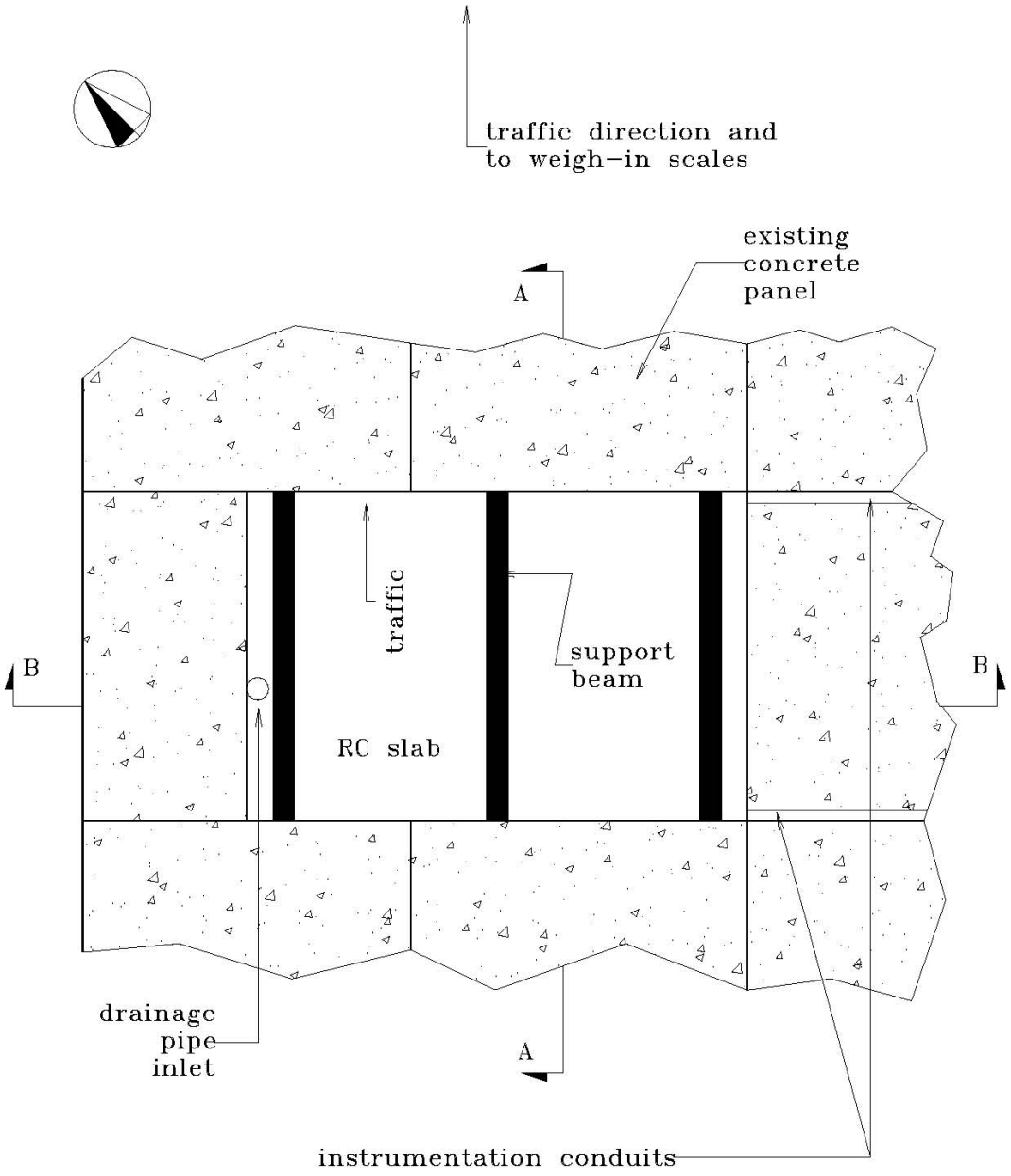


**Figure 3.12 - Plan view of bridge deck test bed at Troutville Weigh Station (Temeles)**

**Figure 3.13 - Installation of weigh station specimen on 12/10/2002**

**Figure 3.14 - Installation of weigh station specimen on 12/10/2002.**

As noted previously, over time the test bed beams experienced differential settlement. This is probably due to the fact that most of the traffic crossing the test bed favors the left portion of the lane, putting the majority of the load on the leftmost and center beams. In an effort to counteract this settling and provide a smooth driving surface, the thickness of the weigh station specimens for this research was modified to fit the bed and meet the grade of the lane. The original design of the test bed was for a 6 ¾ in. thick GFRP deck, but measurements taken during the summer of 2002 showed that the settlement of the bed was as shown in Figure 3.15.

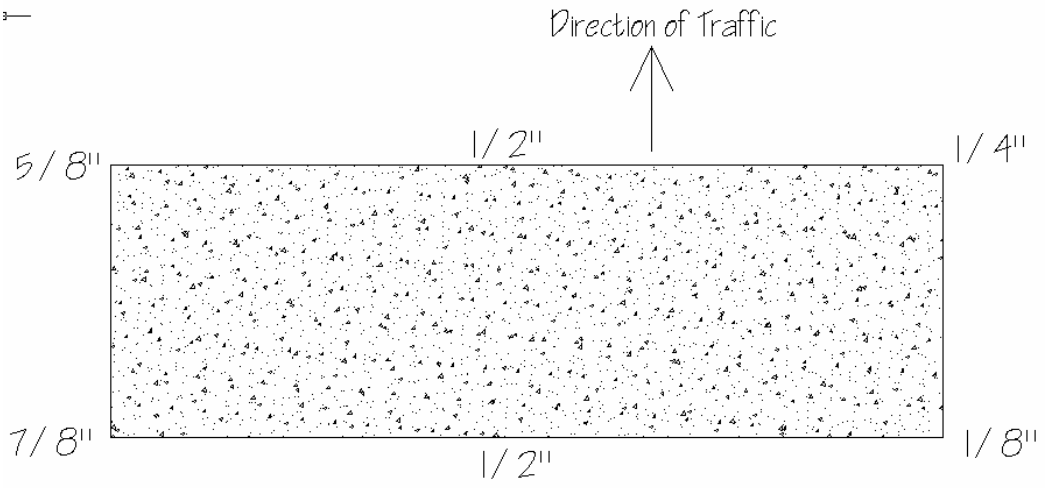


**Figure 3.15 - Settlement of the beams in the weigh station test bed**

These settlement measurements were used to determine the deck thicknesses as presented previously in Figure 3.9.

The weigh station specimen was constructed in the lab simultaneously with the lab specimen and, after being allowed to cure for almost a month, was transported to the weigh station and installed on December 10, 2002, with the assistance of a work crew from the Salem Residency of the Virginia Department of Transportation. The deck matched the grade of the travel lane reasonably well, although it was slightly thick on the right edge. Initially, however, the steel access panels on either side of the deck remained in their original position and, as a result, after installation a drop of approximately ½ in. in front of and behind the deck was created in the lane. There was concern that this vertical variation between the surface of the panels and the surface of the deck would lead to damage of the forward edge of the deck as trucks hit it, so an approximately 45˚ chamfer was cut into the forward edge of the deck as a temporary solution, as shown in Figure 3.16. The access panels were raised two days later with steel shims.

**Figure 3.16 - Chamfering the forward edge of the weigh station specimen**

#### *3.3.2.3 Weigh Station Strength Degradation Testing Procedure*

In an effort to compare performance changes over time, tests were conducted on the specimen installed at the weigh station twice during the fourteen months it was in place. The first test was conducted on August 20, 2003, and the second test was conducted 195 days later on March 2, 2003.

The procedure involved recording the strains experienced by the deck using the embedded strain gages as trucks crossed the specimen. The strains were recorded with a Megadac data acquisition system, which was powered by a gas generator and stored and operated from the back of a cargo van. The wires from the strain gages in the deck were routed through a conduit from the test bed to the shoulder where they were stored inside a thick plastic bag in a below-ground access box. All wire splices were sealed with waterproof electrical tape. However, despite all the precautions made, moisture was found on the wires before connecting them to the Megadac. It is believed that this moisture may have been at least partially responsible for an increase in 60Hz noise in the collected data.

Since there was no control over how the trucks crossed the deck, four different colored marks were made on the rear edge of the deck (the long side closest to the weigh station tower) to help determine the position of the trucks as they crossed. One mark was made at the centerline of the deck and subsequent marks were made at 1 ft spacings towards the right side of the lane. The mark closest to the outside edge of each truck's right front tire was recorded along with the dataset number for the strain data recorded for the particular truck.

After each truck passed the test bed, the weigh station's weigh-in-motion system directed the trucks to either continue back to the highway or to be weighed on the more accurate scales. The weights of each truck that was stopped for more accurate weighing and for which strains were measured were recorded with the appropriate dataset number. The recorded weights for each truck included data for the front, drive, and trailer axles and total weights.

This data and the results are presented and discussed in Chapter 4. The weigh station specimen was removed from the weigh station on March 2, 2004, for further testing at the Structures and Materials Laboratory at Virginia Tech.

#### *3.3.2.4 Strength Degradation Lab Testing Procedure*

The procedure used for testing the strength of both the lab and the weigh station specimens was identical to that used in the shear strength investigation discussed previously.

Bar strains were recorded using the embedded strain gages and the gage factor of each gage was modified to consider resistance in the lead wires as before using Equation 3.4. The gage factors and the gage layout are presented in Appendix B.

ST-type wirepots were used to measure deflection of the deck directly under the two load points. Twelve DEMEC points were applied to the surface of the deck over the center support to form a total of eight DEMEC reading widths as shown in Figure 3.17.

As before, the DEMEC data was used to measure surface strain, help determine formation of cracking, and as an alternative method to determine initial crack widths. Crack widths were more accurately measured using a crack microscope or a crack card.

A 500 kip load cell was used to measure the load applied from the hydraulic ram and an electric pump was used to operate the ram. The load was distributed to the deck with a W14×99 spreader beam to two load points spaced at 6 ft apart centered over the middle support. On the lab specimen, the same 20 in. × 8 in. neoprene pads were used to simulate tire patches and evenly distribute stresses at each load point. For the weigh station specimen, however, limited lab resources required the fabrication of a similar sized rubber patch from layers of ¼ in. smooth-surfaced agricultural belt. Steel plates were

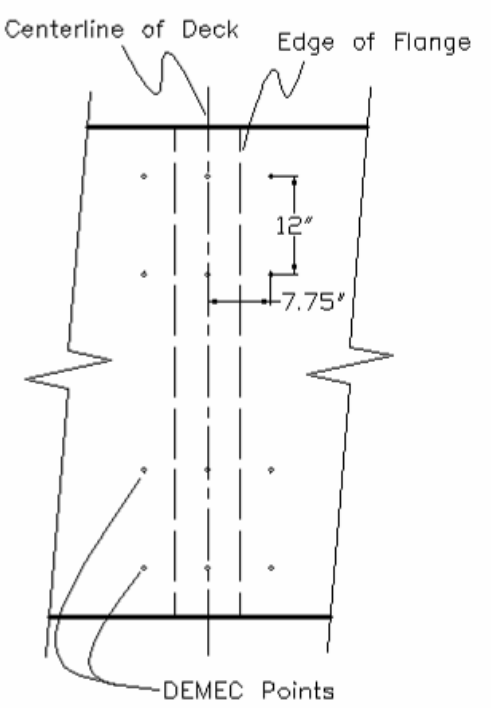


**Figure 3.17 - Layout of DEMEC points for 5 ft deck**

**Figure 3.18 - Load point setup and wirepot (post failure - weigh station deck)**

stacked on top of the pads to transfer the load from the spreader beam through the pads to the deck while holding the spreader beam high enough off the deck so that cracks beneath the spreader beam could be studied. This setup is shown in Figure 3.18.

The System 6000 data acquisition system was used to collect data from the strain gages, wirepots, and the load cell. Although the system performed 10 readings per second, it was setup to only record one reading per second to minimize the file size.

The loading procedure for these two specimens was similar to that performed for the shear investigation. An initial settling load of 5 kips was applied and then removed prior to starting the test. The System 6000 was then started and the load was increased in increments to the cracking (lab deck) or service load (weigh station deck).

In the case of the lab deck, which was tested on January 29, 2004, the load was increased in increments of approximately 5 kips to the calculated combined service load of 37.8 kips (18.9 kips per tire patch, calculated in Section 3.1.4.3). For this case, the first crack was observed at this service load.

In the case of the weigh station specimen, the deck was cracked already due to the truck loadings it experienced while installed at the weigh station. Therefore, there was no need to increase the load in small increments to try to find the cracking load and initial combined load increments used were approximately 10 kips.

During the initial loading sequence, DEMEC measurements were recorded at the end of each loading increment in both decks and crack widths were measured in the weigh station specimen. Once the service load was reached, crack widths and DEMEC measurements were recorded and the load was removed. The load was reapplied and taken directly to the service load where measurements were recorded again. This cycle was repeated a total of three times. After the third cycle, the load application was continued in increments until failure of the deck.

The inclusion of the 5 ft wide deck from the shear strength investigation allows for consideration to be given to three conditions. First, the shear specimen was never loaded prior to the test, had never been exposed to the elements, and was only allowed to age for a total of 57 days from the concrete placing to testing (June 18, 2003 to August 14, 2003). The lab specimen was allowed to age for 441 days from the concrete placement to testing (November 14, 2002 to January 29, 2004), but the deck was never significantly loaded and had never been exposed to the elements. It was maintained in the temperature controlled environment of the Structures and

Materials Laboratory at Virginia Tech for its entire lifespan. The weigh station deck, however, was allowed to age for 488 days from concrete placement to testing (November 14, 2002 to March 16, 2004), of which 448 days (December 10, 2002 to March 2, 2004) were spent installed at the weigh station. During its period in the weigh station, the specimen was subjected to an estimated 1.6 million truck crossings, which was figured assuming 45 days of scale closure and linear traffic growth from 100,000 per month (Temeles 2001) to 151,000 per month (reported by weigh station staff, June 2005). During this period the specimen also experienced temperatures as low as 8˚F and as high as 93˚F, according to preliminary local climatology data for Roanoke from NOAA. More detailed information regarding the weather experienced by the deck is presented in Appendix F of this report. Further discussion of the results of this particular experiment is reserved for the next chapter.

### 3.3.3 GFRP Rebar Tensile Tests

#### *3.3.3.1 Introduction*

The purpose of this portion of the research was to examine the changes in the strength and elasticity of GFRP bars due to aging inside the deck alone and aging inside the deck combined with loading and environmental factors. Previous research has been performed on GFRP bars inside protective tubes embedded in structures during construction so that they could be easily removed for testing at a later time (Bradberry 2001). The method employed in the current research, however, examined rebar specimens that were in direct contact with the concrete matrix and not protected in any way.

Tests involved application of an axial tension force to each bar and recording the associated strains with a 2 in. extensometer. The loading was applied with a universal testing machine and the data was recorded by its controlling computer and data acquisition system. Review of the collected data allowed determination of the ultimate strength and the modulus of elasticity of each bar. All tensile tests done in this phase of the research followed the same procedures and were performed in accordance with the guidelines presented in the ACI 440K (1999) document, which is repeated in English units in the ACI 440.1R-03 (2003) document.

#### *3.3.3.2 Specimen Extraction*

A total of ten GFRP rebar specimens were prepared for this portion of the research program. Three bars were extracted from the weigh station deck, three bars were extracted from the lab deck, and four bars were collected from a cache of unused GFRP rebar that was used as

the stock for the initial construction of the decks. The guidelines outlined ACI 440.1R-03 require that a minimum of five specimens of each group be tested. However, due to time constraints and the rather involved process of extracting the specimens from the decks, only three specimens were tested from each deck. However, three additional rebar specimens were extracted from each deck and tested as a part of the Summer Undergraduate Research Program. The results from these specimens are included in this thesis. Further, only four specimens from the cache were tested because rebar from the same manufacturer was tested in previous research conducted by Defreese, Harlan, and Cawrse (Defreese 2001, Harlan 2004, Cawrse 2002). The results of these tests conducted in previous research will also be included in this research.

After each deck was tested to failure, they were stored inside the Structures and Materials Laboratory to prevent direct exposure of the unprotected rebar to sunlight, rain, and other environmental factors. Just prior to removal of GFRP bars, the decks were taken outside and elevated above the ground about 12 in. with concrete blocks. A 60 lb electric jackhammer was then used to break away the concrete surrounding the bars as shown in Figure 3.19. Much care was taken to prevent the jackhammer from contacting the rebar. There was no significant adhesion of the concrete to the rebar and chunks fell off the bar without effort during the jackhammer process. It was found that the larger jackhammer was easier to control than a smaller 30 lb hydraulic jackhammer previously tried.

**Figure 3.19 - Extraction of GFRP rebar**

As specimens were exposed, the concrete was broken away from all sides and a length greater then necessary for the testing was uncovered. Once an adequate length of the bar exposed, it was cut from the bar remaining in the deck with a battery-powered circular saw. Specimens were then taken inside and stored in the laboratory before preparation.

#### *3.3.3.3 Specimen Preparation*

The tensile test specimens were prepared in conformance with the guidelines of the ACI 440.1R-03 (ACI 2003) and 440K (ACI 1999) documents, which specify specimen dimensions and requirements of the testing procedure itself. These instructions require that the testing length be at least 40 times the nominal diameter of the bar, but not less than 4 in. Therefore, the gage length used for these specimens, which are No. 6 bars, was 30 in. The anchor length, $L_g$, is the portion of the bar at either end of the specimen through which the tensile forces from the universal testing machine (UTM) are applied. Preparation of the anchor length will be discussed shortly. This length is only specified by the ACI 440K document in metric units and the results were converted to English units. This document requires $L_g$ to meet the greater of either the result of Equation 3.7, in millimeters, or 250 mm (9.8 in).

$$L_g = \frac{f_u A}{350} \qquad \text{(Eqn. 3.7)}$$

Where: $f_u$ = maximum tensile strength (MPa)

A = cross sectional area of the specimens ($mm^2$)

Using a maximum tensile strength of 90.5 ksi, converted to 624MPa, and given a cross-sectional area of 0.44 $in^2$, converted to 285 $mm^2$, the anchor length, $L_g$, was calculated to be 508mm, or 20in.

The total length of the specimens consisted of the gage length of 30 in. and two anchor lengths of 20 in. each, leading to a combined length of 70 in. The bars were carefully inspected for damage caused by the extraction process and were then cut to the appropriate length of 70 in. with a band saw.

Due to the anisotropic nature of the GFRP bars, simply gripping the bars directly in the UTM would have crushed the bars or caused premature fiber rupture. Therefore, end anchors were attached to uniformly distribute the tensile load along the length of the anchor zones of each bar without transferring significant non-axial stresses. The end anchors consisted of steel pipe which was adhered to the rebar using an epoxy resin and sand combination.

The steel pipe used for the end anchors was commercially available structural steel pipe with a roughened surface inside. The inside diameter was 1-¼ in. to meet the ACI 440K requirement that it must be at least 0.39 in. – 0.55 in. greater than the nominal bar diameter. The pipe sections were cut to the 20 in. anchor length calculated above. The rough interior of the

pipe did not require further scoring of the interior to improve the bond strength, but the inside of the pipes were cleaned with a CSM-1 degreaser from Micro Measurements, which was the same as that used to prepare the steel rebar for application of strain gages.

PVC end caps were used to cap the ends of the anchors around the bar and contain the epoxy resin. A total of four caps were necessary for each bar, one at each outside end of each anchor and one at each inside end of each anchor. The caps used at the outside ends of the anchors were machined to have a shallow circular indentation in the middle of the inside of the cap with a diameter 1/8 in. larger than the bar. The caps used at the inside ends of each anchor were machined to have a hole in the middle of the cap with a diameter 1/8 in. larger than the bar. The combination of these caps, when attached to the steel pipe, helped ensure correct alignment of the anchor on the bar.

The epoxy resin was a two-part mixture from West Systems of epoxy and hardener. Sand was used in the mixture to improve the bond between the anchor and the bar. The mixture ratio used was three parts sand to five parts epoxy resin to one part epoxy hardener by weight. When preparing each mixture, the sand was weighed first and the epoxy was added to it. The two were mixed together thoroughly and then the hardener was mixed in. No more than three anchors were prepared with each mixture because of the pot life.

The overall step-by-step process of the anchor preparation was as follows. An outside PVC cap was seated completely on the end of a length of steel pipe prepared as discussed above. An inside PVC cap was placed on the GFRP bar so that it could be lowered onto the end anchor later. The bar specimen was then placed inside the pipe and positioned so that it was seated in the indentation of the PVC end cap at the end of the pipe. The sand and epoxy resin sand mixture, prepared as described above, was then poured in slowly until it reached the open end of the pipe and the bar was moved around to work out any air pockets. A small amount of the mixture was added "top off" the pipe and the inside cap was lowered and completely seated on the steel pipe. The specimen with the anchor was then carefully stored in an upright position with the anchor on the bottom and it was securely tied with plastic zip ties to a railing and allowed to cure for at least 24 hours. Only one end of the bar was cast at a time. A typical assembly is shown in Figure 3.20 and a complete specimen in Figure 3.21.

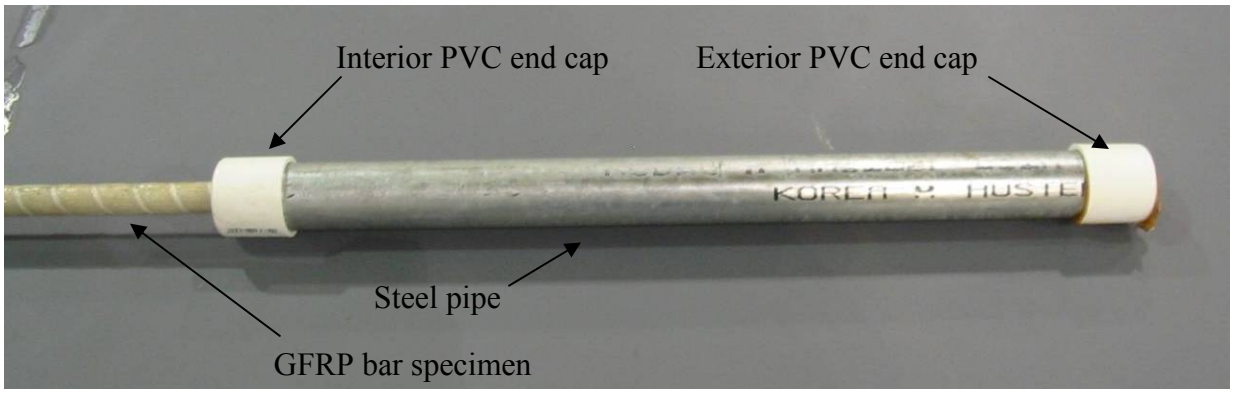


**Figure 3.20 – Typical end anchor assembly**

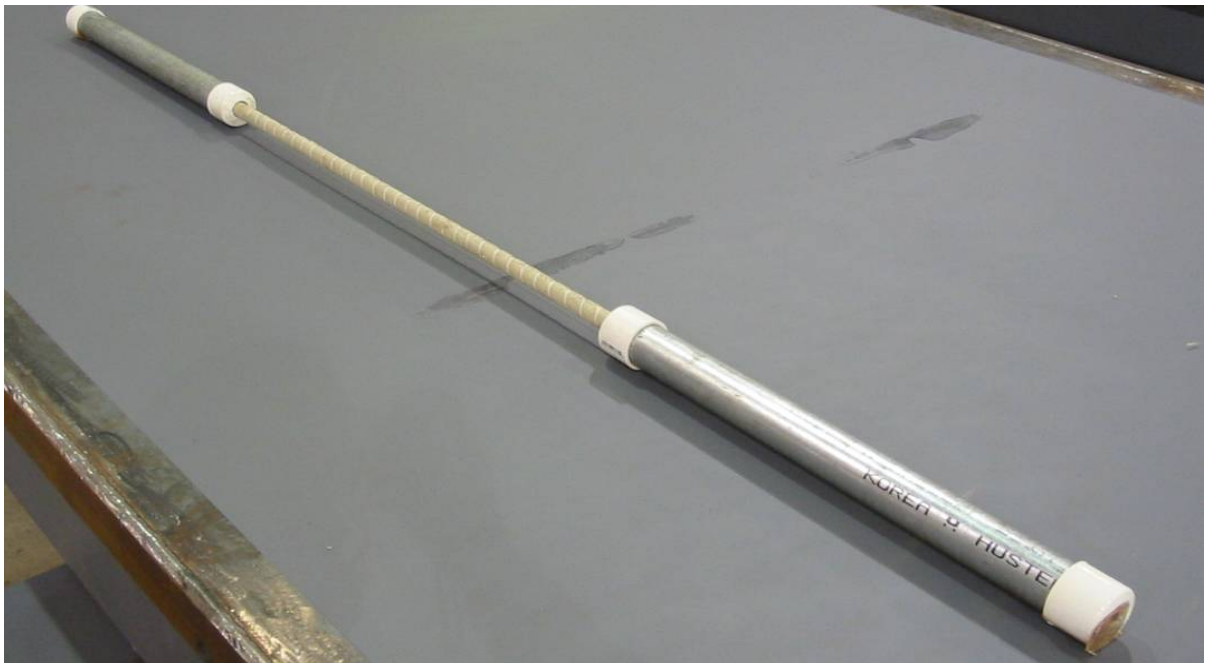

**Figure 3.21 - Typical GFRP bar tensile test specimen with end anchors**

### *3.3.3.4 Experimental Setup*

This phase of the research was conducted in a computer-controlled SATEC universal testing machine, as shown in Figure 3.22, which had a built-in load cell. Strain in the specimen was measured with a clip-on extensometer with a 2 in. gage length. Previous research by Defreese (2001) indicated very good agreement between strain gage and extensometer values, so only the extensometer was used in this research for strain measurement. Data was collected by the computer from both the built-in load cell and the extensometer.

The SATEC was prepared for testing by installing curved-surface grips, which have two angled planes along the gripping surface to provide a better grip on rounded specimens, in both crossheads. Spacers were added to allow a proper grip on the anchors. The specimen to be tested was then loaded into the grips in both crossheads, taking care to ensure a complete seating of the anchors in the grips, thus centering them in the frame. The specimen was gripped in the lower crosshead first because of the lower grips' tendency to lift the specimen while closing. This prevented the development of compression in the bar before the start of the test. After gripping with the upper crosshead, two marks were made 2 in. apart lengthwise on the specimen around the midpoint of the testing length. The 2 in. clip-on extensometer was attached to the bar with rubber bands, with each of its legs lined up with one of the two marks made.


**Figure 3.22 - Tensile test setup**

### *3.3.3.5 Tensile Test Procedure*

The program used on the computer that controlled the test was a modified version of a standard tensile test for coupons. The cross-sectional area was entered into the program so that it could calculate the tensile stress for each specimen and the load rate was adjusted to meet the requirements outlined in the ACI 440.1R-03. This required that the load application rate be between 14.5 ksi and 72.5 ksi per minute for stress controlled testing procedures, which corresponds to a load application rate between 6.4 kips and 32 kips per minute for No. 6 rebar. The load rate used for all of the tensile tests was 10 kips per

minute, which was chosen to allow time to pause the test to remove the extensometer to prevent damage to it.

After each specimen was prepared as outlined in Section 3.2.3.4, all channels were zeroed. The load was then applied at the rate of 10 kips per minute to approximately 20 – 25 kips, at which point the loading was paused so that the extensometer could be removed to prevent damage to it when the specimen failed. The instructions in the ACI 440.1R-03 document require that strain values be known at stress levels of both 20% and 60% of the ultimate strength to calculate the modulus of elasticity. However, because of the expected variability in the ultimate strength of these specimens, it was decided to forego this requirement to ensure that the extensometer was not damaged.

**Figure 3.23 - Typical GFRP tensile test failure**

After the extensometer was removed from the specimen, the test was continued until failure of the specimen. The computer automatically detected each break, defined as a strength reduction of 50% or more and an inability to take on any additional load, and promptly ended each test. The specimen condition following each failure could be described as a "broomstick" with broken fibers spreading apart all the way to the anchors as shown in Figure 3.23. This was similar to previous research with bars of the same size, but is in contrast to previous research with smaller diameter bars that appeared to break in a much cleaner manner.

# *Chapter 4 – Results and Discussion*

## 4.1 Shear Strength

### 4.1.1 Introduction

A total of four GFRP-reinforced concrete bridge decks of varying widths were constructed to investigate their shear strength in a continuous two-span configuration. One of these decks was also used in conjunction with two others to explore the strength degradation issues of GFRP due to environmental factors, which will be discussed later in Section 4.2. The construction details and testing procedures were outlined in Chapter 3. This chapter presents the results and discussion from these tests.

### 4.1.2 Shear strength and comparison with predicted values

All four specimens considered in the shear strength investigation failed in one-way, beam-type, shear next to the center support. The ultimate failure load for each deck is tabulated below in Table 4.1.

***Table 4.1 – Failure Loads of GFRP-Reinforced Decks***

| Deck | Depth to FRP rebar, d | $f_c$ | Failure Load per patch | Failure Type |
|---|---|---|---|---|
| 1 ft Shear | 5-5/8 in. | 6.0 ksi | 30.5 kips | Beam Shear |
| 2 ft Shear | 5-5/8 in. | 6.0 ksi | 49.2 kips | Beam Shear |
| 3.5 ft Shear | 5-5/8 in. | 6.2 ksi | 76.4 kips | Beam Shear |
| 5 ft Shear | 5-5/8 in. | 6.5 ksi | 124 kips | Beam Shear |
| 5 ft Degradation - Lab | 4-3/4 in. | 5.9 ksi | 111 kips | Beam Shear |

Details regarding design and construction of the decks designated as "shear" in the above table are presented in section 3.1 of this report. The "5 ft Degradation - Lab" deck listed above was the deck discussed in section 3.2.2 that was maintained in the temperature-controlled environment of the Structures and Materials Laboratory at Virginia Tech. This nomenclature will be used consistently throughout the remainder of Section 4.1. In reviewing these results, it should be understood that the lab-maintained degradation deck was tested more than a year after its construction while the shear decks were tested only a couple months after their construction. Additionally, the actual concrete strengths were different between the two types, even though the same mix was ordered. Thus, the strength degradation deck is included here only as a reference.

This section seeks to compare the actual shear failure values with predictions from several common models. Specifically, the five methods for predicting shear strength considered here are the guidelines of ACI 440.1 (2003), Frosch (2002), Deitz (1999), the modified compression field theory (Collins, et al., 1996), and ACI 318 (2002).

#### *4.1.2.1 Determination of Shear at Failure*

An effort was made to determine the shear in the specimens at failure for comparison to the design models. Unfortunately, there are no simple, commonly used accurate methods of determining this value directly because, at failure, the specimens are well beyond elastic behavior. Therefore, the actual shear is bounded at the high end by a two-span, elastic-state shear, $V_E$, and at the low end by a single-span, simply supported member shear, $V_{SS}$. The higher bound over considers the flexural strength of the member and the lower bound over considers the presence of a hinge over the center support. A third shear value, described as the moment-applied simple span shear, $V_{MSS}$, was calculated for each deck by determining and applying an approximate moment at the time of shear failure.

The shear values for the indeterminate case of the two-span, elastic state model was calculated with the software program Dr. Beam Pro. The loads used in the analysis included the failure load of the respective deck, the weight of the spreader beam, assuming a steel weight of 489 pcf, and the continuous self weight of the deck assuming a concrete weight of 150 pcf. The dead load from the hydraulic ram and the steel plates that were used between the ram and the spreader beam as well as between the spreader beam and the deck were not included because their effect was insignificant. The loads used for each deck are tabulated in Table 4.2.

***Table 4.2 – Loads Used in Estimating Shear at Failure***

| Deck | Applied Failure Load (per patch) | Spreader Beam Load (per patch) | Self Weight of Deck |
|---|---|---|---|
| 1 ft Shear | 30.5 kips | 0.32 kips | 95 lbs/ft |
| 2 ft Shear | 49.2 kips | 0.32 kips | 191 lbs/ft |
| 3.5 ft Shear | 76.4 kips | 1.1 kips | 334 lbs/ft |
| 5 ft Shear | 124 kips | 1.7 kips | 477 lbs/ft |
| 5 ft Degradation - Lab | 111 kips | 1.7 kips | 477 lbs/ft |

The program produced the shear and moment diagrams and calculated the shear values at 100 points spaced evenly along the model. The shear value at a location of d, the distance from the GFRP rebar to the extreme compression fiber of concrete, from the face of the support, which was 5-5/8 in. for the shear slabs and 4-3/4 in. for the strength degradation slab, was recorded for

comparison with predicted values and is presented in Table 4.5 in the elastic shear column. As an example, the 1 ft shear specimen and the resulting shear and moment diagrams are shown in Figure 4.1.

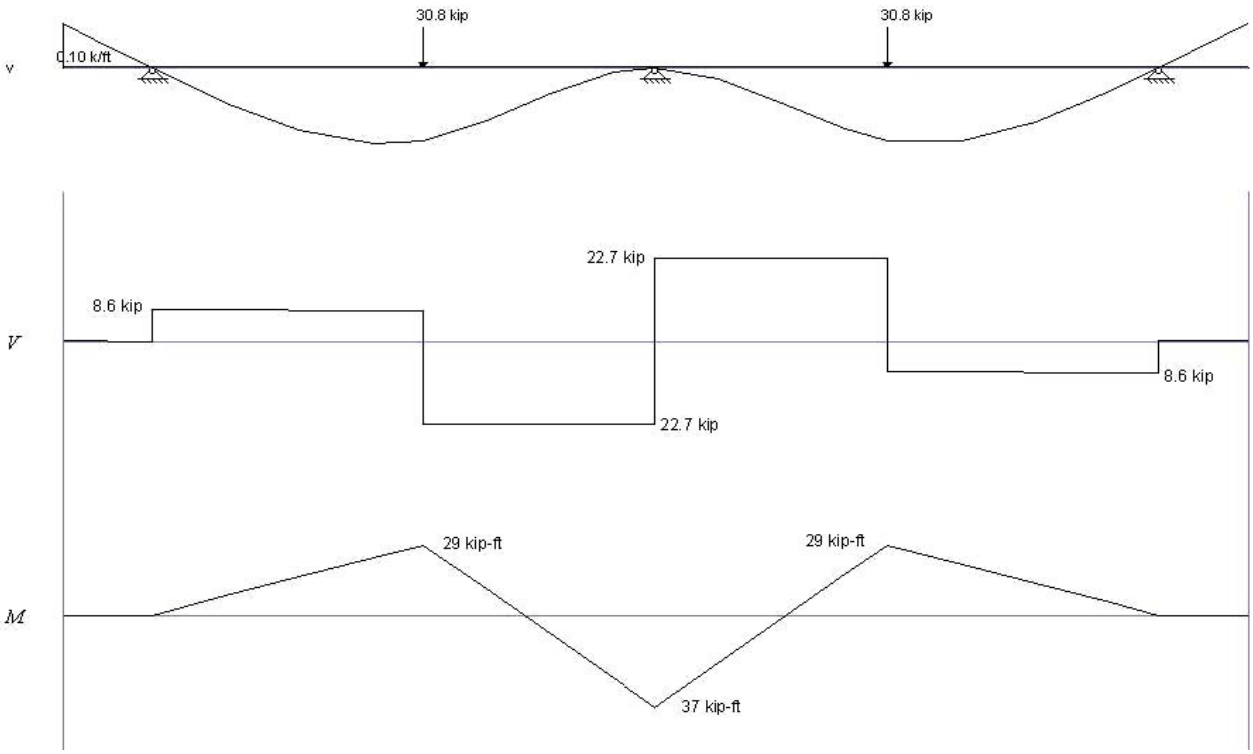


**Figure 4.1 - Shear and moment diagrams for the upper bound, continuous case for the 1 ft shear deck**

The shear values of the determinate case of the simple span beam were also calculated with Dr. Beam Pro for simplicity since the previous model needed to be only slightly modified. The same loads applied to the two span continuous models above were applied to these cases. The shear value was again taken at the location of d from the face of the support and is presented in Table 4.5 in the simply-supported shear column. The shear and moment diagrams are shown in Figure 4.2.

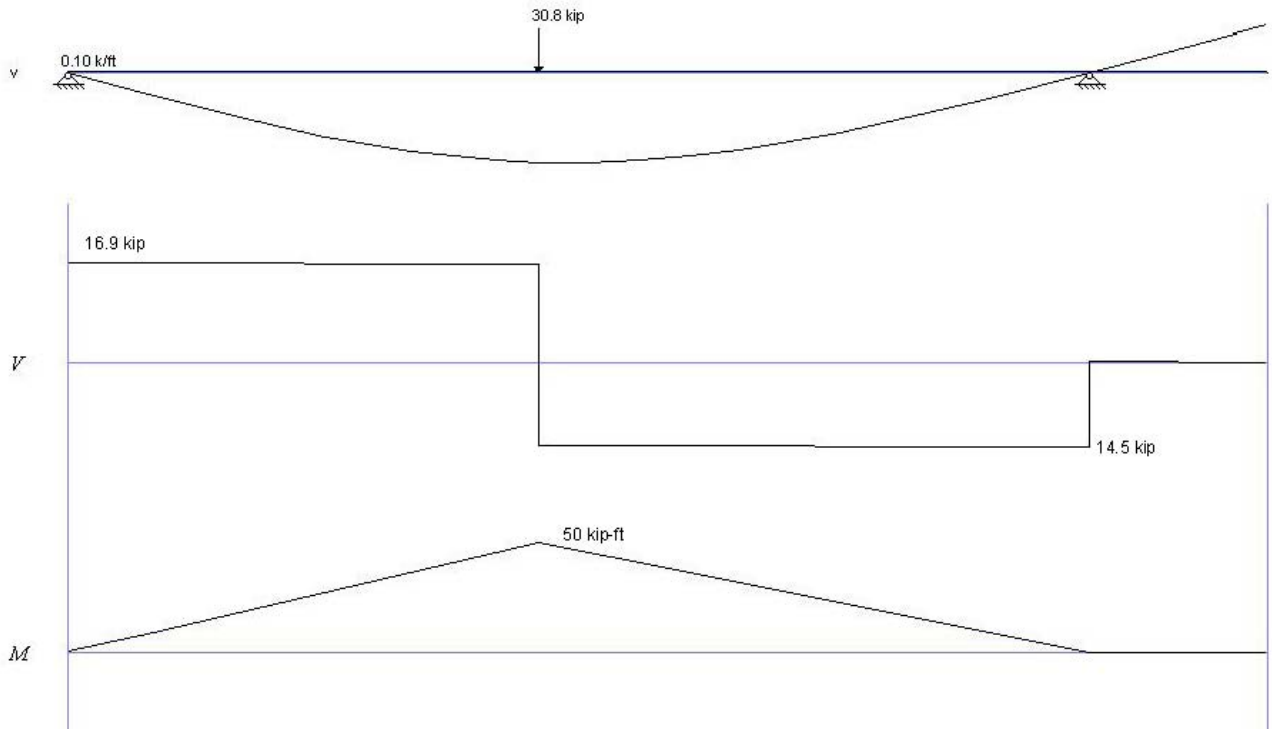


**Figure 4.2 - Shear and moment diagrams for the lower bound, simple span case for the 1 ft shear deck**

Thirdly, since the previous two models formed higher and lower bounds for the shear at the critical section, a more detailed model was developed to describe with greater accuracy the actual behavior of the decks by developing an expression for the moment over the center support and applying this to the simple span configuration above. The moment was calculated through Equation 4.1.

$$M_n = T_s j_s + T_f j_f \qquad \text{(Eqn. 4.1)}$$

where: $T_s$ = tension force in the steel rebar, kip

$j_s$ = distance between steel reinforcement and compression resultant force, in.

$T_f$ = tension force in the GFRP rebar, kip

$j_f$ = distance between GFRP reinforcement and compression resultant force, in.

The strains in the GFRP rebar recorded from each specimen by the data acquisition system just prior to shear failure were averaged and used to calculate the average stress and the total tension in the rebar. It should be noted that at the failure load of the specimens, the bar strain did not necessarily follow the expected pattern of higher strains in the center bars, so a straight average was used rather than a weighted average in determining the bar strain for the moment

calculations. The modulus of elasticity used to determine the stresses was the average of the three lab deck bars from the rebar tensile tests described in section 3.2.3. The modulus from the lab deck rebar, 5600 ksi, was used despite the rebar age difference because the actual rebar in the shear decks had been exposed to and encased in concrete and could no longer be considered pristine. The compressive strength of the concrete was determined from plots of the concrete strength developed from compressive tests of 4 in. diameter cylinders poured at the same time as the decks. Given that the depth of the compression block, c, was not known, an equation for the total tension, assuming a tensile contribution from the steel, was formed in terms of c. An expression for the compressive force based on the modified Hognestad stress-strain relationship was written in terms of c. Until the concrete strain, $\varepsilon_c$, reached a calculated strain of $\varepsilon_0$, the compressive stress in the concrete was assumed to follow Equation 4.2 below.

$$f_c = f'_c \left( \frac{2\varepsilon_c}{\varepsilon_0} - \left( \frac{\varepsilon_c}{\varepsilon_0} \right)^2 \right) \qquad \text{(Eqn. 4.2)}$$

$$\text{where: } \varepsilon_0 = \frac{2f'_c}{E_T}$$

$$E_T = 1.8 \times 10^6 + 460 f'_c$$

Rewriting equation 4.1 in terms of c and integrating over the depth of the compression zone results in an equation for the compressive force, C, in terms of c. From the principles of equilibrium, the total tensile force T was set equal to the compressive force C and the depth of the compression block was determined. All assumptions were checked and found to be satisfactory. Once the depth of the compression block was found, the moment arms to the steel and GFRP bars were calculated and used to find the moment. This procedure was programmed into MathCAD and run for each deck. The inputs into this procedure are tabulated below in Table 4.3.

***Table 4.3 – Input Values for Moment Calculations at Shear Failure***

| Deck | $f_c$ | FRP Area (per ft) | Steel Area (per ft) | d | $\varepsilon_f$ | C | $M_n$ (total) |
|---|---|---|---|---|---|---|---|
| 1 ft Shear | 6.0 ksi | 1.33 $in^2$ | 0.88 $in^2$ | 5-5/8 in. | 0.00553 | 1.59 in. | 21.4 kip-ft |
| 2 ft Shear | 6.0 ksi | 1.33 $in^2$ | 0.66 $in^2$ | 5-5/8 in. | 0.00468 | 1.49 in. | 35.4 kip-ft |
| 3.5 ft Shear | 6.2 ksi | 1.33 $in^2$ | 0.66 $in^2$ | 5-5/8 in. | 0.00465 | 1.47 in. | 61.9 kip-ft |
| 5 ft Shear | 6.5 ksi | 1.33 $in^2$ | 0.66 $in^2$ | 5-5/8 in. | 0.00495 | 1.46 in. | 94.4 kip-ft |
| 5 ft Degradation - Lab | 5.9 ksi | 1.33 $in^2$ | 0.66 $in^2$ | 4-3/4 in. | 0.00514 | 1.33 in. | 77.0 kip-ft |

Calculations for all the decks were performed for a 1 ft section and then multiplied by the actual width of the respective deck. An example of the MathCAD calculations for the 1 ft specimen is presented in Appendix G. To complete the shear calculation, the moment found for each deck was applied at the centerline end of the simple span model in Dr. Beam Pro for the respective deck. An example of the 1 ft model and the shear and moment diagrams produced by the software are shown here in Figure 4.3.

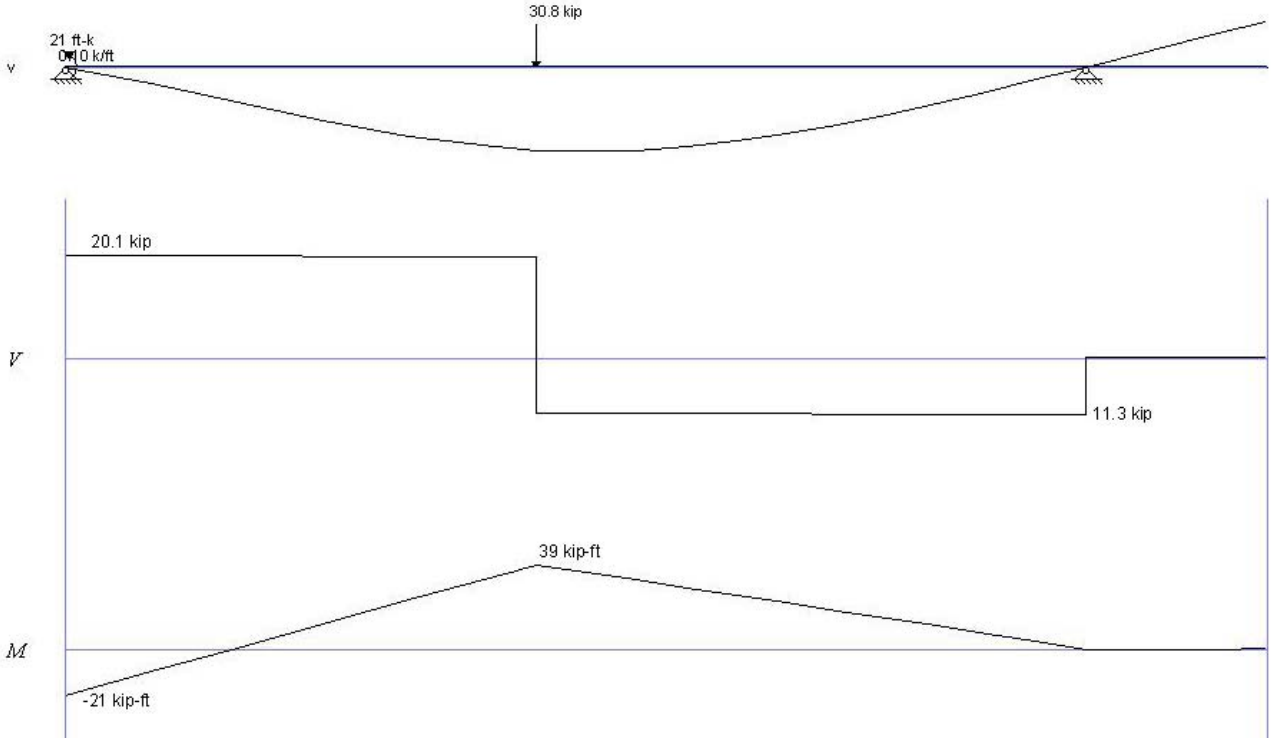


**Figure 4.3 - Shear and moment diagrams for the moment-applied, simple span case for the 1 ft shear deck**

Specifically regarding the 5 ft strength degradation deck, the values for the depth of the slab and concrete cover were taken at the location of the shear failure since these values varied along the length of the deck.

As a check on the calculations for the moment-applied simple span model, the strain measured in the steel rebar within the negative moment region at shear failure of the decks was compared with the steel strain calculated with respect to the depth of the compression zone in the model. These values are tabulated in Table 4.4.

*Table 4.4 – Comparison of Measured versus Calculated Strain in the Steel Rebar*

| Deck | Measured Strain | Average Strain | Calculated Average Strain |
|---|---|---|---|
| 1 ft Shear | 1042.5<br>1446.9 | 1245 | 1076 |
| 2 ft Shear | 1223.7<br>307.7 | 766 | 1002 |
| 3.5 ft Shear | 949.9<br>973.6 | 962 | 1013 |
| 5 ft Shear | 1788.9<br>1546.9<br>872.1<br>1280.9 | 1372 | 1087 |
| 5 ft Degradation - Lab | NA<br>NA<br>NA<br>-33.13 | -33 | 815 |

The strain values marked as NA for the 5 ft strength degradation slab correspond to strain gages that were not working at the time of the test. The data from the fourth strain gage of this particular specimen is also questionable because review of the data from this gage exposes unexplained sporadic shifts in values throughout the testing process.

The calculated strains are similar to the average measured strains in Table 4.4 for the four shear specimens, particularly the 3.5 ft specimen. It should be considered, however, that the calculated strains do not take into account any local bar strain increases which would occur at cracks where all of the tensile force is transferred through the rebar.

The resulting calculated failure shears of the three models discussed are summarized in Table 4.5. Although the calculated and measured strains in Table 4.4 did not necessarily agree, the moment-applied simple span method was used for determining the shear of the specimens at failure because the model accounts for the partial hinge that develops in the decks over the center support. The shears calculated according to this model were between the elastic continuous shear and the simply supported shear as expected.

*Table 4.5 – Calculated Failure Shear of GFRP-Reinforced Decks*

| Deck | Elastic Shear | Simply Supported Shear | Moment-Applied Simple Span Shear |
|---|---|---|---|
| 1 ft Shear | 22.7 kips | 16.9 kips | 20.1 kips |
| 2 ft Shear | 36.6 kips | 27.1 kips | 32.5 kips |
| 3.5 ft Shear | 57.1 kips | 42.3 kips | 51.7 kips |
| 5 ft Shear | 92.5 kips | 68.5 kips | 82.9 kips |
| 5 ft Degradation - Lab | 82.8 kips | 61.3 kips | 73.0 kips |

#### *4.1.2.2 Prediction of Shear Strength – ACI 440.1R-03 Method*

For FRP-reinforced concrete slabs, ACI 440 recommends the use of Equation 4.3 for predicting one-way shear strength.

$$V_{c,f} = \frac{A_f E_f}{A_s E_s} V_c \qquad \text{(Eqn. 4.3)}$$

$$\text{where: } V_c = 2\sqrt{f'_c} b_w d$$

As discussed in Chapter 2, the equation essentially multiplies the typical shear strength of steel reinforced concrete by the ratio of the strength of the GFRP reinforcement to the strength of the steel reinforcement of a deck designed for the same moment capacity. For this project, the ultimate moment capacity of the deck design based on the cross section at the point of shear failure was calculated using the Whitney stress block to approximate the concrete strength. Since the GFRP reinforcement does not experience yielding as steel does, the moment capacity of the specimen was determined assuming that the concrete crushed, at a strain of 0.003, before the GFRP bars yielded, which is the preferred mechanism of failure for FRP-reinforced designs. The depth of the Whitney stress block was determined by solving Equation 4.4 for a.

$$0.85 f'_c a^2 - 0.003 \beta_1 E_f d^2 \rho_f + 0.003 E_f d \rho_f a = 0 \qquad \text{(Eqn. 4.4)}$$

Where: $\beta_1 = 1.05 - 0.05 \frac{f_c'}{1000}$

$f_c'$ = design compressive strength of concrete, psi

$a$ = depth of the Whitney compression block, in.

$E_f$ =modulus of elasticity of concrete, psi

$\rho_f$ =GFRP reinforcement ratio

The depth of the compression zone, c, was subsequently found from Equation 4.5.

$$c = \frac{a}{\beta_1} \qquad \text{(Eqn. 4.5)}$$

For this series, since the actual concrete compressive strength was known from cylinder tests, the known values of $f_c$ were used in place of the design $f'_c$. Once the depth of the compression block was determined, the assumption of failure due to crushing of the concrete was checked by verifying that the stress in the GFRP rebar did not exceed the manufacturer-provided guaranteed ultimate strength of the bars. This was checked using Equation 3.3, for which the strain in the

GFRP rebar was determined through the use of similar triangles assuming the maximum strain in the concrete to be 0.003, which can be represented mathematically according to the Equation 4.6.

$$\varepsilon_f = 0.003 \times \frac{d-c}{c} \quad \text{(Eqn. 4.6)}$$

The moment capacity of the section at the location of the shear failure was computed according to Equation 4.7.

$$M_n = 0.85 f'_c ab\left(d - \frac{a}{2}\right) \quad \text{(Eqn. 4.7)}$$

Now, given the moment capacity of the GFRP-reinforced deck, the area of steel reinforcement needed for a deck of identical strength was determined according to Equation 4.8.

$$A_s = \frac{M_n}{f_y\left(d - \frac{a}{2}\right)} \quad \text{(Eqn. 4.8)}$$

This calculation was performed assuming that the depth of the Whitney stress block, a, remained the same, which was confirmed by recalculating the value for the steel reinforced deck with Equation 4.9:

$$a = \frac{f_y A_s}{0.85 f'_c b} \quad \text{(Eqn. 4.9)}$$

Once the area of steel was found and verified, the predicted shear strength according to ACI 440.1 (2003) was calculated using equation 4.3. The modulus of elasticity used for the GFRP rebar for these calculations was obtained from testing the unused rebar. This is because the intent of the equation is to determine the shear strength based on manufacturer supplied data which is determined from unconditioned bars despite the difference in moduli encountered in this research. An example calculation for the one-way shear strength of the 1 ft shear specimen is included in Appendix G. The resulting shear strength predictions for this method for each deck are presented here in Table 4.6 and in comparison with the other methods discussed in this section in Table 4.11.

*Table 4.6 – Shear Strength Results – ACI 440.1R-03*

| Deck | $A_f$ | $E_f$ | $A_s$ | $E_s$ | $f_c$ | d | $V_{c,f}$ |
|---|---|---|---|---|---|---|---|
| 1 ft Shear | 1.33 $in^2$/ft | 6100 ksi | 1.13 $in^2$/ft | 29000 ksi | 6.0 ksi | 5-5/8 in. | 2.6 kips |
| 2 ft Shear | 1.33 $in^2$/ft | 6100 ksi | 1.13 $in^2$/ft | 29000 ksi | 6.0 ksi | 5-5/8 in. | 5.2 kips |
| 3.5 ft Shear | 1.33 $in^2$/ft | 6100 ksi | 1.15 $in^2$/ft | 29000 ksi | 6.2 ksi | 5-5/8 in. | 9.0 kips |
| 5 ft Shear | 1.33 $in^2$/ft | 6100 ksi | 1.16 $in^2$/ft | 29000 ksi | 6.5 ksi | 5-5/8 in. | 13.1 kips |
| 5 ft Degradation - Lab | 1.33 $in^2$/ft | 6100 ksi | 1.02 $in^2$/ft | 29000 ksi | 5.9 ksi | 4-3/4 in. | 12.0 kips |

#### *4.1.2.3 Prediction of shear strength – Frosch method*

A method for predicting the shear strength of concrete beams was developed by Tureyen and Frosch (2003) and can be applied to either steel- or FRP-reinforced sections. Discussion of their research was presented in Chapter 2 of this document, but the general equation is shown here for convenience as Equation 4.10. From this point forward, this model will be referred to in this paper as the "Frosch method."

$$V_c = 5\sqrt{f'_c}\, b_w c \qquad \text{(Eqn. 4.10)}$$

where: $f'_c$ = specified concrete compressive strength, psi

$b_w$ = beam width, in

$c = kd$ = cracked transformed section neutral axis depth, in.

$k = \sqrt{2\rho n + (\rho n)^2} - \rho n$

$d$ = effective depth, in.

$\rho = \dfrac{A_r}{b_w d}$ = reinforcement ratio

$n = \dfrac{E_r}{E_c}$ = modular ratio

$A_r$ = area of flexural tension reinforcement, $in.^2$

$E_c = 57000\sqrt{f'_c}$ = modulus of elasticity of concrete, psi

$E_r$ = modulus of elasticity of flexural tension reinforcement, psi

An example calculation of the shear strength predicted with this method is presented in Appendix G of this paper. The resulting strength predictions are presented here in Table 4.7 and in comparison with the other methods in Table 4.11.

*Table 4.7 – Shear Strength Results – Frosch Method*

| Deck | $A_f$ | $E_f$ | $E_c$ | $f_c$ | c | $V_c$ |
|---|---|---|---|---|---|---|
| 1 ft Shear | 1.33 $in^2$/ft | 6100 ksi | 4420 ksi | 6.0 ksi | 1.17 in. | 5.4 kips |
| 2 ft Shear | 1.33 $in^2$/ft | 6100 ksi | 4420 ksi | 6.0 ksi | 1.17 in. | 10.8 kips |
| 3.5 ft Shear | 1.33 $in^2$/ft | 6100 ksi | 4490 ksi | 6.2 ksi | 1.16 in. | 19.1 kips |
| 5 ft Shear | 1.33 $in^2$/ft | 6100 ksi | 4600 ksi | 6.5 ksi | 1.15 in. | 27.7 kips |
| 5 ft Degradation - Lab | 1.33 $in^2$/ft | 6100 ksi | 4380 ksi | 5.9 ksi | 1.07 in. | 24.5 kips |

#### 4.1.2.4 Prediction of shear strength – Deitz Method

A model for shear strength of GFRP-reinforced concrete members was developed by Deitz, et al. (1999) based on research performed on reinforced concrete panels. Details regarding this research were presented in Chapter 2, but the equation is presented here for convenience as Equation 4.11. From this point forward, this model will be referred to in this thesis as the "Deitz method."

$$V_c = 3\frac{E_f}{E_s}\left(2\sqrt{f_c'}b_w d\right) \qquad \text{(Eqn. 4.11)}$$

An example calculation of the strength predicted with this method is presented in Appendix G of this paper. The resulting shear strength predictions are presented here in Table 4.8 and in comparison with the other methods in Table 4.11.

*Table 4.8 – Shear Strength Results – Deitz Method*

| Deck | $E_f$ | $E_s$ | $f_c$ | d | $V_c$ |
|---|---|---|---|---|---|
| 1 ft Shear | 6100 ksi | 29000 ksi | 6.0 ksi | 5-5/8 in. | 6.6 kips |
| 2 ft Shear | 6100 ksi | 29000 ksi | 6.0 ksi | 5-5/8 in. | 13.2 kips |
| 3.5 ft Shear | 6100 ksi | 29000 ksi | 6.2 ksi | 5-5/8 in. | 23.5 kips |
| 5 ft Shear | 6100 ksi | 29000 ksi | 6.5 ksi | 5-5/8 in. | 34.3 kips |
| 5 ft Degradation - Lab | 6100 ksi | 29000 ksi | 5.9 ksi | 4-3/4 in. | 27.6 kips |

#### 4.1.2.5 Prediction of shear strength – Modified Compression Field Theory

The modified compression field theory (MCFT) was developed in an effort to replace the numerous empirical shear design equations with a simplified model with "physical significance" (Collins, et al., 1996) The method considers a series of parallel cracks at an angle $\theta$ to the longitudinal direction and average stress states in the section and at a crack. The model also considers a principle tensile strain $\varepsilon_t$ as a "damage indicator" to determine the section's ability to resist compressive and shear stresses across cracks. The equation for shear strength as presented by Collins, et al. is shown as Equation 4.12.

$$V_n = V_c + V_s + V_p = \beta\sqrt{f_c'}\,b_v d_v + \frac{A_v f_y}{s} d_v \cot\theta + V_p \qquad \text{(Eqn. 4.12)}$$

where: $V_c$ = shear strength contributed by tensile stresses in cracked concrete

$V_s$ = shear strength contributed by stirrups

$V_p$ = vertical component of prestressing

$\beta$ = tensile stress factor

$b_v$ = width of the section, in.

$d_v = d - \frac{a}{2}$

$f_y$ = yield strength of steel, psi

$s$ = spacing of shear reinforcement, in.

For a section without stirrups or prestressing steel as is the case with the specimens in this research, the shear equation can be reduced to equation 4.13.

$$V_n = V_c = \beta\sqrt{f_c'}\,b_v d_v \quad \text{(lbs)} \qquad \text{(Eqn. 4.13)}$$

In determining the effective shear depth $d_v$, the depth of the compression zone, a, was found by solving the previously presented Equation 4.4 for a. In the equations the concrete strength $f'_c$ is entered in psi and the result is in pounds. The tensile stress factor $\beta$ was determined from a table given the results of the calculated longitudinal strain $\varepsilon_x$ and an equivalent spacing parameter $s_{xe}$, which can be calculated from equations 4.14 and 4.15 for members without prestressing tendons. The table is presented in Appendix G.

$$\varepsilon_x = \frac{0.5V_u \cot(\theta) + M_u / d_v}{E_f A_f} \qquad \text{(Eqn. 4.14)}$$

Where: $V_u$ = factored shear due to applied load

$M_u$ = factored moment due to applied load

$\theta$ = cracking angle

$E_f$ = GFRP modulus of elasticity

$A_f$ = area of GFRP tensile reinforcement

$$s_{xe} = s_x \frac{1.38}{a_g + 0.63} \qquad \text{(Eqn. 4.15)}$$

Where: $s_{xe}$ = equivalent spacing parameter, in.

$s_x$ = crack spacing parameter

$a_g$ = aggregate size, in.

In calculating the strain $\varepsilon_x$ the values of $V_u$ and $M_u$ were determined assuming an elastic section with a design load consisting of the self-weight of the deck and applied factored point loads, $\gamma P_u$, spaced 6 ft apart centered over the center support. Since all of the deck specimens used in this research had widths that were less than the design effective width, $\gamma P_u$ was adjusted to account for the smaller section and was calculated according to equation 4.16.

$$\gamma P_u = I \times \gamma_1 \times P \times \frac{b}{b_{eff}} \qquad \text{(Eqn. 4.16)}$$

Where: $I$ = impact factor $= 1.33$

$\gamma_1$ = live load factor $= 1.75$

$P$ = wheel load $= 16 kips$

$b$ = width of section $= 1\,ft$

$b_{eff}$ = effective width $= 5\frac{5}{8}\,ft$

The effective width in equation 4.16 was calculated according to the previously presented Equation 3.6. The effective shear depth $d_v$ was calculated in the same manner as equation 4.12. The angle of cracking, θ, was initially guessed to be 45˚, but was replaced and rechecked with the angle obtained from the supplied table of θ and β values.

The determination of shear strength using the MCFT method is conducted in the following order:

1. Determine $V_u$, $M_u$, and $d_v$
2. Calculate $\varepsilon_x$ and $s_{xe}$ assuming a cracking angle θ, typically 45˚
3. Given $\varepsilon_x$ and $s_{xe}$, select θ from the table presented in Appendix G
4. Recalculate $\varepsilon_x$ and $s_{xe}$ based on the new value of θ
5. Given the new values of $\varepsilon_x$ and $s_{xe}$, select θ and β from the table
6. Compare the new θ value to the previous θ; if difference is too great, repeat steps 4 and 5
7. Calculate shear strength according to equation 4.12 with the final value of β

This procedure, performed for a 1 ft wide deck, is presented in Appendix G. The resulting β and θ values for all specimens were 1.96 and 37.1, respectively. It should be noted

that the cracking angle had no direct influence in the shear strength equation and that a β value of 2.0 makes equation 4.12 nearly identical to the commonly used empirical ACI 318 equation for concrete shear strength, $V_c = 2\sqrt{f_c'}b_w d$ , with the only exception being in the definition of the effective depth of the section.

The results of the MCFT analysis for all five shear specimens are summarized in Table 4.9 and compared with the other models in this section in Table 4.11.

***Table 4.9 – Shear Strength Results – MCFT Method***

| Deck | $f_c$ | $d_v$ | $\varepsilon_x$ | $s_{xe}$ | θ | β | $V_n$ |
|---|---|---|---|---|---|---|---|
| 1 ft Shear | 6.0 ksi | 5.07 in. | 0.00296 | 5.07 in. | 37.1˚ | 1.96 | 9.2 kips |
| 2 ft Shear | 6.0 ksi | 5.07 in. | 0.00296 | 5.07 in. | 37.1˚ | 1.96 | 18.5 kips |
| 3.5 ft Shear | 6.2 ksi | 5.07 in. | 0.00296 | 5.07 in. | 37.1˚ | 1.96 | 32.9 kips |
| 5 ft Shear | 6.5 ksi | 5.07 in. | 0.00296 | 5.07 in. | 37.1˚ | 1.96 | 48.3 kips |
| 5 ft Degradation - Lab | 5.9 ksi | 4.24 in. | 0.00346 | 4.24 in. | 37.1˚ | 1.96 | 38.3 kips |

It should be noted that the results are not significantly different from the outcome of the ACI 318 equation for the reasons stated above. This is primarily because the values of both β and θ are dependent on the tensile strain calculated from Equation 4.14, which is limited by the method to 0.002, the approximate yielding strain of steel. Strain values above this are to be treated the same as 0.002 in the tables. This value is also the limit of the charts from which the tables were derived. Therefore, this method, which does offer a "physical feel" in the calculation of shear strength through its inclusion of the modulus of elasticity and area of reinforcement as well as its consideration of cracking angles, has only been developed for the ranges of steel reinforced members and does not fully consider the capabilities of the reinforcing in the prediction of shear strength of FRP-reinforced concrete members.

#### *4.1.2.6 Prediction of Shear Strength – ACI 318*

The calculation of shear strength according to the empirical ACI 318 concrete shear equations has been included in this document as a reference point despite that it was developed for steel-reinforced members. The method predicts shear strength according to equation 4.17.

$$V_c = 2\sqrt{f_c'}b_w d \qquad \text{(Eqn. 4.17)}$$

Where: $f_c'$ = design concrete strength, psi

$b_w$ = width of section, in.

$d$ = effective depth, in.

The shear strength of each of the specimens calculated with this method is shown here in Table 4.10 and comparison to the other models discussed in this section in Table 4.11.

***Table 4.10 – Shear Strength Results – ACI 318***

| Deck | $f_c$ | d | $V_c$ |
|---|---|---|---|
| 1 ft Shear | 6.0 ksi | 5-5/8 in. | 10.5 kips |
| 2 ft Shear | 6.0 ksi | 5-5/8 in. | 20.9 kips |
| 3.5 ft Shear | 6.2 ksi | 5-5/8 in. | 37.2 kips |
| 5 ft Shear | 6.5 ksi | 5-5/8 in. | 54.4 kips |
| 5 ft Degradation - Lab | 5.9 ksi | 4-3/4 in. | 43.8 kips |

### *4.1.2.7 Prediction of Shear Strength – Comparison of Models*

The approximated failure shear from section 4.1.2.1 and the shear strength values calculated from the subsequent models are presented in Table 4.11.

***Table 4.11 – Comparison of Methods***

| Deck | Moment-applied simple span shear | ACI 440.1 | Frosch | Deitz | MCFT | ACI 318 | Service Shear* |
|---|---|---|---|---|---|---|---|
| 1 ft Shear | 20.1 kips | 2.6 kips | 5.4 kips | 6.6 kips | 9.2 kips | 10.5 kips | 3.1 kips |
| 2 ft Shear | 32.5 kips | 5.2 kips | 10.8 kips | 13.2 kips | 18.5 kips | 20.9 kips | 6.2 kips |
| 3.5 ft Shear | 51.7 kips | 9.0 kips | 19.1 kips | 23.5 kips | 32.9 kips | 37.2 kips | 10.8 kips |
| 5 ft Shear | 82.9 kips | 13.1 kips | 27.7 kips | 34.3 kips | 48.3 kips | 54.4 kips | 15.4 kips |
| 5 ft Degradation – Lab | 73.0 kips | 12.0 kips | 24.5 kips | 27.6 kips | 38.3 kips | 43.8 kips | 15.4 kips |

**Service shear is the calculated shear due to service load and self weight on an elastic, continuous specimen*

All five methods of shear prediction reviewed in this research were significantly conservative, particularly the ACI 440, Frosch, and Deitz methods, which apparently grossly overcompensated for the lack of stiffness and dowel action due to the use of the GFRP rebar and fail to fully consider the strength contribution of the concrete in compression. It should be noted that the MCFT and ACI 318 models, which were both conservative but closer to the experimental results than the other two, were both developed for steel reinforced sections. It should also be noted that all five models were conservative with respect to the lower bound experimental shear reported as the "simply supported shear" in Table 4.5.

One reason for the discrepancy between these results and the predictions shown above may be that the equations were developed for beams as opposed to slabs. The difference in aspect ratios of the two types of members may have a significant impact on the shear performance. Additionally, it was noted by Frosch that there appeared to be a correlation between the shear span to effective depth ratio, a/d, and the shear strength of the sections in his studies, a relationship which has been commonly identified for steel-reinforced beams.

Specifically, the shear strength of a member tends to increase as the a/d ratio decreases. Taking the shear span of the test setup in this research to be the distance between the load in one span and the edge of the center support (2 ft 8 in.), the a/d ratio is 5.7. The limited sampling in this region of Frosch's work shows at most a 10% increase in shear strength for this ratio, which is still not enough to explain the differences. The most likely reason for the overly-conservative results of the equations is that they were developed using models in simple-span loading conditions. The specimens in this research were tested as continuous across two spans with loads in each span, which essentially forces the member into triple-curvature due to the support between the loads. This configuration increases the compressive stresses on the concrete in the compressed zone of the cross-section over the center support, which may further increase the shear strength contributed by the uncracked section in this zone (Ruddle 1999).

The bottom layer of steel reinforcement may be another source of additional shear strength in the section that is not considered by the existing models. These bars may add to the shear capacity of the section through dowel action, particularly when the compression zone of the concrete is entirely below the steel mat. The von Mises yield criterion, which is used to estimate the yield strength of ductile materials, can be used to calculate the shear yield strength of the steel rebar. The equation is shown in a simplified form for shear as Equation 4.18. If sufficient bearing strength could be provided by the concrete for the steel rebar, this contribution could be as high as 16 kips for a single No. 6 steel bar.

$$\tau_y = \frac{A_s f_y}{\sqrt{3}} \qquad \text{(Eqn. 4.18)}$$

Where: $A_s$ = cross-sectional area of steel rebar, $in^2$

$f_y$ = yield strength of steel, ksi

Finally, the actual moment experienced by the specimen at the critical section for shear (d from the edge of the center support flange) is unclear. As presented in Section 4.1.2.1, the behavior of the decks is better modeled by a moment-applied simple span configuration than either the continuous or basic simple span conditions. A review of the previously presented Figures 4.1 and 4.2 reveal that the critical section for shear is found in the positive moment and negative moment regions, respectively. When the critical section is located in the negative moment region, the member is assumed to be acting as a GFRP-reinforced section when investigating shear resistance. When it is in the positive moment region, the deck is considered

to be acting as a steel-reinforced section. However, the actual case is between these two bounds; therefore, it is unclear whether the specimens are acting as steel- or GFRP-reinforced sections with regards to shear strength. This issue is illustrated by noting that the location of the inflection point in the moment diagram shown in Figure 4.3 is between that of Figures 4.1 and 4.2.

It should also be noted that the calculated service shear in Table 4.11, which is based on an uncracked, continuous deck, exceeds the results of the ACI 440.1 model. In the design of the decks, it was already known that the model was overly conservative and that it was not possible to economically build the decks to satisfy the ACI 440.1 criteria. However, it is clear that the ultimate shear strength exceeds the service shear strength with a safety factor of at least 4.7.

#### *4.1.2.8 Discussion of Failure Mode*

As discussed previously, all deck specimens in this research failed in one-way shear and failure loads were presented in Table 4.1. Figure 4.4 shows the shear failure of the 3.5 ft shear deck, which is typical of all decks tested in this research. In all four shear decks, the shear failure crack formed from a previously visible flexural crack and its formation and development were observed before failure of the specimen.

**Figure 4.4 - Shear failure of the 3.5 ft shear specimen**

#### *4.1.2.9 Comparison with previous research*

In research performed by Cawrse (2002), a prototype bridge deck reinforced with top-mat GFRP rebar was constructed to similar specifications as the decks in this research and tested to

examine its performance. Details regarding this research were discussed in Chapter 2 of this document.

While several tests were performed in Cawrse's investigation, one, the interior girder test, is of particular interest to the results of the research presented here. The setup of the interior girder test was very similar to the setup for this series of experiments in that two loads were applied with a 6 ft separation centered over an interior girder so that each load was in a separate span. A diagram of the specimen from Cawrse's research is shown in Figure 4.5 with the different loading positions for each test. The vertical center lines labeled as "girder centerline" describe the locations of the girders upon which the deck was directly supported. The horizontal lines labeled as "support centerline" in turn held the girders elevated from the floor. The two wheel load patches in the center section labeled as "Interior Girder Test" correspond to the test which is of primary interest here.

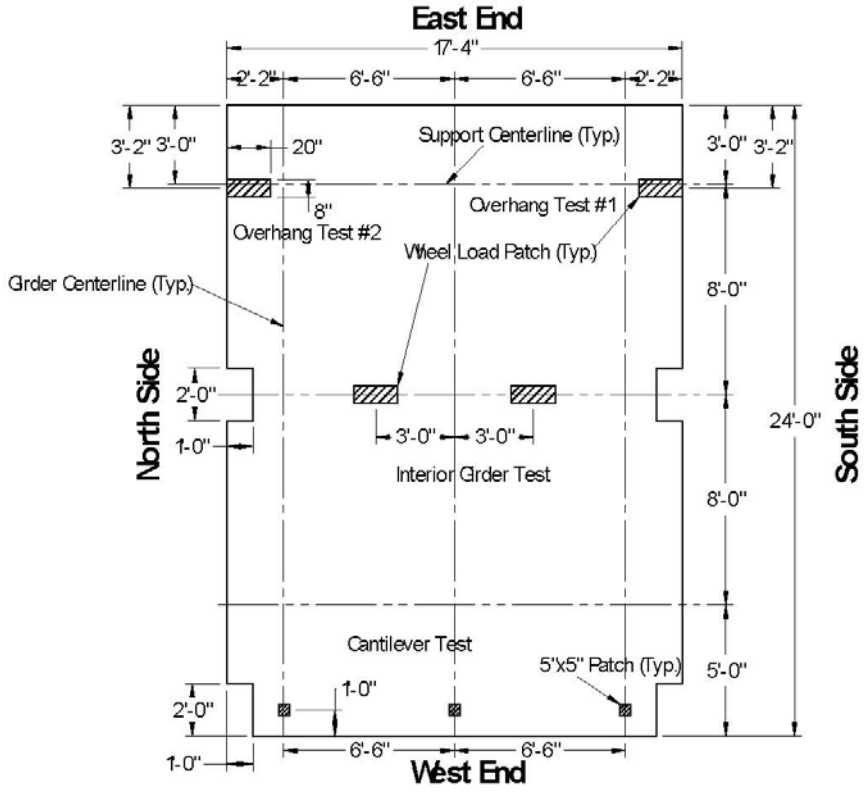


**Figure 4.5 - Test deck from Cawrse showing loading positions for various tests (Cawrse 2002)**

The section failed in two-way, punching-type, shear at 159 kips per load patch. The effective depth, d, of Cawrse's deck was 5-1/8 in. and the average concrete compressive strength determined from compression tests of 4 in. × 8 in. cylinders was 5770 psi. To compare the results from Cawrse with the results from this research, the failure loads of the shear specimens in this investigation and the findings from Cawrse were normalized by dividing them by the square root of the concrete compressive strength, $\sqrt{f_c}$, and the effective depth, d, and plotted against the width of the specimens. The resulting plot is presented in Figure 4.6.

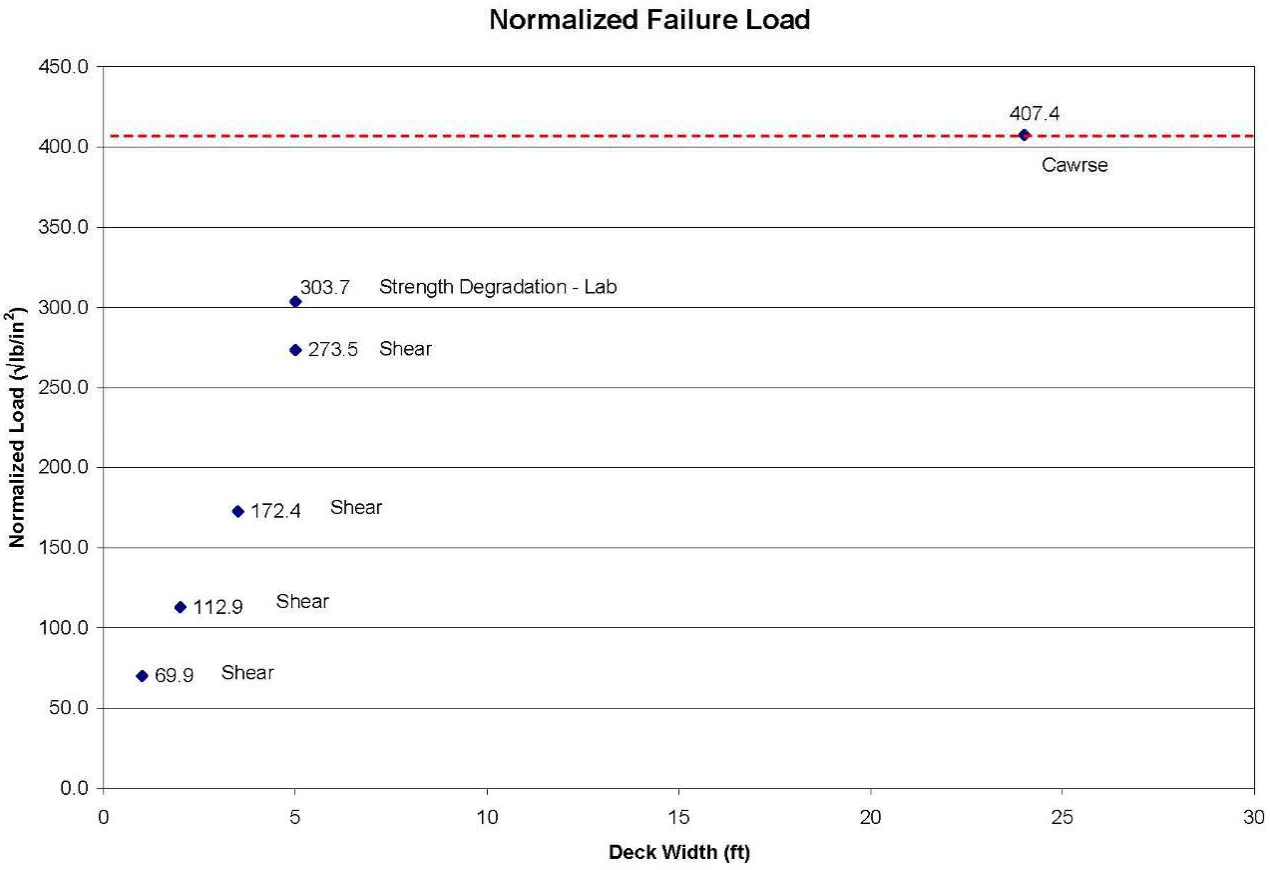


**Figure 4.6 - Normalized failure loads versus width**

Since the specimen in Cawrse's experiment failed in punching shear, it can be considered as an upper bound for the shear failure load and this is indicated by the dashed red line in Figure 4.6. The width of Cawrse's deck was 24 ft, but the same failure load would have likely been achieved at widths somewhat lower than this, but above the point of transition from beam shear to punching shear. The trend in failure load versus deck width of the shear slabs as shown here seems to indicate that the transition from beam to punching shear may occur between

approximately 7 to 12 feet. Assuming d = 5-5/8 in., $f'_c$ = 6500 ksi, and load patch dimensions of 20 in. × 8 in., the ACI 318 equations for one- and two-way shear indicate that this transition occurs at 11.0 ft for decks with steel reinforcement. This is presented in Figure 4.7.

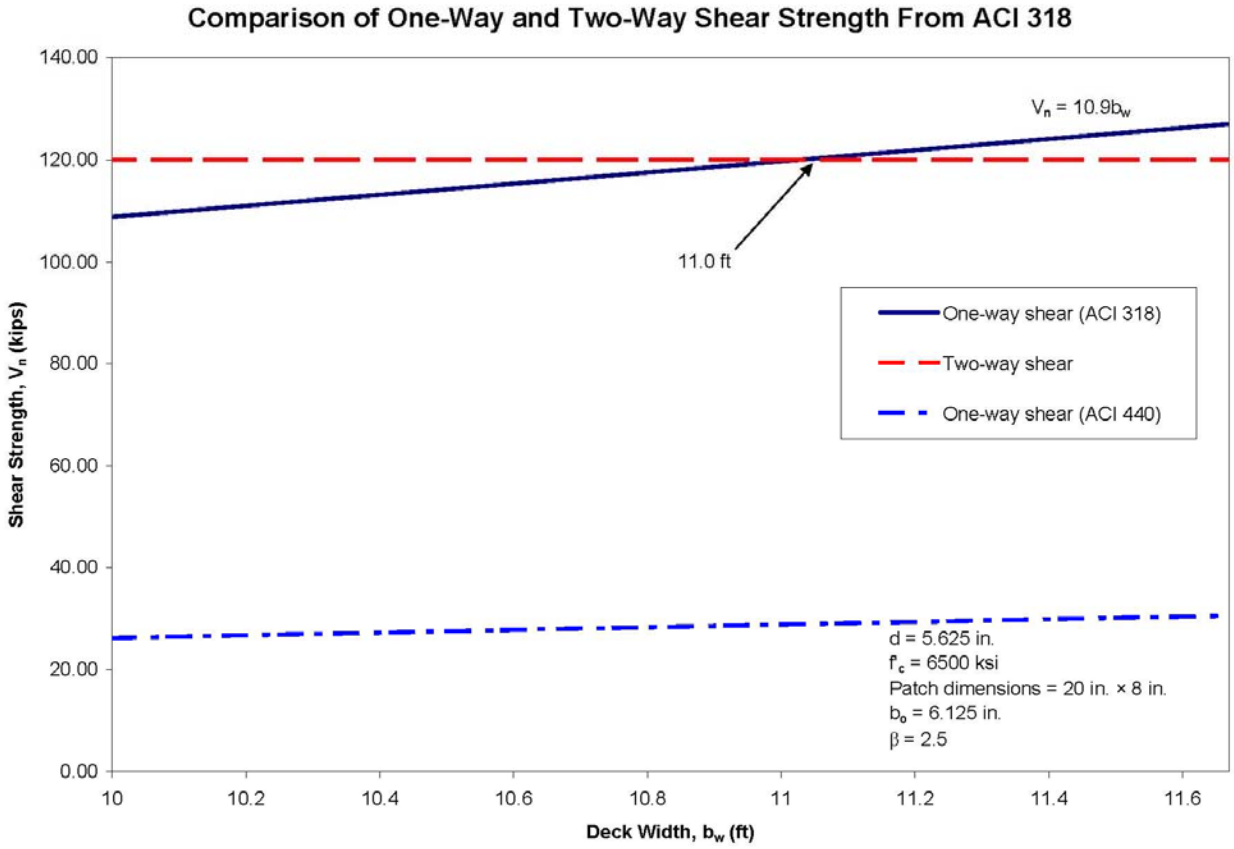


**Figure 4.7 - Plot of one- and two-way shear strengths according to ACI 318**

The ACI 318 equations were used for this approximation despite their development for steel-reinforced sections because at this time, no simple, widely-accepted equation is available for predicting the two-way shear strength of GFRP-reinforced sections. An effort was made to adjust Cawrse's punching shear results for this concrete strength and depth, but the strength he obtained was higher than even the ACI 318 two-way shear equation predicted, which when compared to the ACI 440 one-way shear equation would predict an absurdly high deck width for the transition from one-way to two-way shear failure.

### 4.1.3 Deflections

Deflection measurements were recorded by ST-type wirepots attached to the underside of the decks directly beneath the two load points, as shown in Figure 4.8.

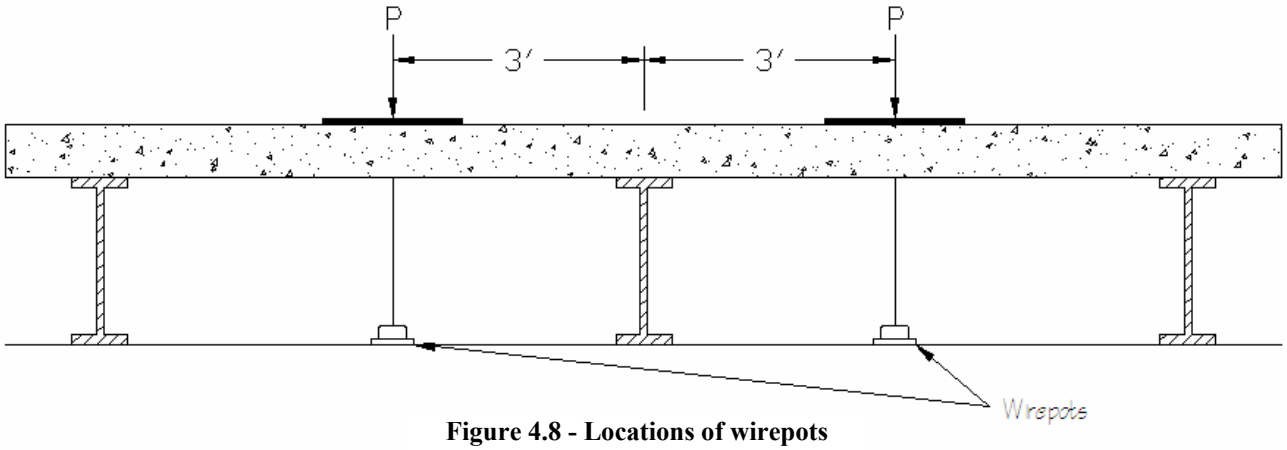


**Figure 4.8 - Locations of wirepots**

Data was collected by the data acquisition system and load versus deflection plots were created. Each of the plots presents a series for both wirepots as well as a theoretical series to compare the accuracy of the ACI 440 deflection equations to the actual measured deflections.

In developing the theoretical series, only the loads applied by the hydraulic ram were considered. The weight of the spreader beam and plates was not included because it would only add negligible deflection. Additionally, the channels to which the wirepots were connected were zeroed just prior to the test. The effective width calculated in Section 3.1.4.3 was 5 ft 7 ½ in, which is larger than the width of all specimens used in this research; therefore, the entire width of each deck was considered "effective" and contributed to the shear strength of the section. More details regarding the participation across the width of the deck will be presented later in Section 4.1.4.

The theoretical deflections were calculated using an effective moment of inertia, $I_e$, that considered the location-dependent properties of the deck through a weighted average of moments of inertia at the positive, $I_{e(m)}$, and negative, $I_{e(l)}$, moment locations. The procedure is presented in ACI 435 (2000) for beams continuous on one end only as shown in Equation 4.19.

$$I_e = 0.85I_{e(m)} + 0.15I_{e(l)} \qquad \text{(Eqn. 4.19)}$$

Where: $I_e$ = Effective moment of inertia, $\text{in}^4$

$I_{e(m)}$ = Effective moment of inertia at midspan, $\text{in}^4$

$I_{e(l)}$ = Effective moment of inertia over center support, $\text{in}^4$

The value for the effective moment of inertia over the center support was calculated according to Equation 8-12a of ACI 440 (2003) which accounts for the lower modulus of elasticity of FRP

bars and the bond behavior between the bars and the concrete. This equation is presented here as Equation 4.20.

$$I_{e(l)} = \left(\frac{M_{cr}}{M_a}\right)^3 \beta_d I_g + \left[1 - \left(\frac{M_{cr}}{M_a}\right)^3\right] I_{cr} \le I_g \qquad \text{(Eqn. 4.20)}$$

Where: $I_{e(l)}$ = Effective moment of inertia at the support, in.$^4$

$M_{cr}$ = Cracking moment, kip-in.

$M_a$ = Applied moment, kip-in.

$\beta_d = \alpha_b\left(\frac{E_f}{E_s} + 1\right)$

$\alpha_b$ = bond-dependent coefficient, 0.5 for GFRP and steel

$I_g$ = Moment of inertia of the gross section, in.$^4$

$E_f$ = Modulus of elasticity of GFRP, ksi

$E_s$ = Modulus of elasticity of steel, 29000 ksi

$I_{cr}$ = Moment of inertia of the cracked section, in.$^4$

The cracked moment of inertia, $I_{cr}$, was calculated according to equation 8-10 of ACI 440 as shown in equation 4.21.

$$I_{cr} = \frac{bd^3}{3}k^3 + n_f A_f d^2 (1-k)^2 \qquad \text{(Eqn. 4.21)}$$

Where: $I_{cr}$ = cracked moment of inertia, in.$^4$

$b$ = deck width, in.

$d$ = effective depth, in.

$k = \sqrt{2\rho_f n_f + (\rho_f n_f)^2} - \rho_f n_f$

$\rho_f$ = FRP reinforcement ratio

$n_f = \frac{E_f}{E_c}$

$A_f$ = Area of GFRP reinforcement, in.$^2$

Due to the fact that the steel is the primary tensile reinforcement for positive moment flexure of the deck, the effective moment of inertia at the midspans was calculated according to the Branson equation of ACI 318 which is presented as Equation 4.22.

$$I_{e(m)} = \left(\frac{M_{cr}}{M_a}\right)^3 I_g + \left[1 - \left(\frac{M_{cr}}{M_a}\right)^3\right] I_{cr} \leq I_g \qquad \text{(Eqn. 4.22)}$$

A spreadsheet was developed in Microsoft Excel to calculate the theoretical deflections of the specimens over a range of applied loads. When the applied load was less than the theoretical cracking load calculated for the region over the center support, the gross section moment of inertia was used to predict deflections. When the applied load exceeded the calculated cracking load, Equations 4.18 through 4.21 were used to calculate the effective moment of inertia for each load point. Each deck was then modeled in RISA-3D for a few specific load cases to determine a constant by which the ratio of the load to the effective moment of inertia, $P/I_e$, could be calculated to find the deflection for a range of applied loads. Important constants for each specimen are listed in Table 4.12. Values for $E_c$ and $E_f$ were the same as presented previously in Table 4.7.

***Table 4.12 – Deflection Calculation Input Values***

| Deck | $M_{cr}$ | $I_g$† | $I_{cr}$ | $\rho_f$ | constant |
|---|---|---|---|---|---|
| 1 ft Shear | 5.63 kip-ft | 443 $in^4$ | 43.1 $in^4$ | 0.0145 | 0.905 $in^5$/kips |
| 2 ft Shear | 11.3 kip-ft | 887 $in^4$ | 86.1 $in^4$ | 0.0145 | 0.905 $in^5$/kips |
| 3.5 ft Shear | 20.0 kip-ft | 1552 $in^4$ | 149 $in^4$ | 0.0145 | 0.892 $in^5$/kips |
| 5 ft Shear | 29.3 kip-ft | 2217 $in^4$ | 208 $in^4$ | 0.0145 | 0.869 $in^5$/kips |
| 5 ft Degradation – Lab | 25.2 kip-ft | 1905 $in^4$ | 152 $in^4$ | 0.0152 | 0.912 $in^5$/kips |

†*$I_{cr}$ used was for cracking at the top of the section*

The theoretical deflection is plotted with the measured deflection values in Figure 4.9 for the 1 ft shear specimen. In this plot the load shown corresponding to each deflection point is the combined load of both tire patches. Plots for the other specimens are presented in Appendix H. The plot represents the data as it was directly recorded by the data acquisition system during the testing procedure. The downward-pointing ticks on the two recorded data series are due to a combination of bleed-off from the hydraulic ram and creep of the deck while the load application was paused to allow for collection of DEMEC readings and crack widths. The loop at the start of the graph of the recorded data is the cycling of the load application between service load and no load. This region is examined more closely in Figure 4.10.

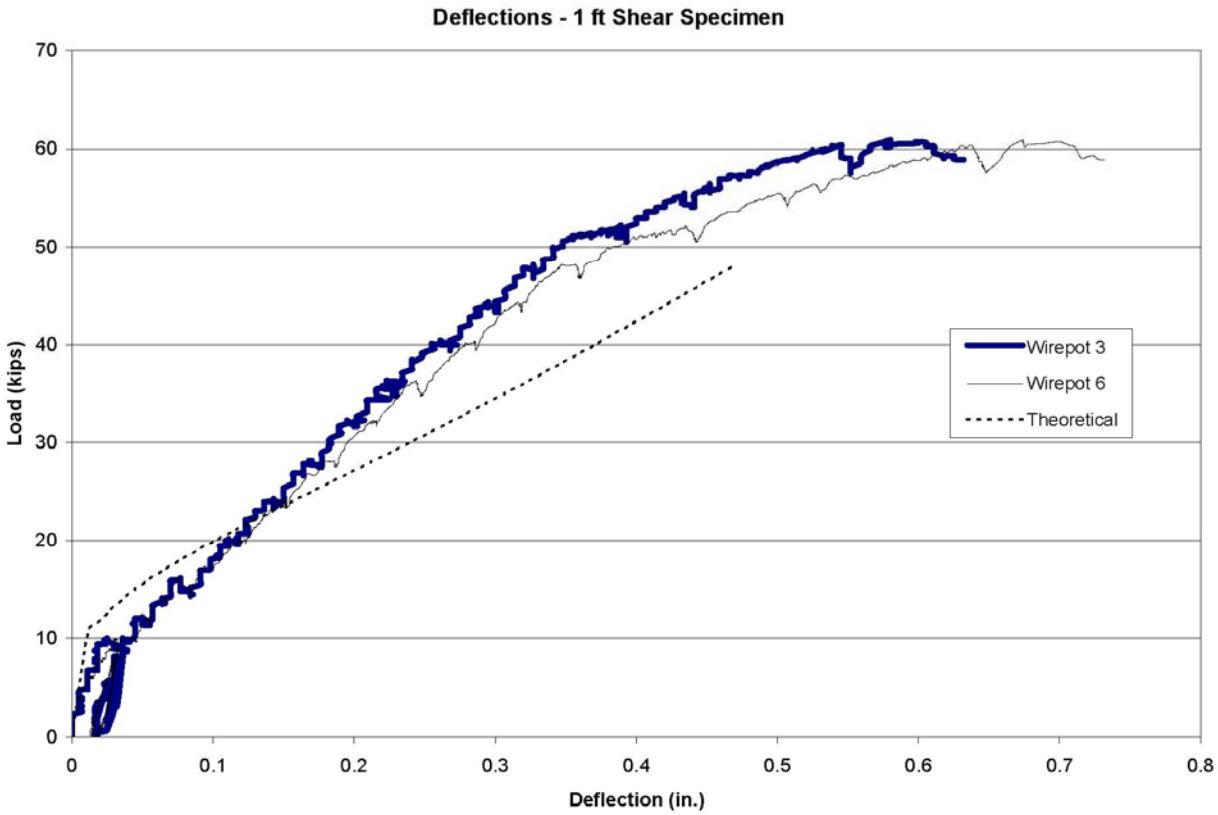


**Figure 4.9 - Plot of the load versus deflection for the 1 ft shear specimen**

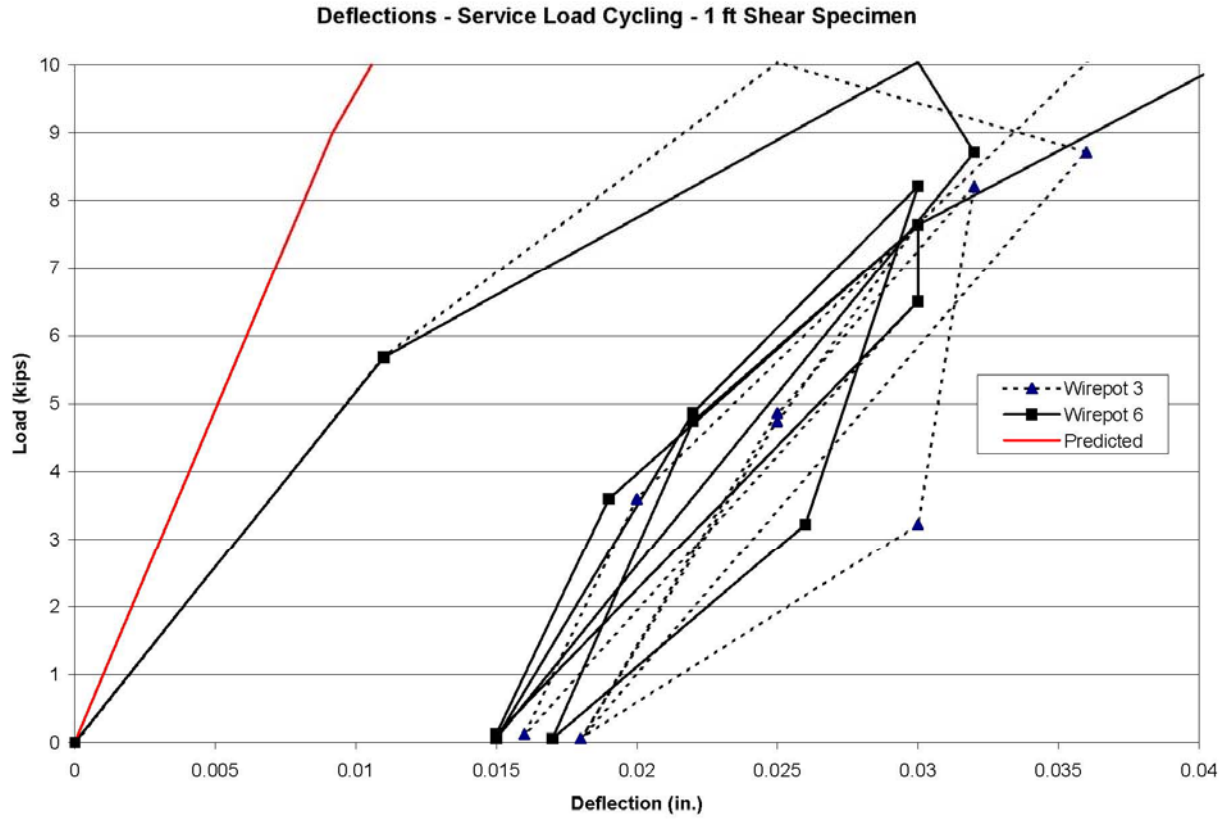


**Figure 4.10 - Plot of load versus deflection during the service load cycling of the 1 ft shear specimen**

A review of this plot in Figure 4.10 reveals the permanent residual deflection of the midspan at the points of no load following cracking of the section. Additionally, there is some small increase in deflection at each consecutive point of zero load. The permanent deflection is due to the reduced stiffness caused by the cracking of the section combined with the continued application of the self-weight and the weight of the spreader beam and loading ram concentrated on the two load patches. The slight increase in the deflection between cycles is caused by the continuation of cracking and therefore the further increase of member flexibility. Another likely cause of this permanent and increasing deflection is plastic bond slip which occurs when the bond between the reinforcement and the concrete slips and the crack does not close after the load is removed.

Overall, the equations presented in the various ACI documents seem to predict the moments of inertia well, leading to a relatively decent prediction of the deflections. The only apparent significant variance was that Equation 4.19 seems to be slightly unconservative in its determination of the moment of inertia prior to cracking in the positive moment regions. Its rather large weighting towards the midspan moment of inertia does not allow proper consideration of the deck flexibility realized after cracking over the center support, which results in the prediction of deflections that are too low prior to cracking of the midspans. Following cracking of the positive moment regions, the slope of the theoretical model becomes too shallow, which makes the overall deflection prediction notably conservative until the prediction is no longer valid when the concrete goes beyond the linear elastic range, which was considered to be when the stress in the section exceeded $0.5f'_c$.

### 4.1.4 Reinforcement Strain

This section presents the details of the strain in the reinforcement obtained throughout the testing of each shear specimen. The strain was measured with electrical resistance strain gages that were applied to both the steel and GFRP rebar and the data was collected by a data acquisition system.

#### *4.1.4.1 Steel Reinforcement Strain – Negative Moment Region*

A review of the load verses strain diagrams for the steel rebar in the negative moment regions of all the shear specimens reveals that the strains were negative, indicating compression, prior to cracking of each deck. Cracking occurred near the calculated service loads; in the 3.5 ft deck cracking occurred just prior to reaching the service load and in the 1 ft and 5 ft shear

specimens, cracking occurred just above the service load. The 2 ft deck was cracked slightly prior to testing, but a more significant crack occurred above the service load. More details on cracking are presented in Section 4.1.5.

Once the deck was cracked, the strain in the steel rebar over the center support changed to tension and remained in tension for the service load cycling procedure for all but the 2 ft and 5 ft shear decks. This change from compression to tension for the steel rebar was expected because, when the section cracked, the neutral axis moved from above the steel to below the steel. Since the 2 ft deck was cracked prior to testing, it was assumed that the section would act as cracked. However, upon review of the data, significant cracking did not occur until after the actual calculated service load, at which point the steel did go into tension. It should also be noted that the service load for the 2 ft specimen was incorrectly calculated prior to testing and the specimen was therefore only cycled to half of the service load.

The 5 ft shear deck was subjected to the complete service load cycling procedure prior to continuing the loading to the cracking load. Therefore, as the section remained uncracked throughout the service loading cycles, the steel in the negative moment region remained in compression until the next phase of testing. This was expected since the neutral axis was above the steel rebar prior to cracking.

One steel bar of the 1 ft shear specimen was gaged in the negative moment region of the member with two strain gages, one over each edge of the center support. These strain readings, as recorded by the data acquisition system, are shown in Figure 4.11.

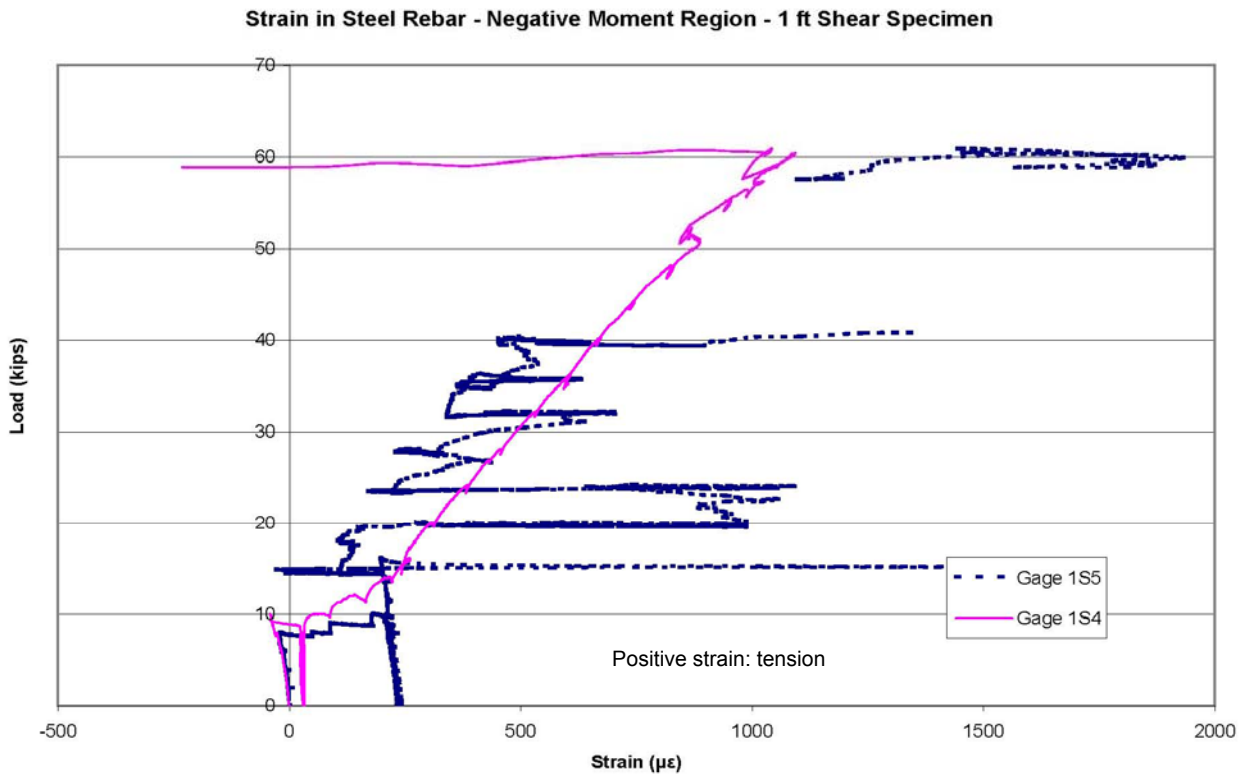


**Figure 4.11 - Strain of the steel rebar over the center support - 1 ft shear specimen**

The strain in the bar on both sides of the center support seems to be similar, with one gage, 1S4, reporting a slightly higher strain up to a load of approximately 40 kips. At this point, the readings in gage 1S5 became very erratic through the remainder of the test. The erratic results, also obtained from this gage at approximately 15 and 20 – 25 kips, indicate that the gage was most likely malfunctioning and this was taken into consideration when reviewing the data above 40 kips. However, several points around the location of 60 kips behave as anticipated, indicating an increase in strain while the other gage reported a decrease in strain at failure of the specimen. This was expected as the shear crack formed on one side of the center support and, upon failure, opened excessively thereby releasing the strains on the other side of the support, to the point that the steel entered slight compression.

Figure 4.12 shows a closer view of the service load cycling region of Figure 4.11. The small compressive strains are easily viewed in this plot in both gages prior to cracking of the section in the first ascension of the load to service levels. The strains of gage 1S5 are considerably higher relative to gage 1S4 during the service load cycling procedure. This may be due to the specimen not being evenly seated on the center support, thereby reducing the support area and moving the supported region more towards one gage than the other. This condition was

discovered after testing of the 2 ft shear specimen and corrected for the 3.5 ft shear specimen and all tests conducted afterwards.

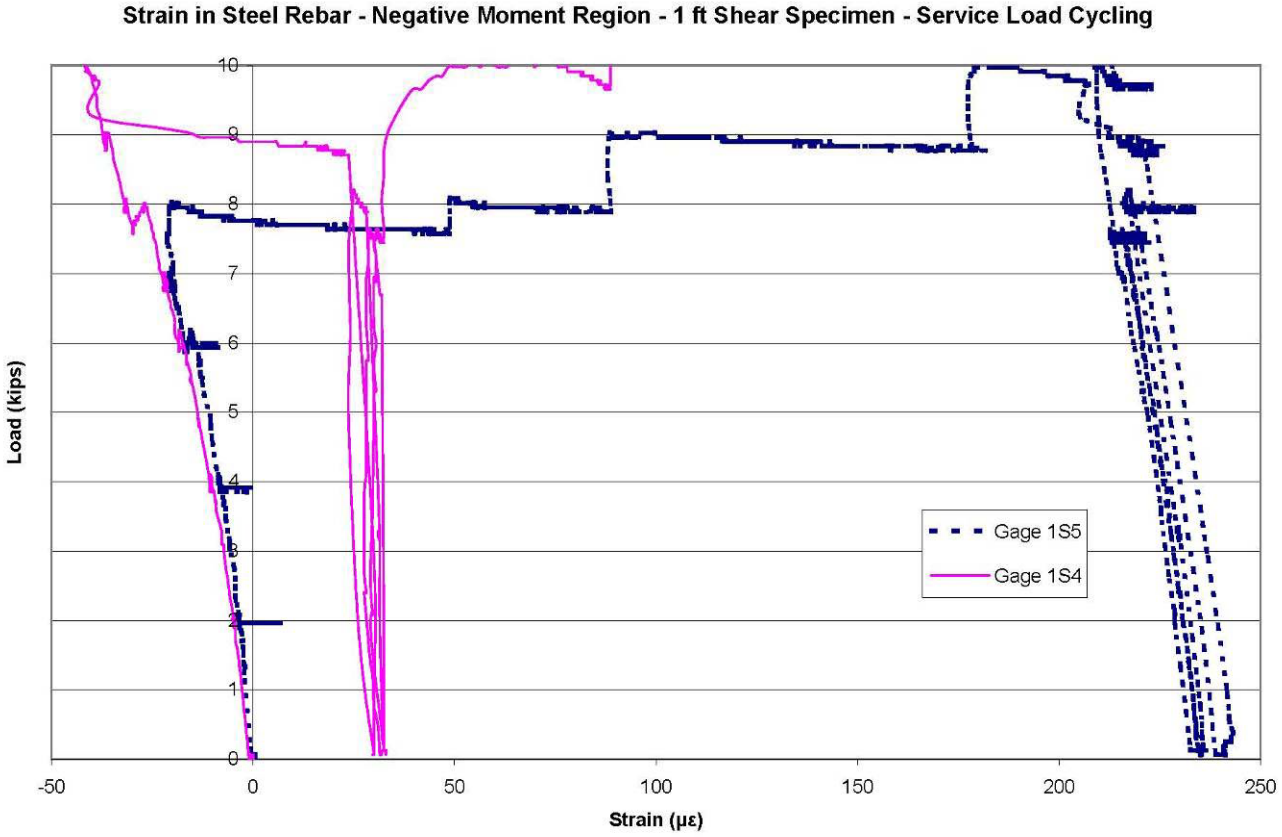


**Figure 4.12 - Strain of the steel rebar in the negative moment region during service load cycling - 1 ft Shear**

The plots for the 2, 3.5, and 5 ft specimens are presented in Appendix I. These specimens exhibited similar behavior as shown for the 1 ft specimen. As with the 1 ft specimen, erratic readings from one of the gages of the 2 ft section render it suspect to malfunction, however, the general trend is evident and useful for consideration. The tests of the 3.5 and 5 ft specimens each were conducted in two parts as discussed previously. Plots of the steel strain in the negative moment regions for these specimens are presented for both the first and combined runs in Appendix I.

### *4.1.4.2 Steel Reinforcement Strain – Positive Moment Region*

Figure 4.13 is a plot of the total load versus strain of the steel reinforcement in the midspans for the 1 ft shear specimen over the entire period of the test. Figure 4.14 is a look at the first portion of the test, up to just after the specimen cracked. The behavior of this specimen is typical of the other decks with the exception of the 3.5 ft specimen. All of the decks exhibited

a sudden increase in strain of the steel rebar in the positive moment regions when the section initially cracked in the negative moment region. The 1 ft, 2 ft, and 5 ft sections each experience a large increase in strain as the section fails, forming a plateau in the plots. The 3.5 ft section, however, appears to fail more suddenly, with no great increase in positive steel strain at the failure load. Figure 4.15 shows the plot for the second run of the 3.5 ft specimen. When observing the strain values of the 3.5 ft deck, it should be noted that the when the test was stopped for the first run of this specimen due to the unexpected yielding of the spreader beam the values of the strain gages were zeroed before continuing with the second run of the test.

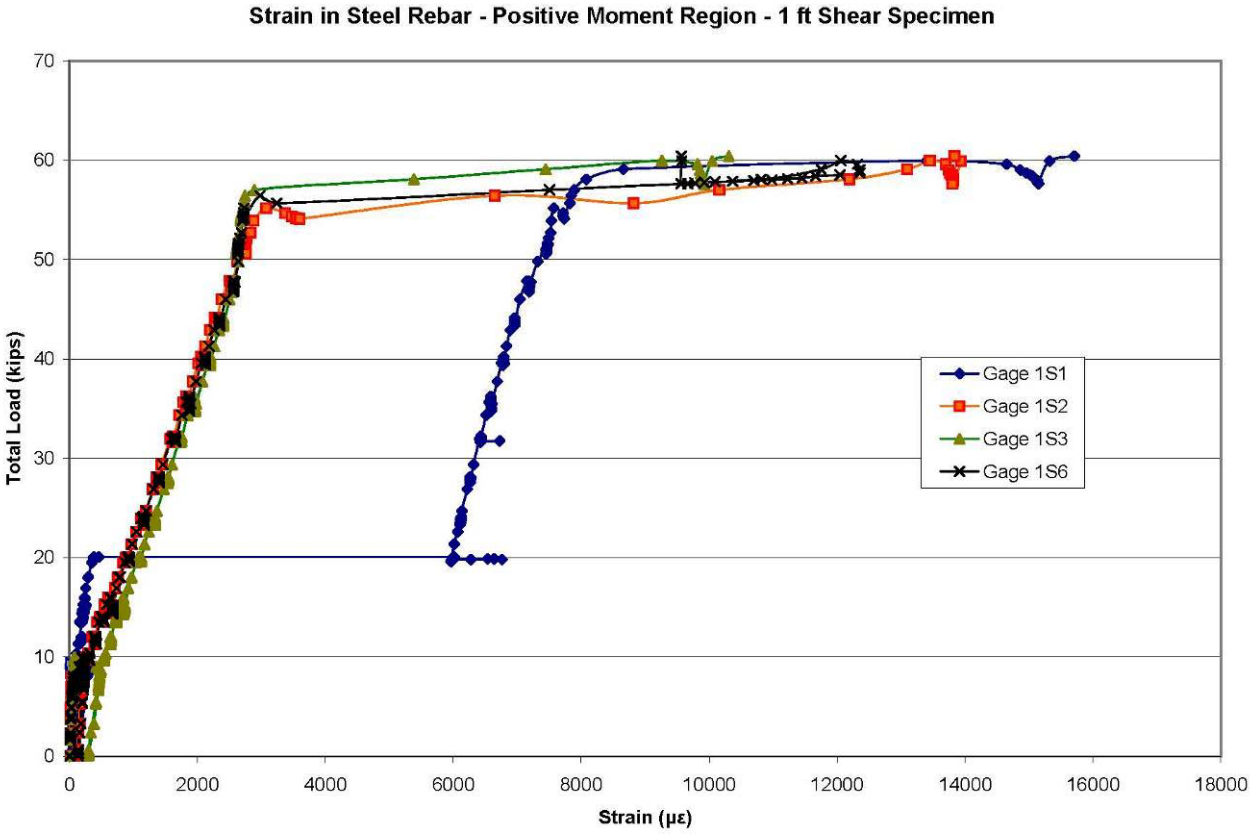


**Figure 4.13 - Plot of the total load versus strain of the steel rebar in the positive moment region of the 1 ft specimen**

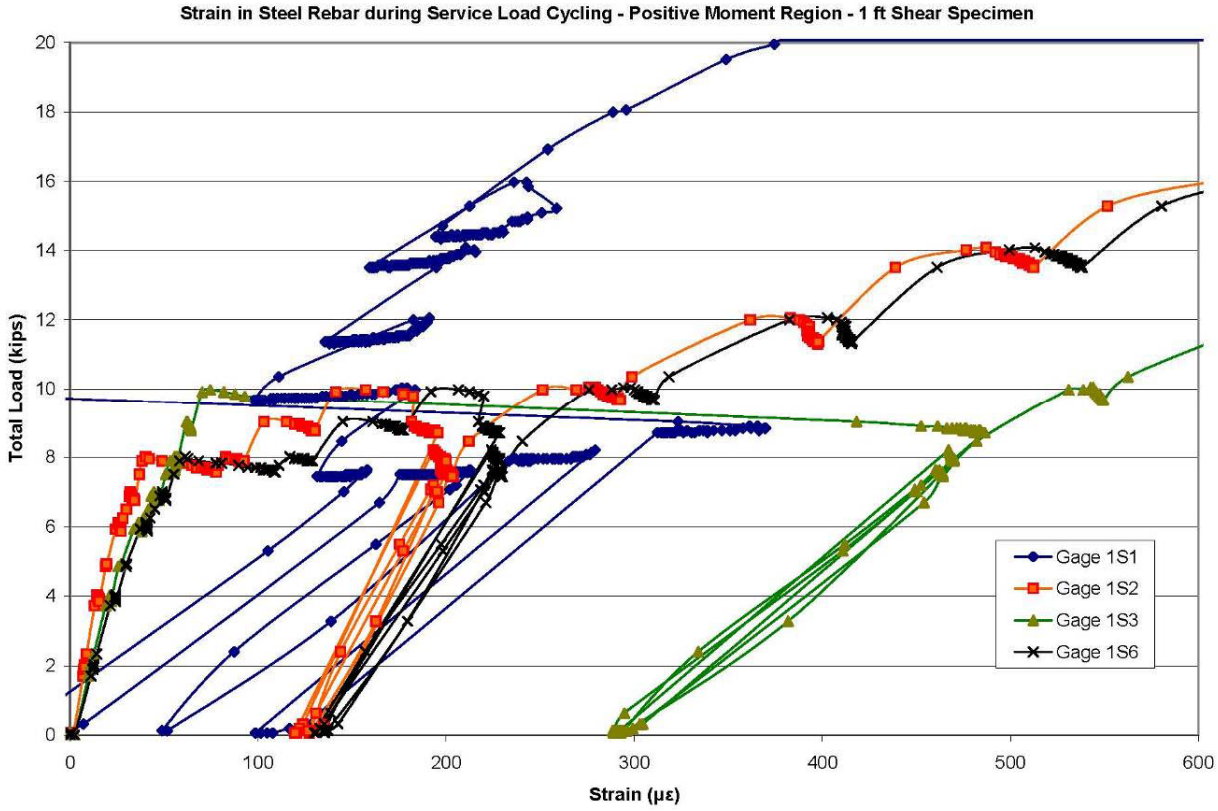


**Figure 4.14 – Strain of the steel rebar in the positive moment region during service load cycling – 1 ft specimen**

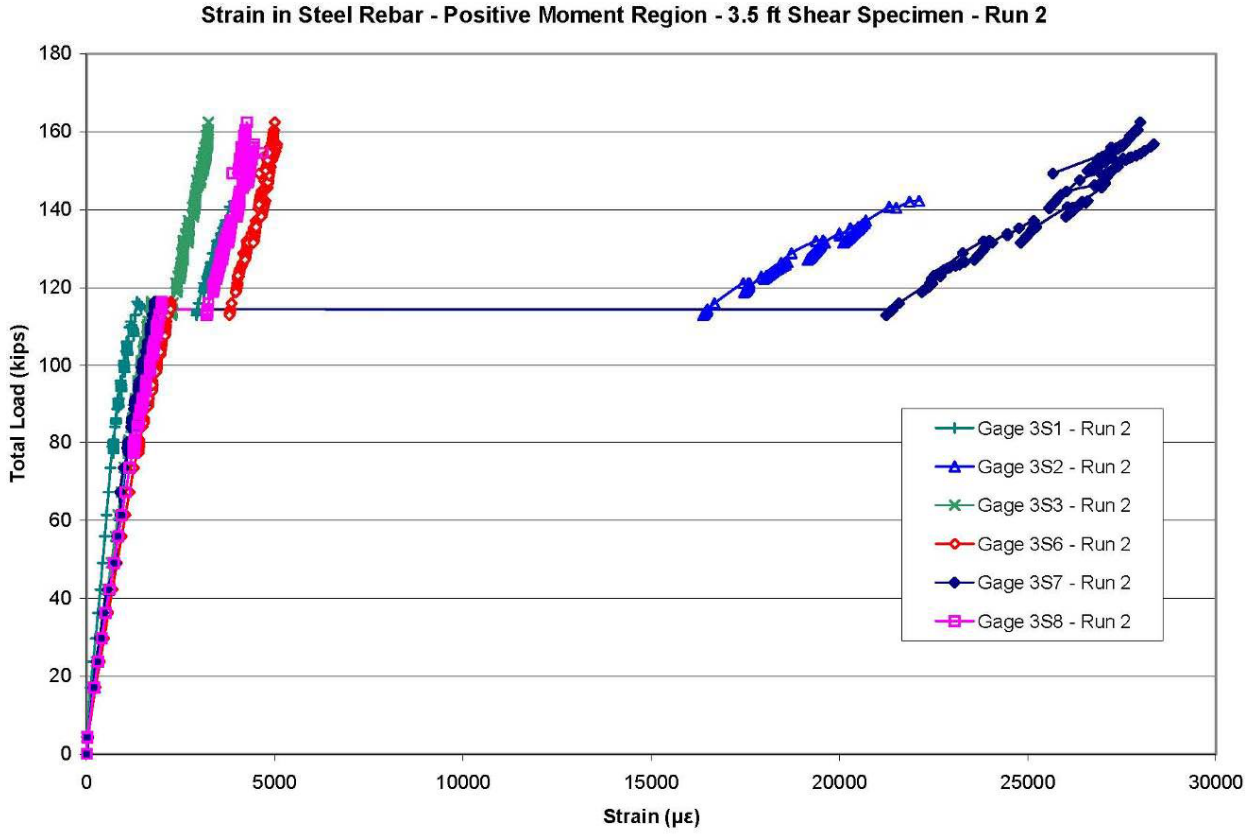


**Figure 4.15 - Strain of the steel rebar in the positive moment region - 3.5 ft specimen**

Assuming a steel yield strain of 0.2%, the steel in the midspan regions of all four specimens yielded prior to shear failure of the section. This behavior was expected based on the comparison of the moment capacity of the section, assuming yielding of the steel, to the resulting moment at the load points at failure.

#### *4.1.4.3 GFRP Reinforcement Strain – Negative Moment Region*

A plot of the total applied load with respect to the strain in the GFRP reinforcement over the center support of the 1 ft shear specimen is presented as Figure 4.16. All six gages are shown, two per bar on either side of the support as detailed in the strain gage maps in Appendix B. The sudden increase in the strain in three of the gages on the same side of the support (gages 1F1, 1F3, and 1F5) around 10 kips in the service load cycling region of the plot indicates formation of the first crack of the section. Figure 4.17 provides a closer view of this portion of the test and clearly shows that the crack forms following the first loading cycle.

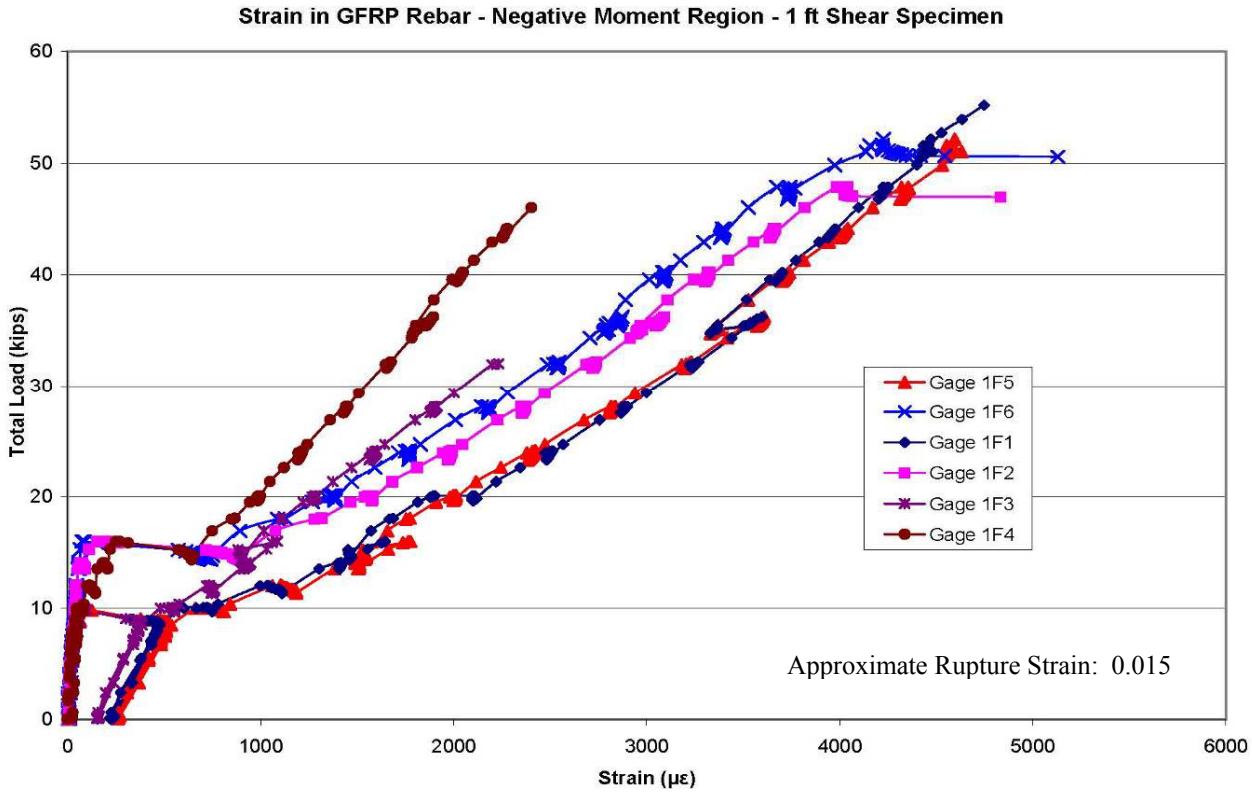


**Figure 4.16 - Strain in the GFRP rebar in the negative moment region - 1 ft specimen**

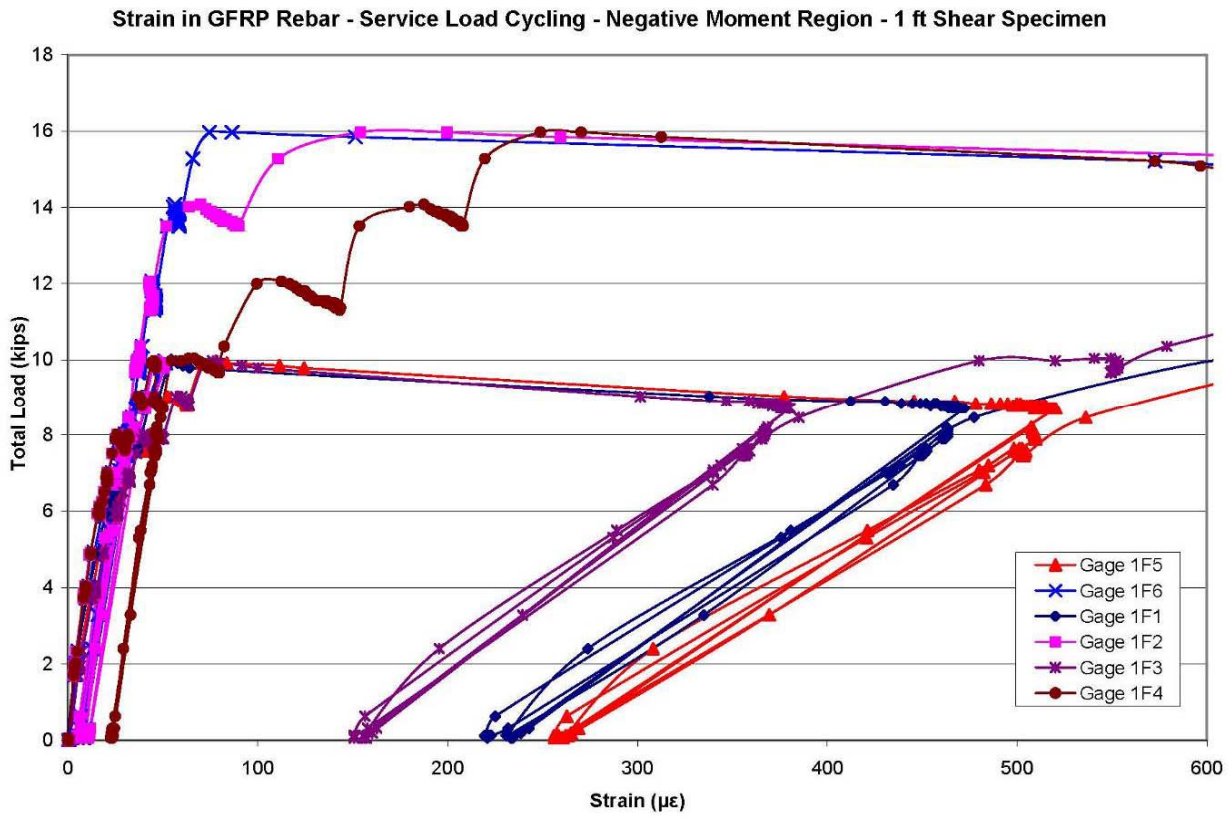


**Figure 4.17 - Strain in the GFRP rebar over the center support during service load cycling - 1 ft shear specimen**

Close inspection of the data indicates a slight reduction in strain of the bar on the side opposite the crack. Prior to crack formation, however, all six gages exhibit the same behavior as well as very similar strain values, which was obviously expected for such a narrow specimen. After cracking, the order of strain magnitude in the odd-numbered gages proceeded from a high in gage 1F5 (an edge bar) to a low in gage 1F3 (on the center bar), indicating that the strain profile was not constant across the narrow section and that the outside bars experienced greater strains than the center bar.

Since the gages on each side of the support show very similar and consistent results, Figure 4.18 shows the data from the entire test for only the center bar for clarity. As previously discussed, the formation of the first crack on one side of the support around 10 kips during the service load cycling procedure is evident. At approximately 16.5 kips similar behavior is noted in the bar on the other side of the support where a large strain increase occurs with a simultaneous decrease in strain in the opposing gage, indicating formation of another crack so that the section is now cracked on both sides of the support. Following each crack, the slope for each respective gage beyond that point decreases indicating a lowering of the neutral axis and an

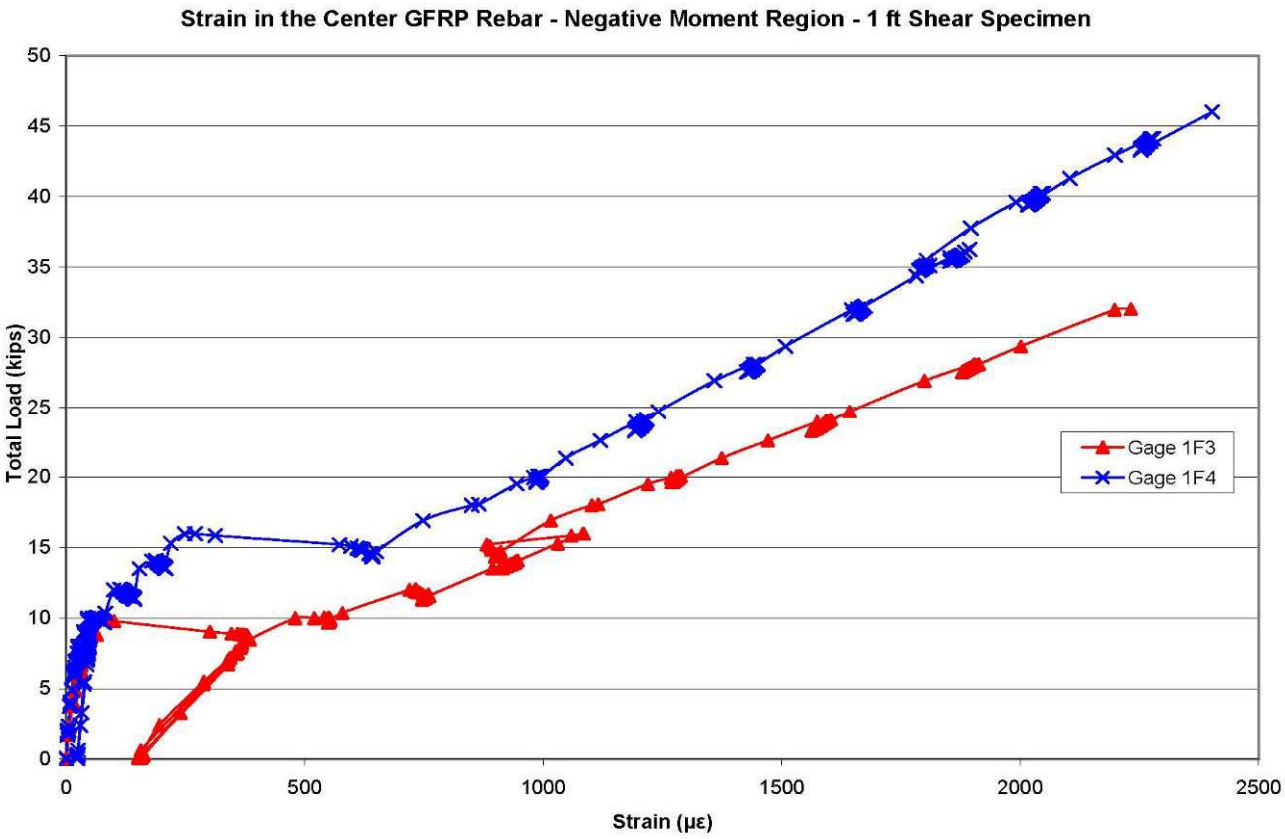


**Figure 4.18 - Strain in the center GFRP rebar over the center support - 1 ft specimen**

increased flexibility of the overall section. No further significant decrease in rigidity is evident after each subsequent crack formation and the span containing gage 1F4 appears to be stiffer and therefore taking a greater portion of the load throughout the test.

The plots from the other specimens are very similar to these and for brevity will not be further discussed here. They are presented in Appendix J.

To better examine the distribution of the load between bars, stress contour graphs were developed by plotting the stress determined for each gage against the horizontal distance of the respective gage from the centerline of the loading patch for a specified load. The stresses were calculated by multiplying the recorded strain in each gage by a modulus of elasticity of 6100 ksi. This was the average modulus found for the unused GFRP rebar specimens in tensile tests conducted as part of the strength degradation portion of this research. In order to allow more direct comparison between the specimens, the three load points chosen for these plots were ½ × service load, service load, and 1.5 × service load. Also, since two recorded strains of a particular bar differed depending on which side of the center support was being considered, the strains obtained from the gages of each bar on each side of the support were averaged for these plots.

This negates the majority of effects caused by the deck not being completely supported by the entire width of the flange of the center support. The plots also include the theoretical stresses calculated for each particular applied load. The moments in the section over the center support were calculated in RISA 3D for an assumed elastic condition. For the uncracked sections, the stress in the GFRP rebar was found by multiplying the moments from RISA by y, the distance from the neutral axis to the FRP rebar, and dividing by the transformed moment of inertia. For the cracked sections, the stresses were found in the same manner as the uncracked sections, except that the cracked moment of inertia was used as well as a larger value of y because of the lower neutral axis. Since the cracked condition produces significantly higher stresses in tensile rebar, a plot for both the uncracked and cracked conditions was made for each of the specimens. Figures 4.19 to 4.25 present the stress contours of the specimens. Note that there is a plot for only the cracked condition for the 2 ft specimen because this deck was prematurely cracked. Although these plots can give a very informative view of the strain behavior through the cross-section of the specimens, caution should be exercised in reviewing this data, particularly when comparing between different specimens. This is because the strain reported here is at one specific location on each bar and may include additional local effects that may not be experienced by the other bars or other specimens. For example, a crack may form at the same location as a strain gage on one bar, which would cause that local area of the bar to undergo additional strain because of the increase in tension at the bar at that location. This could be the cause of the strain profile change in the 2 ft specimen at $1.5 \times$ service load in Figure 4.21.

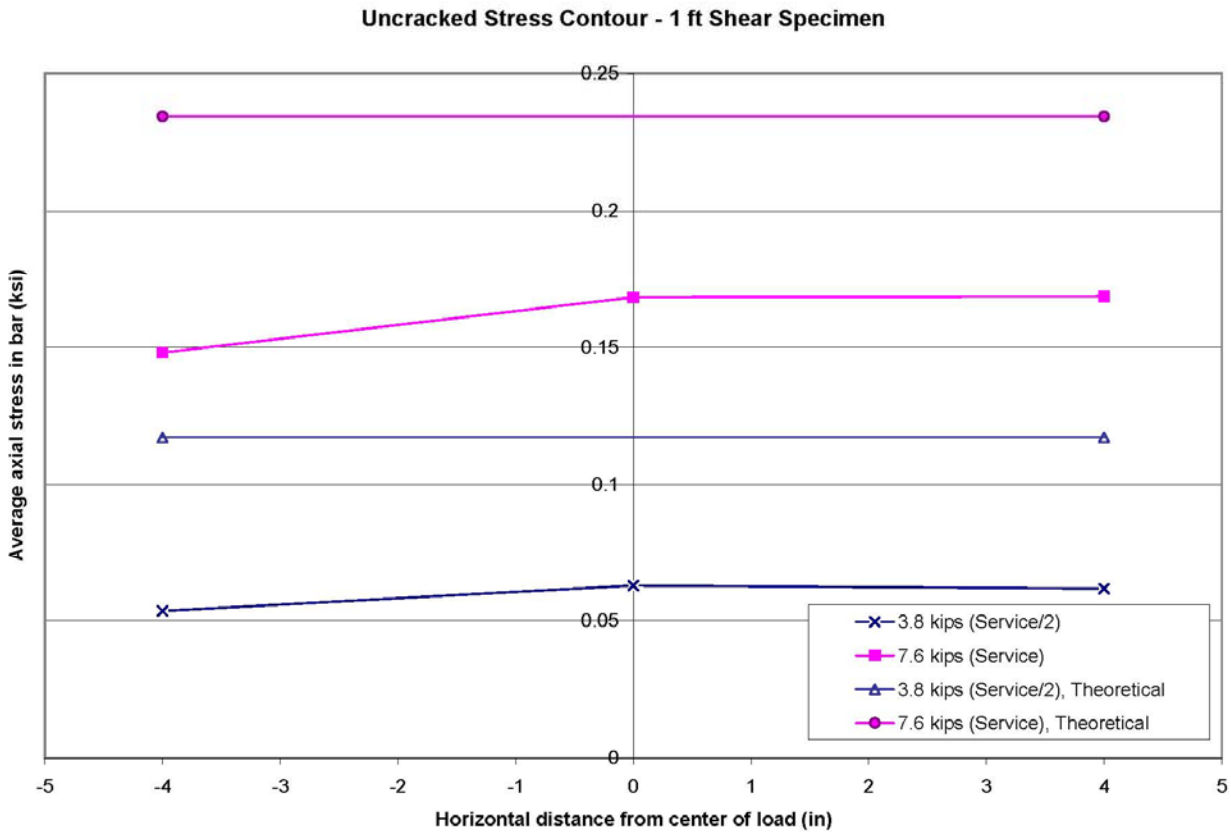


**Figure 4.19 - Contour plot for the stresses in the GFRP rebar - uncracked - 1 ft specimen**

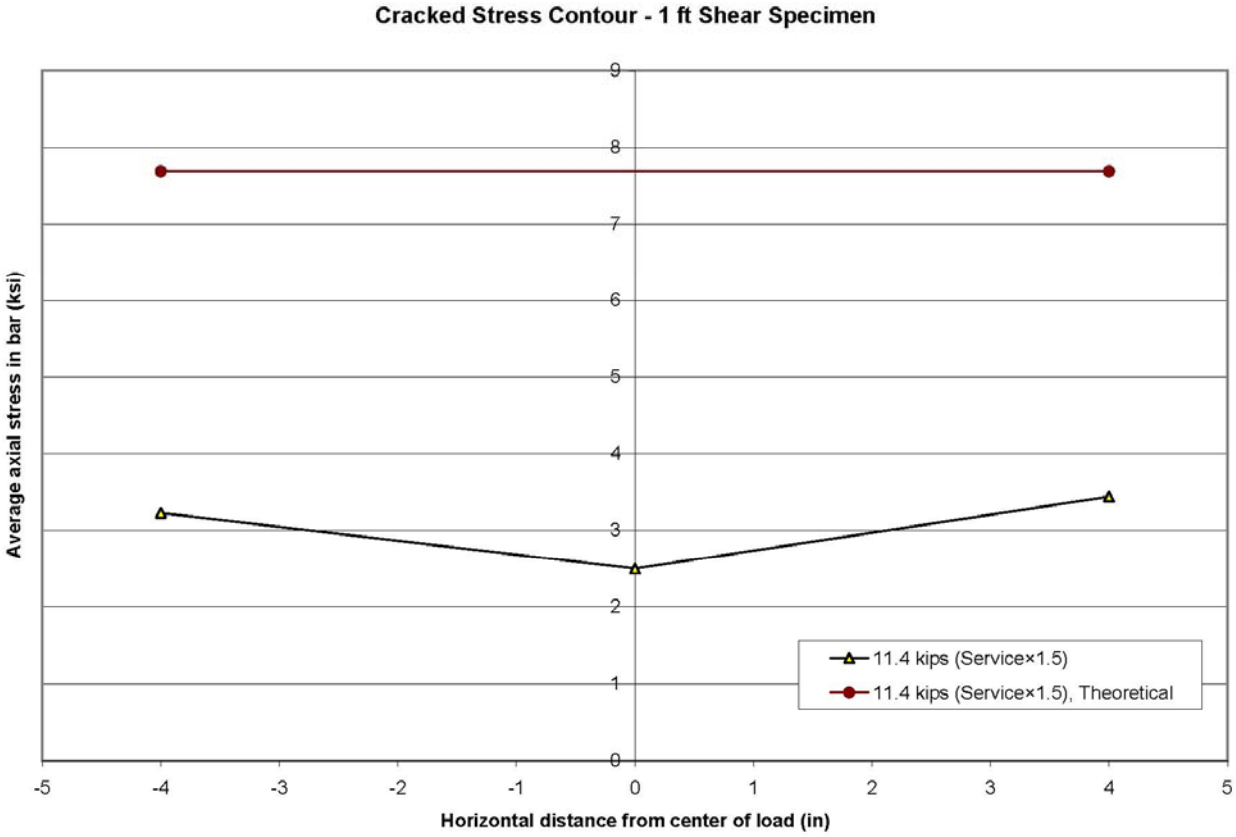


**Figure 4.20 - Contour plot for the stresses in the GFRP rebar - cracked - 1 ft specimen**

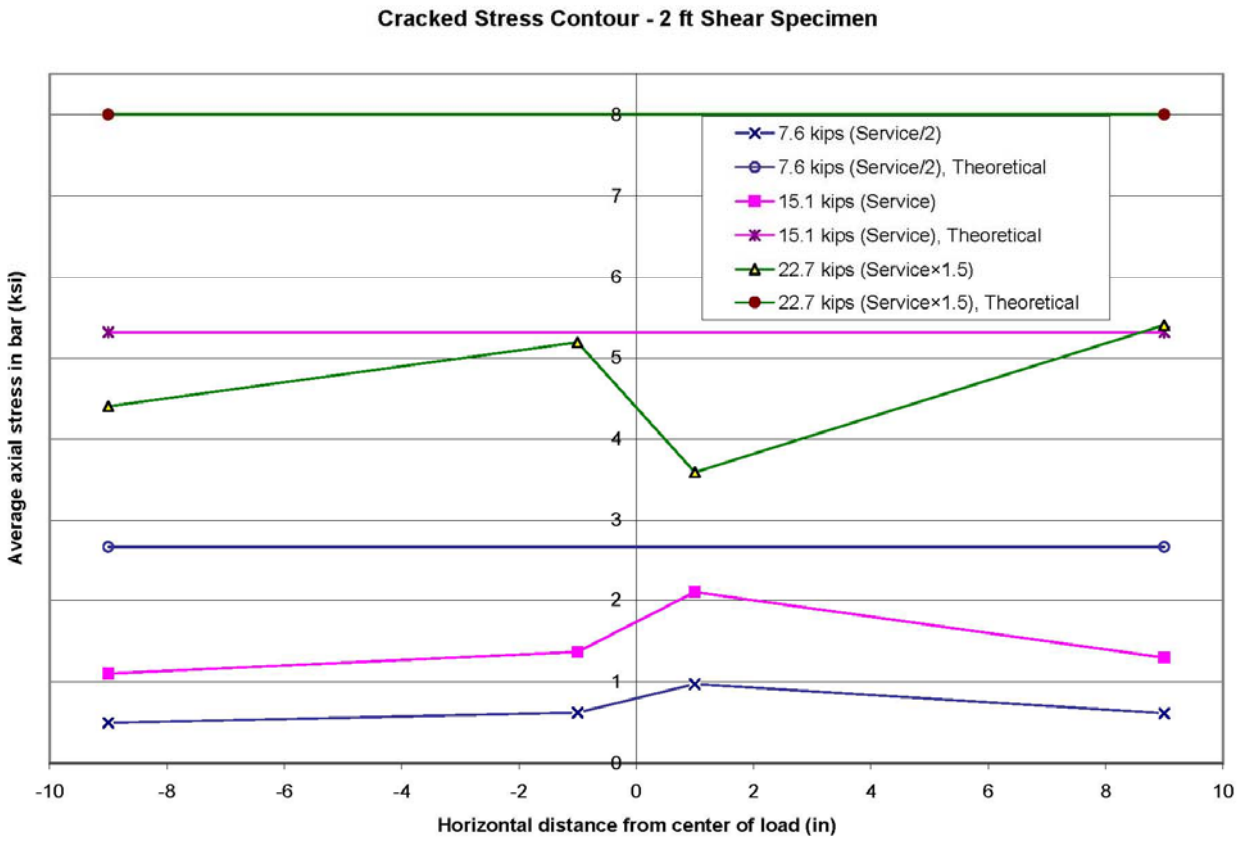


**Figure 4.21 - Contour plot for the stresses in the GFRP rebar - cracked - 2 ft specimen**

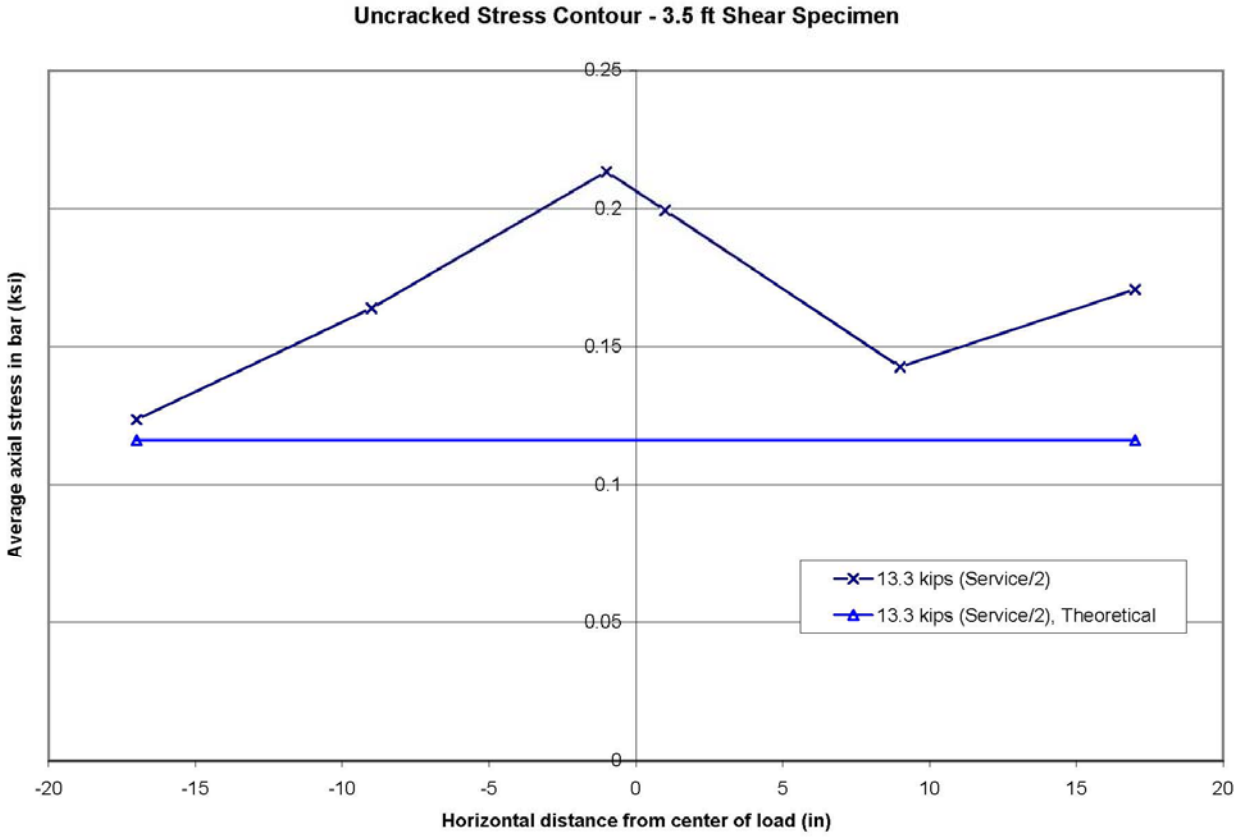


**Figure 4.22 - Contour plot for the stresses in the GFRP rebar - uncracked - 3.5 ft specimen**

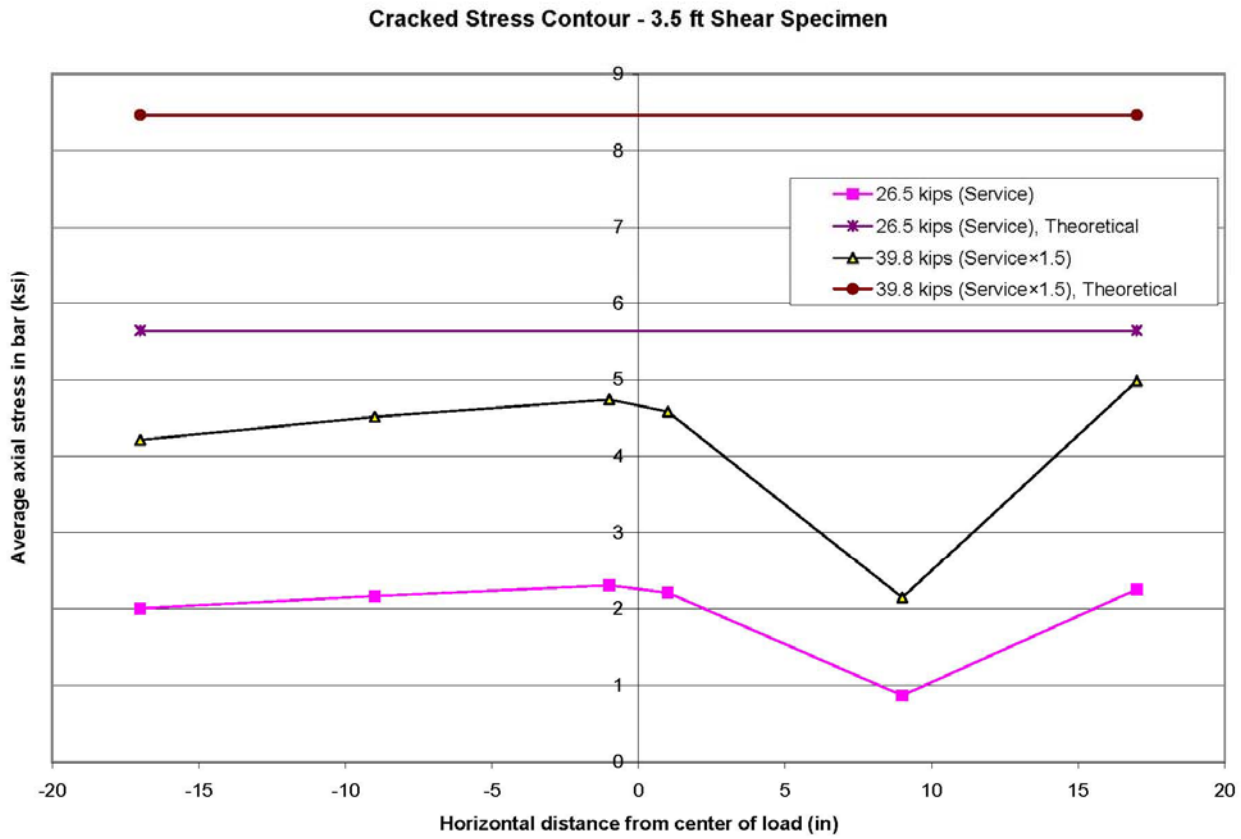


**Figure 4.23 - Contour plot for the stresses in the GFRP rebar - cracked - 3.5 specimen**

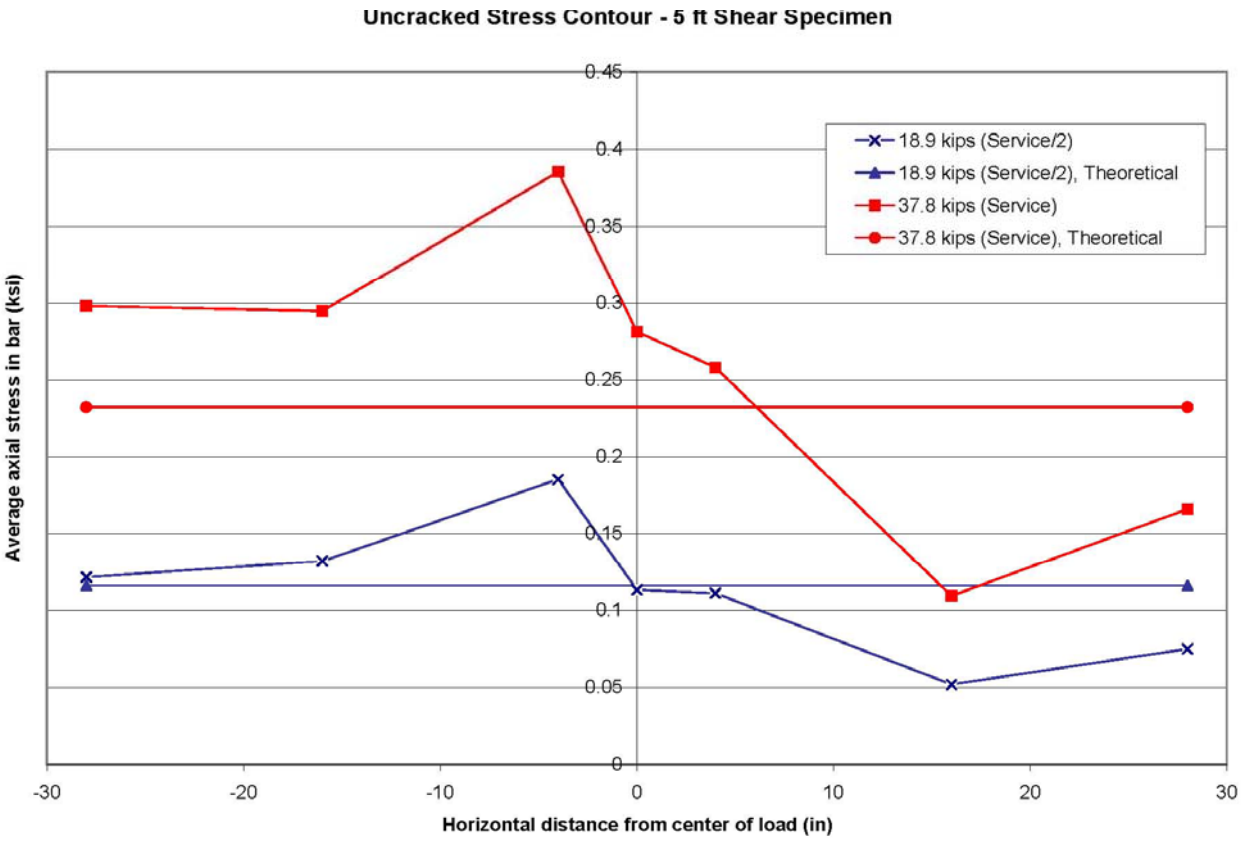


**Figure 4.24 - Contour plot for the stresses in the GFRP rebar - uncracked - 5 ft specimen**

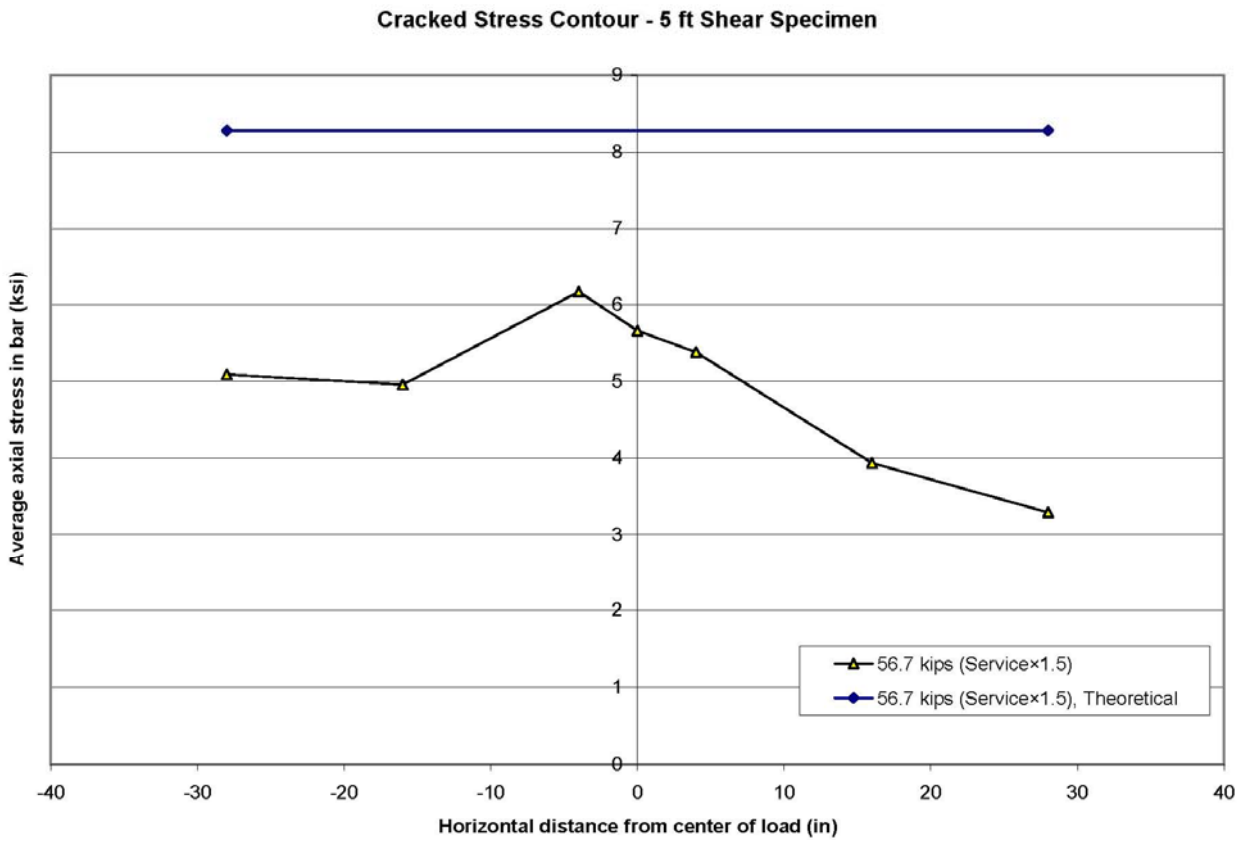


**Figure 4.25 - Contour plot for the stresses in the GFRP rebar - cracked - 5 ft specimen**

The section properties that were used to calculate the theoretical stresses shown on the plots are provided in the Table 4.13 below.

***Table 4.13 – Section Properties Used in Theoretical Stress Calculations***

| Specimen | $f'_c$ | $I_t$ | $I_{cr}$ | $y_{uncr}$ | $y_{cr}$ | Cracking Load (Total) |
|---|---|---|---|---|---|---|
| 1 ft | 6 ksi | 454.2 $in^4$ | 46.3 $in^4$ | 1.88 in. | 4.19 in. | 10 kips |
| 2 ft | 6 ksi | NA | 90.0 $in^4$ | 1.86 in. | 4.25 in. | NA |
| 3.5 ft | 6.2 ksi | 1581 $in^4$ | 149.8 $in^4$ | 1.86 in. | 4.28 in. | 23 kips |
| 5 ft | 6.5 ksi | 2257 $in^4$ | 218.0 $in^4$ | 1.86 in. | 4.27 in. | 40 kips |

In general, the stress in the section was highest at the middle bars and tapers off towards the edges, which was the behavior that was expected. Although there are a couple plots in which the stress was greater in an edge bar, the stress in the bar on the other side of the specimen at the same distance was lower. The only exception to this was with the 1 ft specimen after cracking of the section in which both edge bars clearly experience a higher stress than the center bar. The exact reason for this is unclear, but one cause may be a lower stiffness towards the edges due to a lesser volume of concrete since it is at the border of the section. This effect would only be observed in the narrow specimen because the width of the load patch is only slightly smaller than the width of the deck itself.

The theoretical stresses are intended to predict the peak stresses in the section. However, for the uncracked condition the calculated stresses were slightly below the actual peak stresses in the 3.5 ft and 5 ft specimens and were slightly conservative in the 1 ft specimen.

For the cracked condition, the theoretical stresses greatly overpredicted the actual stresses. This is because the method assumes that the section is completely cracked, which is not the case at these loads. As the load continues to increase, the cracks will continue to grow deeper into the section and the actual properties will approach the assumed fully cracked condition. Therefore, it is expected that as the load increases, the predicted values will become less conservative and a better measure of the actual stresses. Unfortunately, similar plots could not be made at the failure of the section because a large number of the GFRP gages were no longer functioning at that point in the test procedure.

## 4.1.5 Cracking

### *4.1.5.1 Cracking Loads*

The combined loads at which the first visible cracks were seen for each of the decks are presented in Table 4.14 with the predicted cracking load for comparison.

***Table 4.14 – Cracking Loads of Shear Decks***

| Specimen | First Crack from Crack Log | First Crack from Stress Plots | Predicted Cracking Load |
|---|---|---|---|
| 1 ft shear | 10.0 kips | 10 kips | 9.1 kips |
| 2 ft shear | NA | 20 kips | 18.1 kips |
| 3.5 ft shear | 23.2 kips | 23 kips | 32.3 kips |
| 5 ft shear | 39.5 kips | 40 kips | 47.2 kips |

*Loads reported are total applied loads*

The cracking load was predicted by calculating the cracking moment according to Equation 4.23 and dividing this result by the moment over the center support obtained from a RISA-3D analysis for an applied total load of 1 kip, or 0.5 kips per patch.

$$M_{cr} = \frac{f_r I_t}{y} \qquad \text{(Eqn. 4.23)}$$

Where: $M_{cr}$ = cracking moment, k-in.

$f_r = 7.5\sqrt{f_c'}$, psi

$f_c'$ = concrete compressive strength, psi

$I_t$ = transformed moment of inertia, $in^4$

$y$ = distance from the neutral axis to the extreme compression fiber, in.

The calculations predicted the cracking load rather well for the 1 ft and 2 ft shear specimens. Although the formation of the first crack in the 2 ft specimen was not recorded, the load versus strain plot for the GFRP rebar, shown as Figure 4.26, clearly indicates formation of a crack just above the predicted cracking load. Crack formation was determined from the load versus strain diagrams by the first sudden change in slope of the plot indicating a greater flexibility. For the larger two specimens, however, the predicted cracking load was unconservative, with the actual cracking loads of the 3.5 ft and 5 ft decks being only 71% and 85% of the predictions, respectively.

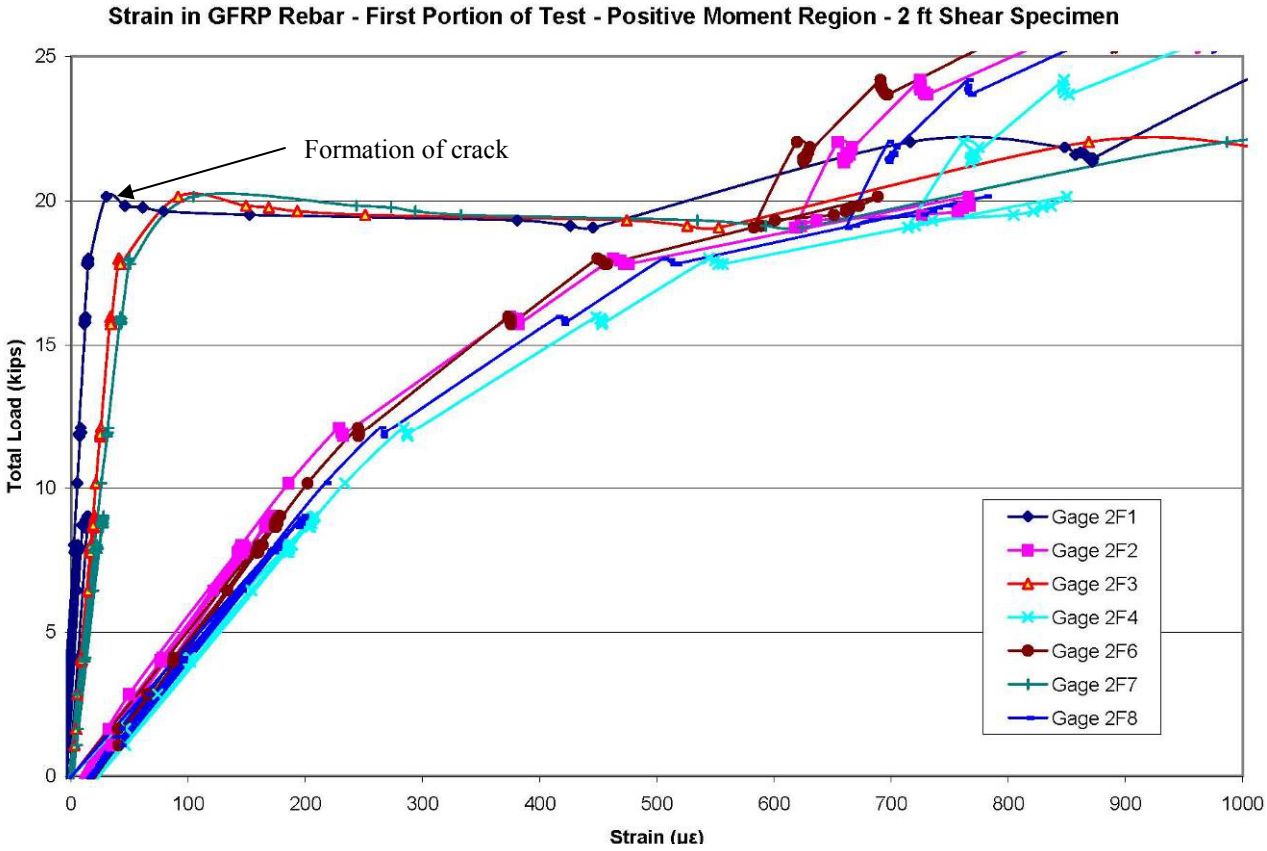


**Figure 4.26 - Strain in the GFRP rebar over the center support for the first portion of testing - 2 ft specimen**

In all four shear specimens, the first observed crack formed over one edge of the flange of the center support and propagated along the support to each side of the deck. This crack was then followed by cracking in the same span on the underside of the deck in the positive moment region under the load point. Additional cracks then formed in both the positive and negative moment regions of the other span, followed by further cracking in the positive and negative

moment regions of both spans. Figure 4.27 shows a crack map for the 2 ft shear specimen; maps for the other specimens are presented in Appendix K.

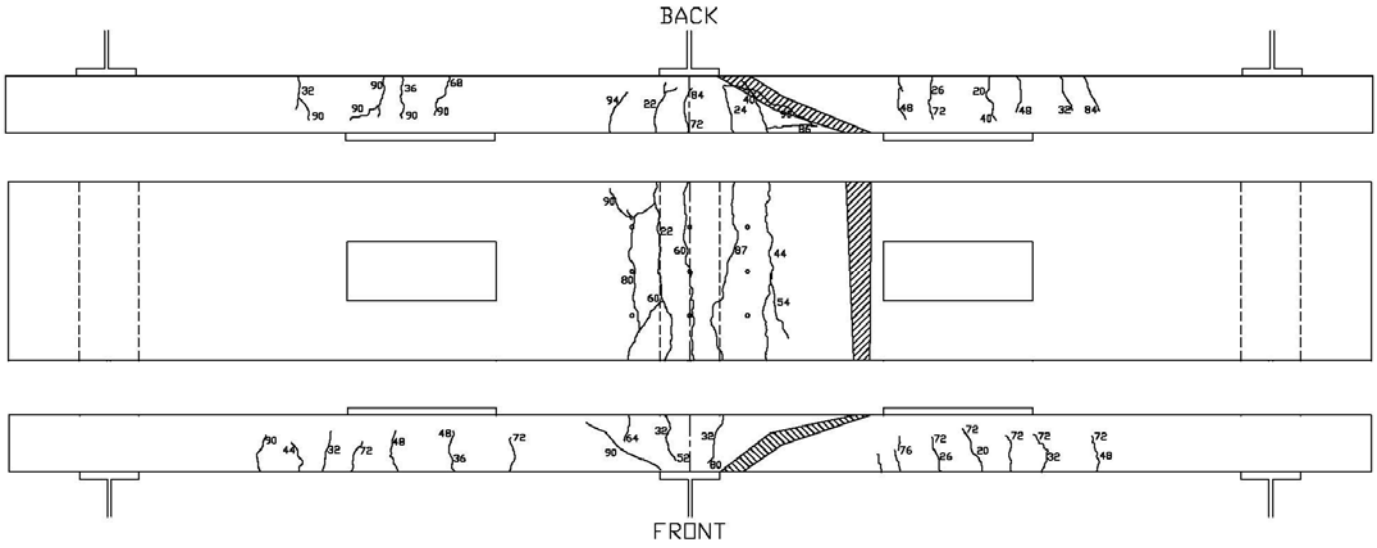


**Figure 4.27 - Crack map for the 2 ft shear specimen. The hatched section represents the shear failure area.**

One interesting observation was made regarding the cracking of the underside of the deck. In the 3.5 ft and 5 ft shear decks, as well as the 5 ft strength decks, cracks formed perpendicular to the center support between the support and the load points. Further, in the 5 ft decks, cracks were observed to form at an angle from under the load point towards the edge of the decks near the center support. These cracks were not observed in the 1 ft and 2 ft shear decks, which indicates that the specimens experienced some flexure in directions perpendicular to the supports. This may hint at the beginning of a transition of failure type from one-way to two-way shear. Figure 4.28 shows the cracking under one span of the 5 ft shear specimen, including the cracking perpendicular to the supports.

**Figure 4.28 - Cracking of the underside of the 5 ft shear specimen. Note the circled crack extending towards the location of the center support.**

#### *4.1.5.2 Crack widths*

Crack widths were measured and recorded for all specimens at various intervals throughout each test using either a crack microscope or a crack card, depending on the size and importance of the particular crack. A demountable mechanical strain gage, or DEMEC gage, was also used to measure the surface behavior of the decks during the same intervals. The recordings from the DEMEC gage included the combination of concrete strain and the sum of all crack widths between the two points used for the reading. This means that despite the precision of the instrument and the presence of only one crack inside its gage length, its results were expected to be larger than the crack width because of the inclusion of concrete strain. The DEMEC gage was also used as an indicator of crack formation; a sudden increase in the DEMEC reading was an indication that a crack had formed and greater care was employed to find it.

The measured crack widths were compared to predicted crack widths determined from the modified Gergely-Lutz equation presented in ACI 440 (2003), which is shown here as Equation 4.24.

$$w = \frac{2200}{E_f} \beta k_b f_f \sqrt[3]{d_c A} \qquad \text{(Eqn. 4.24)}$$

Where: $w$ = crack width, mils ($10^{-3}$ in.)

$E_f$ = modulus of elasticity of GFRP, 6100 ksi

$\beta$ = distance from the neutral axis to the bottom fiber, divided by the distance to the reinforcement

$k_b$ = coeffecient for the degree of bond between GFRP and surrounding concrete, 1.3 (from DeFreese (2001))

$f_f$ = stress in GFRP rebar, ksi

$d_c$ = concrete cover thickness measured from extreme tension fiber to center of closest bar, in.

$A$ = effective tension area of concrete, in.$^2$

The GFRP stress used in Equation 4.24 was an average of the stress in the bars recorded from strain gages on the same side of the center support as the largest crack at the particular load. However, when the specimen was considerably cracked on both sides of the support, the calculated stresses from all GFRP gages were averaged for this equation.

For the purpose of a simple, yet accurate comparison, when comparing DEMEC readings to measured and theoretical crack widths, only the DEMEC readings that crossed over the measured crack were considered and averaged. DEMEC values were converted to millimeters through the procedure in Equation 4.25.

$$w = 200mm \times 1000C\left(x - x_0\right) \qquad \text{(Eqn. 4.25)}$$

Where: $w$ = crack width, mm

$C$ = gage-specific conversion constant, $3.98 \times 10^{-6}$

$x$ = recorded DEMEC reading at a specific load

$x_0$ = recorded DEMEC reading at zero load

Figure 4.29 compares the theoretical maximum crack width with the measured crack width and DEMEC data for the 5 ft shear specimen.

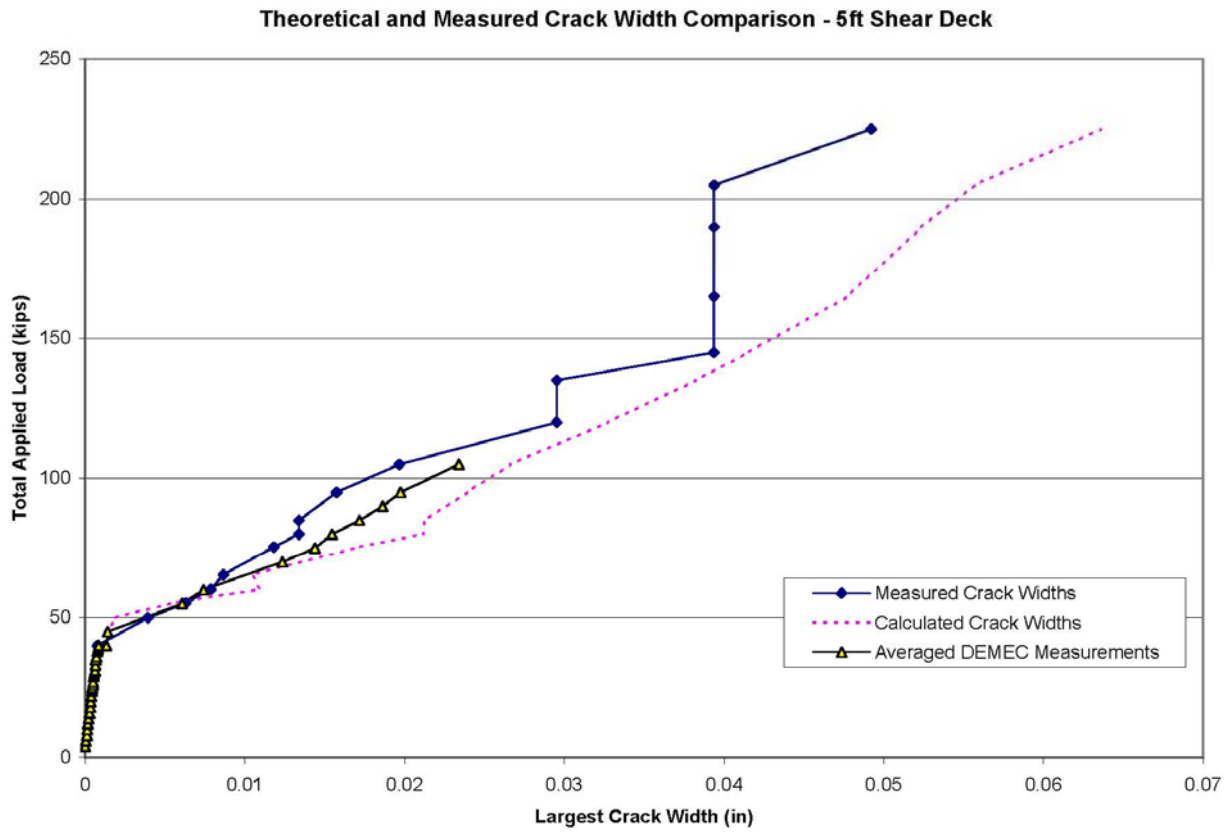


**Figure 4.29 - Theoretical and measured crack widths and DEMEC data for the 5 ft shear specimen.**

As can be seen from the figure, the DEMEC measurements were typically larger than the actual measured crack widths in the 5 ft shear specimen, as expected. However, this was not the case for the 1 ft and 2 ft decks, which is probably due to the location chosen to measure the crack on the deck.

In all four decks, the ACI 440 crack width equation overpredicted the measured crack widths. The only notable exception to this observation is with the points recorded below 20 kips for the 2 ft specimen.

### 4.1.6 Design Criteria

Although not a primary objective of this research, it is informative to review the performance of these specimens with the design criteria outlined by ACI, particularly since this same design was used in the construction of the Route 668 Bridge in Franklin County, Virginia. Table 4.15 shows various design criteria comparisons for each of the specimens. The deflection, stress, and crack width criteria are considered at each specimen's respective service load, which was calculated as described in Section 3.1.4.3.

***Table 4.15 – Design Criteria Comparison***

| Criteria | Specimen | Allowable | Measured | Calculated | Calculated / Measured |
|---|---|---|---|---|---|
| Bar Stress ksi | 1 ft shear | 12.1 | 0.279 | 0.203 / 2.11* | 0.728 / 7.563 |
| | 2 ft shear | 12.1 | 2.32 | 0.203 / 2.11* | 0.088 / 0.909 |
| | 3.5 ft shear | 12.1 | 4.94 | 0.203 / 2.11* | 0.041 / 0.427 |
| | 5 ft shear | 12.1 | 0.518 | 0.203 / 2.11* | 0.392 / 4.073 |
| Deflection in. | 1 ft shear | 0.098 | 0.018 / 0.021† | 0.0077 | 0.428 / 0.367 |
| | 2 ft shear | 0.098 | 0.021 / 0.027† | 0.0077 | 0.367 / 0.285 |
| | 3.5 ft shear | 0.098 | 0.039 / 0.032† | 0.0076 | 0.195 / 0.238 |
| | 5 ft shear | 0.098 | 0.032 / 0.052† | 0.0074 | 0.231 / 0.142 |
| Crack Widths in. | 1 ft shear | 0.020 | Uncracked | 0.0052 | NA |
| | 2 ft shear | 0.020 | 0.008 | 0.0051 | 0.638 |
| | 3.5 ft shear | 0.020 | 0.004 | 0.0053 | 1.325 |
| | 5 ft shear | 0.020 | Uncracked | 0.0053 | NA |
| Moment Capacity kip-ft | 1 ft shear | | 21.4 kip-ft‡ | 28.7 kip-ft | 1.341 |
| | 2 ft shear | | 35.4 kip-ft‡ | 57.4 kip-ft | 1.621 |
| | 3.5 ft shear | | 61.9 kip-ft‡ | 99.9 kip-ft | 1.614 |
| | 5 ft shear | | 94.4 kip-ft‡ | 148.1 kip-ft | 1.569 |
| Shear Capacity kips | 1 ft shear | | 20.1 kips | 2.6 kips | 0.129 |
| | 2 ft shear | | 32.5 kips | 5.2 kips | 0.160 |
| | 3.5 ft shear | | 51.7 kips | 9.0 kips | 0.174 |
| | 5 ft shear | | 82.9 kips | 13.1 kips | 0.158 |

**uncracked / cracked*
*†left span / right span*
*‡calculated from frp strain at shear failure*

For structures subjected to cyclic loading, the ACI 440 document restricts the stress in FRP rebar to prevent fatigue failure. For GFRP rebar, the limit imposed is 20% of the design tensile strength, $f_{fu}$. The design tensile strength is defined as the guaranteed tensile strength, $f^*_{fu}$, multiplied by an environmental factor, $C_E$. The guaranteed tensile strength, which is provided by the manufacturer, is defined as the average ultimate strength minus three standard deviations and for these specimens $f^*_{fu}$ was 90 ksi. The environmental reduction factor prescribed by ACI 440 is 0.7 for GFRP in concrete exposed to earth and weather. The allowable stress resulting from the factors mentioned above was 12.0 ksi. The measured stresses reported here are the maximum bar stress at service load assuming a modulus of elasticity of 6100ksi for the GFRP bar. The calculated stresses were found according to Equation 4.26. For the cracked section the cracked moment of inertia calculated according to Equation 4.21 was substituted in Equation 4.26 for I.

$$\sigma = \frac{M \times y}{I} \qquad \text{(Eqn. 4.26)}$$

Where: $M$ = moment due to applied loads, kip-ft

$y$ = distance from center of cross-section to center of bar

$I$ = moment of inertia

In all four specimens, the tensile stress in the GFRP rebar is significantly below the allowable limits at service load, indicating a conservative design. The stress is much greater in the 2 ft and 3.5 ft specimens than the other two because they are cracked at the service load condition.

The AASHTO LRFD Bridge Design Specification (2002) recommends the limit shown in Equation 4.27 for allowable service load deflections of bridge decks.

$$\Delta \leq \frac{S}{800} \qquad \text{(Eqn. 4.27)}$$

Where: $\Delta$ = deflection, in

$S$ = girder spacing, in

The girder spacing for the specimens in this study was 78 in., which corresponds to a maximum deflection of 0.098 in. at service load. At each respective service load, the measured deflections were well below the AASHTO suggested maximum value, although they were grossly underestimated by the calculations. The deflection calculations were performed according to the procedure outlined in Section 4.1.3, however, in each case the sections were expected to be elastic and uncracked, which partially explains the discrepancy.

Despite the corrosion resistance of FRP, the ACI 440 document recommends following the crack width guidelines in the Canadian Highways Bridge Design Code, which allow for crack widths of up to 0.020 in. for exterior exposure of concrete decks reinforced with FRP under service loads. As shown in Table 4.15, all four specimens were well within these criteria at service load. Even after cracking, all specimens remained below this suggested maximum width for well beyond service loads, indicating a conservative design with respect to cracking. The calculated crack widths shown in Table 4.15 were determined according to the procedure outlined in Section 4.1.5.3 with the only exception being that the stress in the GFRP rebar was predicted in the same manner as the bar stress calculations discussed in this section using the moment due to applied service loads and the cracked moment of inertia rather than an average of recorded strain values. This gives a direct comparison between the actual crack widths to what the designer would have predicted prior to construction.

The measured specimen moments reported in Table 4.15 are copied from Table 4.3 for the convenience of the reader and were calculated according to the procedure outlined in Section

4.1.2.1. Essentially, the procedure uses an average of measured GFRP rebar strain and known section properties to estimate the moment in the specimen at shear failure. The calculated moment capacities shown in the last column were determined from Section 4.2 of the ACI 440 document using the equations shown here as Equations 4.28 and 4.29.

$$f_f = \left( \sqrt{\frac{\left(E_f \varepsilon_{cu}\right)^2}{4} + \frac{0.85\beta_1 f_c^{'}}{\rho_f} E_f \varepsilon_{cu}} - 0.5 E_f \varepsilon_{cu} \right) \le f_{fu} \qquad \text{(Eqn. 4.28)}$$

Where: $f_f$ = stress in FRP rebar, ksi

$E_f$ = modulus of elasticity for FRP rebar, ksi

$\varepsilon_{cu}$ = ultimate strain in concrete, in./in.

$$\beta_1 = 0.85 - 0.05 \frac{f_c^{'} - 4ksi}{1ksi} \ge 0.65$$

$f_c^{'}$ = compressive strength of concrete, ksi

$\rho_f$ = FRP reinforcement ratio

$f_{fu}$ = design tensile strength of FRP, ksi

$$M_n = \rho_f f_f \left(1 - 0.59 \frac{\rho_f f_f}{f_c^{'}}\right) bd^2 \qquad \text{(Eqn. 4.29)}$$

Where: $M_n$ = nominal moment capacity, kip-in.

$b$ = width of specimen, in.

$d$ = distance from compressive face to centroid of tensile reinforcement, in.

It should be noted that the specimens failed in shear, not flexure; hence the calculated flexural capacities exceed the failure loads. Therefore, flexural capacity does not control the design.

The measured shear strengths reported in Table 4.15 are the moment-applied simple span shear values calculated according to the procedure in Section 4.1.2.1 at the failure load of the section and are reprinted from Table 4.5. This method split the specimen into two simple spans and applied a moment to the continuous end equivalent to the moment calculated from the recorded FRP strain at failure of the deck. The calculated shear values were determined according to the equations in Section 9.2 of ACI 440 discussed in Section 4.1.2.2 and are reprinted from Table 4.6. None of the existing methods seemed to accurately predict the shear

strength of the section, but the ACI 440 model is shown here because it is the currently recognized guideline for the design of FRP-reinforced concrete.

## 4.2 Strength Degradation of GFRP Reinforcement – Deck Tests

### 4.2.1 Introduction

A total of three GFRP-reinforced concrete decks of similar dimensions and identical reinforcing layouts were constructed to investigate their changes in performance over time. One of the specimens was used in live load testing on two different dates and all three decks were loaded to failure in the lab. Each was conditioned differently prior to lab testing. The construction details and testing procedures were outlined in Section 3.2.

For ease of reference, the deck specimens will be individually referred to by a consistent nomenclature summarized in Table 4.16.

***Table 4.16 – Strength Deck Nomenclature***

| Name | Description | Concrete Pour Date | Lab Test Date |
|---|---|---|---|
| Strength 1 | Unaged, unexposed to elements and traffic loadings | 18 Jun 03 | 15 Aug 03 |
| Strength 2 | Aged, unexposed to elements and traffic loadings | 14 Nov 02 | 29 Jan 04 |
| Strength 3 | Aged, exposed to elements and traffic loadings | 14 Nov 02 | 16 Mar 04 |

One of these decks, Strength 1, was also used in the investigation of shear behavior discussed in Section 4.1 and was referred to in that discussion as "5 ft Shear." This deck was the youngest of the strength decks at the time of laboratory testing and is only different in its thickness which is a constant 7-5/8 in.

The Strength 2 deck was maintained indoors in the climate-controlled laboratory from casting to lab testing. The deck was only subjected to occasional insignificant loadings and was supported in such a manner that it experienced no flexure from these loadings.

The Strength 3 deck was installed in the weigh station on Interstate 81 in Troutville, Virginia, on December 10, 2002, 26 days after placing the concrete. Details on the installation and the test bed were provided in Section 3.2.2.2. The specimen was subjected to loadings from all truck traffic entering the weigh station during its period of service and the rebar strain resulting from this traffic were recorded on two occasions, August 20, 2003, and March 2, 2004. It was then tested to failure in the laboratory two weeks after the final live load testing.

### 4.2.2 Weigh Station Tests

Details of the weigh station test bed were presented in Section 3.2.2.2 and the field testing procedure was presented in Section 3.2.2.3. Of the 10 electrical resistance strain gages that the deck was instrumented with for measuring the FRP strain, only five were working at the time of the first test and three were working during the second test. Fortunately, the three that continued to work were each on different bars distributed along the longitudinal length of the deck, which allowed for a decent profile of the deck behavior. The strain gage layout is shown in Appendix B.

Electrical noise was a significant issue in the data on both testing days, although it was substantially worse during the testing in March 2004. For example, the noise on Gage 10 had amplitudes of approximately 7 με in August 2003 and 534 με in March 2004. The noise followed a frequency of approximately 60 Hz and the amplitude differences were likely due to the presence of moisture. The relatively constant frequency, however, allowed the noise to be modeled approximately with a sinusoidal function and subtracted out of the recorded data.

To compare the collected data from the weigh station, RISA 3D was used to calculate the moment at the location of the gages for each recorded trailer weight corresponding to the noise-filtered strain. The wheel positions of two random trailers were measured and averaged to determine the placement of the four loads corresponding to the rear tires on the trailer. The axles of tandem trailers were closer than the 5 ft length of deck, so the entire rear trailer load was on the deck at the same time; therefore the forward and rear tires of a tandem pair were considered as one load. Additionally, it was assumed that the rear load of each trailer was evenly distributed between all the tires. The dimensions used were 6 ft from centerline to centerline of the inside tires and 9 in. between the centerlines of each pair on either side. Figure 4.30 shows an example loading for one of the trucks (Dataset 13, Aug 2004, total trailer weight: 33.2 kips).

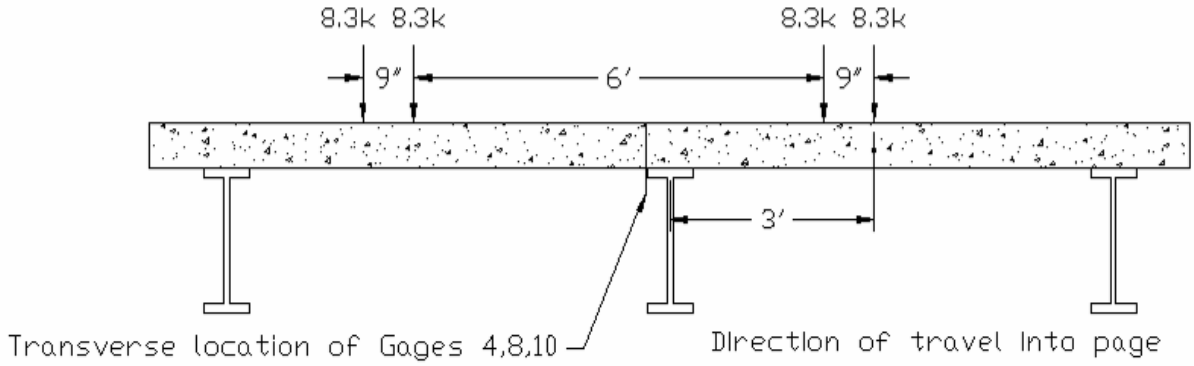


**Figure 4.30 - Positioning of loads applied to the deck by the trailer (Dataset 13, Aug 2004)**

The filtered strain was then plotted against the truck-induced moment for each gage to determine the performance difference between the two test dates. The plot for Gage 10 is shown in Figure 4.31.

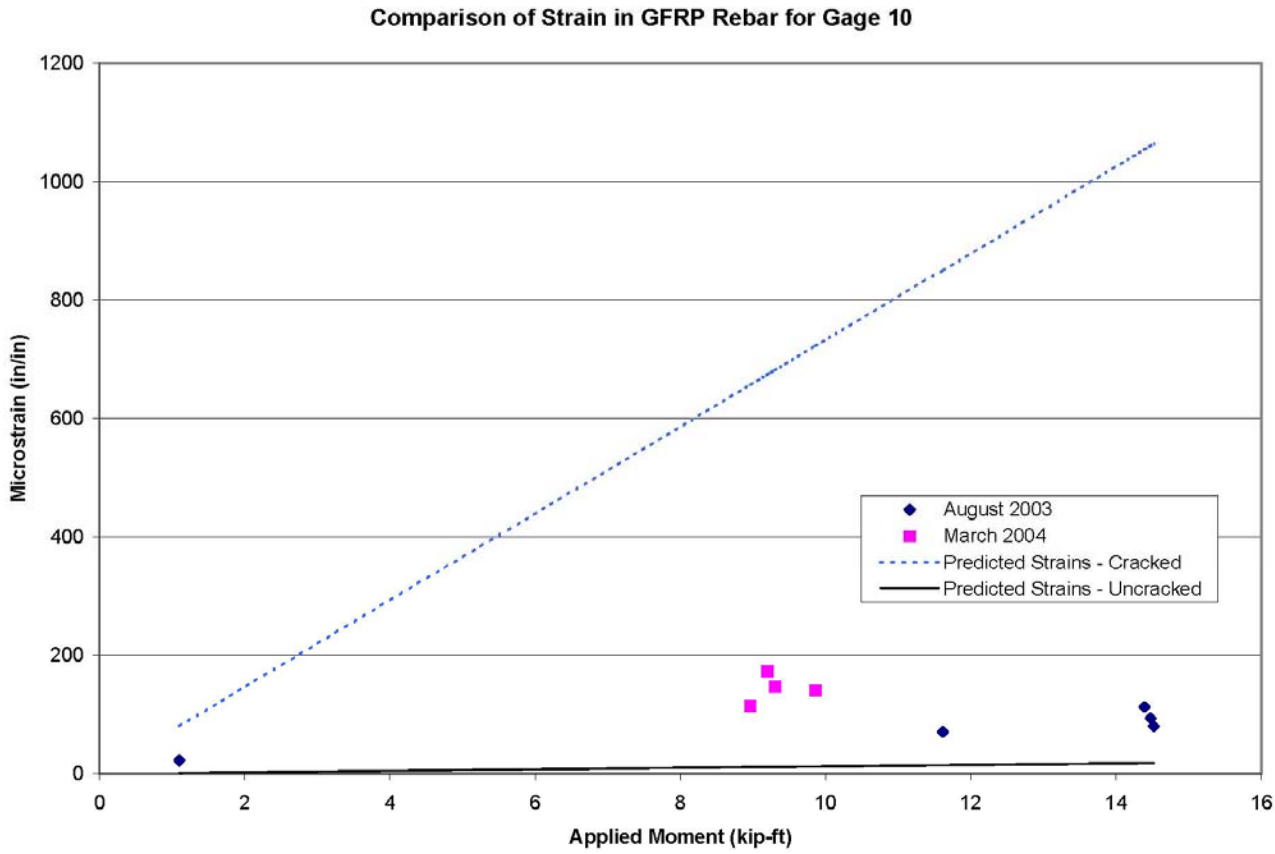


**Figure 4.31 - Strains versus trailer-induced moments for Gage 10 of the Strength 3 Deck**

To bound the predicted behavior of the specimen, the calculated strains for the cracked and uncracked conditions are included in Figure 4.31 for each truck crossing. The specimen had several cracks and the cracked strain was calculated using Equation 4.30.

$$\varepsilon = \frac{M}{E_f A_f jd} \qquad \text{(Eqn. 4.30)}$$

Where: $\varepsilon$ = strain in FRP rebar, in./in.

$M$ = moment due to trailer load, kip-in.

$E_f$ = modulus of elasticity of FRP rebar, ksi

$A_f$ = area of rebar, $in^2$

$j = 1 - k/3$

$k = \sqrt{2\rho_f n_f + (\rho_f n_f)^2} - \rho_f n_f$

$\rho_f$ = FRP reinforcement ratio

$n_f = \frac{E_f}{E_c}$

$d$ = depth to FRP from compression face, in.

All three remaining gages indicated an increase in strain between the two test dates for a given loading. Since the magnitude of strain in the rebar is directly related to the applied moment, the filtered strains were divided by the respective applied moments to create a ratio that could be easily compared between the test dates. Figure 4.32 is a plot of the average strain-moment ratio for each gage separated by date. The increase in strain per moment clearly indicates an increase in flexibility of the deck.

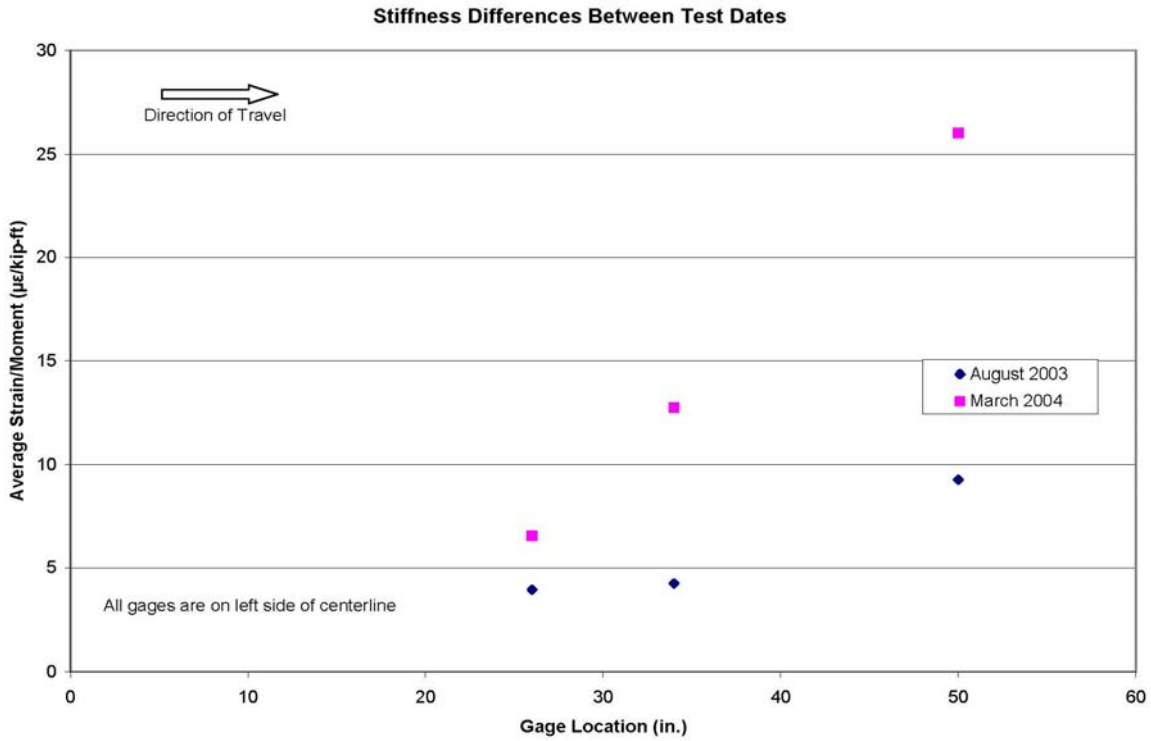


**Figure 4.32 - Average ratio of bar strain to moment for GFRP gages in the Strength 3 deck**

Unfortunately, the specific reason for this change in behavior is not clear. Flexibility may have increased because of additional cracking of the section prior to the later test date, particularly after the winter months including below freezing temperatures. As noted previously, weather data for the period during which the specimen was in place is included in Appendix F. The increase may also be due to the fact that repeated loadings and differential settlement of the supports led to the fatigue failure of the connection of the left most support beam to the underlying concrete slab. This allowed for a greater range of motion as the deck rigidity tended to cause the leftmost support to lift when there was no applied load. Gages were zeroed with no applied loads on the deck, so the left support (facing the weigh station) would have been slightly lifted. As seen in Figure 4.32, the gage located 50 in. from the forward edge of the slab experienced the greatest strain of the three functioning gages. It was observed during removal of the specimen that the unseating of the left support beam was more prominent at this corner of the deck which would lead to greater strains in this particular bar. Finally, a third possibility for the increased flexibility of the deck could be a reduced stiffness of the GFRP rebar.

### 4.2.3 Laboratory Tests

Laboratory tests were conducted to compare deflection, GFRP rebar stresses, cracking information, and failure load and type between the three strength specimens. The tests were conducted according to Section 3.2.2.3 of this report.

#### *4.2.3.1 Deflections*

Deflection measurements were recorded by ST-type wirepots attached to the underside of the decks directly below the two load points, as previously shown in Figure 4.8. Data was collected in the same manner as previously described in Section 4.1.3.

Two theoretical series were developed to compare the measured deflections with the expected results. Two series had to be shown because the Strength 1 specimen had a different concrete strength than the Strength 2 and 3 specimens. The predicted values were determined in the same manner as prescribed in Section 4.1.3 using Equations 4.18 through 4.21 and the method of multiplying the ratio of applied load to the effective moment of inertia, $P/I_e$, by a constant derived from RISA 3D models. The inputs used to predict the deflections are shown in Table 4.17.

*Table 4.17 – Deflection Calculation Input Values*

| Deck | $M_{cr}$ | $f_c$ | $I_g$ | $I_{cr}$ | $\rho_f$ | constant |
|---|---|---|---|---|---|---|
| Strength 1 | 29.3 k-ft | 6500 ksi | 2217 $in^4$ | 208 $in^4$ | 0.0145 | 0.869 |
| Strength 2 | 25.2 k-ft | 5900 ksi† | 1905 $in^4$ | 152 $in^4$ | 0.0152 | 0.912 |
| Strength 3 | 25.2 k-ft | 5900 ksi† | 1905 $in^4$ | 152 $in^4$ | 0.0152 | 0.912 |

†*Estimated from strength plot in Appendix A*

The concrete compressive strength, $f_c$, used to calculate the cracking moment for the Strength 2 and 3 specimens was found from the concrete strength plot in Appendix A rather than compressive tests on the day of each respective deck test. This is because of a shortage of available concrete cylinders after two were damaged prior to testing.

To simplify comparison between the three decks and two theoretical series, only the maximum of the two deflection values was plotted for each level of applied load. Figure 4.33 presents this maximum deflection and corresponding total applied loads for each specimen and the two theoretical series up to failure. The theoretical series is valid until the concrete goes beyond the linear elastic range, which is considered to be when the compressive stress exceeds $0.5f'_c$.

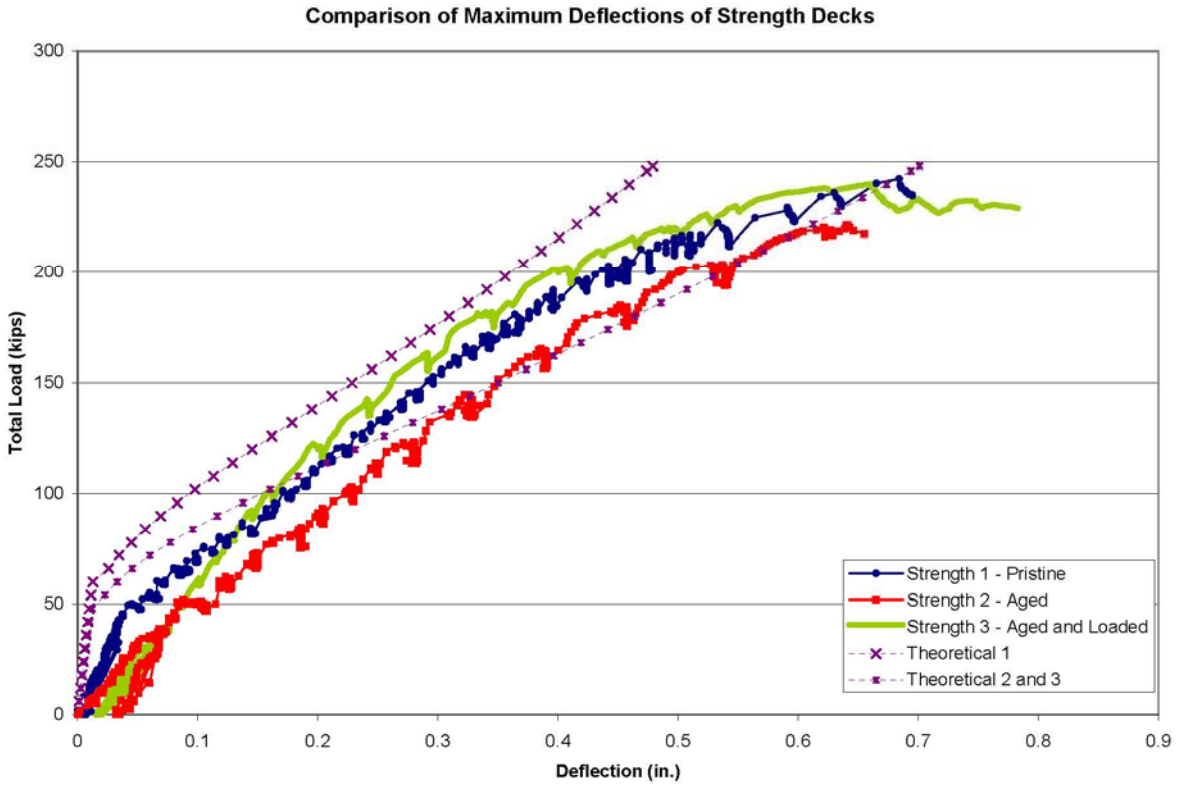


**Figure 4.33 - Comparison of maximum deflections and applied loads of all three specimens**

From observation of Figure 4.33, there was no significant difference in deflection of the three specimens. In general, the Strength 2 specimen exhibited the greatest deflection for a given load through the majority of the testing series. The theoretical series predicted the deflections of the Strength 2 deck rather well, but they underpredicted the Strength 1 deflections throughout the test and began overpredicting the Strength 3 deflections above approximately 100 kips (total applied load between the two patches), which is a little above 2.5 times the service load. Prior to cracking of the decks, the theoretical series greatly overpredicts the stiffness of the section. Over this uncracked region the gross section moment of inertia was used in the calculation of the deflection. Overall though, particularly in the middle to later parts of the loading procedure, the predicted deflections were not grossly off from the actual measured values.

A graph of the deflection behavior was also made for loadings up to service load. This plot is presented as Figure 4.34. As in the overall deflection plot of Figure 4.33, the Strength 2 specimen exhibited the greatest deflections for a given load during the service load cycling procedure. However, after cycling, the deflections of the Strength 2 and 3 specimens were very similar. Both the Strength 2 and 3 specimens also experienced higher residual deflections at the zero load of the service load cycles compared to the Strength 1 deck; but it should be noted that the concrete compressive strength of the Strength 1 deck was higher than the other two. This residual deflection is likely due to further cracking of the specimen, which increases the flexibility of the section and would lead to residual deflections under the decks' self weight and the lab equipment, and plastic bond slip, as described in Section 4.1.3.

This figure also illustrates the poor results of the deflection prediction below service loads, notably underestimating the measured values. The reason for this is understood for the Strength 3 deck, which had been cracked at the weigh station, but the Strength 2 deck, which was not cracked prior to testing, exhibited similar behavior. Below service load, the model assumes an uncracked section.

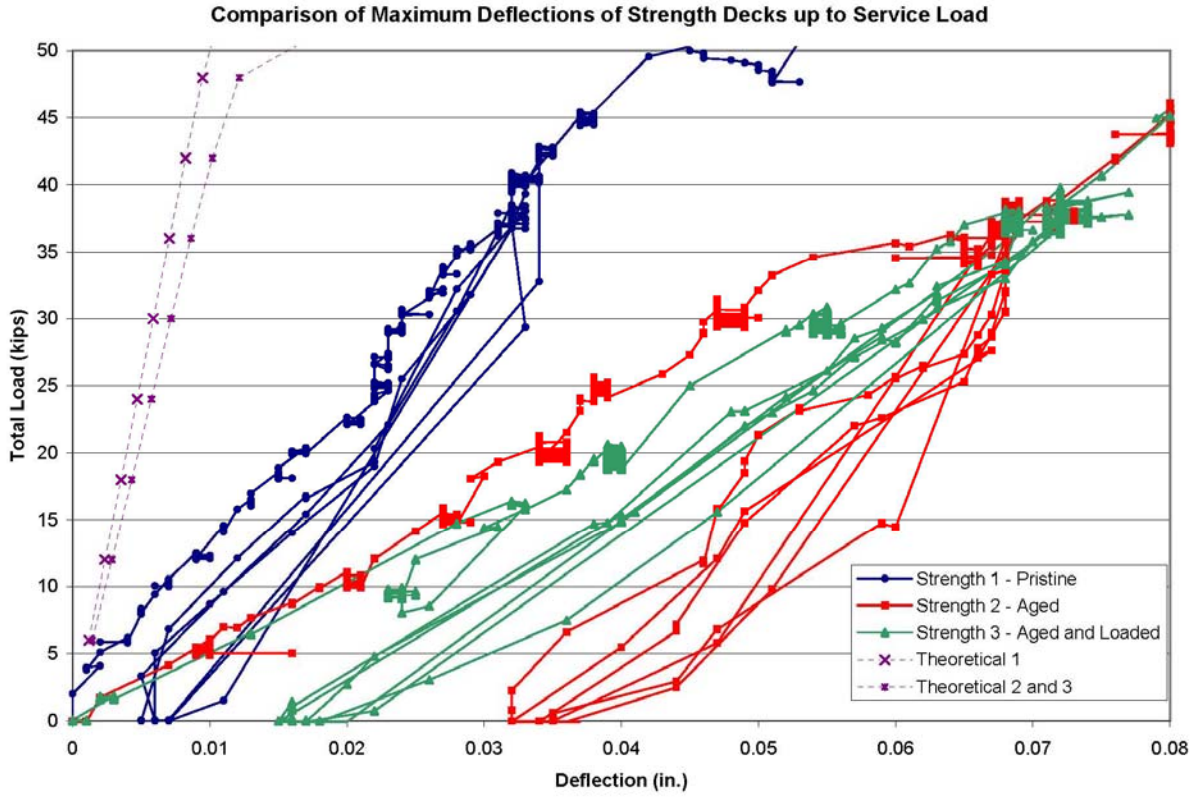


**Figure 4.34 - Maximum deflections for all specimens during service load cycling**

### *4.2.3.2 Reinforcement Strain*

This section presents the details of the strain in the reinforcement obtained throughout the testing of each shear specimen. The strain was measured with electrical resistance strain gages that were applied to both the steel and GFRP rebar and the data was collected by a data acquisition system.

A plot of the recorded strain in the FRP rebar over the center support is shown with the total applied load in Figure 4.35 for the Strength 2 specimen. A theoretical series is also included assuming a partially cracked section in which the effective moment of inertia was calculated using the previously presented Equation 4.20. Since there were a large number of functioning gages at the time of testing in this deck, the gages on either side of the center support for each bar were averaged to reduce confusion in the plot. This series was developed assuming a modulus of elasticity of 6100 ksi for the FRP rebar.

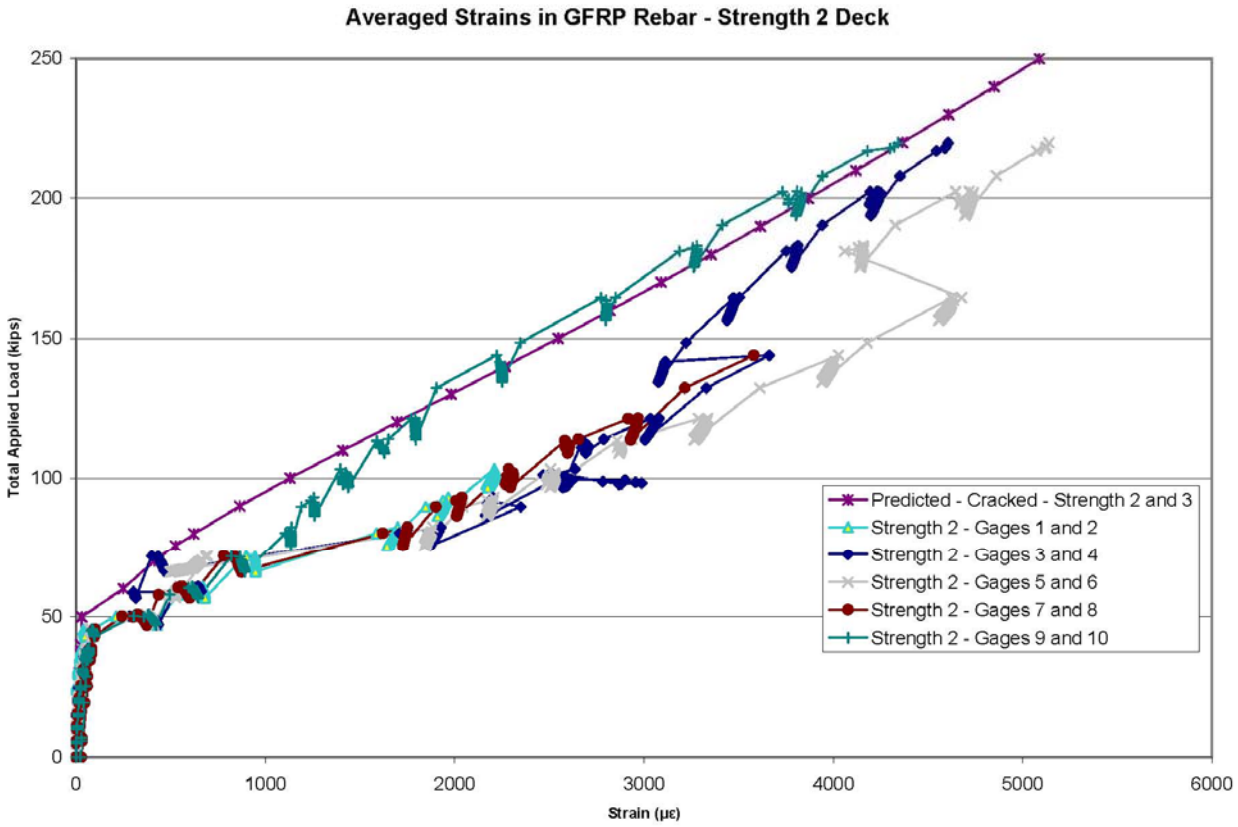


**Figure 4.35 - Strain in GFRP rebar over center support - Strength 2 Specimen**

With the exception of Gage 10, the predicted strain is unconservative throughout the test, being roughly only 35% of the average recorded strain at an applied load of 100 kips. The cracking of the deck is evident in the sudden change of slope of all the recorded data around a total applied load of 50 kips, which is also seen in the theoretical series. Additionally, the slope of the theoretical series is similar to that of the recorded data, which is a good indication of the stiffness of the section following cracking. However, the break in slope is much more pronounced in the recorded data. As before, the downward ticks in the plot correspond to periods in the test during which the load application was paused for collection of crack width and DEMEC recordings.

Figure 4.36 shows the same averages of recorded values over the period of the service load cycling stage of the testing procedure.

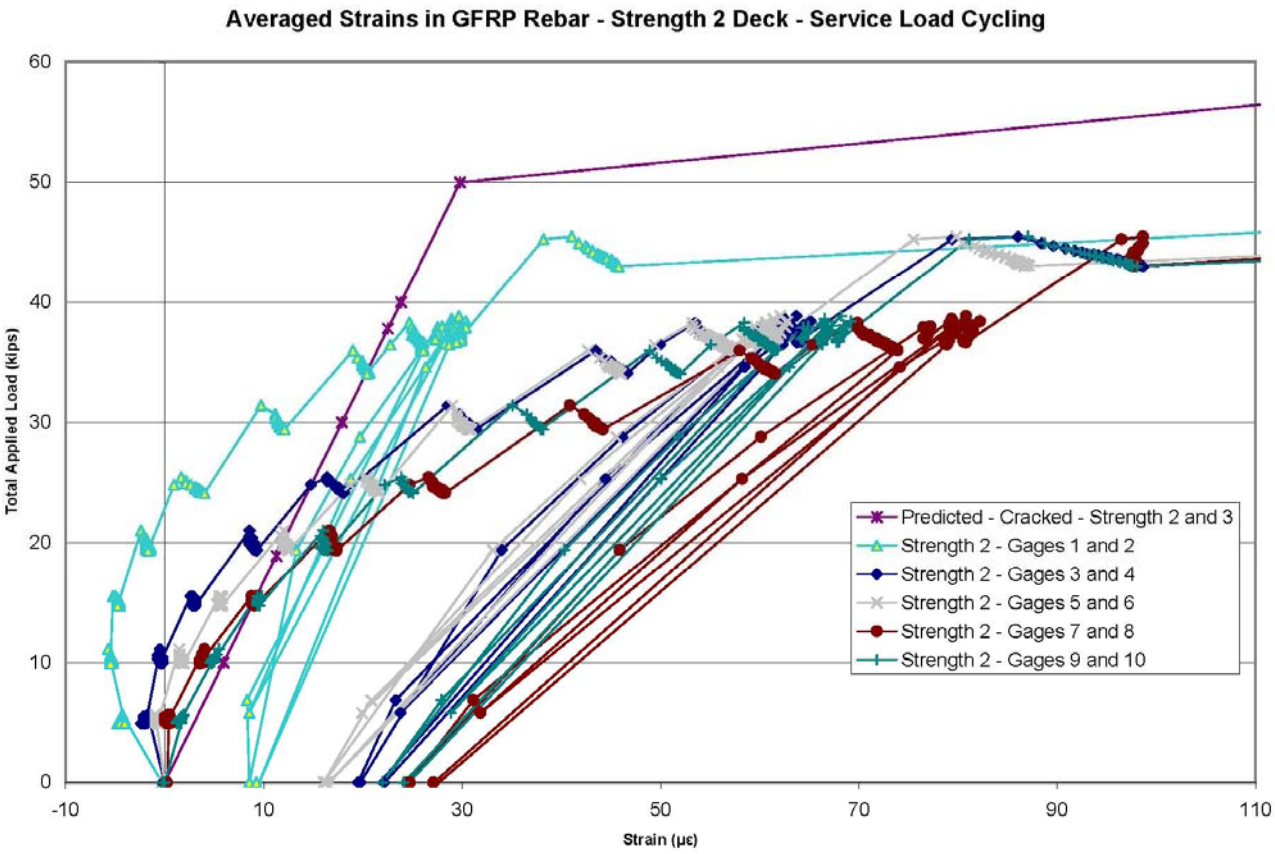


**Figure 4.36 - Strain in GFRP rebar over center support during service load cycling - Strength 2 Specimen**

The development of the first crack is clearly seen in Figure 4.36 when the slope of the strain growth of all the bars suddenly decreases significantly around 45 kips of total applied load. The actual first crack is recorded at 38 kips, but it was not yet significant.

Figure 4.36 also indicates that the strain in several gages, particularly gages 1 and 4, begins the test negative, or in compression. The reason for this is not clearly understood, but it should be noted that after the first loading cycle all gages remained in tension for the remainder of the test. Additionally, it is also of interest to note the residual strain at the bottom of each subsequent loading cycle. The section is not significantly cracked until after the service load cycling procedure, so this is residual strain is likely due to microcracking in the deck and plastic bond slip as described in section 4.1.3.

The plots for the Strength 1 specimen are very similar to Figures 4.35 and 4.36 and are therefore presented in Appendix J. The only major difference in the Strength 1 plot is that the strain prediction agrees much better with the recorded strain values and there are no gages recorded in compression.

Figures 4.37 and 4.38 present the strain plots for three remaining FRP gages in the Strength 3 specimen over the entire testing procedure and during the service load cycling, respectively.

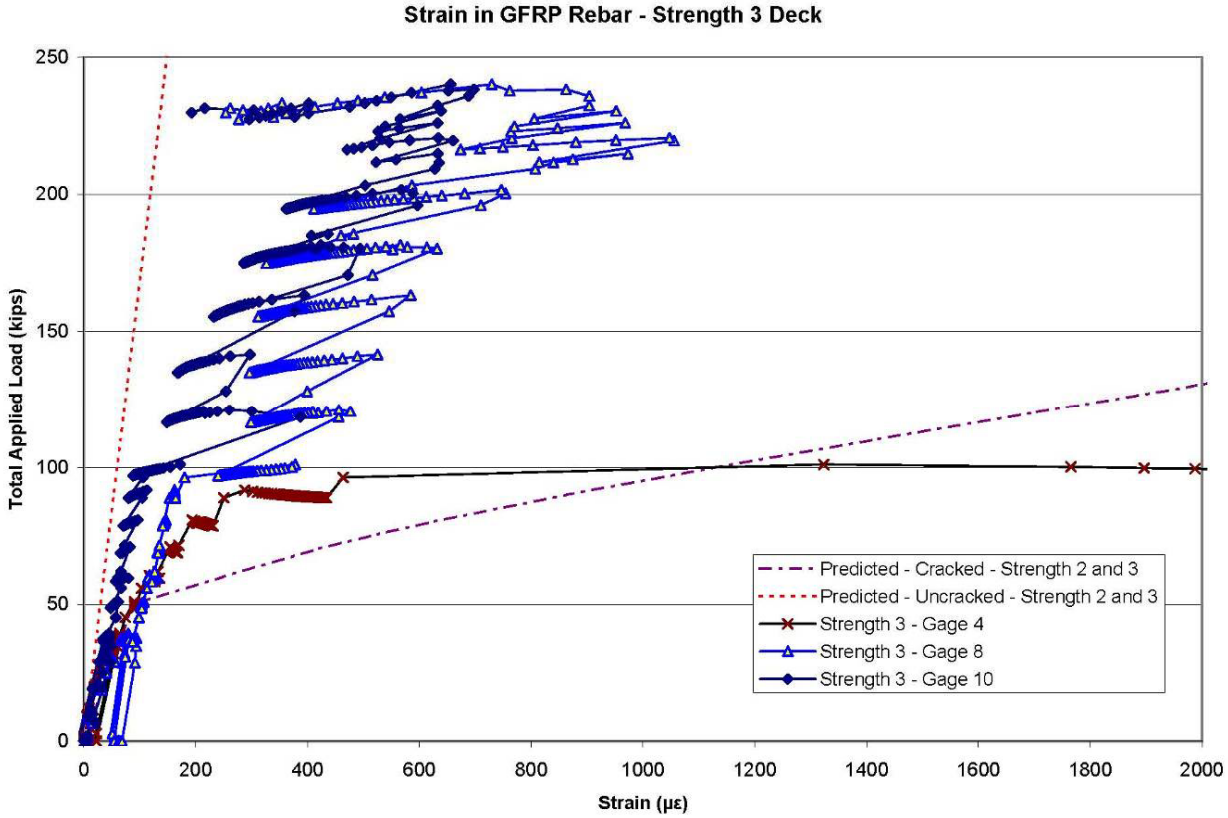


**Figure 4.37 - Strain in GFRP rebar over center support - Strength 3 Specimen**

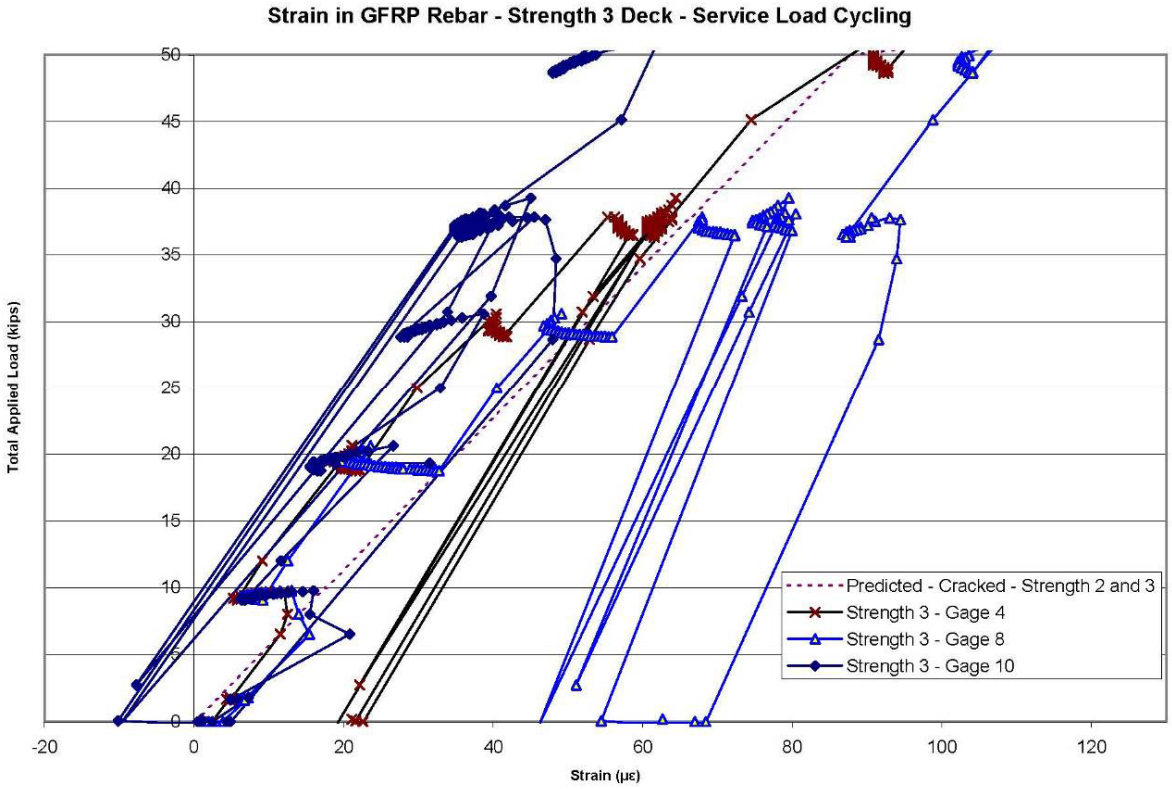


**Figure 4.38 - Strain in GFRP rebar over center support during service load cycling - Strength 3 Specimen**

As expected, because the section was already cracked prior to testing, there is no significant change in slope for the strain indicating the formation of a major crack during the loading procedure. However, the strain prediction in Figure 4.37 grossly overestimates the recorded strain values. This is clearly unanticipated based on the results from the Strength 1 and 2 tests and the fact that this section was initially more cracked than the other two for the first portion of the test. On the other hand, the strain values recorded during the service load cycles seem to agree with the other two specimens relatively well. The most likely reason for this discrepancy is that the remaining functioning gages are all on the same side of the support. If a major crack is on the side opposite these gages, then a much larger strain would be recorded on the other side of the support. Unfortunately, the gages on the opposite side were not functioning so that it could be confirmed.

Attention should also be drawn to the fact that the deck still experienced residual strains beyond the start of the testing at the bottom of the service load cycles. This is mostly likely due to the fact that the center of the deck experienced compression during placement in the lab, which, if the straps supporting the deck from the overhead crane were far enough apart to create a large enough moment, could have negated any residual strains due to plastic bond slip

experienced in the field from the truck loadings. It is also possible that the deck rarely experienced the full service load moment in the field. For instance, the highest truck load recorded on the slab during the weigh station tests was 35.7 kips, whereas the service load used in the lab was 37.8 kips. Although this difference does not seem significant, according to notes taken during the field investigations most trucks stayed to the left of the deck rather than straddling the center support because of the common drift of traffic due to the lane curvature. This path of the trucks would have reduced the negative moment experienced by the deck.

To examine the distribution of the load between bars and the performance of each differently conditioned deck, strain contour graphs were developed by plotting the recorded strain for each gage against the position of the gage with respect to the direction of traffic. All gages were located along the center support. Since the intent of this portion of the research was to investigate any difference in material properties, only strain was considered; stress plots similar to those created in the shear deck portion of this research assumed a modulus of elasticity and was valid since all four of those decks were relatively young and of the same age. However, as before, in this portion an elastic modulus had to be assumed for the development of the theoretical series; the modulus of elasticity used for the FRP rebar was 6100 ksi. This was the average modulus found for the unused GFRP rebar specimens in tensile tests conducted as part of this research and will be discussed in the next section.

Three load points were chosen for these plots to provide a good understanding of the behavior differences between the specimens over the entire spectrum of the test. These loadings were half of the service load, service load, and twice the service load. Also, since two recorded strains of a particular bar differed depending on which side of the center support was being considered for the Strength 1 and 2 specimens, the strains obtained from the gages of each bar on each side of the support were averaged for these plots, which negates the majority of effects caused by the deck not being completely supported by the entire width of the flange of the center support. However, although these plots can give a very informative view of the strain behavior through the cross-section of the specimens, caution should be exercised in reviewing this data, particularly when comparing between different decks. This is because the strain reported is at one specific location on each bar and may include additional local effects that may not be experienced by the other bars or other specimens. For example, a crack may form at the same location as a strain gage on one bar, which would cause that local area of the bar to undergo

additional strain because of the increase in tension in the bar at that location, thereby causing a higher strain reported by the gage.

Figures 4.39, 4.40, and 4.41 present the strain contour comparisons for the three load cases described above, respectively.

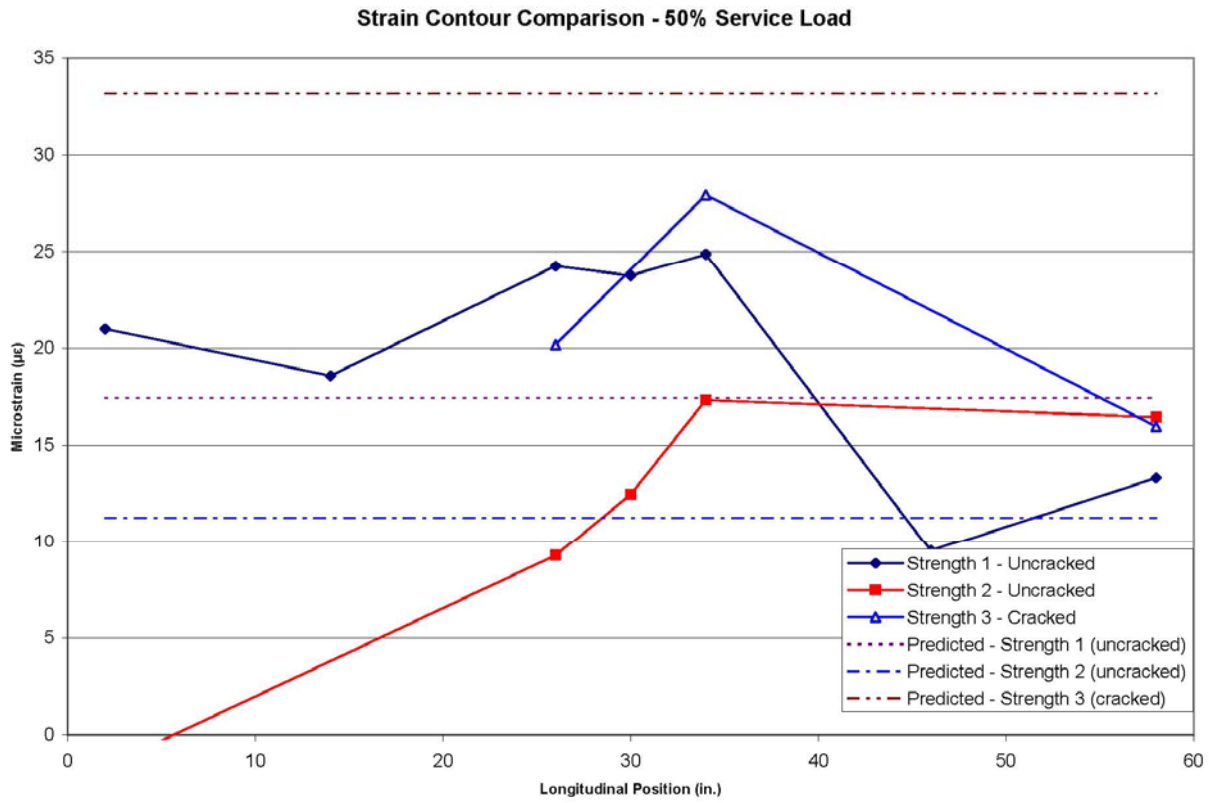


**Figure 4.39 – Strain Contour Comparison at 50% of Service Load (18.9 kips)**

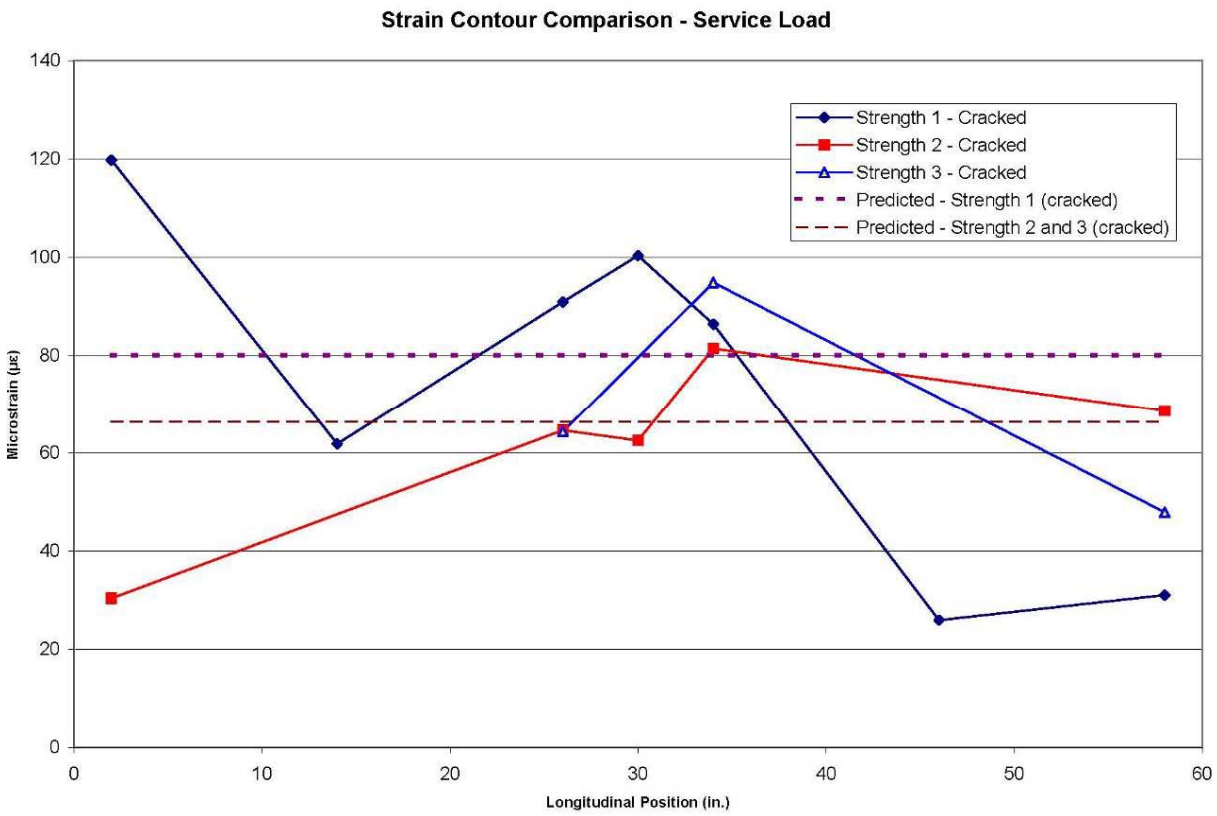


**Figure 4.40 - Strain Contour Comparison at Service Load (37.8 kips)**

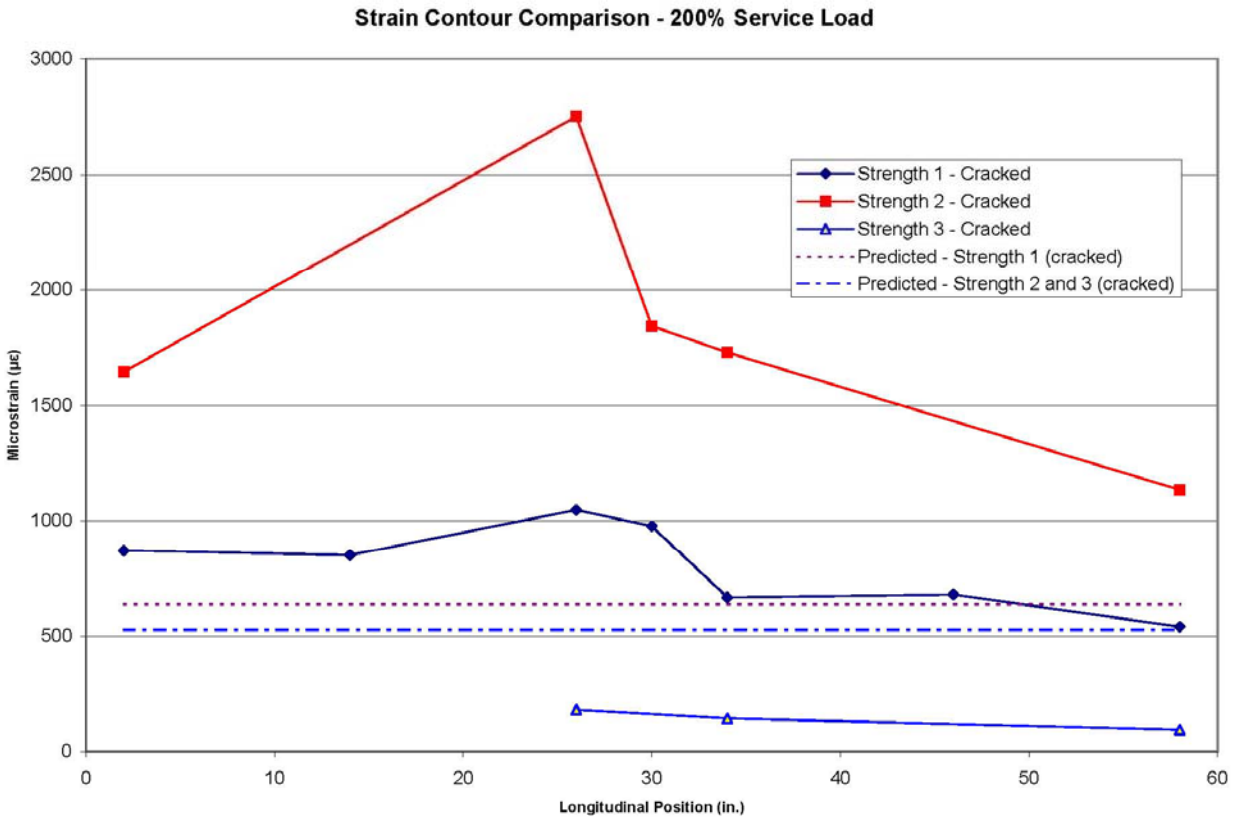


**Figure 4.41 - Strain Contour Comparison at 200% of Service Load (75.6 kips)**

In general, with the exception of the Strength 1 specimen at service load, the strain in the sections was highest at the middle bars and tapered off towards the edges, which was the behavior that was expected. The theoretical strains were intended to predict the peak strains in the section. However, for all specimens, except the Strength 3 at twice the service load, the calculated strains underestimated the actual peak strains. The Strength 3 specimen was cracked at the outset of the lab testing, so it was expected that it would experience more strain in the rebar due to the lower neutral axis and lower stiffness of the section. Nevertheless, the predictions still underestimated the strains in the other two specimens throughout the loading application. This may be due to a lower actual elastic modulus for the rebar than was used in the predictions, which would cause the greater strains.

The difference in behavior between these sections is of particular interest. As noted above, the Strength 3 specimen experiences the greatest strain at half of the service load most likely because it was cracked prior to testing. However, the section performs more like the uncracked Strength 2 specimen than the predicted cracked section. By service load, on the other hand, the Strength 1 section experiences more strain in the middle of the deck and considerably more at one edge. Taking the difference between their dimensions and properties into consideration by examining the predicted strain values and ignoring the gage at the one edge, the Strength 1 and 3 specimens would have experienced very similar strains. The Strength 2 deck has also experienced a larger strain increase than the Strength 3 specimen, but not yet enough to surpass it on the plot.

At twice the service load, the Strength 2 specimen experiences considerably more strain than the other two specimens, even after taking the difference in concrete strengths and section dimensions between it and the Strength 1 deck into account. This strongly indicates the possibility of a reduction of GFRP rebar stiffness over the 14 month lifespan of the Strength 2 deck. Although it appears that the Strength 3 specimen contradicts this theory since it is found to be well below the other two specimens as well as the predicted strain value, it has already been noted that all remaining operating strain gages in this specimen were on the same side of the center support. It is very likely that the section on the opposite side of the support experienced much larger strains. It can be hypothesized that the gages on the other side of the support were damaged by water and chemical infiltration due to a greater amount of cracking on that side because of the previously discussed tendency of the truck traffic to drift to the left side

of the lane while the deck was in place at the weigh station. This would also decrease the overall rigidity of the section and increase the strains experienced by the rebar at the location of the damaged gages. Unfortunately, there is not enough information available to completely confirm this theory.

#### *4.2.3.3 Cracking*

The combined loads at which the first visible cracks were seen for each of the decks are presented in Table 4.18 below with the predicted cracking load for comparison.

***Table 4.18 – Cracking Loads of Strength Decks***

| Specimen | First Crack from Crack Log | First Crack from Strain Plots | Predicted Cracking Load |
|---|---|---|---|
| Strength 1 | 39.5 kips | 40 kips | 47.2 kips |
| Strength 2 | 38 kips | 43 kips | 41.1 kips |
| Strength 3 | NA | NA | 41.1 kips |

*Loads reported are total applied loads*

The cracking load was predicted by calculating the cracking moment according to the previously presented Equation 4.22 and dividing this result by the moment over the center support obtained from a RISA-3D analysis for an applied total load of 1 kip, or 0.5 kips per patch. Crack formations were determined from the load versus strain diagrams by the first sudden change in slope of the plot towards a lower stiffness and were also recorded during the testing.

The calculations predicted the cracking load rather well for the Strength 2 specimen and were less than 8 kips too high for the Strength 1 specimen. No crack formation was determined for the Strength 3 deck because it was cracked prior to lab testing and there were no sudden changes in the strain plot.

#### *4.2.3.3a Crack patterns*

In both the Strength 1 and 2 specimens, the first observed crack formed over one edge of the flange of the center support and propagated along the support to each side of the deck. This was mimicked in additional crack formations in the Strength 3 deck. This crack was then followed by cracking on the underside of the deck in at least one of the positive moment regions under the load point and then additional cracks formed in both the positive and negative moment regions. As the load increased, the flexure cracks began to form a general arc in the top of the deck in which they were closer to the support in the middle of the specimen and further from the support towards the edge of the deck. The final shear crack, however, ran parallel to the center support in all three specimens as would be expected. As seen in the 3.5 ft and 5 ft (same as

Strength 1) shear decks previously discussed, the Strength 2 and 3 decks also formed cracks in the bottom of the slab perpendicular to the center support between the support and the load points. Crack maps for the Strength 1, 2, and 3 specimens are presented in Appendix K.

#### *4.2.3.3b Crack widths*

Crack widths were measured and recorded for all specimens at various intervals throughout each test using either a crack microscope or a crack card, depending on the size and importance of the particular crack. A DEMEC gage was also used to measure the surface behavior of the decks during the same intervals. Details about the gage were discussed in Section 4.1.5.3.

The measured crack widths were compared to predicted crack widths determined from the modified Gergely-Lutz equation presented in ACI 440 (2003), which was shown previously as Equation 4.23. The GFRP stress used in Equation 4.23 was an average of the stress in the bars recorded from strain gages on the same side of the center support as the largest crack at the particular load. However, when the specimen was considerably cracked on both sides of the support, the calculated stresses from all GFRP gages were averaged for this equation.

For the purpose of a simple, yet accurate comparison, when comparing DEMEC readings to measured and theoretical crack widths, only the DEMEC readings that crossed over the measured crack were considered and averaged. DEMEC values were converted to millimeters through the procedure in Equation 4.24.

Figure 4.29 compared the theoretical maximum crack width with the measured crack width and DEMEC data for the 5 ft shear specimen, which is referred to here as Strength 1. Figures 4.42 and 4.43 show the same comparisons for the Strength 2 and 3 decks. In these plots, the measured crack width points appear to advance in a stepwise or jagged fashion. This is because they were measured with a crack card that had approximately 0.2 mm increments.

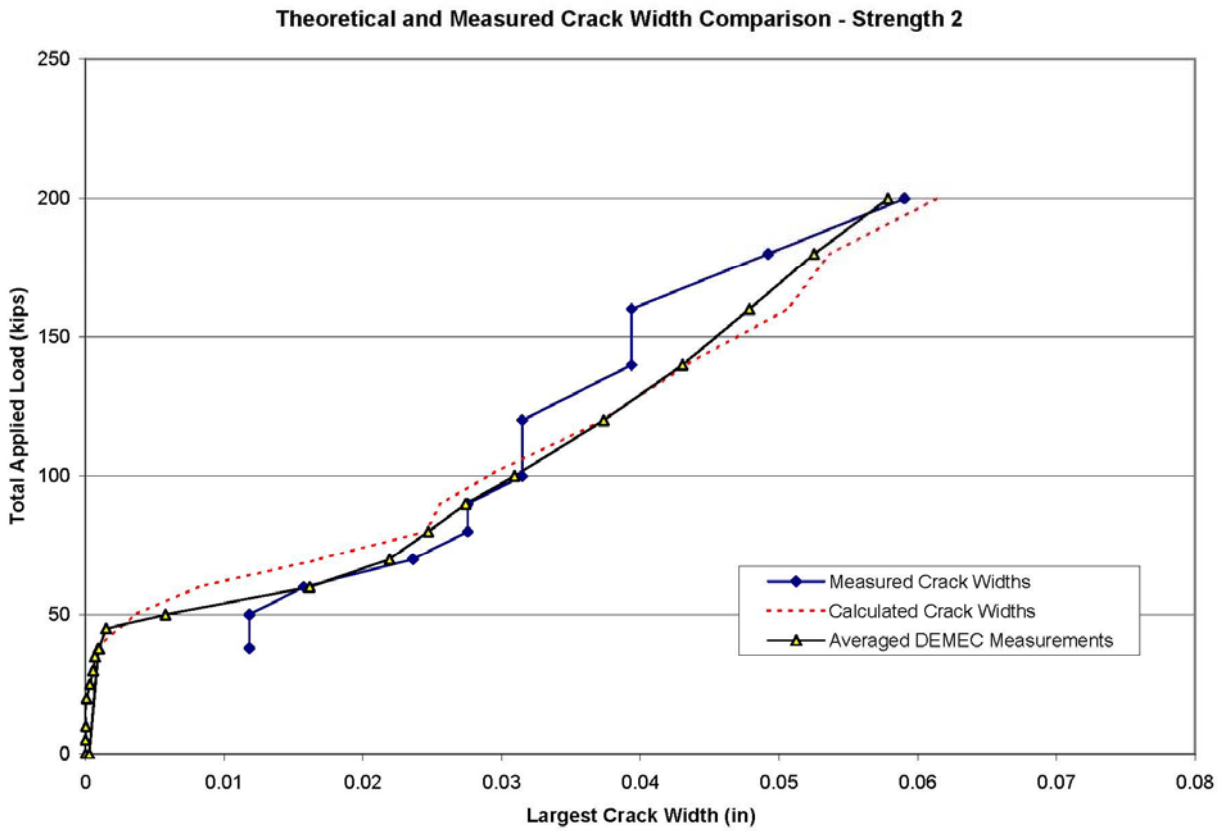


**Figure 4.42 – Comparison of DEMEC measurements and recorded and theoretical crack widths – Strength 2**

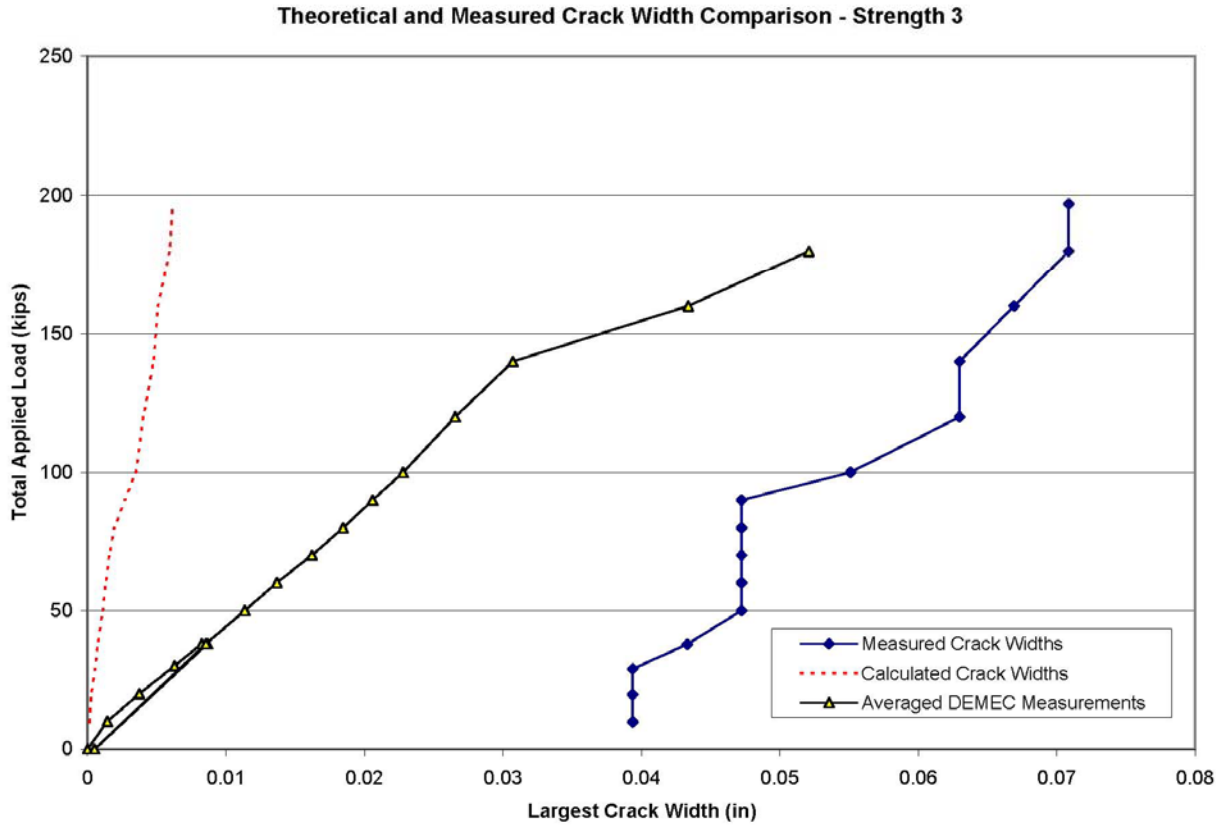


**Figure 4.43 – Comparison of DEMEC measurements and recorded and theoretical crack widths – Strength 3**

As previously seen in Figure 4.29, the DEMEC measurements in the Strength 1 deck were typically larger than the actual measured crack widths, as expected. In the Strength 2 case, the DEMEC measurements were greater than the recorded crack widths only towards the end of the record where the formation of additional cracks within the DEMEC gage length began to occur. Otherwise, the DEMEC measurements agreed rather well with the actual crack widths. Additionally, the ACI 440 crack width equation predicted the actual crack widths acceptably, although it was just slightly unconservative up to approximately three times the service load.

For the Strength 3 specimen, none of the three measurements seem to agree at all. The measured crack widths greatly exceed both the DEMEC values and the calculated values because the deck was cracked prior to the test, with the largest crack being approximately 1 mm. The zero points for the DEMEC gage were taken at the start of the test, obviously neglecting the existing crack widths. However, visual comparison of the DEMEC data and the recorded crack widths reveals a relatively similar slope, which would indicate that the DEMEC results still agree rather well with the actual crack widths if the two had had the same starting point.

The predicted crack width series for Strength 3, however, is significantly off from the recorded crack widths. This is because the recorded strains were used in the crack width prediction and, as previously suggested, the cracking on the other side of the center support from the surviving strain gages may have been substantially greater.

#### *4.2.3.2 Failure Load and Mode of Failure*

All three specimens failed in one-way, beam-type, shear next to the center support. The ultimate failure load for each deck is tabulated in Table 4.19. Additionally, since the concrete strength and rebar depth were not constant, a normalized failure load was calculated by dividing the recorded failure loads by the square root of the concrete compressive strength, $\sqrt{f_c}$, and the effective depth, d. The concrete compressive strength was determined by breaking 4 in. diameter concrete cylinders, which yielded $f_c$ values of 6.5 ksi for the Strength 1 specimen and 5.9 ksi for the Strength 2 and 3 specimens.

***Table 4.19 – Failure Loads of Strength Specimens***

| Deck | Depth to FRP rebar, d | Failure Load per patch | Failure Type | Normalized Failure Load |
|---|---|---|---|---|
| Strength 1 | 5-5/8 in. | 124 kips | Beam Shear | 0.274 |
| Strength 2 | 4-3/4 in. | 111 kips | Beam Shear | 0.304 |
| Strength 3 | 4-3/4 in. | 120 kips | Beam Shear | 0.329 |

As shown in Table 4.19, there is no evidence of a loss of shear strength among these specimens due to aging of the decks or exposure to traffic and weather. In fact, the normalized failure load shows an increase in strength as both age and conditioning increases. The compressive strengths stated above are at the date of testing, so the increased strength cannot be directly attributed to the maturity differences between the specimens.

In order to compare the failure loads with the predicted strengths, the shear at failure was estimated using RISA 3D assuming both an elastic section continuous over the center support and a simply supported section created by adding a hinge at the center support. Due to the lack of functioning gages in the Strength 3 specimen at the time of the lab test, no effort was made to more precisely determine the shear at failure as was done with the moment-applied simple span method of Section 4.1.2.1. The simple span model forms the lower bound of the expected shear values while the continuous model defines the upper bound. Both models included a uniform load of 0.477 kip/ft for the deck self weight and point loads of 1.7 kips at each load patch for the weight of the spreader beam. These results are compared in Table 4.20 with the shear predictions from ACI 440.1, the Frosch method, modified compression field theory, and the ACI 318 method for steel reinforced members, which were detailed in Sections 4.1.2.2, 4.1.2.3, 4.1.2.4, and 4.1.2.5, respectively. Table 4.20 also includes the calculated shear at service load with self weight assuming an uncracked, continuous deck for comparison with the models. This was calculated using a service load of 18.9 kips per tire patch per Equations 3.5 and 3.6

***Table 4.20 – Shear Strength Comparison of Strength Specimens***

| Deck | Simple Span Shear | Elastic Shear | ACI 440.1 | Frosch | MCFT | ACI 318 | Service Shear* |
|---|---|---|---|---|---|---|---|
| Strength 1 | 68.5 kips | 92.5 kips | 13.1 kips | 27.7 kips | 48.3 kips | 54.4 kips | 15.1 kips |
| Strength 2 | 61.3 kips | 82.8 kips | 12.0 kips | 24.5 kips | 38.3 kips | 43.8 kips | 15.1 kips |
| Strength 3 | 67.0 kips | 90.4 kips | 12.0 kips | 24.5 kips | 38.3 kips | 43.8 kips | 15.1 kips |

**Service shear is the calculated shear due to service load and self weight on an elastic, continuous specimen*

As was observed in the previous stages of this research, none of the available shear models accurately predict the actual shear strength of the specimen. In fact, the best prediction is the method presented in ACI 318 which does not consider the difference in stiffness between the steel and GFRP rebar. These models were developed from data collected primarily from simply-supported beams rather than continuous reinforced slabs and it is apparent from this research that they do not translate well for use with continuous GFRP-reinforced decks. Additionally, it should be noted that the service shear exceeds the ACI 440.1 prediction. In the design of the

decks, it was already known that the model was overly conservative and that it was not possible to economically build the decks to satisfy the ACI 440.1 criteria. However, it is clear that the ultimate shear strength exceeds the service shear strength with a safety factor of at least 4.

As noted above, all three specimens failed in one-way shear. Figure 4.44 shows the shear failure of the Strength 2 deck, which was typical of all three specimens.


**Figure 4.44 - Shear failure of the Strength 2 specimen**

The progression towards failure of the Strength 1 specimen was similar to the shear decks previously discussed (which were of approximately the same age) in that the shear failure crack formed from a previously visible flexural crack and its formation and development were observed before failure of the specimen. However, the shear failure crack in the Strength 2 deck was not visible prior to failure. Video taken during the testing of this deck shows the shear crack forming in almost the same instant that the failure occurred, suggesting that the crack began within the section and propagated outward to the sides of the deck causing a more sudden failure. The shear crack formation of the Strength 3 specimen was not observed.

## 4.3 Strength Degradation of GFRP Reinforcement – Tensile Tests

### 4.3.1 Introduction

In order to more directly examine the effect on the GFRP rebar due to environmental, load, and time factors, tensile tests were conducted on several bars extracted from the Strength 2 and Strength 3 specimens as well as four unused bars using a SATEC Universal Testing Machine

(UTM). The extraction method and testing procedure were detailed in Section 3.2.3. No effort was made to identify the contributions of particular environmental factors; rather, only the overall effect of environmental exposure and time were considered.

Ten No. 6 rebar specimens were tested. To simplify identification and references to the specimens, each bar was assigned a designation based on the deck they were removed from and an assigned number. The nomenclature used is detailed in Table 4.21.

***Table 4.21 – Rebar Tensile Test Specimen Nomenclature***

| Specimen Source | Source Explanation | Specimens |
|---|---|---|
| U | Unused Rebar, stored in lab | U1, U2, U3, U4 |
| LAB | Strength 2 Deck, maintained in lab | LAB1, LAB2, LAB3 |
| WS | Strength 3 Deck, installed in weigh station | WS1, WS2, WS3 |

### 4.3.2 Discussion of Bar Tensile Test Failures

Of the ten bars tested, nine experienced a tensile failure within the gage length. The typical progression to failure began with the intermittent rupture of individual fibers. As the load application continued the rate of fiber failure increased more rapidly as the number of intact fibers able to carry the load was reduced. The helical threading around the outside of the bar ruptured as well thereby allowing the broken fibers to spread out in a "broomstick" manner. Additionally, the extent of the broomstick fiber spread, which was the entire gage length of all nine specimens, indicates extensive failure of the plastic matrix bonding the fibers together. Although not part of this research, it was noticed in other projects at Virginia Tech that the failure zone of bars undergoing similar testing was significantly reduced and much cleaner as the bar diameter decreased. Figure 4.45 shows specimen U3 after tensile failure. All nine specimens failed in a similar manner, but it was also noted that the aged specimens broke in a slightly cleaner manner with less fiber spreading and dust dispersal.

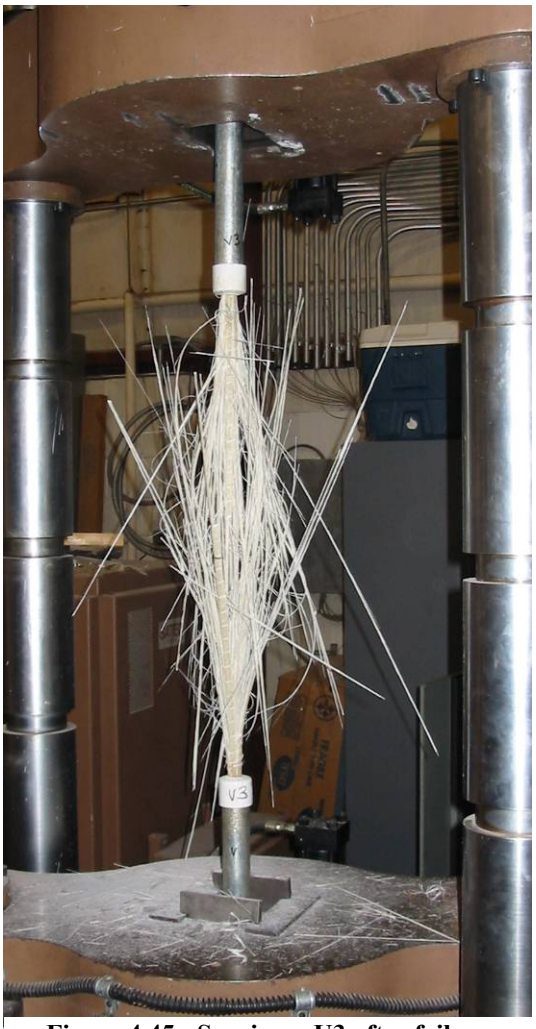

**Figure 4.45 - Specimen U3 after failure**

Of the nine successful tests, one of the bars from the Strength 2 deck, Lab 2, initially slipped about 1.5 in. along the interface of the rebar and the hardened epoxy resin in the end anchor, but caught again and continued to hold until failure of the bar in tension inside the gage length.

One of the bars from the weigh station, specimen WS1, experienced bond failure between the inside surface of the pipe and the epoxy, which caused the end anchor assembly to slip along the specimen above a certain load. This is the bar of the set of ten that did not result in tensile failure as described above. After considering the few specimens available for testing and the importance of this particular bar due to its source, the slipping steel pipe was removed from the end of the specimen by intentionally pulling it off with the UTM. The bar was then reloaded in the machine without the steel sleeve and tested with the intent of obtaining the modulus of elasticity. After attaining a sufficiently high load to meet the intent, the epoxy on the exposed end failed and the test was halted. The results of this bar and the other specimens are presented in the next section.

### 4.3.3 Modulus of Elasticity

Plots of stress verses strain were developed for each bar to investigate the modulus of elasticity and tensile strength. The stress was calculated by dividing the applied load, which was obtained from the UTM, by the cross-sectional area of the bar, 0.44 $in^2$. Strain was measured with a clip-on extensometer. The corresponding load was measured by the UTM during testing. Figures 4.46, 4.47, and 4.48 show the plots of stress verses strain for the unused bars (U) and the bars from the Strength 2 (LAB) and Strength 3 (WS) specimens, respectively.

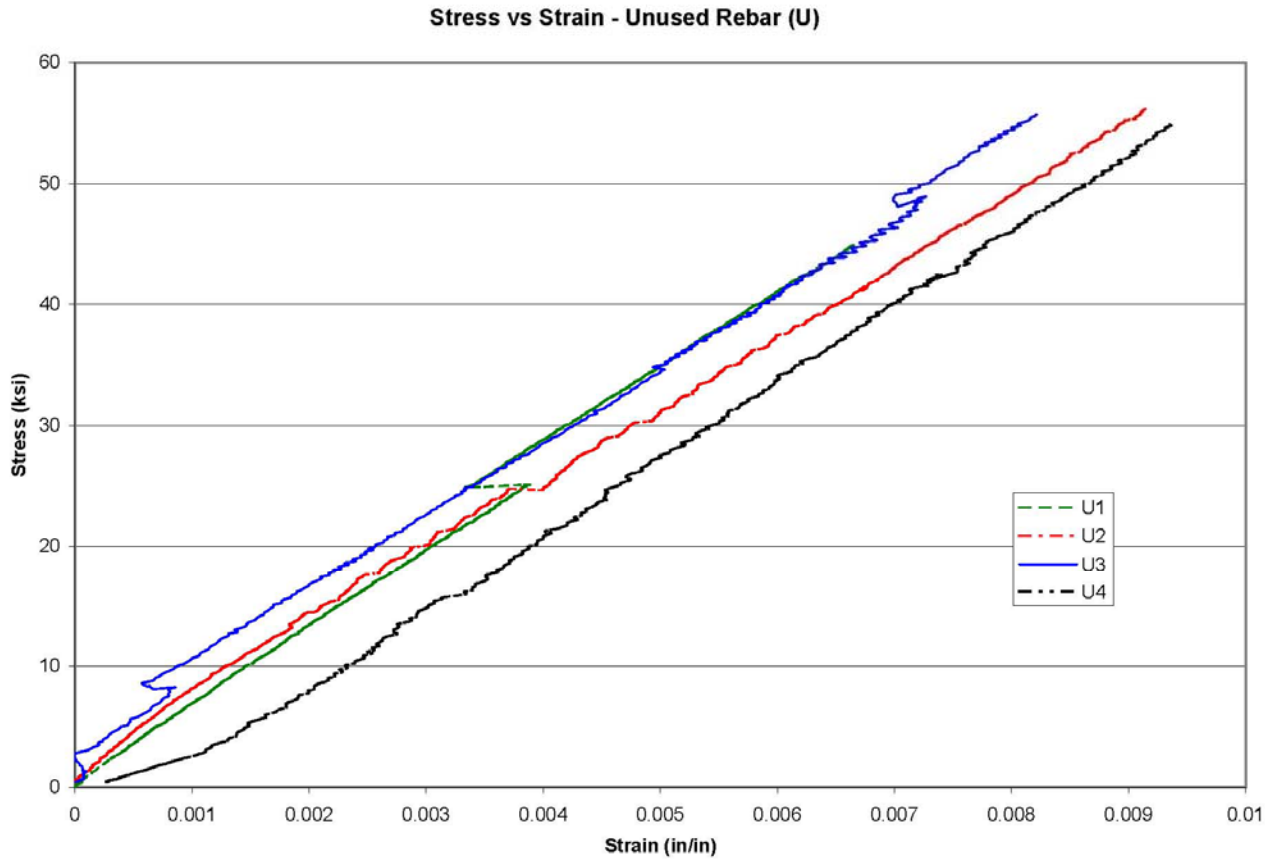


**Figure 4.46 - Stress versus strain diagram for unused rebar specimens (U)**

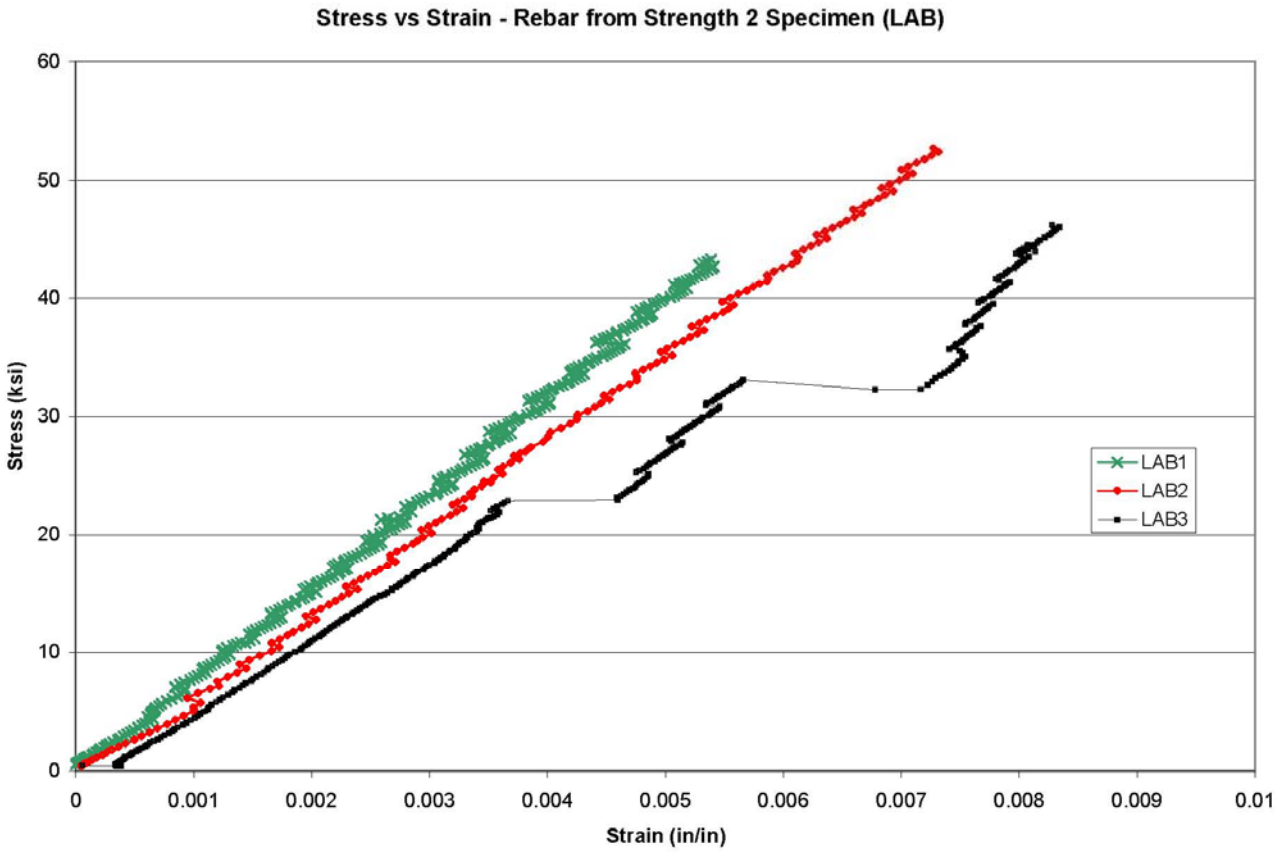


**Figure 4.47 - Stress versus strain diagram for specimens from Strength 2 deck (LAB)**

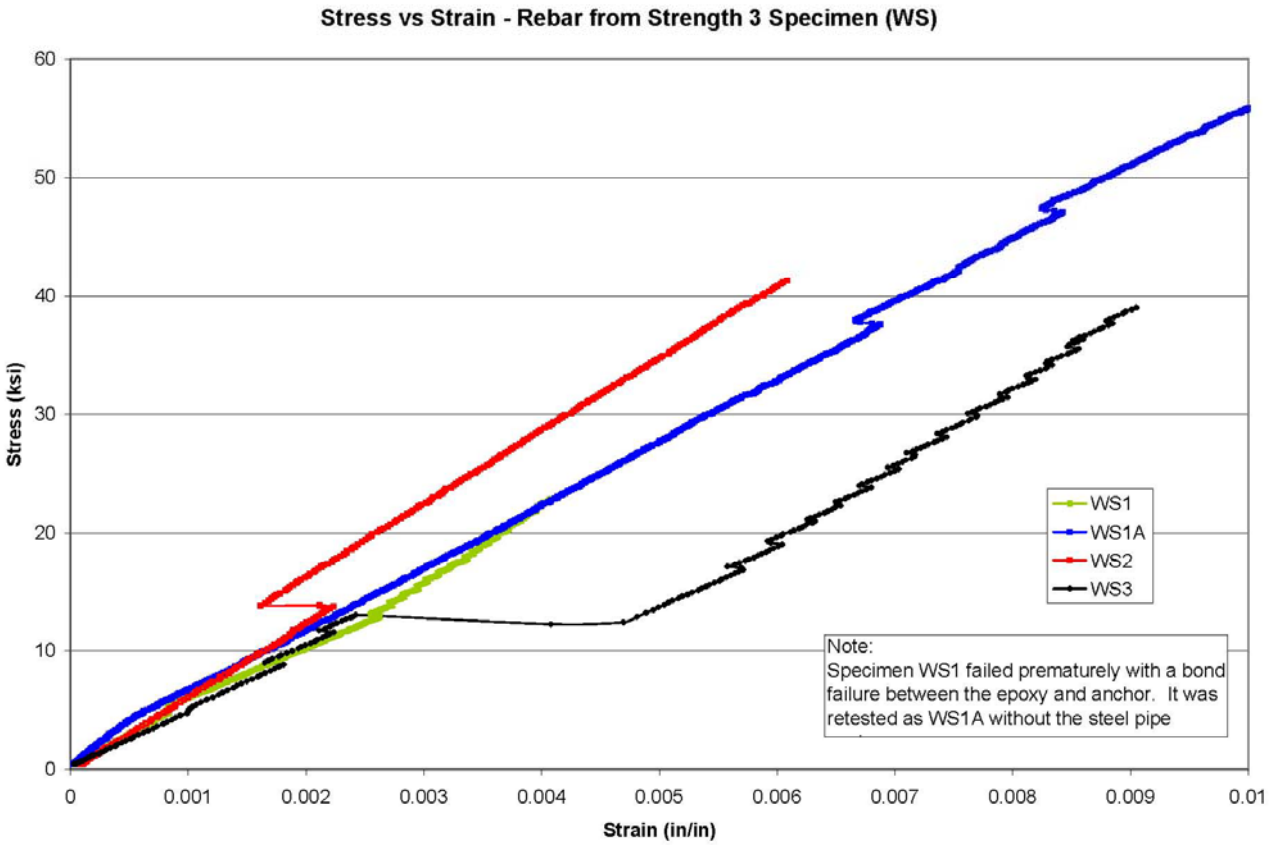


**Figure 4.48 - Stress versus strain diagram for specimens from Strength 3 deck (WS)**

According to ACI 440, in determining the modulus of elasticity, strain values should be recorded until the applied load reaches at least 60% of the tensile strength. However, it was not clear how the specimens would perform given their atypical conditioning so the extensometer was removed from the bar early to avoid damaging the equipment. Additionally, the guide recommends testing a minimum of five specimens; however, due to the difficulty in obtaining the bars from the concrete decks, only three were collected from each deck. Only four unused bars were tested because results from tests on unconditioned bars performed by Cawrse (2002) and Defreese (2001) were available since the same supplier was used. Cawrse tested ten bars total, split between no. 5 and no. 6 bars, and Defreese tested fifteen bars, five each of three different sizes.

Typically the modulus of elasticity is determined by finding the ratio of the change in stress to the change in strain, which is the slope of the stress-strain diagram. Unfortunately, the stress-strain plots of Figures 4.48 through 4.50 indicate slippage of the extensometer during testing. Therefore, the modulus was calculated for several straight-line portions of each

specimen's diagram and averaged to find an overall modulus of elasticity for the specimen. The results are presented in Table 4.22.

In addition to the ten bars investigated in this research, six more specimens were tested through the SURP program at Virginia Tech (Summer Undergraduate Research Program). Three specimens were extracted from both the Strength 2 and Strength 3 decks using the same extraction procedure. The results of the tensile tests of these bars are included here and they are identified as SL1 through SL3 for the Strength 2 deck and SW1 through SW3 for the Strength 3 deck. The modulus of elasticity observed in the SURP data is somewhat higher than what was found for the LAB and WS series, although this may be attributed to the use of a different extensometer. Regardless, the two datasets are being combined here because they are from the same source and both used acceptable procedures for the determination of material properties.

***Table 4.22 – Modulus of Elasticity***

| Specimen | Individual E | Average E |
|---|---|---|
| U1 | 6177 ksi | 6246 ksi |
| U2 | 6221 ksi | |
| U3 | 5947 ksi | |
| U4 | 6202 ksi | |
| Cawrse | 6210 ksi* | |
| Defreese | 6300 ksi† | |
| Lab1 | 4912 ksi | 6220 ksi |
| Lab2 | 5035 ksi | |
| Lab3 | 6734 ksi | |
| SL1 | N/A | |
| SL2 | 7621 ksi | |
| SL3 | 6796 ksi | |
| WS1 | 5212 ksi | 5829 ksi |
| WS2 | 6278 ksi | |
| WS3 | 4198 ksi | |
| SW1 | 6460 ksi | |
| SW2 | 6518 ksi | |
| SW3 | 6310 ksi | |

**10 Specimens, †15 Specimens*

From the averages in Table 4.22 it appears that there is a slight correlation between the modulus of elasticity of GFRP rebar and the environment it is exposed to. The average modulus of elasticity is essentially identical between the bars that were allowed to age in the lab-maintained concrete deck and those that were never installed in a concrete member. The average modulus for the six bars that were installed in the deck that experienced exposure to the elements and truck traffic was slightly lower, although only by about 7%. However, in each of the LAB and WS series there was a significant increase in variance of the modulus values. In fact, the modulus of elasticity for three of the Lab specimens and four of the Weigh Station specimens were found to be higher than the average elastic modulus for the unconditioned bars. One of these, the SL2 specimen, exceeded the unconditioned modulus by more than 22%. On the other hand, two tested specimens in both the LAB and WS series had significantly lower values. The tensile modulus of elasticity published by the manufacturer (Hughes Brothers, Inc.) is 5920 ksi,

which is exceeded by all of the unconditioned bars. However, the two lowest specimens each of the LAB and WS sets are below this published value.

Unfortunately, due to the small number of specimens in this dataset, no succinct statement can be made from these results regarding how conditioning affects the stiffness of GFRP rebar. The reason for the slight decrease in stiffness is unclear as questions may be raised about the effect of the jackhammer vibrations on the glass fibers during retrieval of the specimens. Further, the moduli obtained from the SURP research are all greater than the LAB and WS series discussed here. Although it is possible that this is due to material variability, it is more likely caused by the difference in extensometer setup. It would have been beneficial to have modulus results of unconditioned bars performed by the SURP program as well in order to better observe any differences between the setups. However, the fact that the same setup was used for the U, LAB, and WS series bars and the modulus results of the U series matched previous unconditioned observations quite well strengthens the validity of the LAB and WS data shown. As such, the nature of the low individual values of some specimens in the LAB and WS series clearly identifies a need for further study in this subject.

### 4.3.4 Ultimate Tensile Strength

The stress at tensile failure of the specimens was determined by dividing the failure load by the cross-sectional area of the rebar, 0.44 $in^2$. The load was recorded by the UTM during the testing procedure and the maximum applied load was used in the calculation of the ultimate tensile strength. As in Section 4.3.3, the data collected by Cawrse (2002) and Defreese (2001) for the same manufacturer (Hughes Brothers, Inc.) was included in the average ultimate tensile strength for the unconditioned rebar. However, only No.6 bars from these two sources were considered due to concerns regarding the affect of interlaminar shear lag on the overall strength of the bars. Additionally, results obtained from the SURP program were also included for the Lab and Weigh Station bars. Table 4.23 summarizes the ultimate tensile strengths of the specimens.

Unlike the observations regarding the modulus of elasticity, the ultimate tensile strengths of all of the LAB specimens were notably greater than the average strength of the unconditioned specimens. This may have been caused by additional curing of the resin matrix by the heat of hydration, but it does strongly suggest that damage to the longitudinal glass fibers during retrieval of the bars from the concrete deck is not a likely culprit for the lower stiffness of the specimens observed in the previous section as there is clearly no loss of ultimate strength.

***Table 4.23 – Ultimate Tensile Strength***

| Specimen | Individual $\sigma_{max}$ | Average $\sigma_{max}$ |
|---|---|---|
| U1 | 85.6 ksi | 94.2 ksi |
| U2 | 87.3 ksi | |
| U3 | 100.0 ksi | |
| U4 | 95.1 ksi | |
| Cawrse | 89.3 ksi† | |
| Defreese | 98.0 ksi† | |
| Lab1 | 104.3 ksi | 103.2 ksi |
| Lab2 | 106.4 ksi | |
| Lab3 | 95.8 ksi | |
| SL1 | 112.4 ksi | |
| SL2 | 98.2 ksi | |
| SL3 | SLIPPED | |
| WS1 | SLIPPED | 78.7 ksi |
| WS2 | 77.0 ksi | |
| WS3 | 88.7 ksi | |
| SW1 | 75.0 ksi | |
| SW2 | 73.9 ksi | |
| SW3 | SLIPPED | |

*†5 Specimens*

The average tensile strength of the WS bars, however, was significantly lower than the unconditioned case. On the other hand, specimen WS3 exhibited a notably greater ultimate tensile strength than the other WS specimens as well as two of the unconditioned specimens. Oddly, this specimen had the lowest modulus of elasticity of all the rebar specimens in the previous section. Again, this greater tensile strength seems to confirm that the glass fibers of the GFRP bar were intact following specimen retrieval.

The guaranteed ultimate tensile strength published by the manufacturer is 90 ksi for No. 6 GFRP rebar. Two of the unconditioned specimens, U1 and U2, as well as the average of the results reported by Cawrse (2002) failed to meet this minimum strength.

ACI 440 recommends a reduction in the design tensile strength of GFRP used in concrete members to account for the effects of environmental exposure on tensile strength and creep rupture and fatigue endurance. This is presented here as Equation 4.31.

$$f_{fu} = C_E f_{fu}^{*} \qquad \text{(Eqn. 4.31)}$$

Where: $f_{fu}$ = design tensile strength of FRP rebar, ksi

$C_E$ = Environmental reduction factor, 0.7 for GFRP in concrete exposed to earth and weather

$f_{fu}^{*}$ = guaranteed tensile strength of FRP rebar, ksi

According to Equation 4.31, the design tensile strength of the LAB and WS specimens is 90 ksi and 63 ksi, respectively. All specimens clearly met this requirement.

Although the observations presented here suggest a decrease in ultimate tensile strength of the GFRP rebar that was exposed to the elements and traffic loadings over the brief 1-year period of installation at the weigh station, as with the modulus of elasticity results from the previous section, there is not enough data to make a definitive conclusion regarding the environmental impact on the material performance.

# *Chapter 5 – Conclusions*

## 5.1 Introduction

The research presented in this thesis had two objectives. First, this work sought to expand the understanding of the effect of GFRP reinforcement on the one-way shear strength of concrete bridge decks. The research examined several aspects of the decks' behavior including deflections, crack widths, cracking load, reinforcement strain, failure load, and failure mode. Results were compared with existing suggestions for predicting the shear strength based on previous research. Second, the effects of heavy live load application and exposure to real-world environmental factors on GFRP-reinforced concrete decks were analyzed. In addition to examining the same performance characteristics of the decks analyzed in the shear investigation portion, the GFRP reinforcement itself was removed and subjected to tensile testing. Conclusions and recommendations are summarized by section following this introduction and final conclusions and recommendations follow at the end of the chapter.

## 5.2 Shear strength of GFRP-reinforced concrete decks

This portion of the research involved the testing and analysis of four concrete decks with similar reinforcement ratios, effective depths, and material properties. Only the length varied between decks from 1 ft to 5 ft long in the direction of traffic. The decks were compared for shear strength, deflections, strain in the reinforcement, and cracking. Additionally, the performance was compared to the currently prescribed design criteria from ACI 440.

### 5.2.1 Shear strength and comparison with predicted values

Given the nature of the continuous specimens that were tested in this phase of the research, the shear strength exhibited by the decks was not as simple to determine as it would be for a simply-supported setup; however, the use of the known rebar strains over the center support to develop the moment-applied simple span model seems to have worked well, resulting in shear strengths between the bounds of a simply supported and continuous elastic condition.

The resulting shear strengths of the specimens were compared to suggested shear strength equations from ACI 440, Frosch, Deitz, the modified compression field theory, and ACI 318. All five models reviewed were quite conservative, particularly the ACI 440, Frosch, and Deitz

methods. The modified compression field theory and the ACI 318 method were both developed for steel-reinforced concrete beams. The methods outlined in ACI 440 and proposed by Frosch sought to adjust the ACI 440 method to consider the lower stiffness of GFRP rebar and its effect on the shear strength of the concrete. The majority of previous research, however, has been on shear in beams as opposed to one-way slabs, which may be one reason for their discrepancies with the findings reported here. The aspect ratio differences may make a tremendous impact on the performance of the member. Although it was shown by Frosch that the ratio of the shear span to effective depth ratio may influence the shear strength of GFRP-reinforced concrete beams, this was found not to be the cause of the excessive conservatism of the proposed equations.

In addition to the fact that the proposed models are mostly based on experimentation with beams instead of slabs, all of the research reviewed for this study considered members in a simply-supported loading condition. The more likely configuration experienced by a concrete deck would be a continuous condition across several supports, as was tested in this research. This paper proposes that three factors lead to an increase in shear resistance of the section over that predicted by these models. First, the subsequent forcing of the member into triple-curvature over the center support may increase the compressive stresses on the concrete below the neutral axis of the section, thereby increasing the contribution of this uncracked concrete to the shear strength of the section. This proposal is based on the fact that the ends of the member in a simply-supported condition are allowed to rotate, thereby relieving the some of the compressive stresses experienced by the concrete at the ends of the member. However, in a continuous multi-span configuration, this rotation is restricted by the presence of, and the loads within, the adjacent spans, which neglects the member of this stress-relieving rotation. According to the Mohr-Coulomb failure criterion, the higher normal compressive stress in the uncracked portion of the concrete increases the shear strength of the member. Figure 5.1 shows the Mohr-Coulomb stress construction. In this diagram, the shear failure envelope is defined by drawing lines

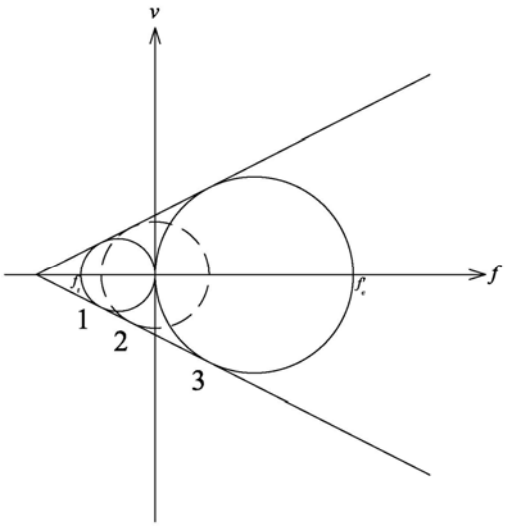


**Figure 5.1 – Mohr-Coulomb stress diagram**

tangent to the stress circles for pure tension (Circle 1) and pure compression (Circle 3). Pure shear is represented by Circle 2. It is clear that increasing the compressive stress shifts the stress state towards Circle 3, thereby increasing the shear strength of the section (Ruddle 1999). To take this into account, the Equation 5.1 was proposed by Ruddle (1999) for members with moment to shear ratios greater than 2.5.

$$V_c = 0.43 f_c'^{2/3} \left(\frac{Vd}{M}\right)^{1/3} bx\left(\frac{200}{d}\right)^{1/4} \quad \text{(SI Units)} \qquad \text{(Eqn. 5.1)}$$

Where: $f_c'$ = design compressive strength of concrete, N/mm$^2$

$V$ = shear due to applied load, N

$M$ = moment due to applied load, N-mm

$d$ = effective depth of section, mm

$b$ = width of section, mm

$x = d\left(-n\rho + \sqrt{(n\rho)^2 + 2n\rho}\right)$, mm

Second, the lower layer of steel reinforcement likely contributes to the shear strength of the specimens through dowel action, particularly when the compression zone is entirely below the level of the steel rebar. If sufficient bearing strength could be developed by the concrete, this contribution could be as high as 16 kips for a single No. 6 rebar.

Finally, since the actual behavior of the section is between that of simple-span and continuous configurations, there is uncertainty as to how the specimen is acting at the critical section for shear. In a simple-span case, the critical section is in the positive moment region, causing the member to act as a steel-reinforced section. In a continuous case the critical section is in the negative moment region, which causes the member to act as a GFRP-reinforced section. However, in the case of a cracked continuous member, as in this research, the inflection point between positive and negative moment is near the critical section, which makes it difficult to determine if the deck is acting as steel- or GFRP-reinforced.

Based on the results of this study, the equations outlined in the ACI 440 document for one-way shear, as well as those proposed by Frosch and Deitz, are overly conservative for the case of one-way concrete decks continuous over multiple spans with GFRP rebar as top-mat reinforcement. As such, it is recommended that additional research be pursued to consider this situation and that the ACI 440 equations for shear be modified or expanded upon for application to this common use of GFRP in reinforcement of concrete bridge decks. Additionally, although

the Ruddle model shown in Equation 5.1 was not considered in this research, it is recommended that it be reviewed in future studies of continuous decks with modifications for GFRP reinforcement for comparison with existing models.

### 5.2.2 Shear failure mode

Comparison of the normalized failure loads from this study with the interior beam tests in the research performed by Cawrse (2002) resulted in an intriguing plot of the shear strength verses specimen length in the direction of traffic (parallel to the supports). Having failed in two-way, punching-type, shear, Cawrse's results provide a good suggestion for the upper bound of shear strength of GFRP-reinforced decks. Based on the trend observed in Section 4.1.2.9, it appears that a transition from one-way to two-way shear may occur around a length of 7 ft for this load configuration. Identifying the point of this transition as a function of deck thickness and span length would help engineers predict the behavior of GFRP-reinforced bridge decks. Experimentation on additional specimens with the same loading and span configuration, particularly in the range of 6 ft to 10 ft long, would help identify this failure mode transition point.

### 5.2.3 Deflections

The ACI 440 document was used in conjunction with ACI 435 to develop an expression for the effective moment of inertia for the decks considering the cracking in the positive and negative moment regions and the uncracked regions in between. The method was relatively successful in predicting the deflection behavior of the specimens, typically being slightly conservative for the majority of the testing procedure. The only major variation from this is during the period when the section is cracked over the center support, but not yet at the midspans. The rather large weighting of the midspans moment of inertia in this method leads to an unconservative prediction of deflection in this particular situation. Although it did attempt to, the method also does not seem to account enough for the increase in overall flexibility of the section as it becomes more cracked. Finally, there appeared to be some slight increase in residual deflection of the specimens at the zero-load end of each service cycle. Plastic bond slip is suggested as the primary contributor to this observation.

### 5.2.4 Strain of the GFRP rebar in the negative moment region

The strain in the steel and GFRP rebar of the four specimens was analyzed and compared to theoretical values derived from the ACI 440 document. In general, with the exception of the 1

ft section, the theoretical stress in the rebar, which is intended to describe the maximum stress experienced by the bars in the section, was unconservative for the uncracked cases. Although it may have been a good indicator of the average rebar stress, there was always at least one bar in each specimen that exceeded this stress. For the cracked case, the theoretical values were always conservative, at times greatly so with predictions 250% greater than what was recorded by the strain gages. This was because the cracked moment of inertia was used in the stress calculation since the section was cracked at the location of the gage. However, the cracked moment of inertia assumes a fully cracked section and thus indicated more flexibility than was actually present in these cases.

### 5.2.5 Cracking loads

The theoretical cracking loads were calculated using an uncracked transformed moment of inertia and the generally accepted modulus of rupture for concrete. The predictions, when compared with the cracking loads identified from significant changes in the GFRP strain data, matched particularly well, for the 1 ft, 2 ft, and 5 ft sections, although it was approximately 18% unconservative for the 5 ft section. However it was more than 40% unconservative for the 3.5 ft specimen. It is not clear from this small data set whether the unconservative nature of the of this method is related to the width of the sections considered. Additional research with varying width members would be useful in identifying such trends.

### 5.2.6 Crack widths

The adjusted Gergely-Lutz equation presented in ACI 440 was used to predict crack widths. Actual crack widths of the specimens were measured with either a crack card or a crack microscope, depending on the size and importance of the crack. Additionally, a DEMEC gage was used to measure crack widths while the specimens were only slightly cracked. The ACI 440 equation predicted the crack widths relatively well throughout the testing procedure, typically being slightly conservative when compared to the largest measured crack widths. The cracking calculations were based on measured bar strains, which were converted to stresses using the appropriate modulus of elasticity. The equation was generally smoother throughout the loading than what was measured, but this was due to inconsistencies in measuring the crack widths and the 0.2 mm increments on the crack cards that were used. Although crack width predictions based on calculated bar stress were not presented in this paper, they were found for a couple specimens to compare with the method of using measured bar strain. Figure 5.2 shows this

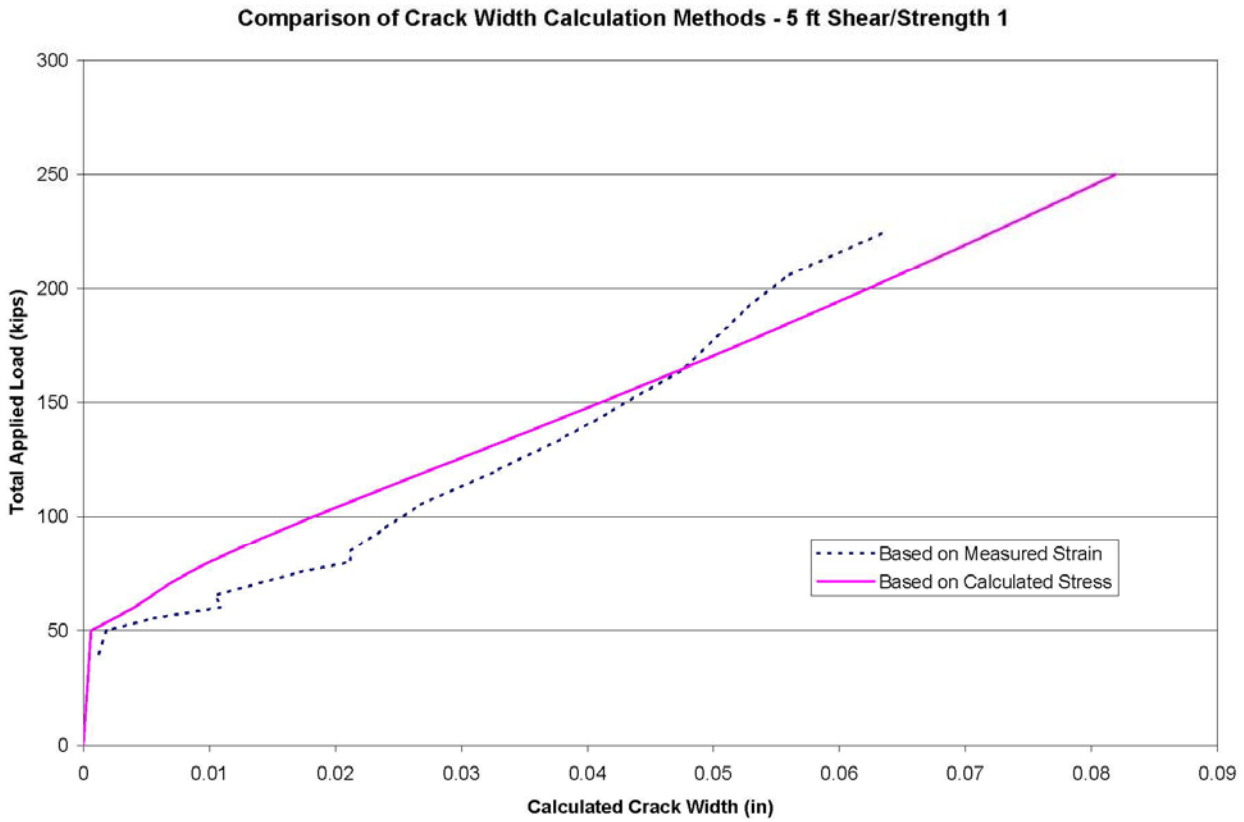


**Figure 5.2 - Comparison of methods for predicting crack widths for the Strength 1 specimen**

comparison for the 5 ft Shear/Strength 1 specimen. Overall, the use of measured strains as a base for the crack width predictions agreed fairly well with the results from using calculated sresses after cracking of the deck. However, prior to cracking of the deck, crack widths based on measured bar strains were up to twice as large.

## 5.3 Strength degradation of GFRP reinforcement

Three decks with identical reinforcement ratios and similar dimensions were tested in the lab after each being conditioned differently. One was constructed and tested within weeks, the second was constructed and maintained in the climate-controlled laboratory for over a year, and the third was installed in a weigh station ramp on a major interstate and subjected to environmental factors and significant truck loadings for over a year. The specimens were compared for performance in deflections, reinforcement strain, cracking load, crack widths, and failure load.

Following testing of the deck specimens, several of the GFRP reinforcing bars were removed from the second and third slabs to be compared to unconditioned bars in tensile tests.

Specifically, this second phase sought to find differences in the modulus of elasticity and the ultimate tensile strength.

### 5.3.1 Weigh station tests

As described above, one of the deck specimens was installed at a major weigh station in southwest Virginia and subjected to harsh environmental factors and vehicle loadings. Twice while this deck was at the site tests were conducted to monitor its performance over time. The strains experienced by the GFRP rebar were more than 200% greater during the second visit compared to the first. The exact reason for this could not be determined, but possible explanations include additional cracking of the section between the two test dates and reduction in stiffness of the GFRP rebar due to environmental and loading factors.

This particular test method shows great promise in that it subjects the specimen to the exact environmental conditions it would be exposed to in real bridge. However, these same conditions are harsh on the instrumentation used in the deck as well, leaving only three gages operable at the end of the 14-month life of the deck. Further, the presence of moisture may have exacerbated noise in the data that was presumed to be caused by an electronic source as its frequency was approximately constant at 60 Hz. Removal of this noise was not trivial and future studies similar to this one should employ methods of shielding the wires from electromagnetic waves. However, the benefits of conditioning a specimen in this manner are clear.

### 5.3.2 Deflections

In comparing only the measured deflection values of the three specimens, there was no obvious correlation between conditioning of the specimens and deflections. In fact, the Strength 3 specimen, which had been installed at the weigh station, exhibited the lowest deflections of the three specimens. The largest deflections were recorded from the Strength 2 deck, which had been stored at the lab. However, this comparison did not take into account the difference in concrete strengths as the Strength 1, or unconditioned, specimen contained a different batch of concrete. Assuming a reduction in concrete strength would lead to higher deflection values, this fact only serves to further denounce the possibility of any trend towards greater deflections with harsher conditioning. However, there were not enough specimens considered in this study to solidly rule out any effect from the conditioning on deflections.

Two theoretical series were developed for these three specimens: one for the unconditioned specimen and one for both the Strength 2 and 3 specimens. The lower concrete

strength of the Strength 2 and 3 specimens caused the prediction for these decks to be lower, but as was pointed out above, this was not the case in the actual recorded data.

Despite the lack of correlation between conditioning and deflections, more research with a larger dataset would be necessary before such a relationship could be discounted.

### 5.3.3 Strain of the GFRP rebar in the negative moment region

Unfortunately, there was not enough data to accurately compare the specimens in this area. Only three strain gages survived on the Strength 3 slab from the weigh station, all of which were on the same side of the center support. As previous experience showed that there were significant differences between the strain experienced on either side of the support, no attempt was made to compare the specimens in this matter. It should be noted, however, that the prediction for strain in the Strength 2 deck was unconservative after the section was cracked.

This question of rebar stiffness following conditioning and its effect on bridge deck performance is an important one and ACI 440 recognizes it through its equation for the design tensile strength of GFRP rebar. However, further research should be performed to better quantify the environmental effects. In conducting such research, it is strongly advised that a replacement be considered for measuring strain rather than using electrical resistance gages.

### 5.3.4 Cracking Loads

Since the Strength 3 slab was cracked at the weigh station, no cracking load was found for this specimen in the lab. However, according to rebar strain data, the first crack in the Strength 2 specimen was at 43 kips, just 3 kips higher than the Strength 1 specimen. The predicted cracking load was also lower for the Strength 2 specimen given the lower compressive strength of the concrete. The cracking load of the Strength 2 specimen exceeded the predicted cracking load by only 4.6%. Given that the cracking load is most greatly affected by the concrete strength, changes in the strength or stiffness of GFRP are not expected to greatly affect it.

### 5.3.5 Crack widths

The adjusted Gergely-Lutz equation presented in ACI 440 was used to predict crack widths. Actual crack widths of the specimens were measured with either a crack card or a crack microscope, depending on the size and importance of the crack. Additionally, a DEMEC gage was used to measure crack widths while the specimens were only slightly cracked.

The ACI 440 equation for crack widths predicted the measured widths exceptionally well for the Strength 2 specimen when compared to the DEMEC readings. It was only slightly

conservative during the latter portions of the test when compared with the crack microscope and crack card readings.

For the Strength 3 specimen, however, the equation was considerably unconservative. This is easily explained by the low strain values recorded from the strain gages on the GFRP bars. As discussed previously, these gages were all on the same side of the center support and do not reflect the strain in the bar on the other side of the support. Previous experience shows that these may be very different depending on how well the deck is supported on the center support.

Disregarding the results from the Strength 3 specimen, this research shows the ACI 440 equation to be very accurate in predicting crack widths.

### 5.3.6 Failure Load

The shear strength of reinforced concrete bridge decks is most greatly influenced by a combination of concrete strength and the modulus of elasticity of the reinforcement. All three specimens in this study failed in one-way shear. Since the concrete strength and the effective depth of the specimens differed somewhat, the failure load was normalized to these two variables before comparing the results. Surprisingly, the Strength 3 specimen exhibited the highest normalized failure load, followed by the Strength 2 and Strength 1 specimens. This was certainly unanticipated because the weigh station slab had been conditioned by truck loadings and environmental factors, which were expected to have adversely affected the deck. The trend here, however, shows in increase in shear strength with an increase in conditioning.

As discussed in Section 5.2.1, the predicted shear strengths of the specimens, developed from research on simply-supported beams, were grossly overconservative. This fact was attributed to the aspect ratio differences between beams and decks combined with the suggested increase in compressive stress in the concrete over the center support due to forced double-curvature and the contribution of the steel rebar of the bottom mat. Further research is strongly recommended to clarify the effects of conditioning on the shear strength of GFRP-reinforced concrete bridge decks.

### 5.3.7 Modulus of elasticity of GFRP rebar

This study subjected sixteen GFRP rebar specimens, twelve of which were obtained from the Strength 2 and Strength 3 deck specimens discussed above, to tensile testing in the lab to find the effects of conditioning on their modulus of elasticity and ultimate tensile strength. The results of this study suggest a slight decrease in the modulus of elasticity of GFRP rebar after one

year of the composite section being subjected to environmental factors and traffic loadings. However, a bar in each of the two conditioned cases (from the Strength 2 and Strength 3 decks) exhibited stiffness equal to or exceeding an unconditioned state. The small number of specimens significantly limits the impact of the trend found in this research, but does clearly identify a need for further study in this matter. Additionally, although the individual ultimate strengths of the specimens, which will be discussed shortly, indicate otherwise, it could be argued that using a jackhammer to retrieve the rebar from the concrete decks may have damaged the glass fibers. Future research on this matter should find a retrieval method that is less likely to damage the bars such as the installation of a "tattle-tail" bar that can be easily removed. However, the method or material used to break the bond between the bar and the surrounding concrete needs to be able to transfer all chemicals and stresses to the bar to obtain accurate results.

### 5.3.8 Ultimate tensile strength of GFRP rebar

The ultimate tensile strengths of the GFRP rebar discussed in the previous section showed a clear decrease in the specimens retrieved from the weigh station slab. However, the bars that were in the slab that was stored in the laboratory actually exhibited a greater tensile strength compared to the unconditioned bars. This may be due to additional curing of the resin caused by the heat of hydration, but it does suggest that the bars were not damaged in the process of removing them from the slab with the jackhammer. The lower tensile strengths of the WS specimens from the Strength 3 deck confirm the need for the reduction in design strength as recommended by ACI 440. After considering this reduction, a factor of 0.7 for the case of the WS specimens, all rebar specimens exceeded their predicted ultimate tensile strengths except two of the unconditioned specimens which failed to meet the manufacturer's guaranteed tensile strength by less than 5%.

As with the modulus of elasticity, there were not enough specimens in this study to solidly confirm or denounce a trend. Further research in this area should be pursued as previously suggested.

## 5.4 Recommendations for future research

The use of GFRP rebar in the country's infrastructure is severely hindered by a lack of understanding and trust in its performance. The material shows great possibility as reinforcement in concrete bridges decks, particularly as top-mat reinforcement, primarily

because of its resistance to corrosion. However, current engineering practice tends to an overly-conservative design when using FRP because of a lack of understanding of the material properties. As shown in this research, the one-way shear strength of continuous GFRP-reinforced bridge decks is substantially higher than predicted by existing equations. Before a change to these guidelines can be made, further research must be performed with greater numbers of specimens to confirm the results of these findings.

In the area of strength degradation of GFRP rebar, a reduction in stiffness of the material was not reported in any of the literature reviewed prior to conducting this research. This lower modulus of elasticity could affect the growth of cracks in GFRP-reinforced structures and should be studied more closely.

The loss of tensile strength of GFRP rebar is a known phenomenon and is already considered in ACI 440. However, there is not a lot of experience with the material to know how this loss of strength occurs over time. Knowledge of the rate of strength loss with time and exactly what environmental factors affect it would be highly beneficial to the engineer designing with GFRP.

# References


AASHTO, *AASHTO LRFD Bridge Design Specification,* Second Edition, 2002, Washington, DC.

AASHTO, *AASHTO Standard Specifications for Highway Bridges,* 17th Edition, 2002, Washington, DC.

ACI, *Building Code Requirements for Structural Concrete,* ACI 318R-02 (2002), American Concrete Institute Committee 318, Farmington Hills, MI.

ACI, *Control of Deflections in Concrete Structures*, ACI 435R-95 (2000), American Concrete Institute Committee 435, Farmington Hills, MI.

ACI, *Guide for the Design and Construction of Concrete Reinforced with FRP Bars*, ACI 440.1R-03 (2003), American Concrete Institute Committee 440, Farmington Hills, MI.

Bradberry, T.E., "FRP-Bar-Reinforced Concrete Bridge Decks," *Transportation Research Board Proceedings, 80th Annual Meeting*, TRB, Washington, DC, 2001.

Brown, V.L. and Bartholomew, C.L., "FRP Reinforced Bars in Reinforced Concrete Members," *ACI Materials Journal*, Vol. 90, No. 1, 1993, pp. 34-39.

Cawrse, J., "Laboratory Tests of a Bridge Deck Prototype with Glass Fiber Reinforced Polymer Bars as the Top Mat of Reinforcement," M.S. Thesis, Virginia Polytechnic Institute and State University, Blacksburg, VA, 2002.

Collins, M.P., Mitchell, D., Adebar, P., and Vecchio, F.J., "A General Shear Design Method," *ACI Structural Journal*, Vol. 93, No. 1, 1996, pp. 36-45

Defreese, J.M., "Glass Fiber Reinforced Polymer Bars as the Top Mat Reinforcement for Bridge Decks," M.S. Thesis, Virginia Polytechnic Institute and State University, Blacksburg, VA, 2001.

Deitz, D. H., Harik I. E., and Gesund, H., "One-Way Slabs Reinforced with Glass Fiber Reinforced Polymer Reinforcing Bars," *ACI Proceedings, 4th International Symposium*, 1999, pp. 279-286

Erki, M.A. and Rizkalla, S.H., "FRP Reinforcement for Concrete Structures," *Concrete International: Design and Construction*, Vol. 15, no. 6, 1993, pp. 48-53.

Harlan, M.D., "Field Test of a Bridge Deck with Glass Fiber Reinforced Polymer Bars as the Top Mat of Reinforcement," M.S. Thesis, Virginia Polytechnic Institute and State University, Blacksburg, VA, 2004.

Hassan, T., Abdelrahman, A., Tadros, G., and Rizkalla, S., "Fibre Reinforced Polymer Reinforcing Bars for Bridge Decks," *Canadian Journal of Civil Engineering*, Vol. 27, No. 5, 2000, pp. 839-849.

Liao, K., Schultheisz, C.R., and Hunston, D.L., "Effects of Environmental Aging on the Properties of Pultruded GFRP," *Composites: Part B*, Vol. 30, 1999, pp. 485-493.

Micelli, F. and Nanni, A., "Durability of FRP Rods for Concrete Structures," *Construction and Building Materials*, Vol. 18, 2004, pp. 491-503.

Ruddle, M. E., Rankin, G. I. B., and Long, A. E., "Mohr Approach to Prediction of Beam Shear Strength," *Proceedings of the Institution of Civil Engineers – Structures and Buildings*, Vol. 134, 1999, pp. 363-372.

Temeles, A. B., "Field and Laboratory Tests of a Proposed Bridge Deck Panel Fabricated from Pultruded Fiber-Reinforced Polymer Components," M.S. Thesis, Virginia Polytechnic Institute and State University, Blacksburg, VA, 2001.

Thippeswamy, H.K., Franco, J.M., and GangaRao, H.V.S., "FRP Reinforcement in Bridge Decks," *Concrete International: Design and Construction*, Vol. 20, No. 6, 1998, pp. 47-50.

Tureyen, A.K. and Frosch, R.J., "Shear Tests of FRP-Reinforced Concrete Beams without Stirrups," *ACI Structural Journal*, Vol. 99, No. 4, 2002, pp. 427-434.

Tureyen, A.K. and Frosch, R.J., "Concrete Shear Strength: Another Perspective," *ACI Structural Journal*, Vol. 100, No. 5, 2003, pp. 609-615.

*TTI FRP Reinforcing Bars in Bridge Decks: State of the Art Review*, TTI Report 1520-2, Texas Transportation Institute, College Station, TX, 2000.

Vishay Measurements Group, *Application of M-Coat J Protective Coating, Instruction Bulletin B-147-5*, 2002, Wendell, NC

Yost, J.R., Gross, S.P., and Dinehart, D.W., "Shear Strength of Normal Strength Concrete Beams Reinforced with Deformed GFRP Bars," *Journal of Composites for Construction*, Vol. 5, No. 4, 2001, pp. 268-275.

Weyers, R., "Engineer's Predictions Dismal for Nation's Highways and Bridges," Science From Virginia Tech, Lynn Nystrom, 2001, Virginia Tech, November, 2004. http://www.research.vt.edu/resmag/sciencecol/2001weyers.html

# Appendix A – Concrete Strength Plots

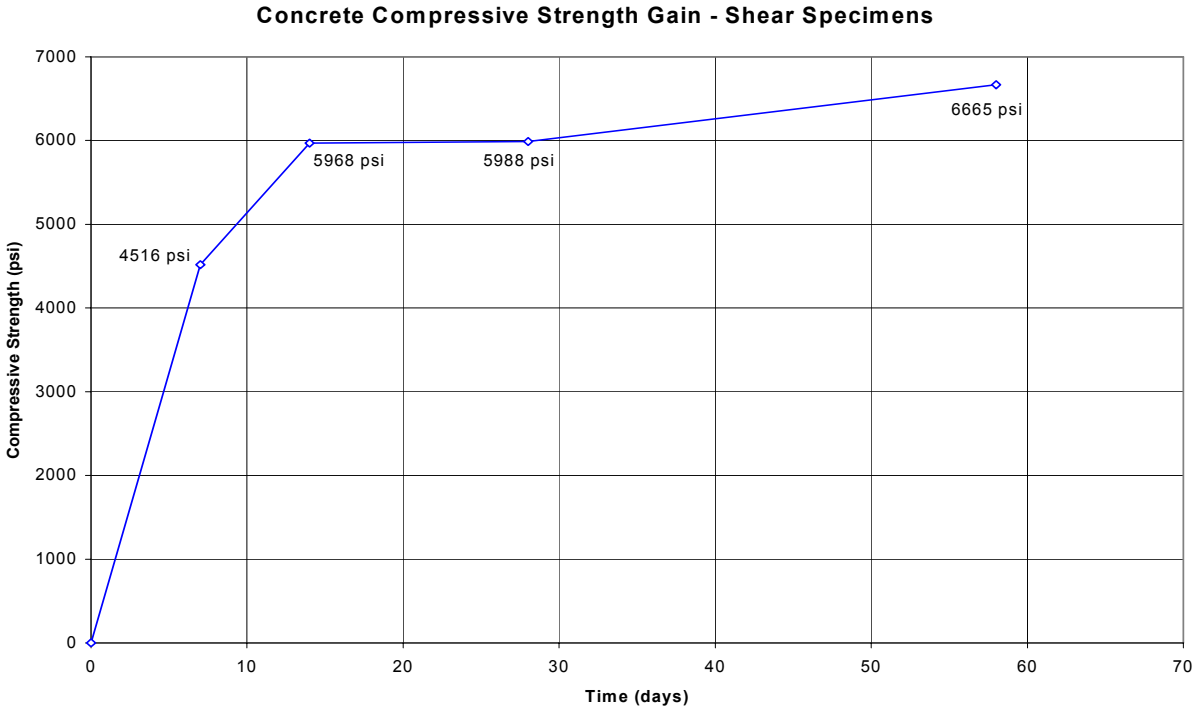


**Figure A.1 – Concrete strength gain plot for the shear strength specimens**

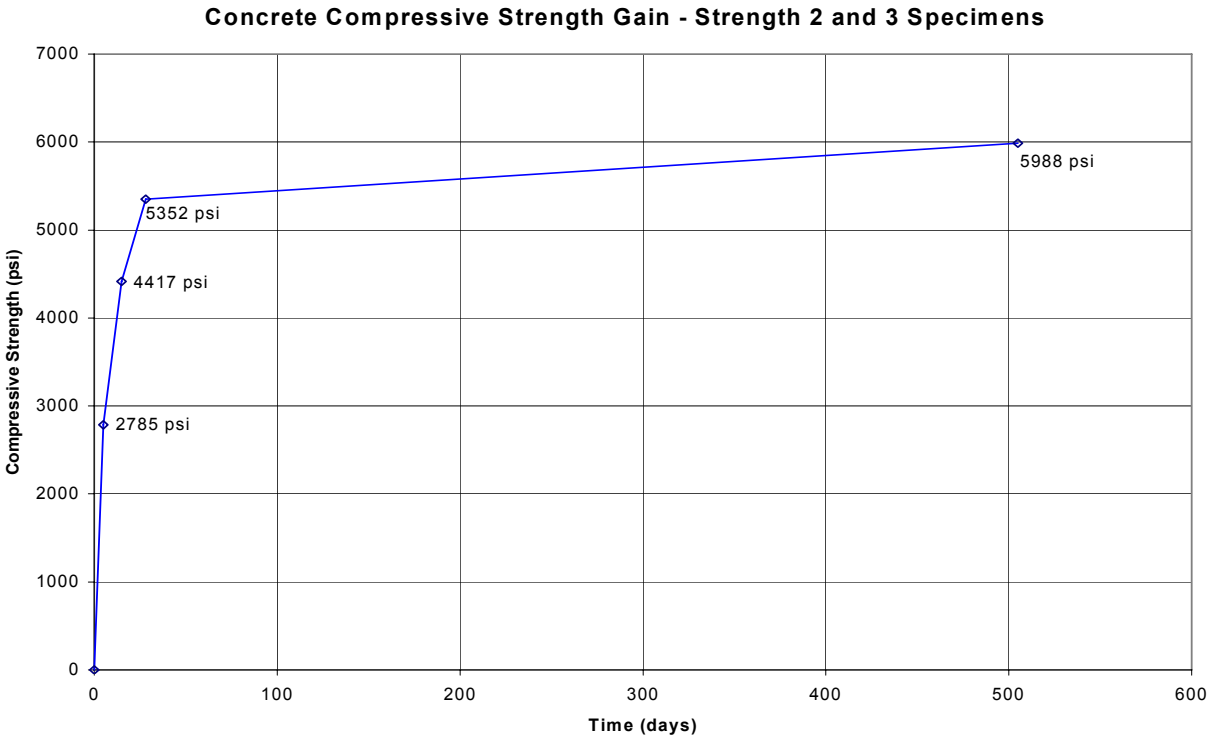


**Figure A.2 – Concrete strength gain plot for the Strength 2 and 3 specimens**

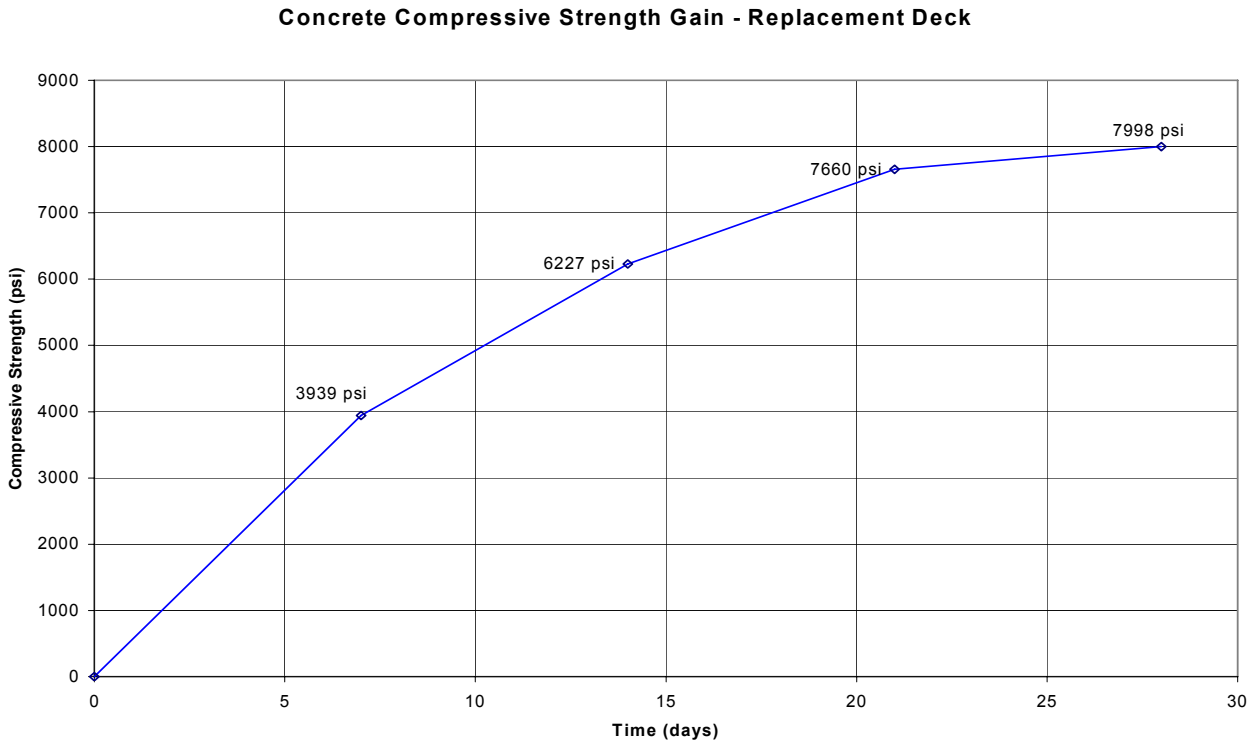


**Figure A.3 – Concrete strength gain plot for the replacement deck in the weigh station**[†]

[†]The replacement deck referred to here is a deck with dimensions and characteristics similar to the Strength 2 and 3 specimens. It was installed in the I-81 weigh station after the Strength 3 specimen was removed from the test bed. The deck was placed for an indefinite period and the strength curve provided here is for information only.

# *Appendix B – Strain Gage Information*

## B.1 – Strain Gage Maps

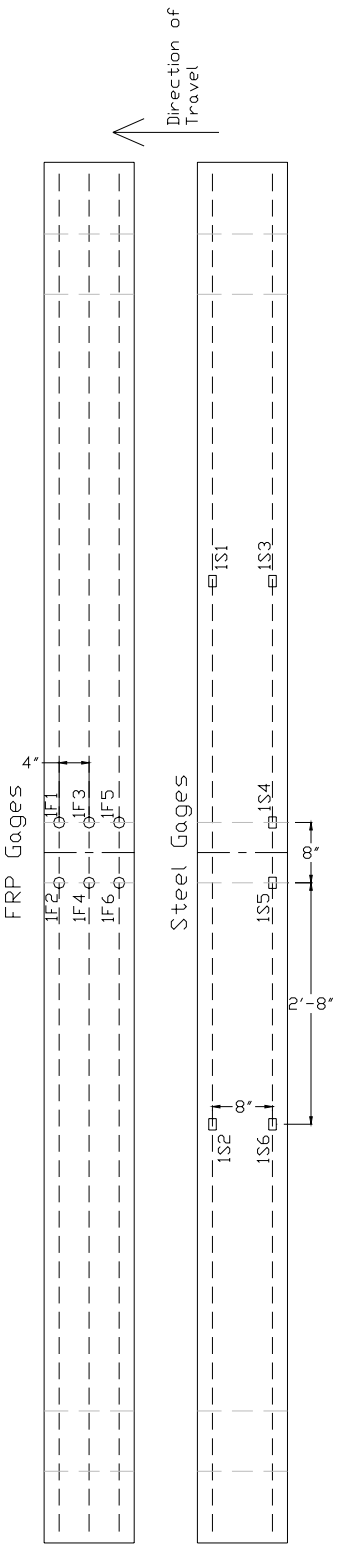


**Figure B.1 – Strain gage map for the 1 ft shear specimen**

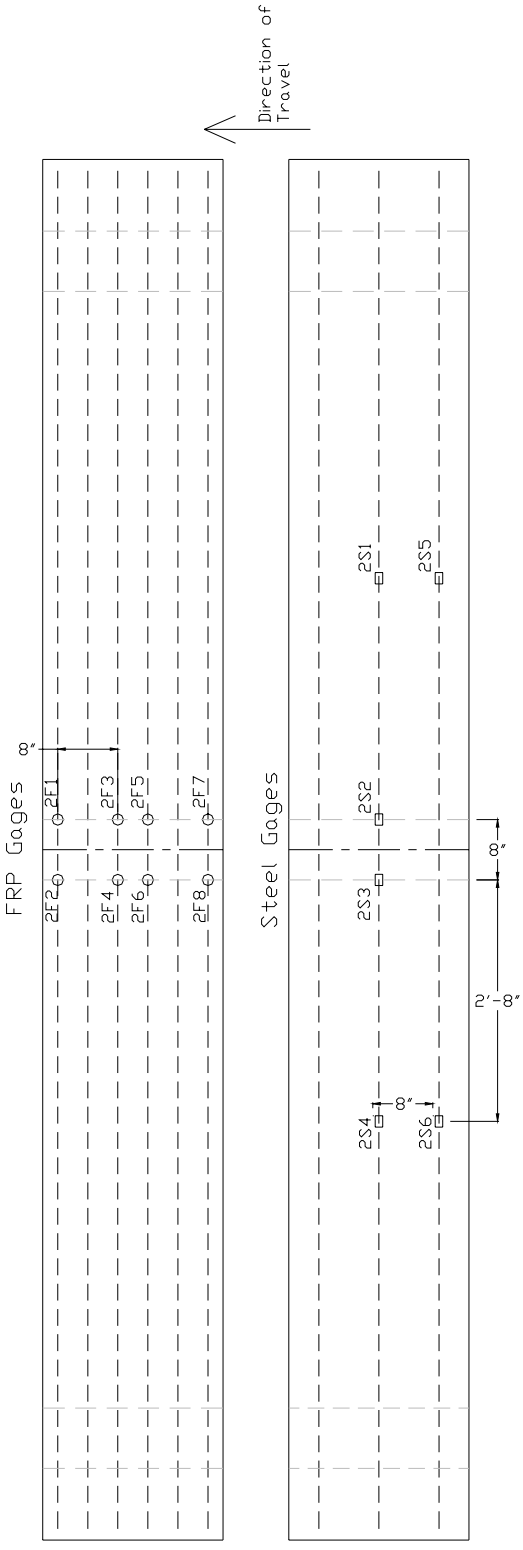


**Figure B.2 – Strain gage map for the 2 ft shear specimen**

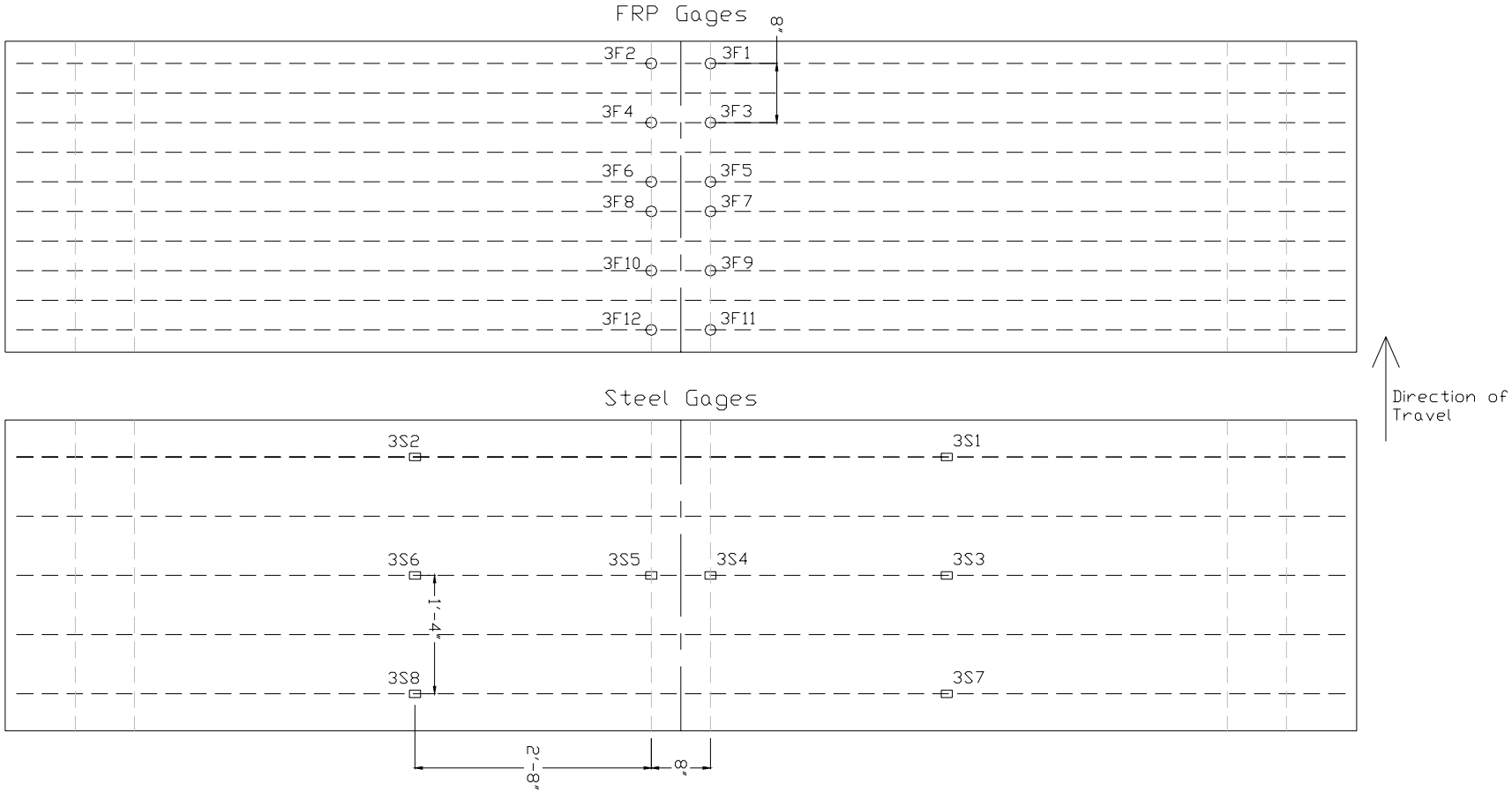


**Figure B.3 – Strain gage map for the 3.5 ft shear specimen**

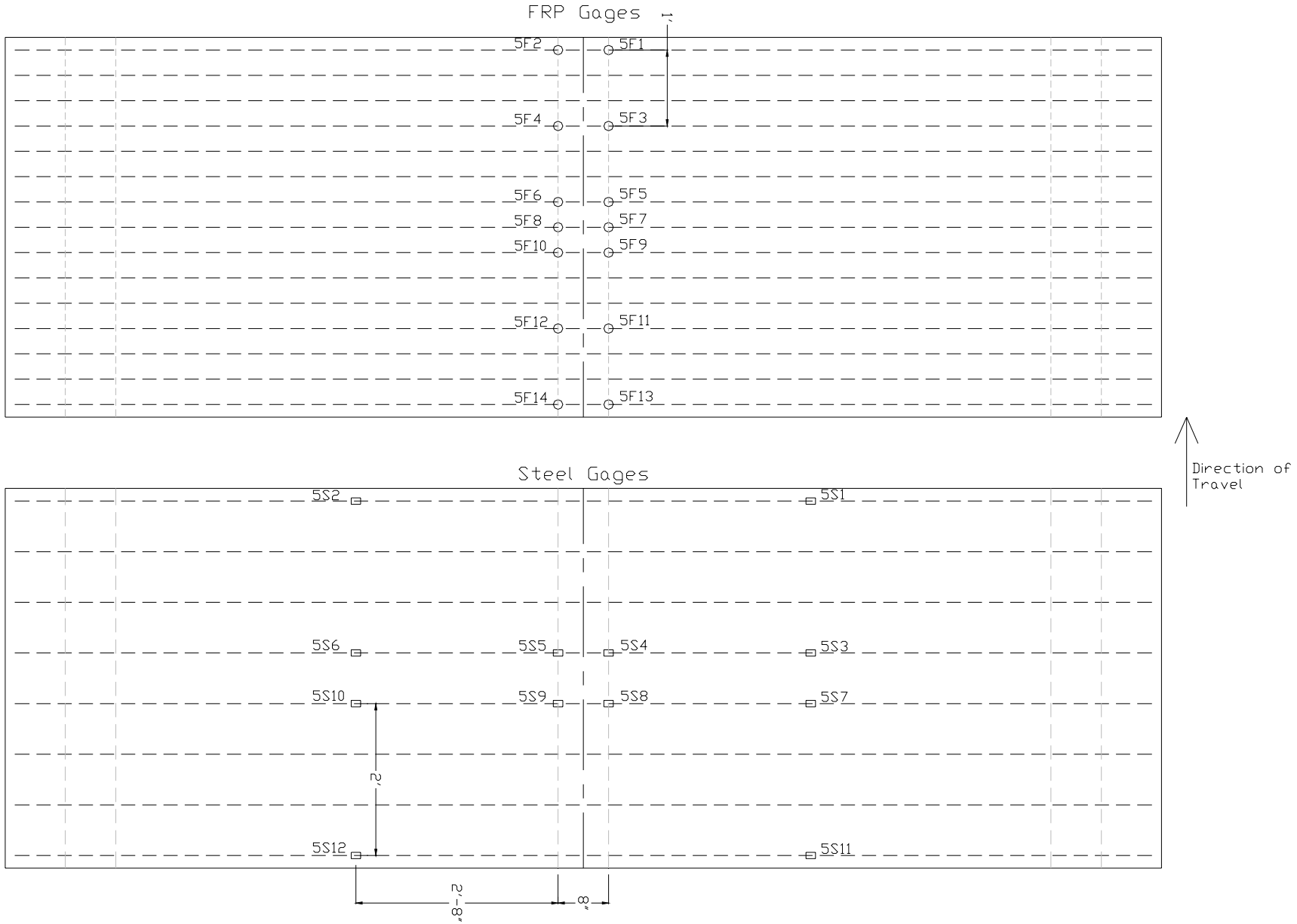


**Figure B.4 – Strain gage map for the 5 ft shear (Strength 1) specimen**

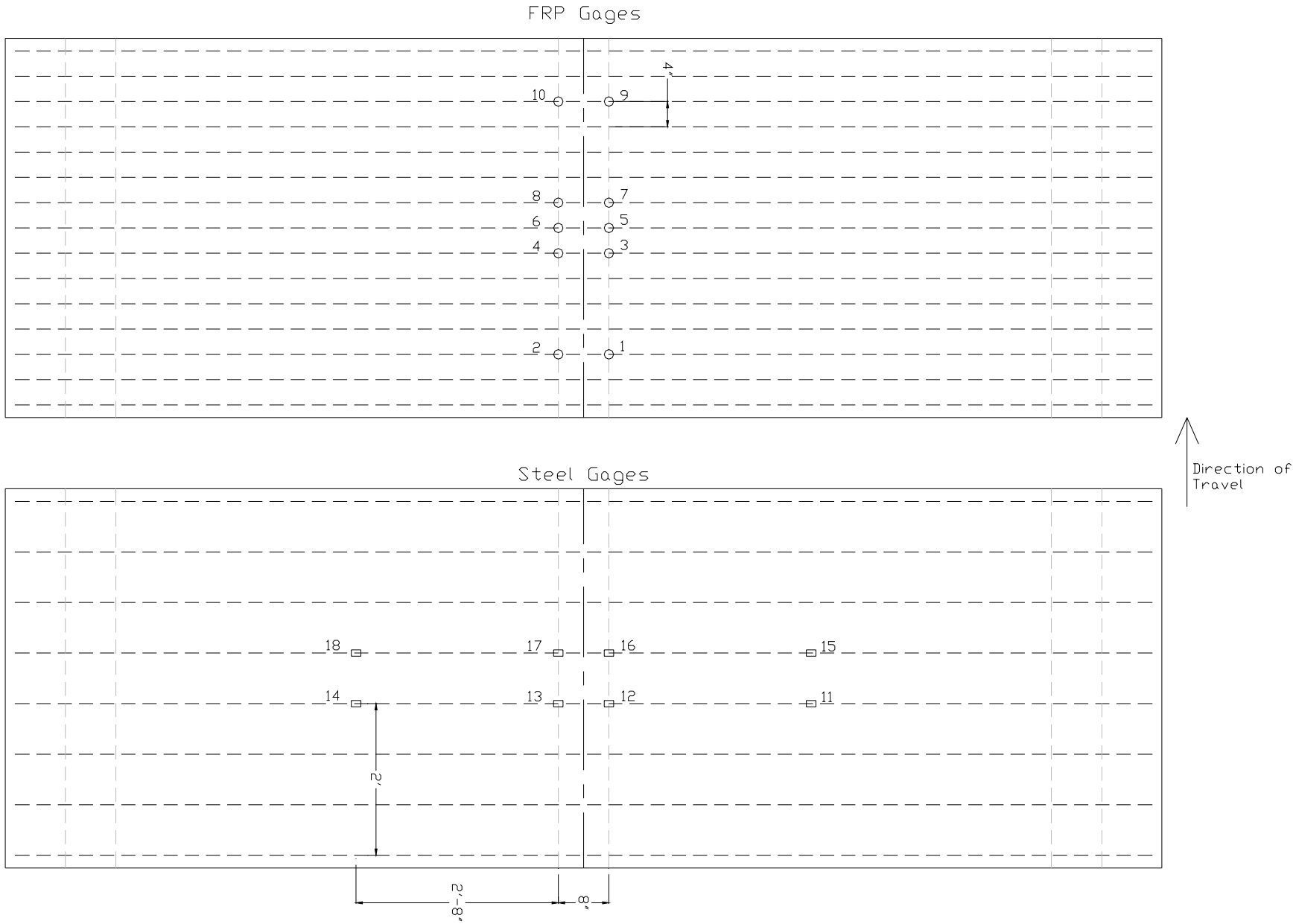


**Figure B.5 – Strain gage map for the Strength 2 and 3 specimens**

## B.2 – Strain Gage Details

*Table B.1 - Strain Gage Types – Shear Decks*

| Deck Width | Bar Type | Gage Designation | Gage Factor | Resistance |
|---|---|---|---|---|
| 1 ft Shear | GFRP | CEA-13-250UW-350 | 2.110 ± 0.5% | 350Ω |
| | Steel | CEA-06-250UN-350 | 2.080 ± 0.5% | 350Ω |
| 2 ft Shear | GFRP | CEA-13-250UN-350 | 2.105 ± 0.5% | 350Ω |
| | Steel | CEA-06-250UN-350 | 2.080 ± 0.5% | 350Ω |
| 3.5 ft Shear | GFRP | CEA-13-250UW-350 | 2.110 ± 0.5% | 350Ω |
| | Steel | CEA-06-250UN-350 | 2.080 ± 0.5% | 350Ω |
| 5 ft Shear | GFRP | CEA-13-250UW-350 | 2.110 ± 0.5% | 350Ω |
| | Steel | CEA-06-250UN-350 | 2.080 ± 0.5% | 350Ω |

*Table B.2 - Strain Gage Types – Strength Degradation Decks*

| Deck ID | Bar Type | Gage Designation | Gage Factor | Resistance |
|---|---|---|---|---|
| Strength 1 | See 5 ft specimen in Shear Deck table above. | | | |
| Strength 2 | GFRP | CEA-13-250UW-350 | 2.110 ± 0.5% | 350Ω |
| | Steel | CEA-06-250UN-350 | 2.080 ± 0.5% | 350Ω |
| Strength 3 | GFRP | CEA-13-250UW-350 | 2.110 ± 0.5% | 350Ω |
| | Steel | CEA-06-250UN-350 | 2.080 ± 0.5% | 350Ω |

# *Appendix C – Strain Gage Installation Details*

The strain gage installation procedure described in this appendix was used for the application of gages to the rebar in the four shear investigation decks. Using a multimeter to measure the electrical resistance of the gages after substantial curing of the concrete, it was found that only one of the 72 gages attached to the bars was inoperable, which translated into an unprecedented 98.6% installation success rate. It is for this reason that the details of the installation are presented here.

***Strain Gage Installation for GFRP Rebar***

A. Specimen Preparation
    1. Sand application sites down with a fine sanding attachment on a Dremel tool to remove the sand impregnations and provide a smooth surface for gage adhesion.
    2. Brush off dust remaining from sanding in step 1.
    3. Apply the conditioner (Vishay MicroMeasurements MCA-1 Conditioner A) to the site with a clean cotton swab and remove with a clean, dry cotton swab. Repeat this step until the cotton swab is clean after wiping off the conditioner.
    4. Apply the neutralizer (Vishay MicroMeasurements Neutralizer 5A) to the site with a clean cotton swab and remove with a clean, dry cotton swab. Allow the site to dry for at least 2 minutes.

B. Gage Preparation and Application
    1. Carefully remove the gage from the plastic sheath with tweezers and lay it down on the clean surface of the plastic strain gage box with the shiny side up.
    2. Lay a 2 in. long piece of cellophane tape over the gage and peal the tape and gage off the box.
    3. Place the tape with gage over the now dry application site on the bar and peel it back so that the bottom of the gage (dull side) is facing upwards and the gage is not in contact with the bar.
    4. Coat the bottom of the gage with a small amount of the catalyst provided in the M-bond 200 installation kit and allow the catalyst two minutes to dry.

5. Apply a drop of adhesive to one end of the gage and press the gage and tape onto the bar from one end of the gage to the other with the thumb so that the adhesive is spread over the entire length of the gage.
6. Immediately apply firm pressure with the thumb over the entire gage for two minutes to increase the temperature for the reaction and ensure complete contact between the gage and the bar.
7. After two minutes, apply another piece of tape perpendicular to the gage, around the bar, to hold pressure on the gage and allow it to sit overnight.
8. Carefully remove the tape and inspect the bond. Remove and replace any gages that are found to have poor bonding to the bar.

C. Attaching the strain gage wires
1. Rub the two terminals of the strain gage with a standard pencil eraser to remove the protective coating and brush off the erasings.
2. Place a small (approximately ¼ in. × ¼ in.) piece of butyl rubber on the bar next to the terminal side of the strain gage; this will help ensure successful waterproofing.
3. Strip the end of the strain gage wires about ¼ in. and lay in the butyl rubber square so that the ends hang over the terminals.
4. Solder the wires to the strain gage terminals. Lead-based solder is easier to work with than lead-free soldier; however, if used, it should only be done in an area with good ventilation and users should avoid the resulting fumes.

D. Waterproofing
1. Brush the gages to clear them of dust.
2. Apply one coat of white acrylic coating (Vishay MicroMeasurements M-Coat D) to the gage terminals and exposed wires.
3. After the M-Coat D has dried, cut a piece of butyl rubber about ½ in. larger then the gage and exposed wiring and lay it over the gage. Press the rubber down firmly so as to create a seal around the gage with the bar.
4. Place a rectangular piece of neoprene rubber pad (Vishay Micromeasurements) that is just slightly smaller than the butyl rubber on the butyl rubber.

5. Starting on the bar about 1 in. before the butyl rubber edge, wrap aluminum tape around the bar so as to seal the gage and the rubber layers. Be sure to press out any wrinkles along the edge of the tape to achieve the best possible seal.
6. Liberally apply nitrile rubber (Vishay MicroMeasurements M-Coat B) along the edges of the aluminum tape so as to seal the tape.
7. Check the resistance of the gage to ensure that the wires have not been disconnected from the gage terminals.

***Strain Gage Installation for Steel Rebar***

A. Specimen Preparation

1. Use an electric handheld grinder to remove the epoxy coating and the rebar deformations to create a site on the bar to apply the gage. Use a fine pad on the grinder to create a smooth surface on the bar. Be sure to wear long sleeves and safety glasses for this portion because the grinder emits a sizeable shower of sparks. Also try to minimize any section loss when grinding the bar.
2. Spray a solvent (Vishay MicroMeasurements CSM1-A Degreaser) on the site and wipe off with a cotton cloth. Repeat this step until there is no greasy residue on the cloth after wiping.
3. Wet the gage site with conditioner (Vishay MicroMeasurements MCA-1 Conditioner A) and use silicon-carbide paper to abrade the area. Wipe dry with a gauze sponge.
4. Apply the conditioner (Vishay MicroMeasurements MCA-1 Conditioner A) to the site with a clean cotton swab and remove with a clean, dry cotton swab. Repeat this step until the cotton swab is clean after wiping off the conditioner.
5. Apply the neutralizer (Vishay MicroMeasurements Neutralizer 5A) to the site with a clean cotton swab and remove with a clean, dry cotton swab. Allow the site to dry for at least 2 minutes.

All other steps for applying gages to steel rebar are identical to the procedure for GFRP rebar.

The procedure above is similar to that used to install the strain gages for the Gills Creek Bridge discussed in Harlan (2004). The two major differences are that the gages for the Gills Creek Bridge were installed at the construction site rather than in a laboratory setting and M-

Line rosin solvent was used after waterproofing step 1 to remove the excess soldering flux. The rosin solvent step was included during the laboratory construction of the final weigh station replacement deck; however, several gages were found to be inoperable after the concrete was placed. There is not enough information to conclude that the gage failures were a result of using the rosin solvent, but the possibility should be considered.

# *Appendix D – Rebar Placement Details*

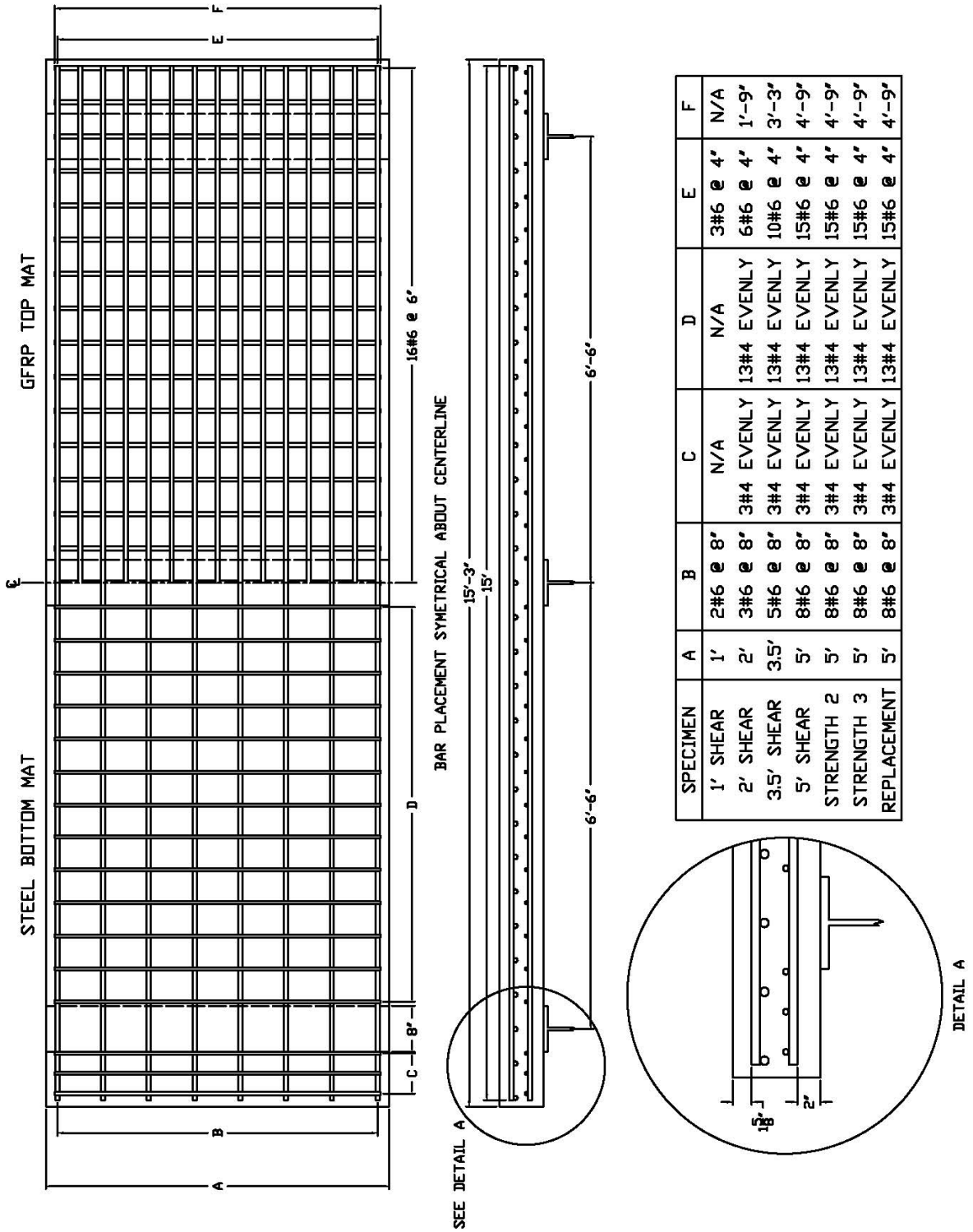


| SPECIMEN | A | B | C | D | E | F |
|---|---|---|---|---|---|---|
| 1' SHEAR | 1' | 2#6 @ 8' | N/A | N/A | 3#6 @ 4' | N/A |
| 2' SHEAR | 2' | 3#6 @ 8' | 3#4 EVENLY | 13#4 EVENLY | 6#6 @ 4' | 1'-9" |
| 3.5' SHEAR | 3.5' | 5#6 @ 8' | 3#4 EVENLY | 13#4 EVENLY | 10#6 @ 4' | 3'-3" |
| 5' SHEAR | 5' | 8#6 @ 8' | 3#4 EVENLY | 13#4 EVENLY | 15#6 @ 4' | 4'-9" |
| STRENGTH 2 | 5' | 8#6 @ 8' | 3#4 EVENLY | 13#4 EVENLY | 15#6 @ 4' | 4'-9" |
| STRENGTH 3 | 5' | 8#6 @ 8' | 3#4 EVENLY | 13#4 EVENLY | 15#6 @ 4' | 4'-9" |
| REPLACEMENT | 5' | 8#6 @ 8' | 3#4 EVENLY | 13#4 EVENLY | 15#6 @ 4' | 4'-9" |

**Figure D.1 – Rebar placement details for research specimens**

# *Appendix E – Recorded DEMEC Data*

***Table E.1 – DEMEC Data – 1 ft Shear***

| Load | Raw DEMEC Measurements | | | | | |
|---|---|---|---|---|---|---|
| | **1** | **2** | **3** | **4** | **5** | **6** |
| 0 kips | 2.753 | 2.754 | 2.734 | 2.759 | 2.752 | 2.751 |
| 2 kips | 2.756 | 2.753 | 2.735 | 2.762 | 2.747 | 2.757 |
| 4 kips | 2.762 | 2.760 | 2.741 | 2.766 | 2.755 | 2.763 |
| 6 kips | 2.764 | 2.763 | 2.742 | 2.772 | 2.754 | 2.765 |
| 7 kips | 2.768 | 2.767 | 2.745 | 2.775 | 2.758 | 2.772 |
| 8 kips | 2.772 | 2.772 | 2.749 | 2.782 | 2.761 | 2.777 |
| 9 kips | 2.778 | 2.778 | 2.752 | 2.790 | 2.767 | 2.785 |
| 10 kips | 2.780 | 2.787 | 2.754 | 2.887 | 2.761 | 2.898 |
| 0 kips | | | | | | |
| 8.1 kips | 2.776 | 2.900 | 2.752 | 2.911 | 2.762 | 2.914 |
| 0 kips | | | | | | |
| 7.6 kips | 2.775 | 2.900 | 2.751 | 2.910 | 2.76 | 2.914 |
| 0 kips | 2.763 | 2.833 | 2.738 | 2.842 | 2.75 | 2.843 |
| 7.6 kips | 2.776 | 2.900 | 2.751 | 2.911 | 2.761 | 2.915 |
| 10 kips | 2.781 | 2.991 | 2.755 | 3.007 | 2.764 | 3.009 |
| 12 kips | 2.783 | 3.107 | 2.757 | 3.126 | 2.768 | 3.126 |
| 14 kips | 2.788 | 3.232 | 2.761 | 3.251 | 2.771 | 3.257 |
| 16 kips | 2.997 | 3.269 | 2.980 | 3.285 | 2.996 | 3.286 |
| 20 kips | 3.284 | 3.426 | 3.263 | 3.440 | 3.278 | 3.440 |

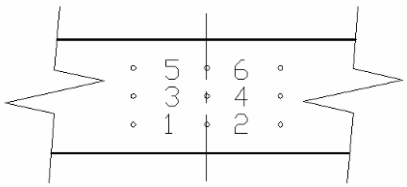


**Figure E. 1 - DEMEC gage length designations for 1 ft shear specimen**

$3.98 \times 10^{-6}$ strain/unit

*Table E.2 – DEMEC Data – 2 ft Shear*

| Load | Raw DEMEC Measurements | | | | | |
|---|---|---|---|---|---|---|
| | 1 | 2 | 3 | 4 | 5 | 6 |
| 0 kips | 2.748 | 2.866 | 2.665 | 2.905 | 2.726 | 2.868 |
| 9 kips | 2.768 | 2.926 | 2.684 | 2.961 | 2.741 | 2.918 |
| 0 kips | 2.754 | 2.875 | 2.672 | 2.919 | 2.733 | 2.880 |
| 4 kips | 2.764 | 2.901 | 2.680 | 2.938 | 2.735 | 2.898 |
| 8 kips | 2.767 | 2.922 | 2.684 | 2.955 | 2.739 | 2.913 |
| 0 kips | 2.757 | 2.874 | 2.675 | 2.916 | 2.732 | 2.879 |
| 8 kips | 2.768 | 2.913 | 2.768 | 2.947 | 2.740 | 2.906 |
| 0 kips | 2.755 | 2.872 | 2.670 | 2.911 | 2.729 | 2.872 |
| 8 kips | 2.770 | 2.917 | 2.685 | 2.954 | 2.745 | 2.912 |
| 0 kips | 2.763 | 2.878 | 2.679 | 2.920 | 2.739 | 2.873 |
| 8 kips | 2.774 | 2.922 | 2.687 | 2.958 | 2.746 | 2.912 |
| 12 kips | 2.770 | 2.941 | 2.687 | 2.971 | 2.747 | 2.927 |
| 16 kips | 2.774 | 2.985 | 2.692 | 3.021 | 2.753 | 2.975 |
| 18 kips | 2.780 | 3.014 | 2.696 | 3.045 | 2.756 | 3.000 |
| 20 kips | 2.802 | 3.102 | 2.721 | 3.125 | 2.777 | 3.079 |
| 22 kips | 3.023 | 3.082 | 2.930 | 3.110 | 2.985 | 3.059 |
| 24 kips | 3.086 | 3.105 | 2.989 | 3.133 | 3.041 | 3.081 |
| 26 kips | 3.161 | 3.158 | 3.062 | 3.185 | 3.114 | 3.133 |
| 28 kips | 3.223 | 3.209 | 3.121 | 3.235 | 3.173 | 3.185 |
| 30 kips | 3.247 | 3.244 | 3.159 | 3.271 | 3.215 | 3.227 |
| 32 kips | 3.327 | 3.307 | 3.221 | 3.330 | 3.271 | 3.226 |
| 34 kips | 3.374 | 3.352 | 3.264 | 3.372 | 3.312 | 3.319 |
| 36 kips | 3.409 | 3.385 | 3.301 | 3.407 | 3.348 | 3.357 |
| 38 kips | 3.459 | 3.440 | 3.351 | 3.461 | 3.400 | 3.404 |
| 40 kips | 3.508 | 3.485 | 3.398 | 3.502 | 3.442 | 3.443 |
| 44.2 kips | 3.620 | 3.590 | 3.505 | 3.600 | 3.549 | 3.540 |

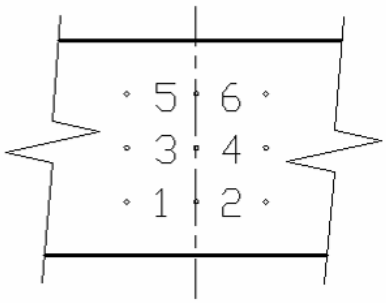


**Figure E.2 – DEMEC gage length designations for 2 ft Shear specimen**

$3.98 \times 10^{-6}$ strain/unit

*Table E.3 – DEMEC Data – 3.5 ft Shear*

| Load | Raw DEMEC Measurements | | | | | | | |
|---|---|---|---|---|---|---|---|---|
| | 1 | 2 | 3 | 4 | 5 | 6 | 7 | 8 |
| 0 kips | 2.747 | 2.747 | 2.763 | 2.730 | 2.727 | 2.720 | 2.720 | 2.746 |
| 2 kips | 2.752 | 2.744 | 2.766 | 2.733 | 2.733 | 2.721 | 2.725 | 2.747 |
| 4 kips | 2.749 | 2.740 | 2.764 | 2.731 | 2.728 | 2.725 | 2.724 | 2.748 |
| 6 kips | 2.756 | 2.747 | 2.771 | 2.742 | 2.734 | 2.730 | 2.727 | 2.745 |
| 8 kips | 2.756 | 2.749 | 2.773 | 2.743 | 2.737 | 2.731 | 2.732 | 2.751 |
| 10 kips | 2.760 | 2.751 | 2.776 | 2.744 | 2.738 | 2.735 | 2.734 | 2.752 |
| 11 kips | 2.760 | 2.751 | 2.776 | 2.749 | 2.739 | 2.736 | 2.736 | 2.754 |
| 12 kips | 2.762 | 2.755 | 2.778 | 2.748 | 2.742 | 2.734 | 2.734 | 2.755 |
| 14 kips | 2.765 | 2.755 | 2.781 | 2.750 | 2.744 | 2.740 | 2.738 | 2.757 |
| 15 kips | 2.768 | 2.757 | 2.782 | 2.752 | 2.743 | 2.741 | 2.739 | 2.758 |
| 17 kips | 2.770 | 2.759 | 2.783 | 2.759 | 2.741 | 2.744 | 2.739 | 2.761 |
| 18 kips | 2.776 | 2.757 | 2.783 | 2.760 | 2.750 | 2.745 | 2.741 | 2.761 |
| 19 kips | 2.775 | 2.759 | 2.781 | 2.762 | 2.752 | 2.746 | 2.741 | 2.764 |
| 21 kips | 2.779 | 2.764 | 2.784 | 2.767 | 2.751 | 2.754 | 2.744 | 2.767 |
| 22 kips | 2.780 | 2.767 | 2.782 | 2.779 | 2.753 | 2.762 | 2.744 | 2.767 |
| 23 kips | 2.769 | 2.768 | 2.778 | 2.874 | 2.756 | 2.774 | 2.748 | 2.773 |
| 0 kips | | | | | | | | |
| 23 kips | 2.764 | 2.911 | 2.778 | 2.910 | 2.745 | 2.885 | 2.739 | 2.880 |
| 24 kips | 2.769 | 2.922 | 2.780 | 2.920 | 2.746 | 2.897 | 2.738 | 2.892 |
| 26 kips | 2.759 | 2.943 | 2.781 | 2.938 | 2.752 | 2.911 | 2.741 | 2.904 |
| 0 kips | | | | | | | | |
| 26 kips | 2.773 | 2.953 | 2.781 | 2.951 | 2.752 | 2.921 | 2.740 | 2.912 |
| 0 kips | | | | | | | | |
| 26 kips | 2.770 | 2.957 | 2.778 | 2.955 | 2.751 | 2.927 | 2.741 | 2.920 |
| 0 kips | 2.759 | 2.870 | 2.768 | 2.863 | 2.735 | 2.847 | 2.729 | 2.855 |
| 26 kips | 2.770 | 2.959 | 2.780 | 2.960 | 2.749 | 2.932 | 2.740 | 2.924 |
| 28 kips | 2.772 | 2.971 | 2.779 | 2.970 | 2.752 | 2.944 | 2.742 | 2.935 |
| 30 kips | 2.772 | 2.989 | 2.782 | 2.990 | 2.754 | 2.961 | 2.743 | 2.950 |
| 34 kips | 2.773 | 3.086 | 2.787 | 3.083 | 2.758 | 3.051 | 2.746 | 3.032 |
| 38 kips | 2.775 | 3.140 | 2.790 | 3.122 | 2.761 | 3.096 | 2.749 | 3.077 |
| 40 kips | 2.780 | 3.198 | 2.797 | 3.187 | 2.764 | 3.154 | 2.753 | 3.125 |
| 42 kips | 2.787 | 3.237 | 2.805 | 3.223 | 2.767 | 3.190 | 2.752 | 3.159 |
| 46 kips | 3.087 | 3.272 | 3.084 | 3.285 | 3.029 | 3.267 | 3.006 | 3.233 |

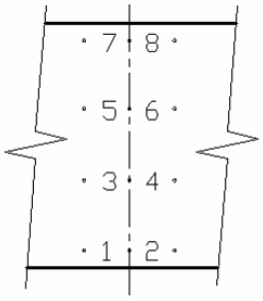


**Figure E.3 - DEMEC gage length designations for 3.5 ft shear specimen**

$3.98 \times 10^{-6}$ strain/unit

*Table E.4 – DEMEC Data – 5 ft Shear / Strength 1*

| Load | Raw DEMEC Measurements | | | | | | | | | |
|---|---|---|---|---|---|---|---|---|---|---|
| | 1 | 2 | 3 | 4 | 5 | 6 | 7 | 8 | 9 | 10 |
| 4 kips | 2.759 | 2.741 | 2.749 | 2.730 | 2.756 | 2.784 | 2.739 | 2.776 | 2.770 | 2.918 |
| 6 kips | 2.762 | 2.747 | 2.750 | 2.736 | 2.754 | 2.787 | 2.739 | 2.773 | 2.769 | 2.919 |
| 8 kips | 2.763 | 2.748 | 2.753 | 2.738 | 2.758 | 2.791 | 2.741 | 2.777 | 2.770 | 2.922 |
| 10 kips | 2.765 | 2.747 | 2.755 | 2.739 | 2.759 | 2.790 | 2.744 | 2.777 | 2.770 | 2.922 |
| 12 kips | 2.765 | 2.750 | 2.754 | 2.739 | 2.761 | 2.790 | 2.745 | 2.778 | 2.772 | 2.923 |
| 14 kips | 2.765 | 2.752 | 2.755 | 2.740 | 2.763 | 2.791 | 2.747 | 2.780 | 2.773 | 2.925 |
| 16 kips | 2.768 | 2.754 | 2.757 | 2.739 | 2.767 | 2.793 | 2.748 | 2.785 | 2.776 | 2.926 |
| 18 kips | 2.768 | 2.755 | 2.758 | 2.744 | 2.768 | 2.795 | 2.750 | 2.787 | 2.777 | 2.927 |
| 20 kips | 2.770 | 2.755 | 2.758 | 2.743 | 2.769 | 2.795 | 2.750 | 2.786 | 2.778 | 2.928 |
| 22 kips | 2.770 | 2.757 | 2.760 | 2.745 | 2.770 | 2.795 | 2.748 | 2.788 | 2.780 | 2.930 |
| 24 kips | 2.772 | 2.757 | 2.763 | 2.745 | 2.770 | 2.798 | 2.753 | 2.790 | 2.781 | 2.932 |
| 25 kips | 2.771 | 2.758 | 2.761 | 2.746 | 2.773 | 2.798 | 2.754 | 2.790 | 2.783 | 2.933 |
| 26 kips | 2.772 | 2.760 | 2.763 | 2.750 | 2.773 | 2.798 | 2.756 | 2.793 | 2.783 | 2.933 |
| 27 kips | 2.772 | 2.761 | 2.763 | 2.751 | 2.773 | 2.799 | 2.756 | 2.794 | 2.783 | 2.933 |
| 29 kips | 2.773 | 2.761 | 2.763 | 2.750 | 2.776 | 2.801 | 2.758 | 2.794 | 2.784 | 2.934 |
| 30 kips | 2.774 | 2.762 | 2.764 | 2.752 | 2.775 | 2.802 | 2.761 | 2.797 | 2.784 | 2.932 |
| 31 kips | 2.775 | 2.764 | 2.765 | 2.752 | 2.777 | 2.803 | 2.763 | 2.798 | 2.787 | 2.937 |
| 33 kips | 2.775 | 2.764 | 2.766 | 2.754 | 2.776 | 2.804 | 2.763 | 2.800 | 2.789 | 2.938 |
| 35 kips | 2.775 | 2.765 | 2.766 | 2.754 | 2.778 | 2.805 | 2.764 | 2.800 | 2.791 | 2.939 |
| 36 kips | 2.778 | 2.767 | 2.767 | 2.755 | 2.779 | 2.808 | 2.767 | 2.800 | 2.791 | 2.941 |
| 38 kips | 2.775 | 2.768 | 2.769 | 2.757 | 2.781 | 2.809 | 2.767 | 2.804 | 2.793 | 2.942 |
| 39 kips | 2.777 | 2.770 | 2.770 | 2.758 | 2.781 | 2.810 | 2.770 | 2.807 | 2.795 | 2.943 |
| 40 kips | 2.779 | 2.772 | 2.770 | 2.759 | 2.783 | 2.811 | 2.772 | 2.807 | 2.795 | 2.947 |
| 0 kips | 2.770 | 2.759 | 2.760 | 2.750 | 2.773 | 2.808 | 2.758 | 2.804 | 2.797 | 2.926 |
| 38 kips | 2.781 | 2.774 | 2.772 | 2.762 | 2.787 | 2.825 | 2.776 | 2.832 | 2.821 | 2.950 |
| 0 kips | | | | | | | | | | |
| 38 kips | 2.782 | 2.773 | 2.772 | 2.761 | 2.787 | 2.825 | 2.775 | 2.830 | 2.821 | 2.948 |
| 0 kips | 2.771 | 2.762 | 2.762 | 2.752 | 2.774 | 2.810 | 2.761 | 2.811 | 2.801 | 2.932 |
| 38 kips | 2.782 | 2.775 | 2.774 | 2.764 | 2.790 | 2.828 | 2.777 | 2.832 | 2.822 | 2.950 |
| 40 kips | 2.782 | 2.777 | 2.774 | 2.764 | 2.792 | 2.832 | 2.780 | 2.836 | 2.826 | 2.953 |
| 45 kips | 2.783 | 2.777 | 2.778 | 2.767 | 2.793 | 2.837 | 2.784 | 2.847 | 2.854 | 2.948 |
| 55 kips | 2.778 | 2.994 | 2.783 | 2.980 | 2.824 | 3.030 | 2.859 | 2.966 | 3.041 | 2.947 |
| 60 kips | 2.784 | 3.051 | 2.789 | 3.038 | 2.836 | 3.084 | 2.886 | 3.009 | 3.101 | 2.950 |
| 70 kips | 2.787 | 3.321 | 3.034 | 3.081 | 3.037 | 3.179 | 2.963 | 3.223 | 3.202 | 3.116 |
| 75 kips | 2.787 | 3.418 | 3.106 | 3.115 | 3.103 | 3.225 | 3.000 | 3.303 | 3.250 | 3.184 |
| 80 kips | 2.793 | 3.482 | 3.158 | 3.138 | 3.168 | 3.248 | 3.061 | 3.333 | 3.307 | 3.216 |
| 85 kips | 3.007 | 3.530 | 3.401 | 3.158 | 3.406 | 3.273 | 3.293 | 3.355 | 3.549 | 3.232 |
| 90 kips | 3.054 | 3.567 | 3.463 | 3.186 | 3.466 | 3.308 | 3.345 | 3.402 | 3.611 | 3.267 |
| 95 kips | 3.096 | 3.601 | 3.515 | 3.214 | 3.513 | 3.339 | 3.378 | 3.435 | 3.648 | 3.287 |
| 105 kips | 3.191 | 3.722 | 3.653 | 3.302 | 3.659 | 3.440 | 3.504 | 3.556 | 3.801 | 3.364 |

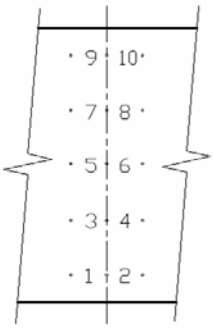


**Figure E.4 - DEMEC gage length designations for 5 ft shear / Strength 1 specimen**

$3.98 \times 10^{-6}$ strain/unit

***Table E.5 – DEMEC Data – Strength 2***

| Load | Raw DEMEC Measurements | | | | | | | |
|---|---|---|---|---|---|---|---|---|
| | **1** | **2** | **3** | **4** | **5** | **6** | **7** | **8** |
| 0 kips | 2.623 | 2.747 | 2.753 | 2.769 | 2.741 | 2.763 | 2.788 | 2.881 |
| 5 kips | 2.620 | 2.744 | 2.751 | 2.768 | 2.748 | 2.762 | 2.787 | 2.884 |
| 10 kips | 2.619 | 2.745 | 2.753 | 2.767 | 2.749 | 2.767 | 2.787 | 2.886 |
| 15 kips | 2.616 | 2.741 | 2.751 | 2.765 | 2.750 | 2.765 | 2.787 | 2.886 |
| 20 kips | 2.622 | 2.745 | 2.758 | 2.774 | 2.747 | 2.757 | 2.794 | 2.889 |
| 25 kips | 2.622 | 2.747 | 2.762 | 2.779 | 2.762 | 2.780 | 2.798 | 2.898 |
| 30 kips | 2.630 | 2.752 | 2.768 | 2.785 | 2.773 | 2.788 | 2.806 | 2.905 |
| 35 kips | 2.633 | 2.756 | 2.775 | 2.785 | 2.777 | 2.792 | 2.812 | 2.911 |
| 37.8 kips | 2.641 | 2.763 | 2.782 | 2.796 | 2.785 | 2.803 | 2.818 | 2.912 |
| 0 kips | | | | | | | | |
| 37.8 kips | 2.647 | 2.764 | 2.784 | 2.798 | 2.787 | 2.805 | 2.821 | 2.914 |
| 0 kips | | | | | | | | |
| 37.8 kips | 2.638 | 2.761 | 2.782 | 2.797 | 2.783 | 2.804 | 2.822 | 2.914 |
| 0 kips | 2.625 | 2.748 | 2.759 | 2.779 | 2.758 | 2.777 | 2.796 | 2.894 |
| 37.8 kips | 2.641 | 2.762 | 2.782 | 2.793 | 2.787 | 2.808 | 2.822 | 2.917 |
| 45 kips | 2.650 | 2.770 | 2.794 | 2.810 | 2.802 | 2.832 | 2.856 | 2.932 |
| 50 kips | 2.656 | 2.970 | 2.795 | 3.076 | 2.784 | 3.170 | 2.808 | 3.280 |
| 60 kips | 2.672 | 3.150 | 2.803 | 3.258 | 2.786 | 3.359 | 2.807 | 3.457 |
| 70 kips | 2.684 | 3.316 | 2.822 | 3.443 | 2.783 | 3.557 | 2.806 | 3.643 |
| 80 kips | 3.088 | 3.361 | 3.238 | 3.498 | 3.132 | 3.685 | 2.792 | 3.771 |
| 90 kips | 3.192 | 3.449 | 3.530 | 3.597 | 3.258 | 3.769 | 2.790 | 3.845 |
| 100 kips | 3.289 | 3.556 | 3.459 | 3.714 | 3.358 | 3.889 | 2.788 | 3.950 |
| 120 kips | 3.507 | 3.809 | 3.711 | 4.009 | 3.531 | 4.042 | 2.784 | 4.070 |
| 140 kips | 3.710 | 3.997 | 3.933 | 4.196 | 3.703 | 4.274 | 2.781 | 4.189 |
| 160 kips | 3.904 | 4.138 | 4.142 | 4.321 | 3.958 | 4.451 | 2.777 | 4.360 |
| 180 kips | 4.150 | 4.302 | 4.436 | 4.477 | 4.226 | 4.577 | 2.771 | 4.510 |
| 200 kips | 4.299 | 4.487 | 4.916 | 4.657 | 4.582 | 4.716 | 2.763 | 4.685 |

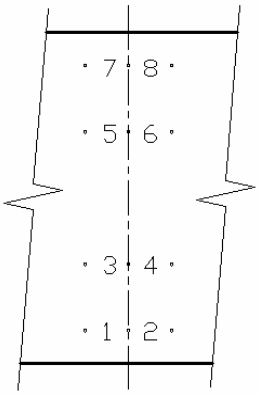


**Figure E.5 - DEMEC gage length designations for Strength 2 specimen**

$3.98 \times 10^{-6}$ strain/unit

***Table E.6 – DEMEC Data – Strength 3***

| Load | Raw DEMEC Measurements | | | | | | | |
|---|---|---|---|---|---|---|---|---|
| | **1** | **2** | **3** | **4** | **5** | **6** | **7** | **8** |
| 0 kips | 2.935 | 2.565 | 2.547 | 3.046 | 2.719 | 3.504 | 4.129 | 1.008 |
| 10 kips | 2.956 | 2.593 | 2.553 | 3.094 | 2.724 | 3.561 | 4.138 | 1.058 |
| 20 kips | 3.002 | 2.625 | 2.558 | 3.204 | 2.726 | 3.641 | 4.146 | 1.13 |
| 30 kips | 3.033 | 2.676 | 2.561 | 3.283 | 2.732 | 3.743 | 4.155 | 1.223 |
| 38 kips | 3.081 | 2.702 | 2.564 | 3.366 | 2.735 | 3.818 | 4.159 | 1.291 |
| 0 kips | | | | | | | | |
| 38 kips | 3.103 | 2.71 | 2.564 | 3.376 | 2.736 | 3.832 | 4.16 | 1.306 |
| 0 kips | | | | | | | | |
| 38 kips | 3.091 | 2.725 | 2.563 | 3.376 | 2.734 | 3.826 | 4.158 | 1.302 |
| 0 kips | 2.95 | 2.571 | 2.551 | 3.068 | 2.72 | 3.522 | 4.131 | 1.026 |
| 38 kips | 3.088 | 2.722 | 2.563 | 3.37 | 2.734 | 3.824 | 4.158 | 1.299 |
| 50 kips | 3.131 | 2.756 | 2.569 | 3.489 | 2.743 | 3.933 | 4.172 | 1.395 |
| 60 kips | 3.16 | 2.803 | 2.575 | 3.583 | 2.755 | 4.016 | 4.188 | 1.467 |
| 70 kips | 3.201 | 2.872 | 2.584 | 3.678 | 2.767 | 4.103 | 4.208 | 1.539 |
| 80 kips | 3.264 | 2.909 | 2.595 | 3.779 | 2.784 | 4.188 | 4.235 | 1.604 |
| 90 kips | 3.272 | 2.913 | 2.615 | 3.888 | 2.816 | 4.282 | 4.273 | 1.668 |
| 100 kips | 3.419 | 3.026 | 2.801 | 3.918 | 2.926 | 4.354 | 4.352 | 1.735 |
| 120 kips | 3.77 | 3.113 | 3.108 | 4.045 | 3.207 | 4.508 | 4.465 | 1.847 |
| 140 kips | 3.958 | 3.044 | 3.326 | 4.293 | 3.449 | 4.738 | 4.553 | 1.969 |
| 160 kips | 4.214 | - | 3.593 | 4.612 | 3.703 | 5.086 | 4.672 | 2.014 |
| 180 kips | 4.494 | - | 4.252 | 4.992 | 3.98 | 5.466 | 4.855 | 2.088 |

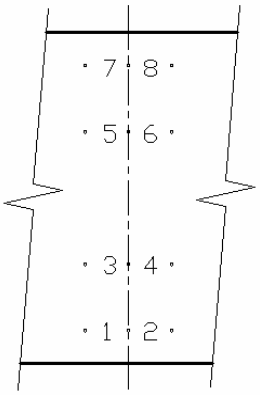


**Figure E.6 - DEMEC gage length designations for Strength 3 specimen**

$3.98 \times 10^{-6}$ strain/unit

# *Appendix F – Weather Data*

The weather data presented in this appendix is from NOAA preliminary local climatology data records available publicly on the internet at http://www.erh.noaa.gov. The station used was ROANOKE (Latitude 37˚19'N, Longitude 79˚58'W), which was the closest available weather station to the Troutville, VA, weigh station.

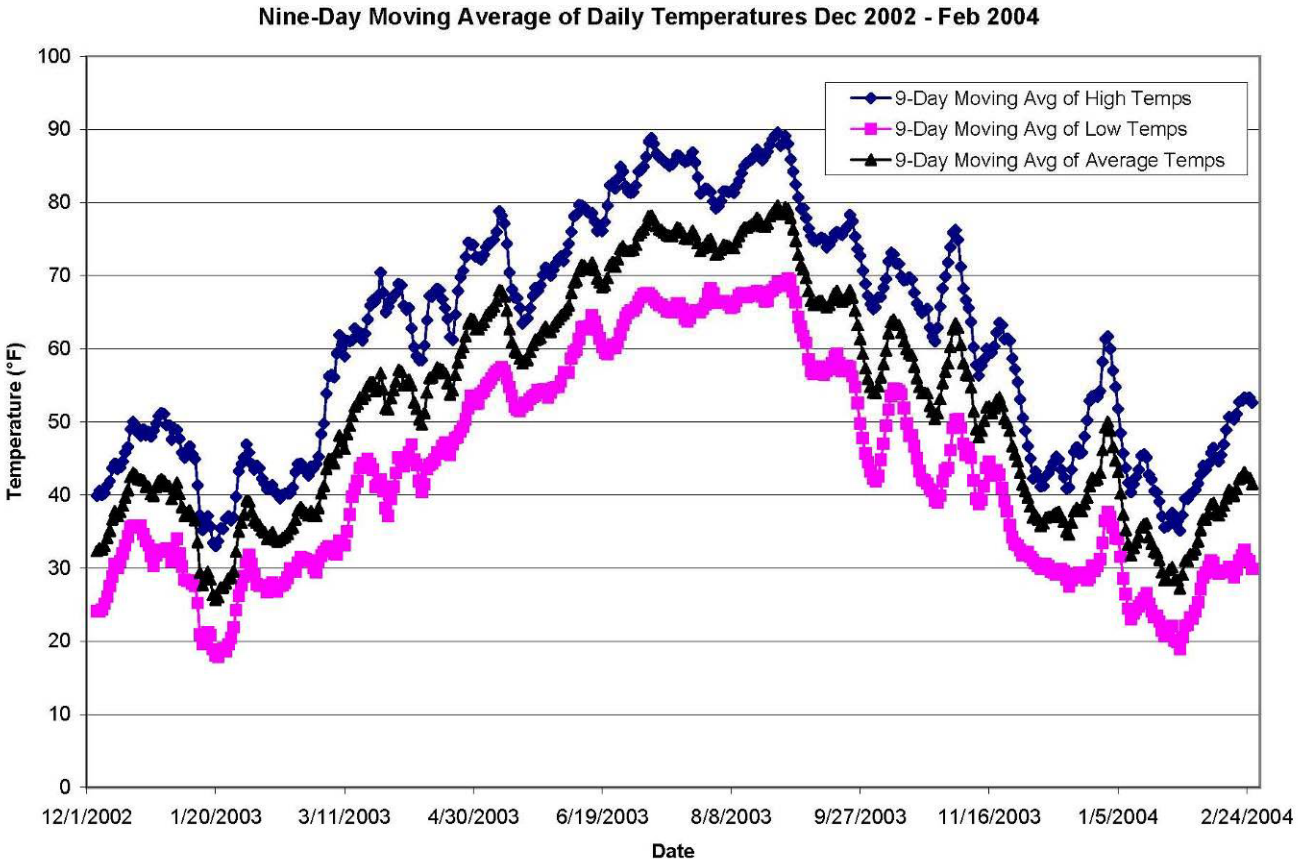


**Figure F.1 - Nine-day moving average of daily temperatures for Roanoke, VA (Dec 2002 - Feb 2004).**

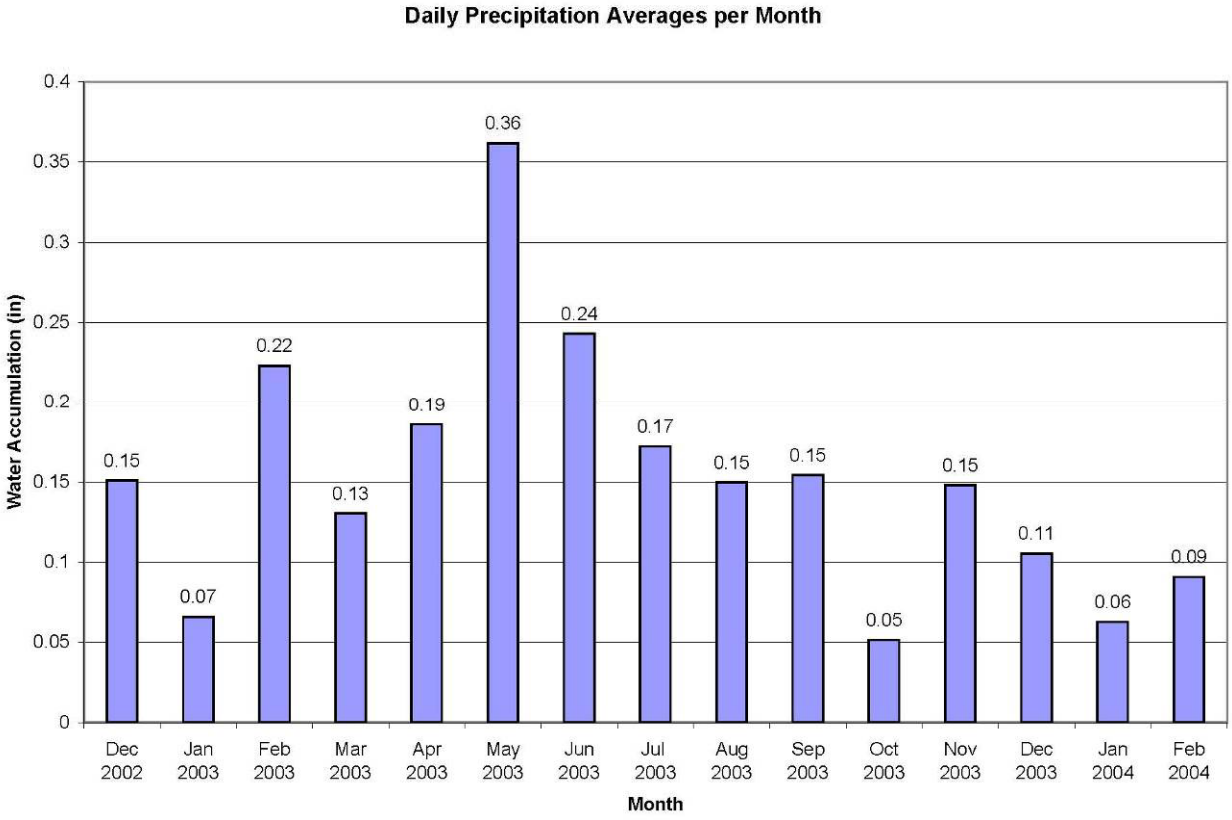


**Figure F.2 - Monthly daily precipitation averages for Roanoke, VA (Dec 2002 - Feb 2004).**

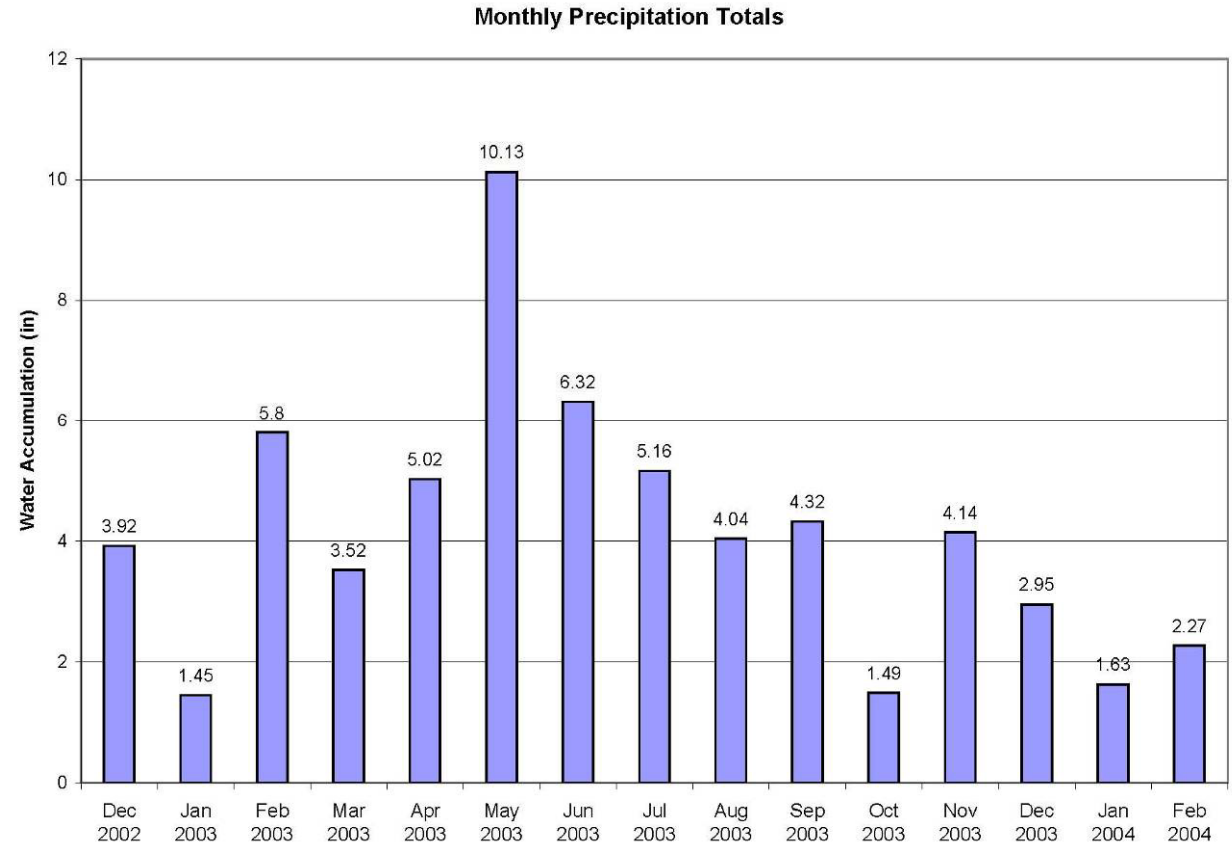


**Figure F.3 - Total monthly precipitation for Roanoke, VA (Dec 2002 - Feb 2004)**

# *Appendix G – Sample Calculations*

The following sample calculations are presented for the "pristine" 1 ft shear specimen and were evaluated using MathCAD. All inputs and assumptions are listed with each example.

## G.1 – Shear Strength Calculation according to ACI 440

1. Nominal Moment Capacity of GFRP-Reinforced Deck

$E_f := 6100$ Modulus of elastiticity of GFRP bar according to tests, ksi

$A_{bar} := \left(\frac{.75}{2}\right)^2 \cdot \pi$ $A_{bar} = 0.442$ Area of a No. 6 bar, in^2

$A_f := A_{bar} \cdot 3$ $A_f = 1.325$ Area of FRP reinforcement in a 1' width of deck, in^2

$h := 7 + \frac{5}{8}$ Total thickness of deck

$f_c := 6$ concrete strength, ksi

$\beta_1 := 1.05 - .05 \cdot f_c$ $\beta_1 = 0.75$

$b := 12$ section width, in

$d := 5.625$ depth to bar, in

$f_{fu} := .8 \cdot 90$ guaranteed maximum tensile strength, ksi

$\rho_f := \frac{A_f}{12 \cdot d}$ FRP reinforcement ratio

Solve for a:

$$.85 f_c \cdot a^2 - \beta_1 E_f \cdot .003 \cdot d^2 \cdot \rho_f + E_f \cdot .003 \cdot \rho_f \cdot d \cdot a = 0 \text{ solve }, a \rightarrow \begin{pmatrix} -1.5062793567639512445 \\ 1.1099709085054961692 \end{pmatrix}$$

$a := 1.110$ From calculation entered above, in

Check that $e_f$ is less than $e_{fu}$

$c := \frac{a}{\beta_1}$ $c = 1.48$

$e_f := .003 \frac{(d - c)}{c}$ $e_f = 8.402 \times 10^{-3}$ FRP Strain in Deck

$e_{fu} := \frac{f_{fu}}{E_f}$ $e_{fu} = 0.012$ Ultimate strain

$e_f < e_{fu} = 1$ OK !

$M_n := .85 f_c \cdot a \cdot b \cdot \left(d - \frac{a}{2}\right)$ $M_n = 344.415$ Moment capacity, kip-in

$\frac{M_n}{12} = 28.701$ Moment capacity, kip-ft

2. Design of Steel Alternative

$f_y := 60$ Yield strength of steel bar, ksi

$E_s := 29000$ Modulus of Elasticity of Steel, ksi

$$A_s := \frac{M_n}{f_y \cdot \left(d - \frac{a}{2}\right)} \qquad A_s = 1.132$$ Initial area of steel calculation, $in^2$

$$a_{steel} := \frac{\left(f_y \cdot A_s\right)}{.85 \cdot f_c \cdot b} \qquad a_{steel} = 1.11$$ Recalculated a, in

Check that steel yields before concrete crushes

$$c_{steel} := \frac{a_{steel}}{\beta_1} \qquad c_{steel} = 1.48$$ Depth of compression zone

$$\varepsilon_s := .003 \frac{\left(d - c_{steel}\right)}{c_{steel}} \qquad \varepsilon_s = 8.402 \times 10^{-3}$$ Steel strain at max concrete strain of 0.003, in/in

$$\varepsilon_y := \frac{f_y}{29000} \qquad \varepsilon_y = 2.069 \times 10^{-3}$$ Yield strain of steel, in/in

$\varepsilon_s > \varepsilon_y = 1$ Steel yields before concrete crushes

Calculate actual $M_n$ with new a and As

$$M_{nsteel} := A_s \cdot f_y \cdot \left(d - \frac{a_{steel}}{2}\right) \qquad M_{nsteel} = 344.415$$ kip/in

3. Calculation of Shear Strength according to ACI 440.1R-03

$$V_c := 2 \cdot b \cdot d \cdot \frac{\sqrt{f_c \cdot 1000}}{1000} \qquad V_c = 10.457$$ Shear strength of concrete, kips

$$V_{cf} := \left[\frac{\left(A_f \cdot E_f\right)}{\left(A_s \cdot E_s\right)}\right] V_c \qquad V_{cf} = 2.575$$ Shear strength of FRP reinforced deck, kips

## G.2 – Shear Strength Calculation according to the Frosch Method

$b_w := 12$ Width of deck cross-section, in

$d := 5.625$ Effective depth, in

$E_r := 6100$ Modulus of elastiticity of GFRP bar according to tests, ksi

$f_c := 6000$ concrete strength, psi

$E_c := 57\sqrt{f_c}$ Modulus of elasticity of concrete, ksi

$E_c = 4.415 \times 10^3$ ksi

$$n := \frac{E_r}{E_c}$$

$n = 1.382$ modular ratio

$A_{bar} := \left(\frac{.75}{2}\right)^2 \cdot \pi$ $A_{bar} = 0.442$ Area of a No. 6 bar, in^2

$A_r := A_{bar} \cdot 3$ $A_r = 1.325$ Area of FRP reinforcement in a 1' width of deck, in^2

$$\rho := \frac{A_r}{12 \cdot d}$$ $\rho = 0.02$ reinforcement ratio

$k := \sqrt{2 \cdot \rho \cdot n + (\rho \cdot n)^2} - \rho \cdot n$ $k = 0.207$

$c := k \cdot d$ $c = 1.166$ cracked transformed section neutral axis dpth, in

$V_c := \frac{5}{1000} \cdot \sqrt{f_c} \cdot b_w \cdot c$

$V_c = 5.421$ kips

## G.3 – Shear Strength Calculation according to the Deitz Method

$$b_w := \begin{pmatrix} 12 \\ 24 \\ 42 \\ 60 \\ 60 \end{pmatrix} \text{in} \qquad d := \begin{pmatrix} 5.625 \\ 5.625 \\ 5.625 \\ 5.625 \\ 4.75 \end{pmatrix} \text{in} \qquad f_c := \begin{pmatrix} 6000 \\ 6000 \\ 6200 \\ 6500 \\ 5900 \end{pmatrix} \text{psi}$$

$E_f := 6100\text{ksi}$ Modulus of elastiticity of GFRP bar according to tests, ksi

$E_s := 29000\text{ksi}$ Modulus of elasticity of steel rebar

$j := 0..4$

$$V_{c_j} := 3\text{lbf} \cdot \left(\frac{E_f}{E_s}\right) \cdot 2 \cdot \left(\sqrt{\frac{f_{c_j}}{\text{psi}}}\right) b_{w_j} \frac{d_j}{\text{in}^2}$$

$$V_c = \begin{pmatrix} 6.599 \\ 13.198 \\ 23.477 \\ 34.341 \\ 27.628 \end{pmatrix} \text{kip}$$

## G.4– Shear Strength Calculation according to MCFT

1. Calculation of Mu and Vu

$d := 5.625$ in

$b := 12$ in width of deck

$f_c := 6$ ksi concrete compressive strength

$E_f := 6100$ ksi GFRP Modulus of Elasticity

$A_{bar} := \left(\frac{.75}{2}\right)^2 \cdot \pi$ $A_{bar} = 0.442$ Area of a No. 6 bar, in^2

$A_f := A_{bar} \cdot 3$ $A_f = 1.325$ Area of FRP reinforcement in a 1' width of deck, in^2

$\beta_1 := 1.05 - .05 \cdot f_c$ $\beta_1 = 0.750$

$\rho_f := \frac{A_f}{12 \cdot d}$ FRP reinforcement ratio

Solve for a

$$.85 f_c \cdot a^2 - \beta_1 E_f \cdot .003 \cdot d^2 \cdot \rho_f + E_f \cdot .003 \cdot \rho_f \cdot d \cdot a = 0 \text{ solve }, a \rightarrow \begin{pmatrix} -1.5062793567639512445 \\ 1.1099709085054961692 \end{pmatrix}$$

$a := 1.110$ From calculation entered above, in

$d_v := d - \frac{a}{2}$

Determine Applied Factored Live Load - Strength 1 AASHTO LRFD

$I := 1.33$ Impact factor

$\gamma_1 := 1.75$ Live load factor

$P := 16$ kips Truck tire load

$\gamma P_u := I \cdot \gamma_1 \cdot P$ kips

$\gamma P_u = 37.240$

$b_{eff} := 5.625 \cdot 12$ Effective Width

$$Applied := \frac{b \cdot \gamma P_u}{b_{eff}} \qquad Applied = 6.620$$

$M_u := 8.67$ kip – ft From Dr. Beam

$V_u := 5.19$ kips From Dr. Beam

## 2. Calculate $\varepsilon x$

$\theta := 37.1$

$$\varepsilon_x := \frac{\left[.5\left(V_u\right) \cdot \cot d\left(\theta\right) + \frac{M_u \cdot 12}{d_v}\right]}{E_f \cdot A_f}$$

$\varepsilon_x = 0.00296$ $\beta := 1.96$

$a_g := .75$ Aggregate size, in.

$$s_{xe} := d_v \cdot \frac{1.38}{a_g + .63} \qquad s_{xe} = 5.070$$

## 3. Recalc $\varepsilon x$

$M_u \cdot 12 = A_f \cdot F_f \cdot \left(d_v - \frac{a}{2}\right)$ solve, $F_f \rightarrow 17.3863703354902687$

$F_f := 17.39$

$$\varepsilon_f := \frac{F_f}{E_f} \qquad \varepsilon_f = 2.851 \times 10^{-3}$$

$\frac{\left(\varepsilon_f - \varepsilon_x\right)}{\varepsilon_f} = -0.039$ *Close Enough*

$V_c := \beta \cdot \sqrt{f_c \cdot 1000}\, d_v \cdot b$

$\frac{V_c}{1000} = 9.237$ kips

***Table G.1 – Values of θ and β for MCFT (members without web reinforcement)***

| $s_x$ | | Longitudinal Strain $\varepsilon_x \times 1000$ | | | | | |
|---|---|---|---|---|---|---|---|
| | | **≤ 0** | **≤ 0.25** | **≤ 0.50** | **≤ 1.00** | **≤ 1.50** | **≤ 2.00** |
| ≤ 5 in. | θ deg | 27.00 | 29.00 | 31.00 | 34.00 | 36.00 | 38.00 |
| | β | 4.94 | 3.78 | 3.19 | 2.56 | 2.19 | 1.93 |
| ≤ 10 in. | θ deg | 30.00 | 34.00 | 37.00 | 40.00 | 43.00 | 45.00 |
| | β | 4.65 | 3.45 | 2.83 | 2.19 | 1.87 | 1.65 |
| ≤ 15 in. | θ deg | 32.00 | 37.00 | 40.00 | 45.00 | 48.00 | 50.00 |
| | β | 4.47 | 3.21 | 2.59 | 1.98 | 1.65 | 1.45 |
| ≤ 25 in. | θ deg | 35.00 | 41.00 | 45.00 | 51.00 | 54.00 | 57.00 |
| | β | 4.19 | 2.85 | 2.26 | 1.69 | 1.40 | 1.18 |
| ≤ 50 in. | θ deg | 38.00 | 48.00 | 53.00 | 59.00 | 63.00 | 66.00 |
| | β | 3.83 | 2.39 | 1.82 | 1.27 | 1.00 | 0.83 |
| ≤ 100 in. | θ deg | 42.00 | 55.00 | 62.00 | 69.00 | 72.00 | 75.00 |
| | β | 3.47 | 1.88 | 1.35 | 0.87 | 0.65 | 0.52 |

*From Collins, 1996*

# Appendix H – Deflection Plots

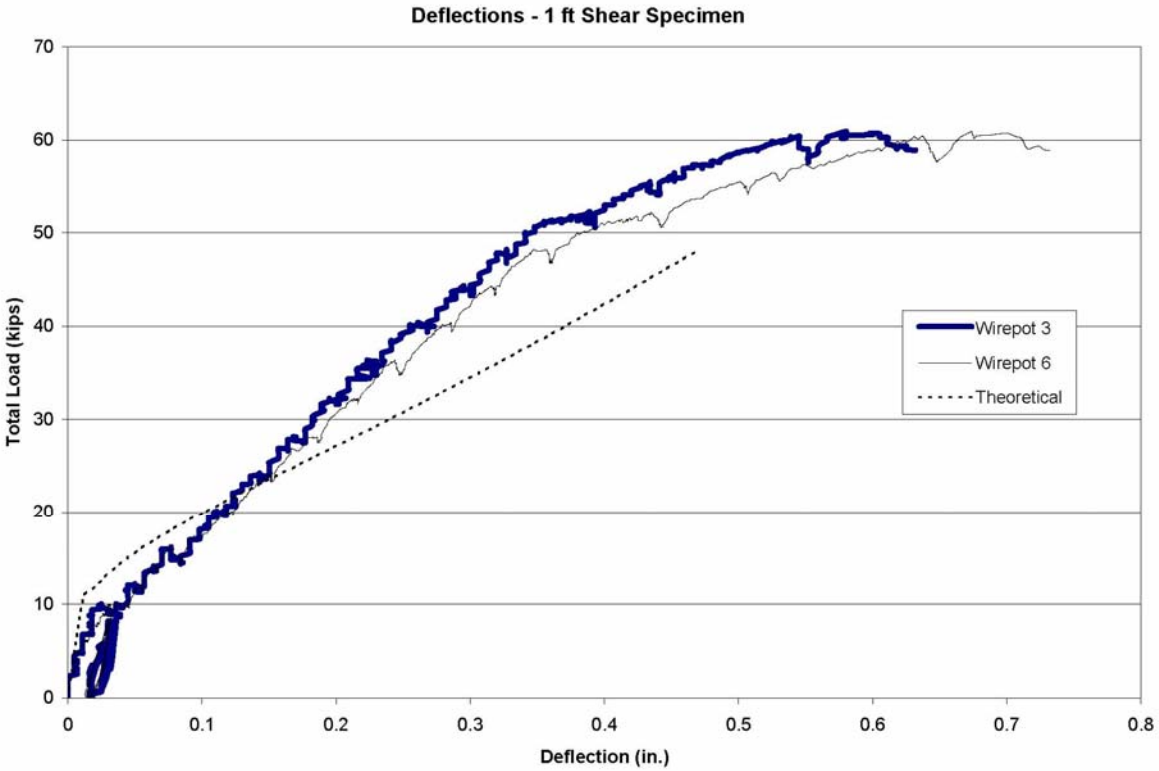


**Figure H.1 – Deflection plot for the 1 ft shear specimen**

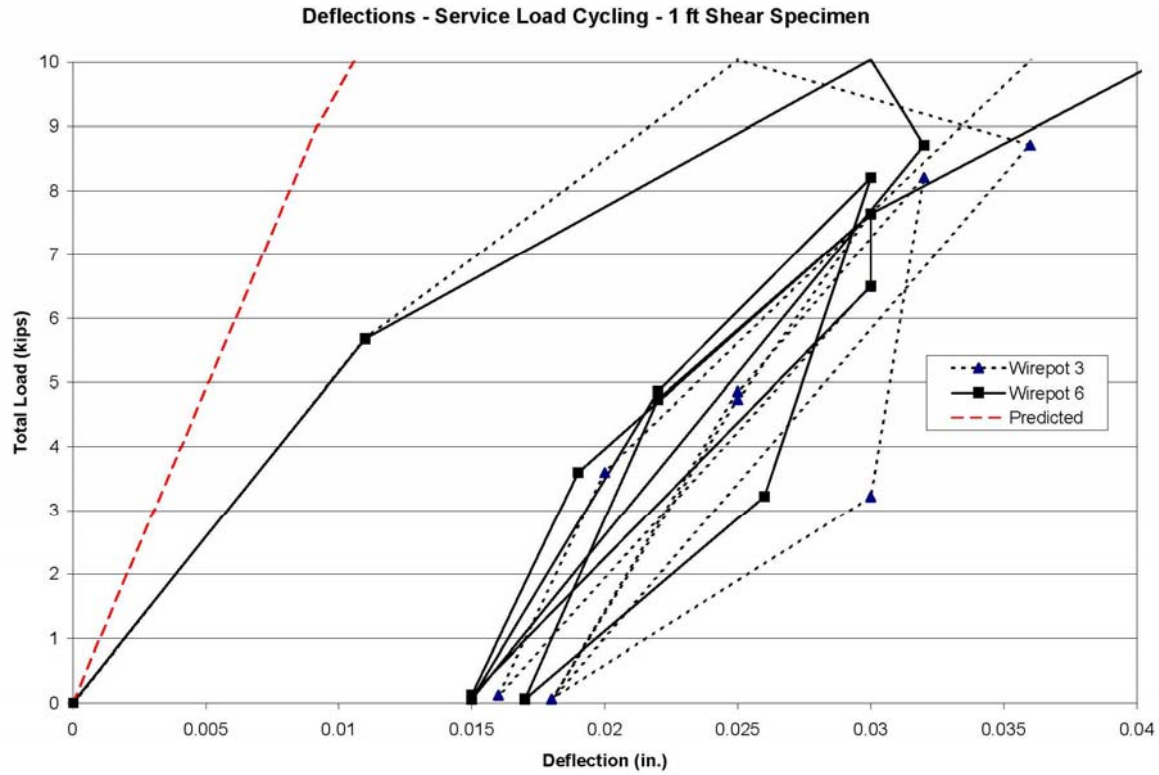


**Figure H.2 – Deflection plot for the 1 ft shear specimen during service load cycling**

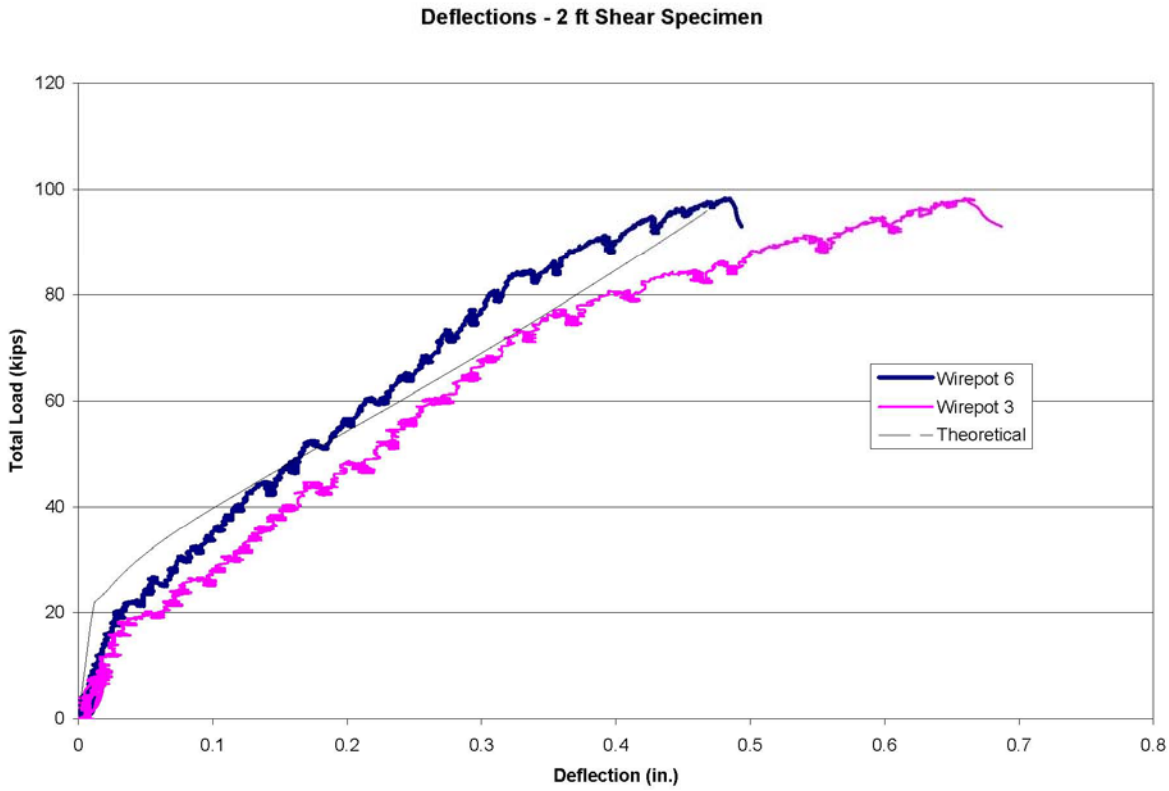


**Figure H.3 – Deflection plot for the 2 ft shear specimen**

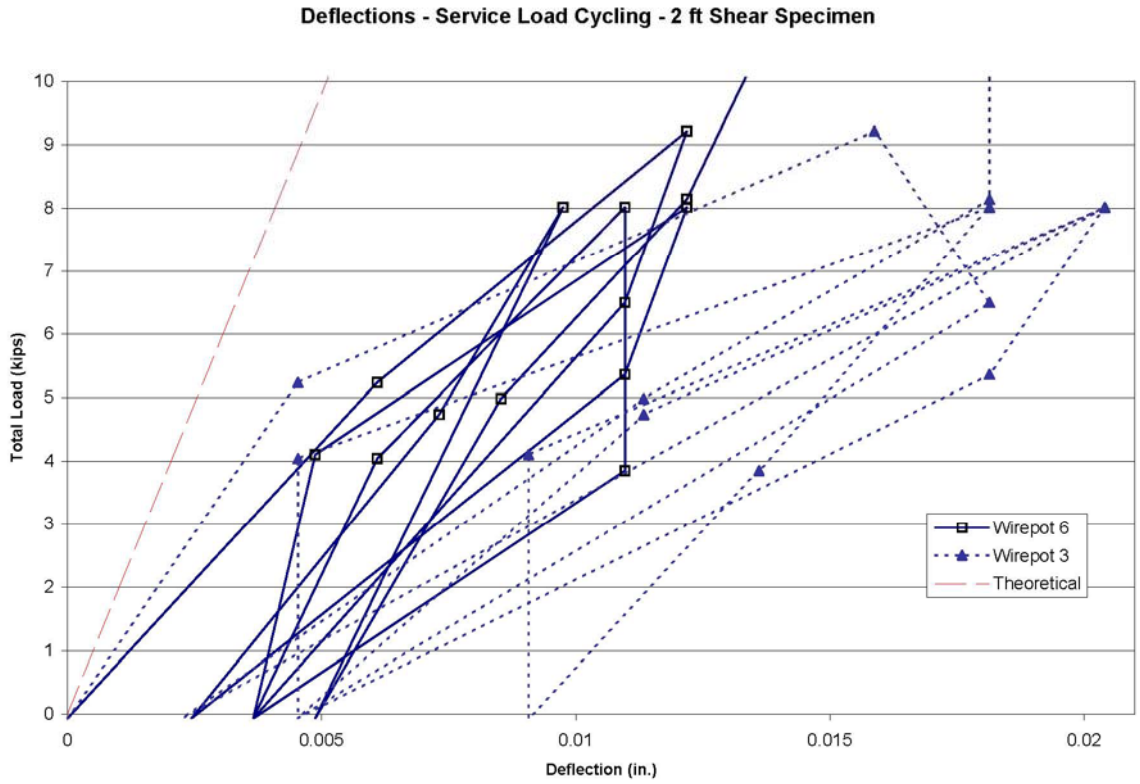


**Figure H.4 – Deflection plot for the 2 ft shear specimen during service load cycling**

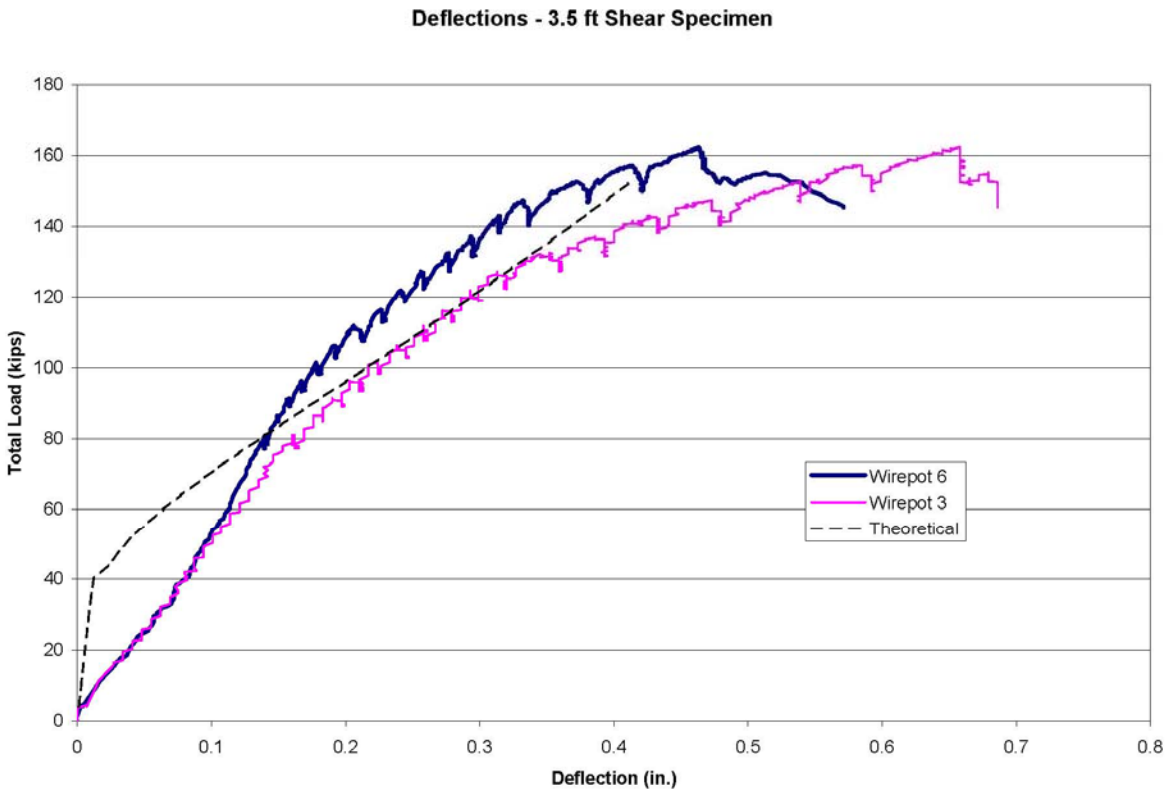


**Figure H.5 – Deflection plot for the 3.5 ft shear specimen**

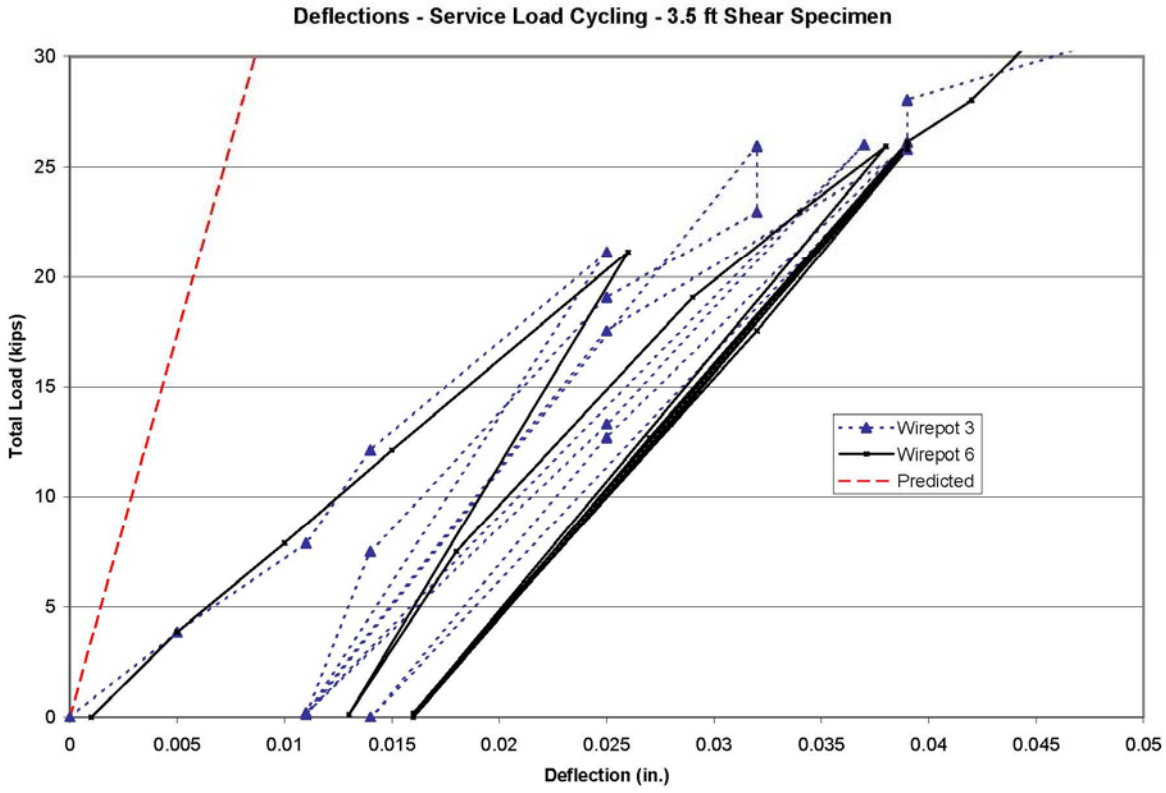


**Figure H.6 – Deflection plot for the 3.5 shear specimen during service load cycling**

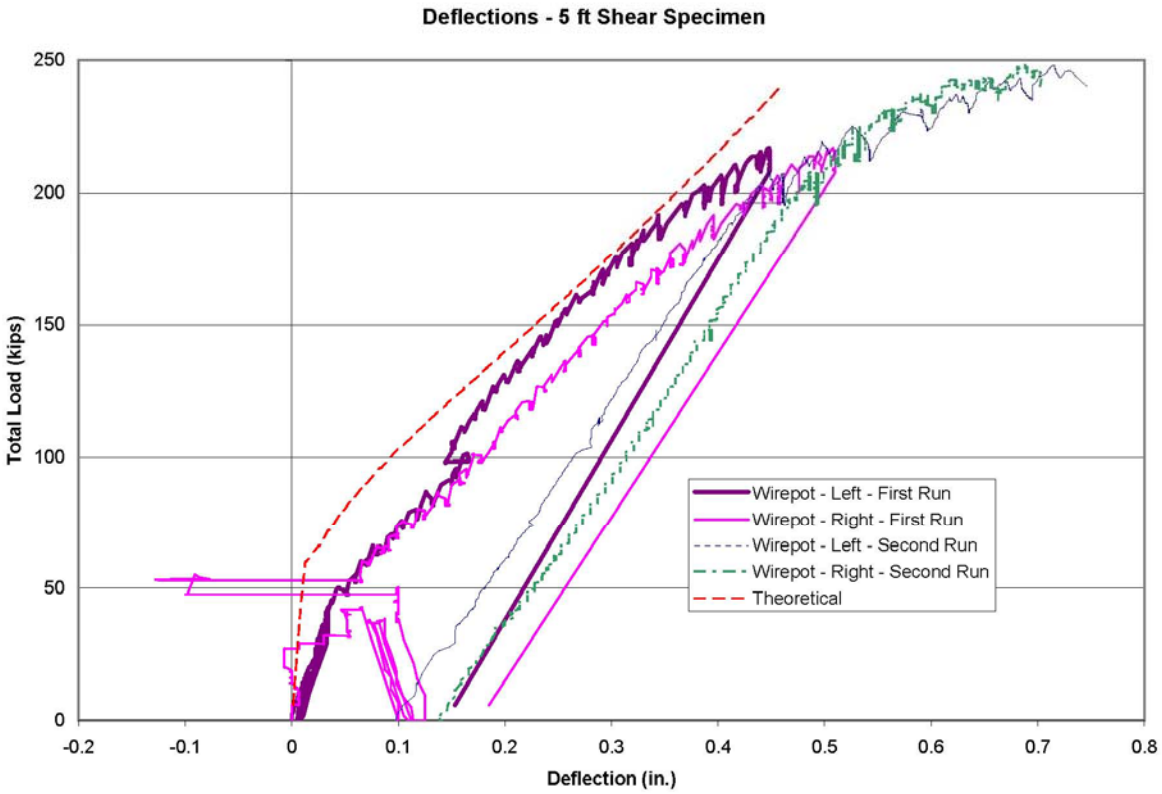


**Figure H.7 – Deflection plot for the 5 ft shear specimen**


**Figure H.8 – Deflection plot for the 5 ft shear specimen during service load cycling**

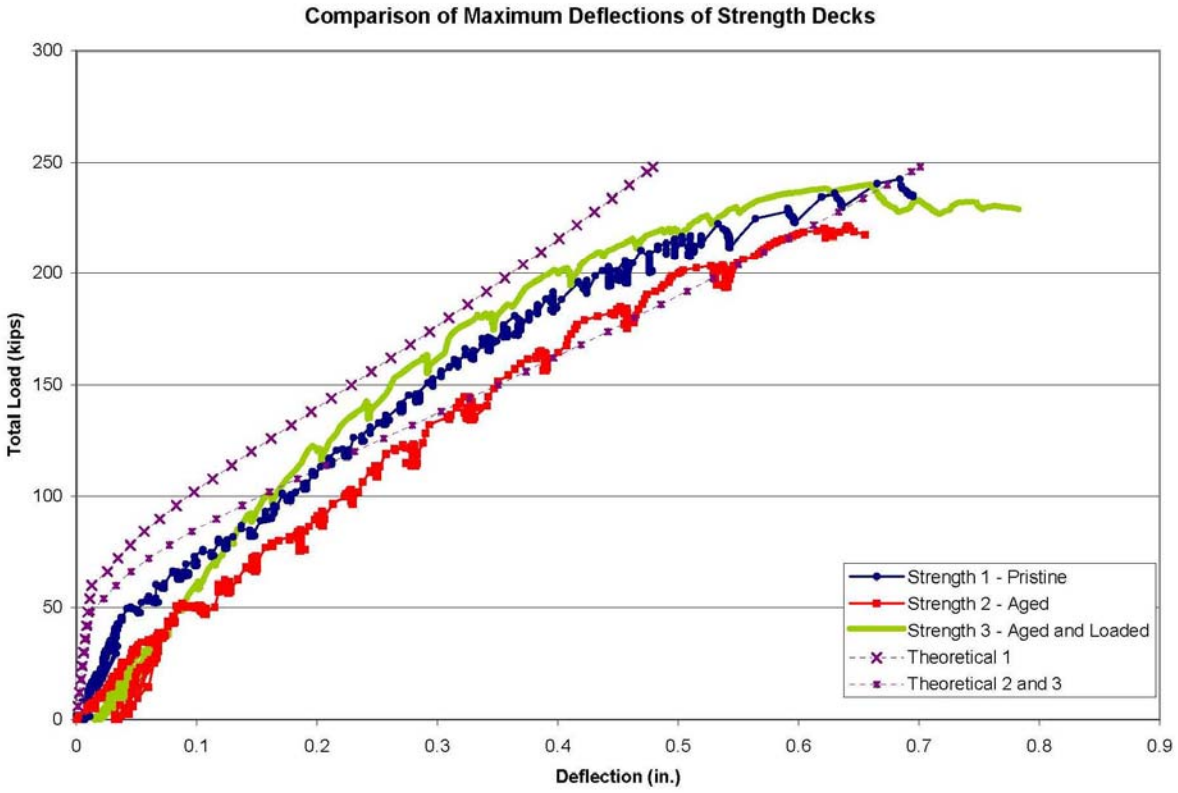


**Figure H.9 - Deflection plot for the three strength specimens**

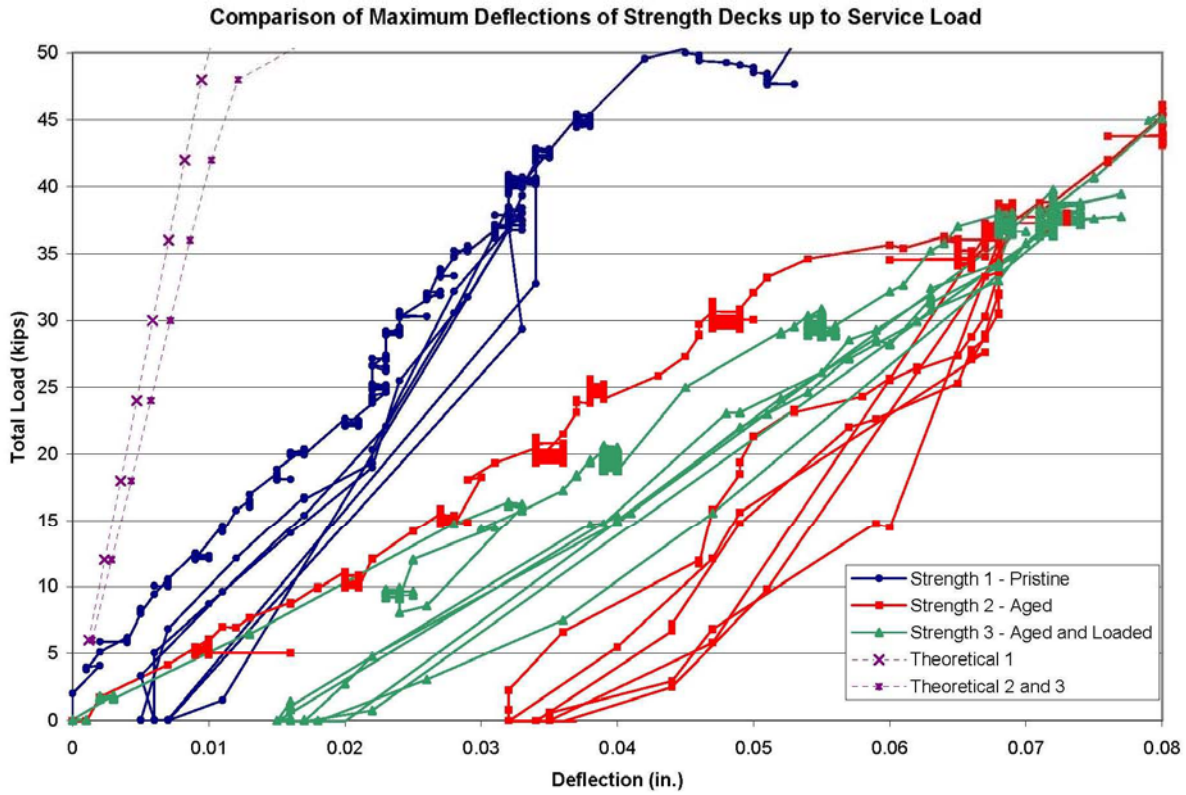


**Figure H.10 – Deflection plot for the three strength specimens during service load cycling**

# Appendix I – Steel Strain Plots

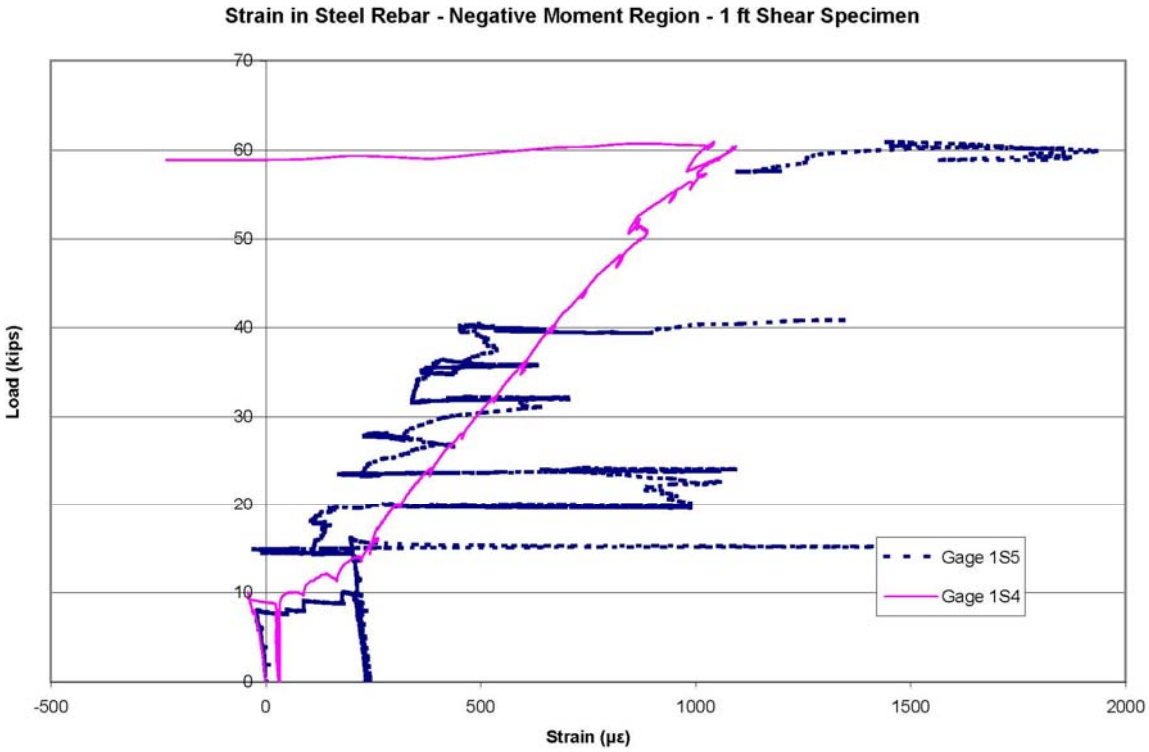


**Figure I.1 - Strain in steel rebar over the center support - 1 ft Shear**

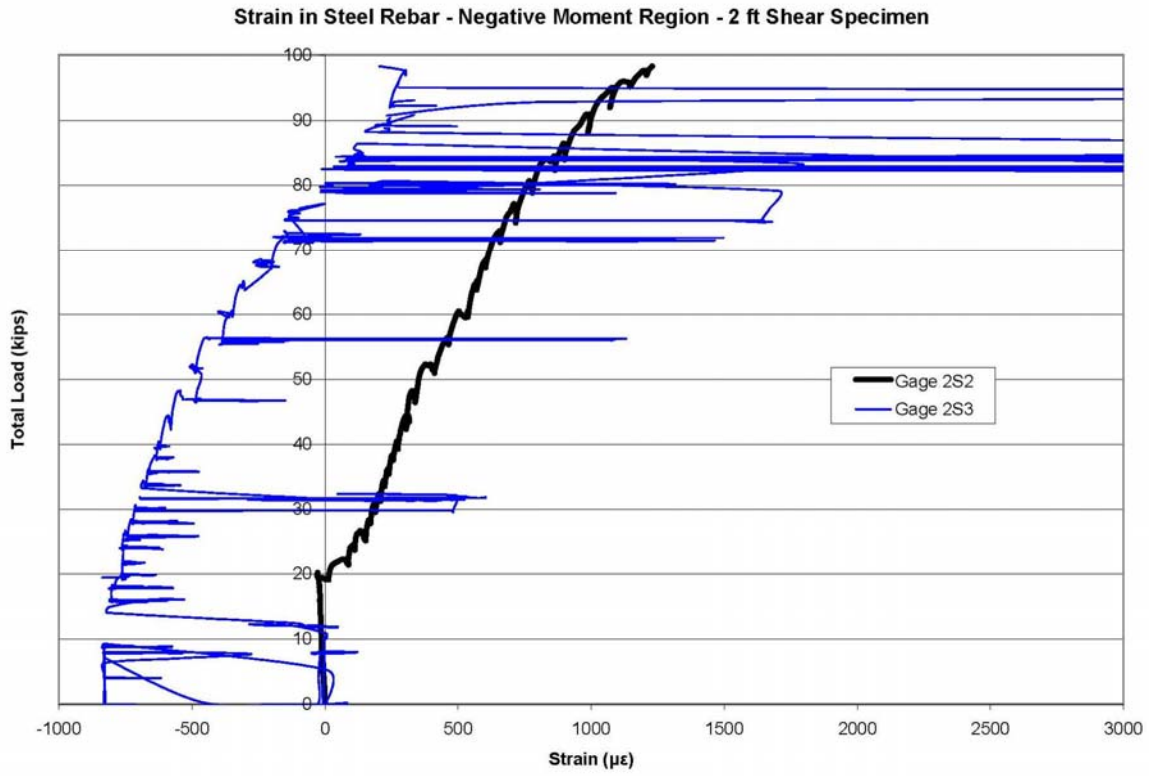


**Figure I.2 - Strain in steel rebar over the center support - 2 ft Shear**

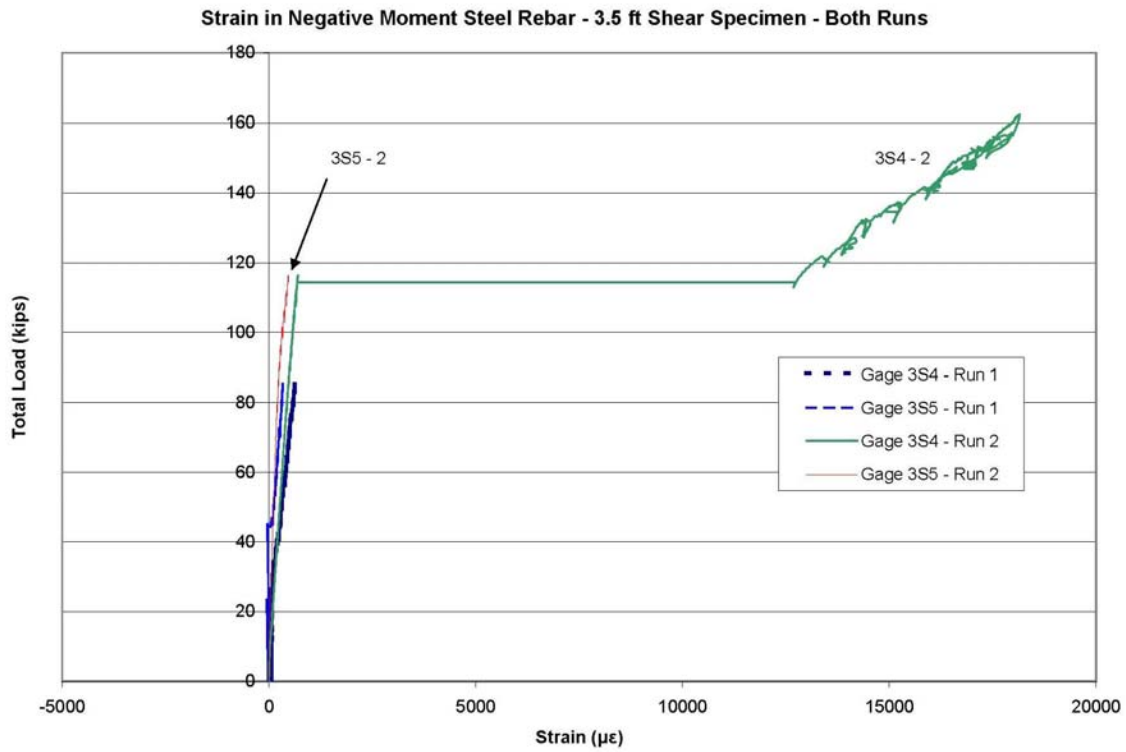


**Figure I.3 - Strain in steel rebar over the center support – 3.5 ft Shear**

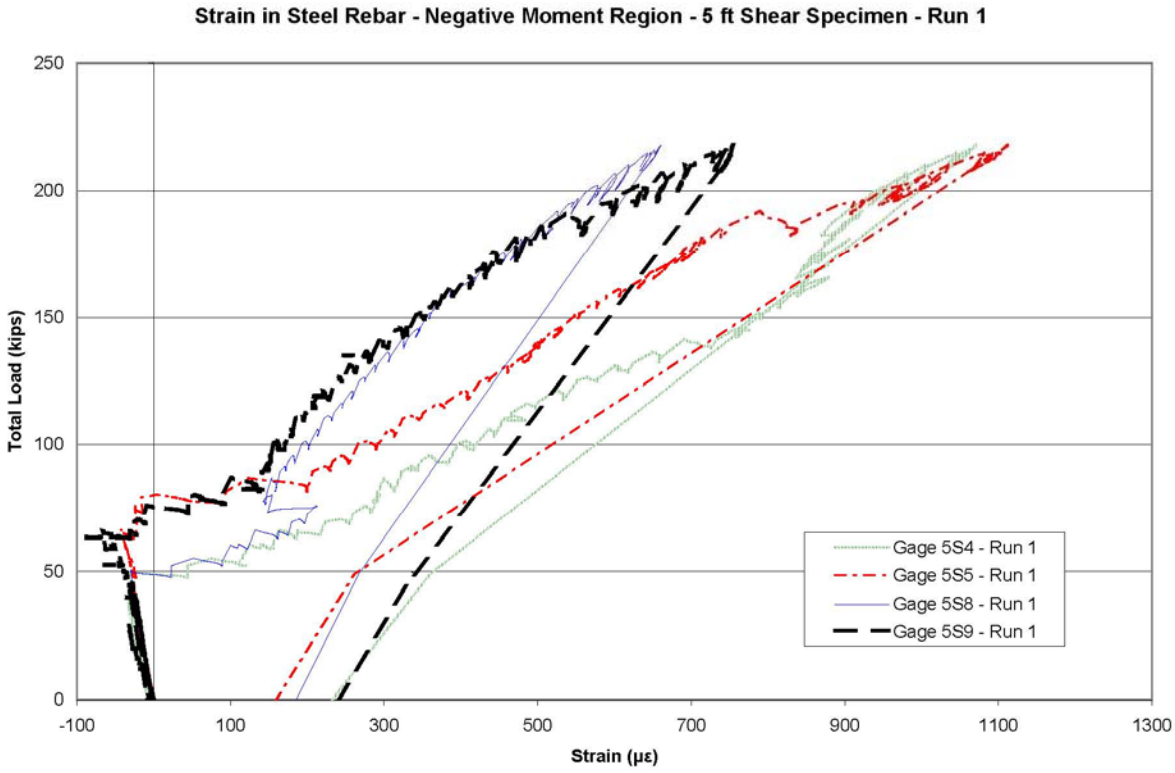


**Figure I.4 - Strain in steel rebar over the center support - 5 ft Shear/Strength 1 - Run 1**

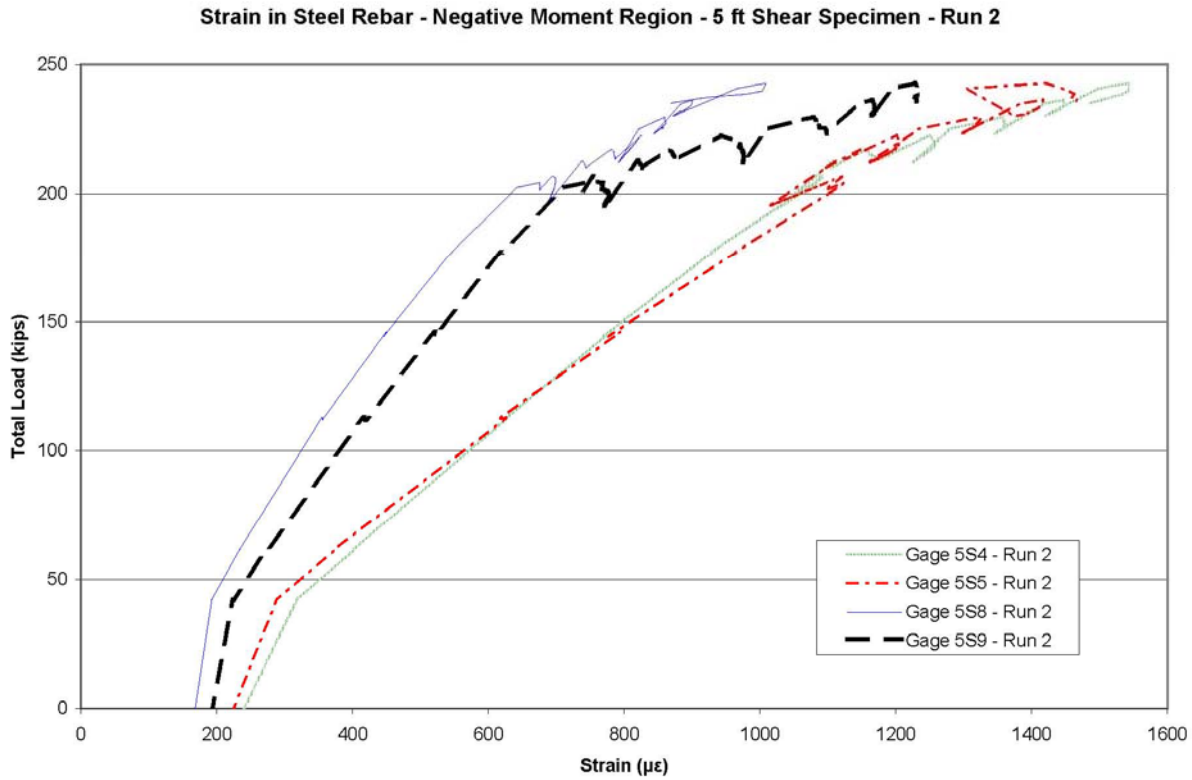


**Figure I.5 - Strain in steel rebar over the center support - 5 ft Shear/Strength 1 - Run 2**

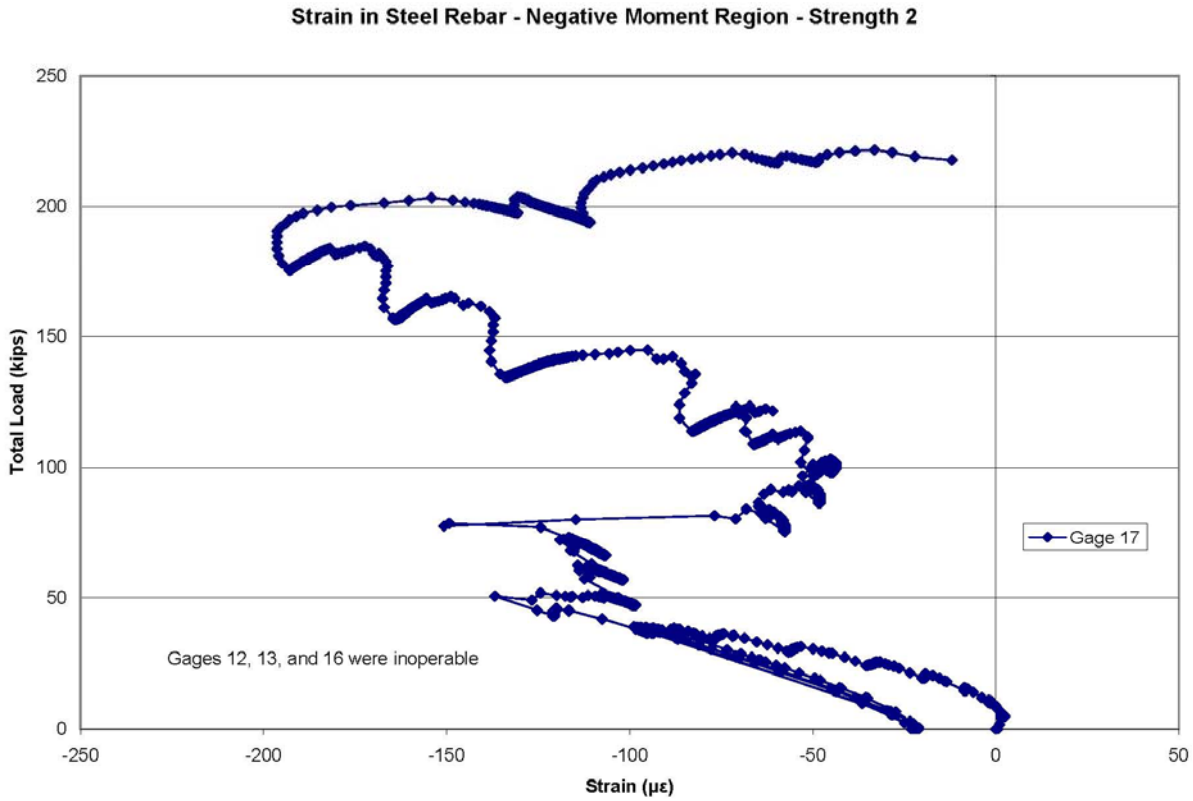


**Figure I.6 - Strain in steel rebar over the center support - Strength 2**

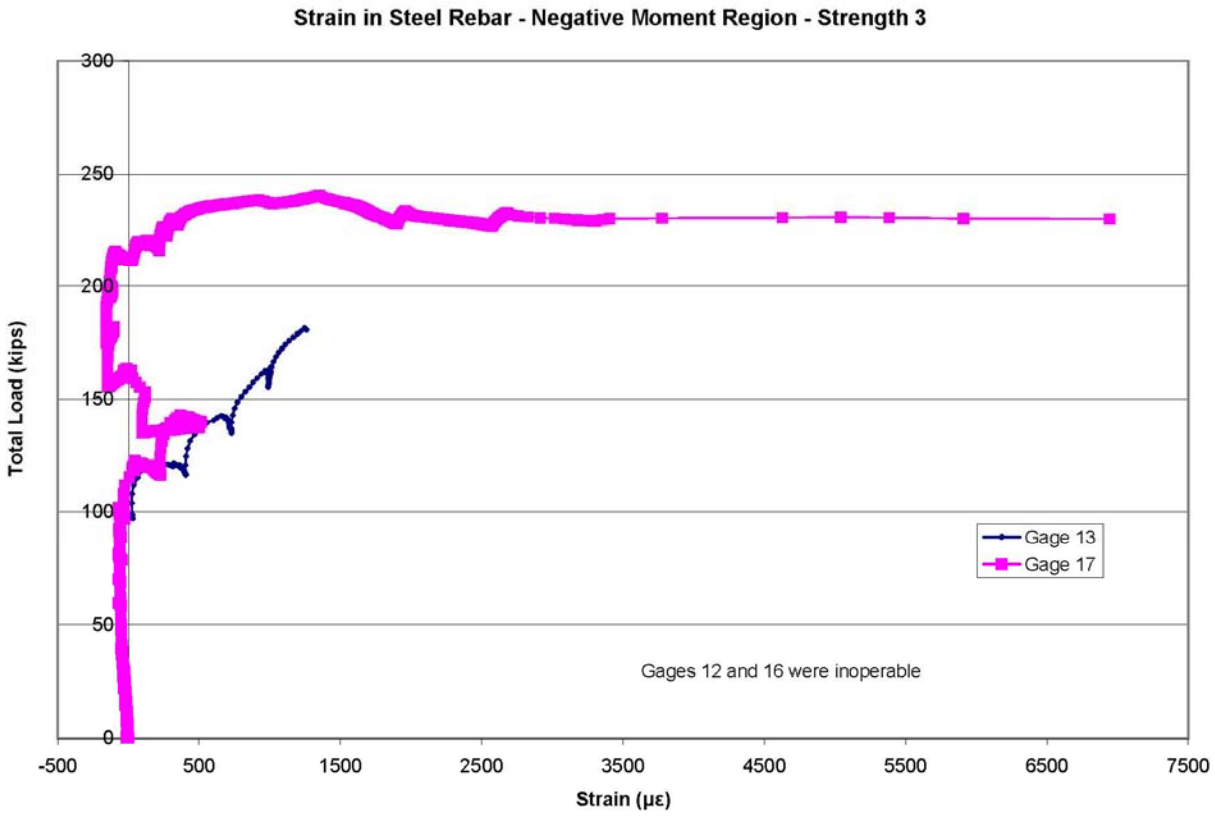


**Figure I.7 - Strain in steel rebar over the center support - Strength 3**

# Appendix J – GFRP Strain Plots

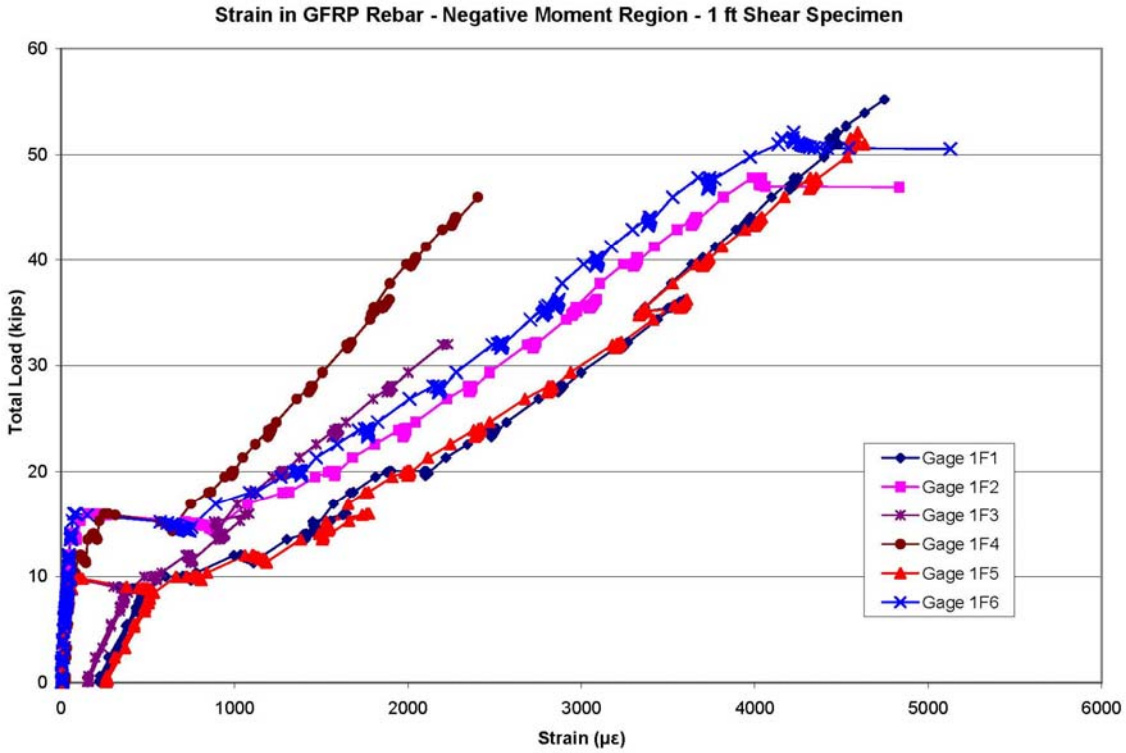


**Figure J.1 - Strain in GFRP rebar over the center support - 1 ft Shear**

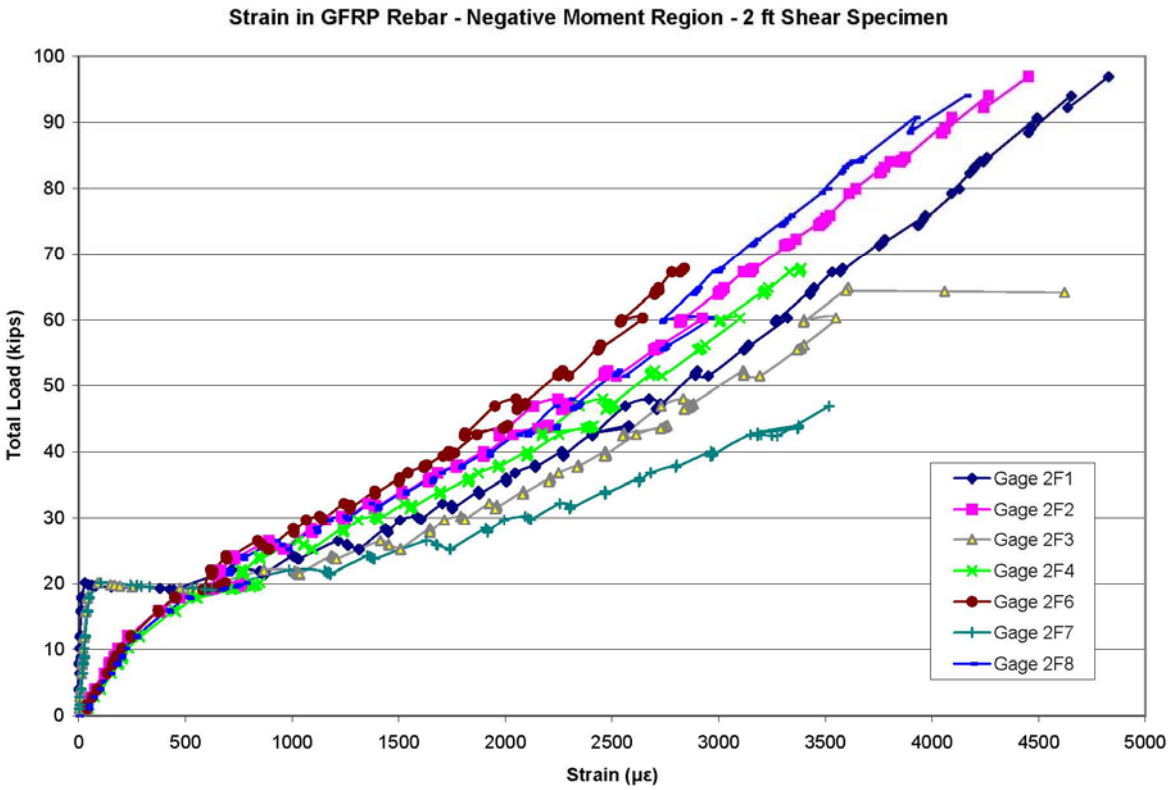


**Figure J.2 - Strain in GFRP rebar over the center support - 2 ft Shear**

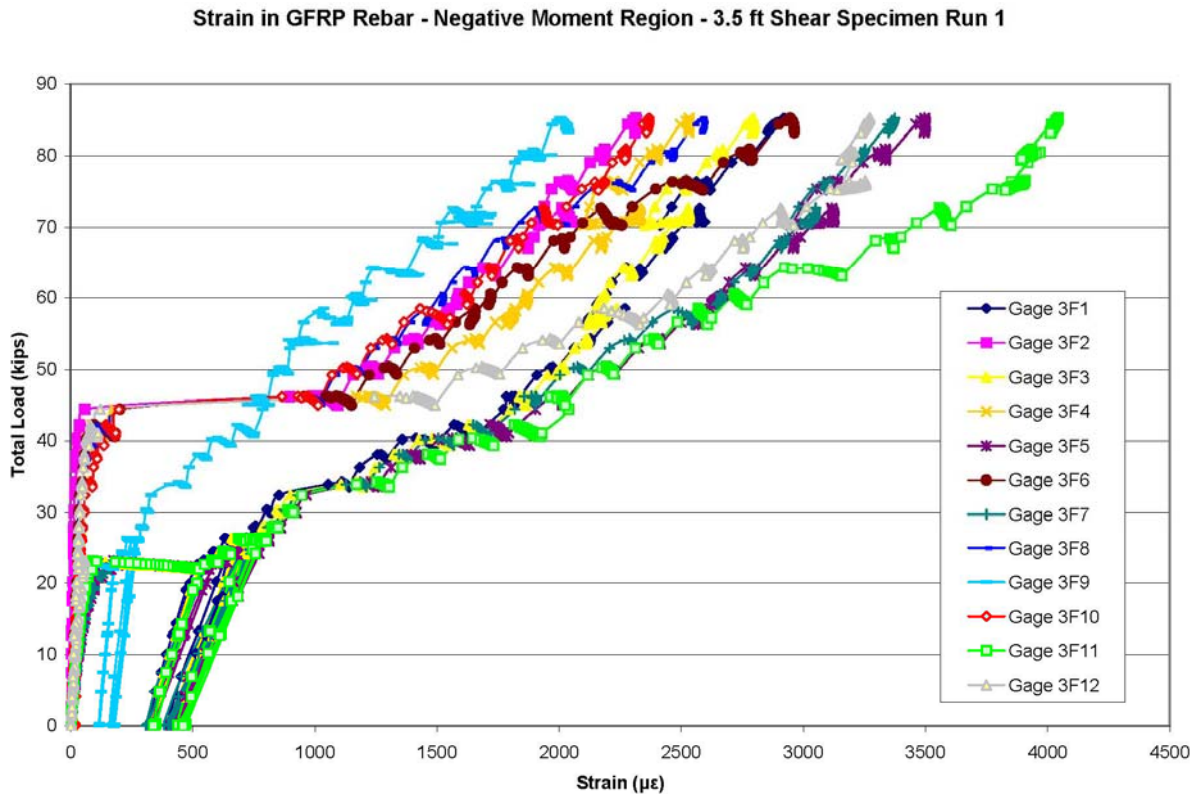


**Figure J.3 - Strain in GFRP rebar over the center support - 3.5 ft Shear - Run 1**

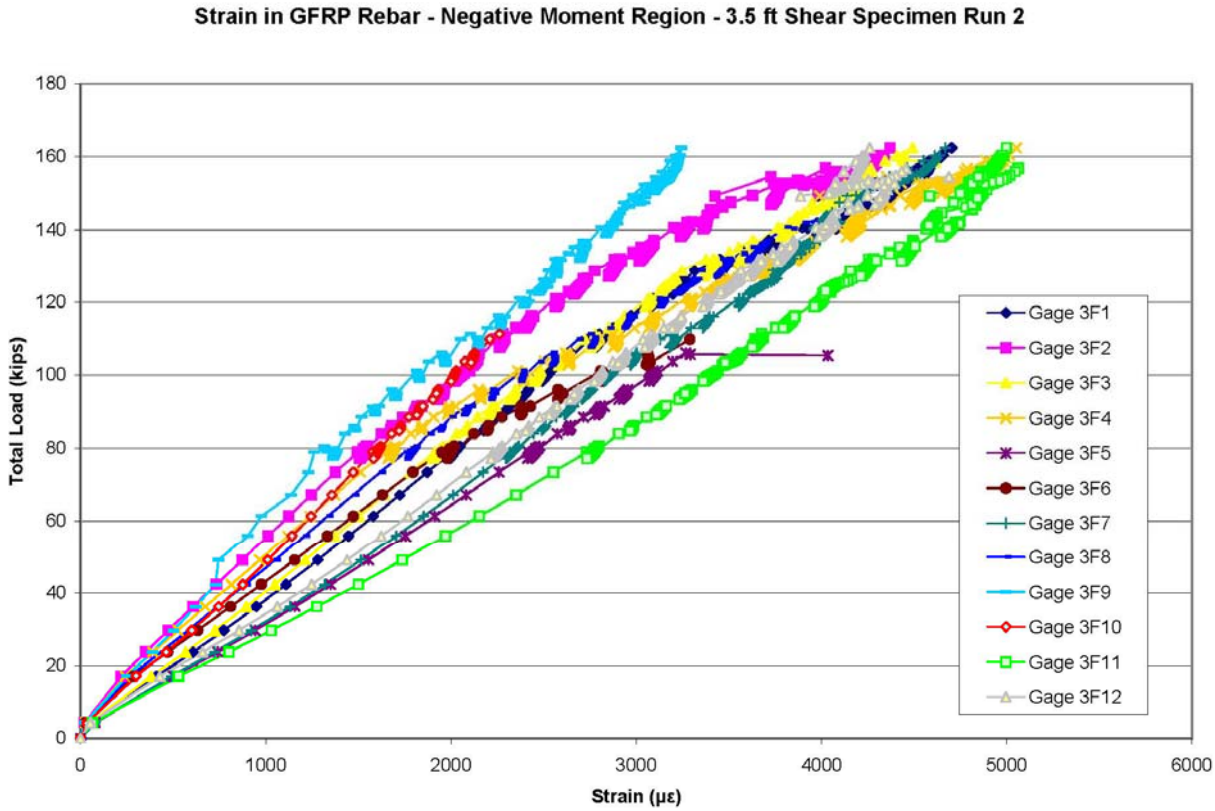


**Figure J.4 - Strain in GFRP rebar over the center support - 3.5 ft Shear - Run 2**

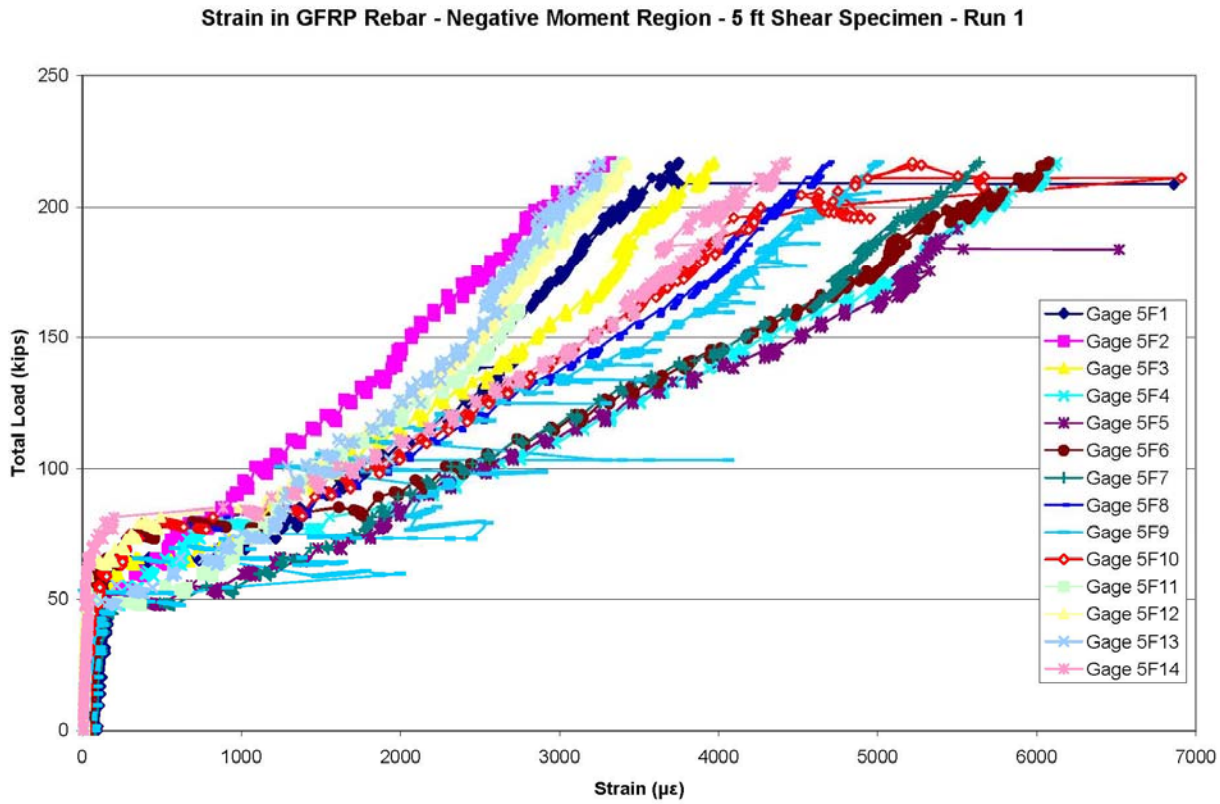


**Figure J.5 - Strain in GFRP rebar over the center support - 5 ft Shear / Strength 1 - Run 1**

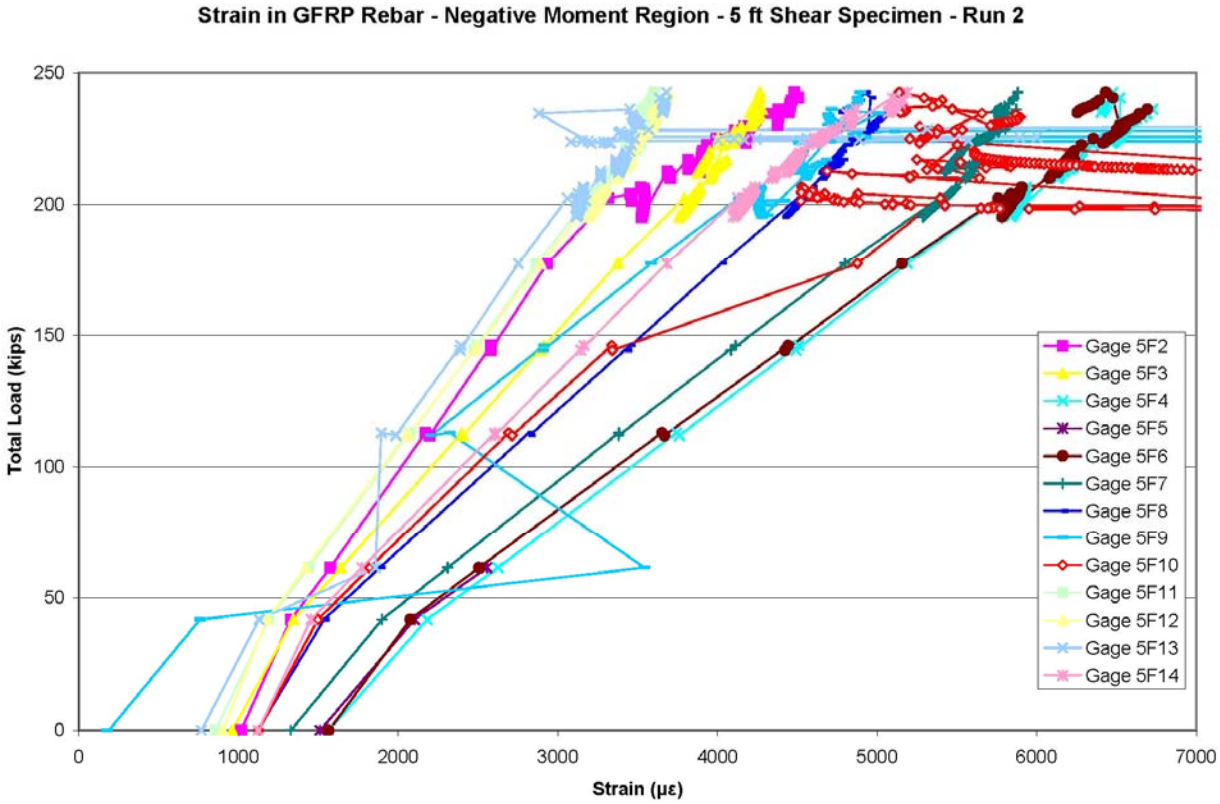


**Figure J.6 - Strain in GFRP rebar over the center support - 5 ft Shear / Strength 1 - Run 2**

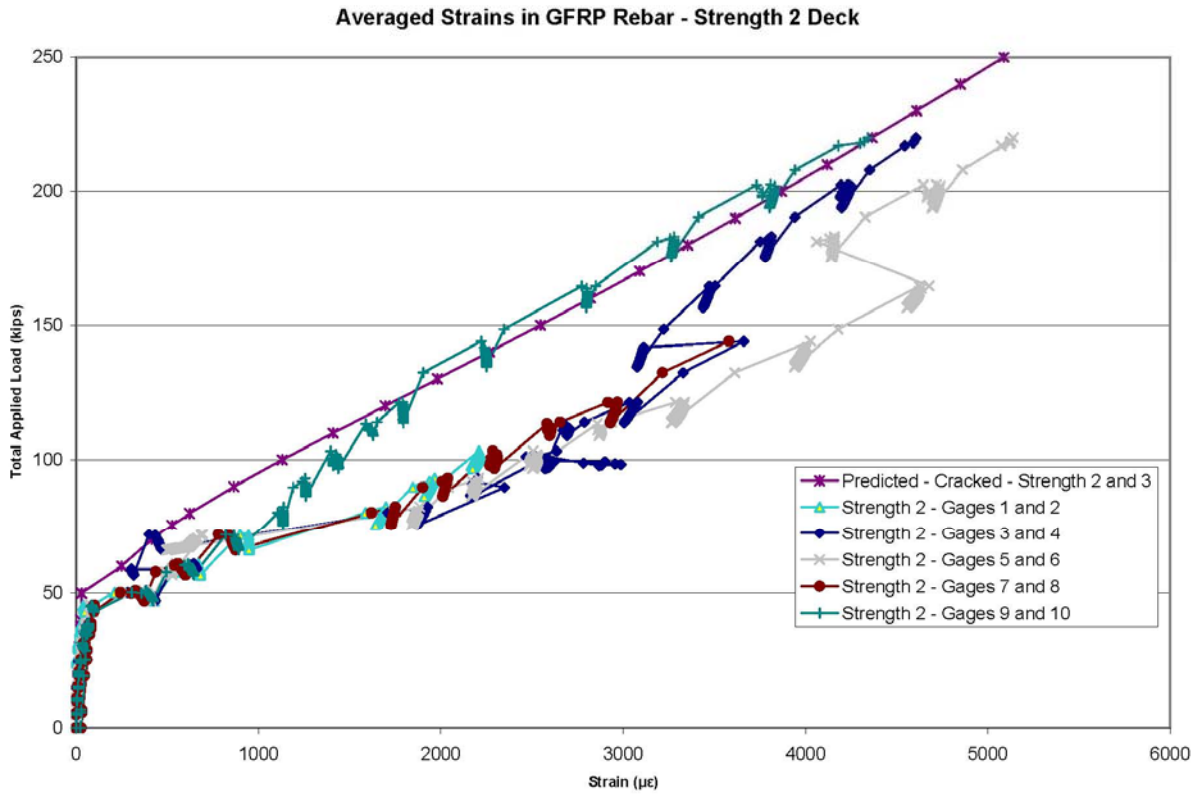


**Figure J.7 - Strain in GFRP rebar over the center support - opposite gages averaged - Strength 2**

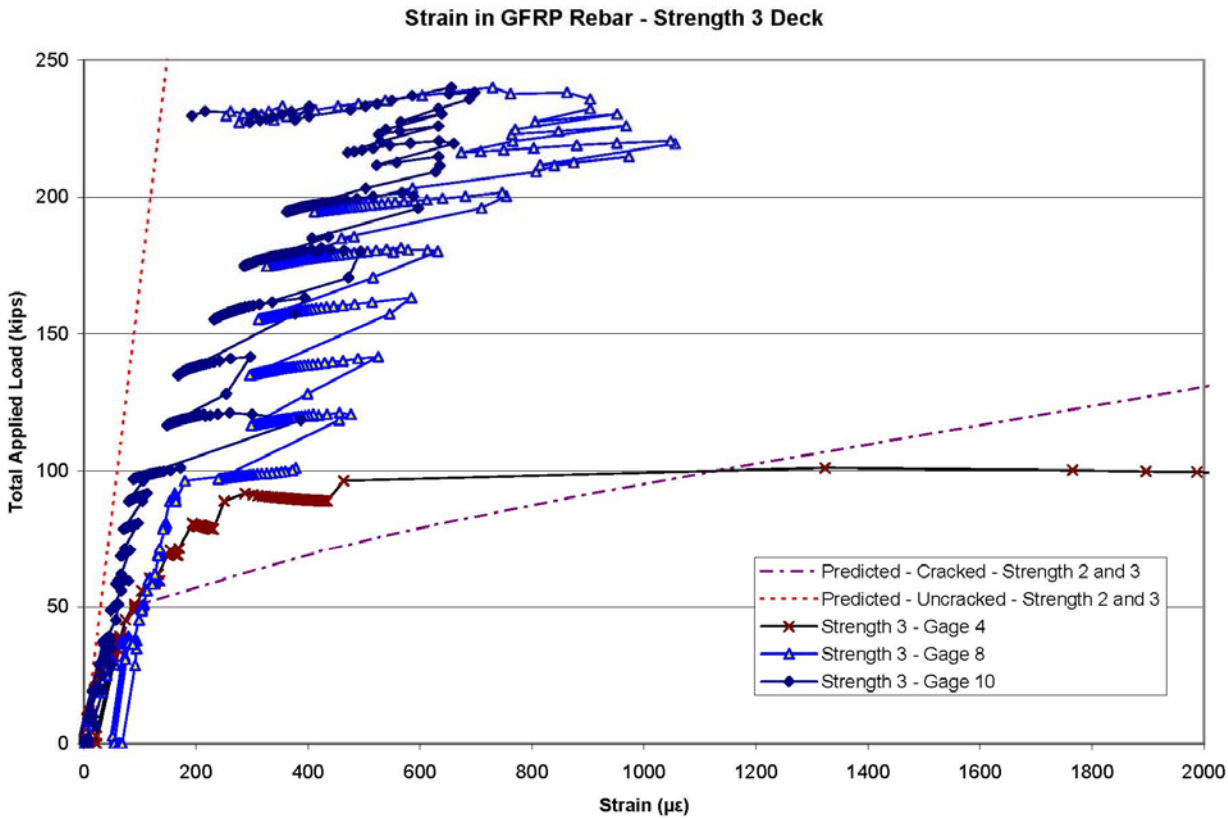


**Figure J.8 - Strain in GFRP rebar over the center support - Strength 3**

## *Appendix K – Crack Maps*

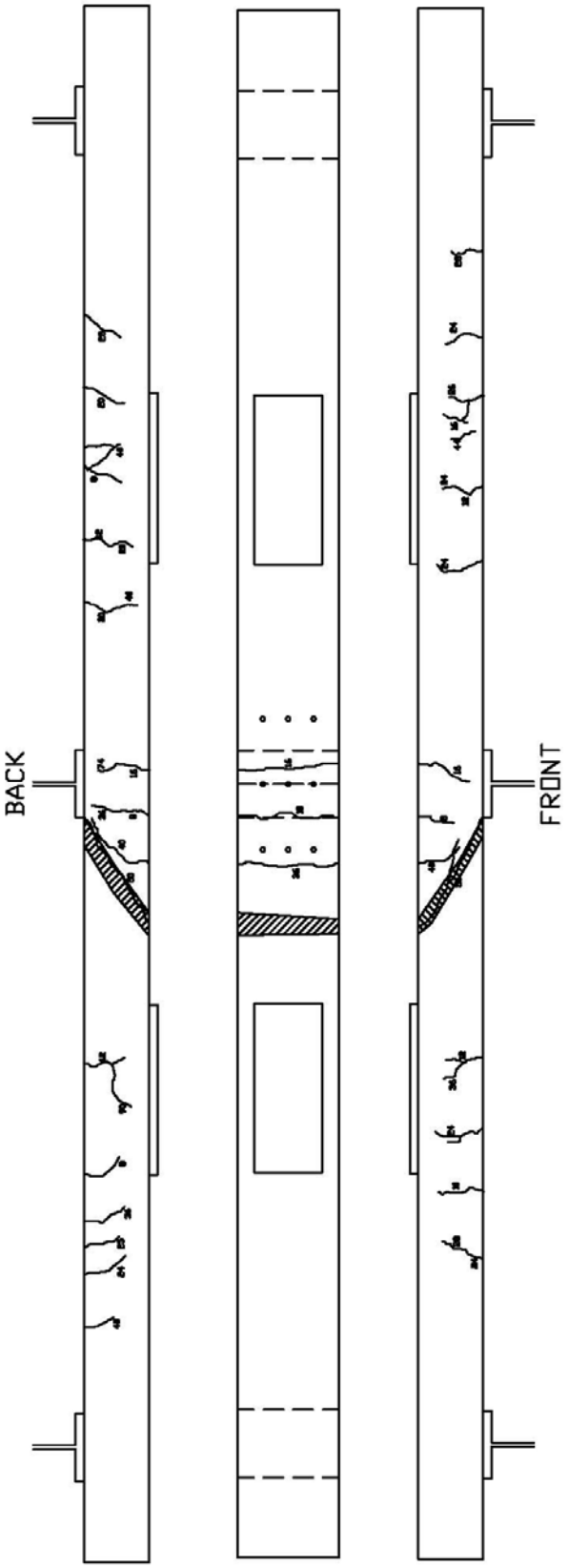


**Figure K.1 – Crack map for 1 ft Shear (hatched area represents shear failure zone; loads are total loads in kips)**

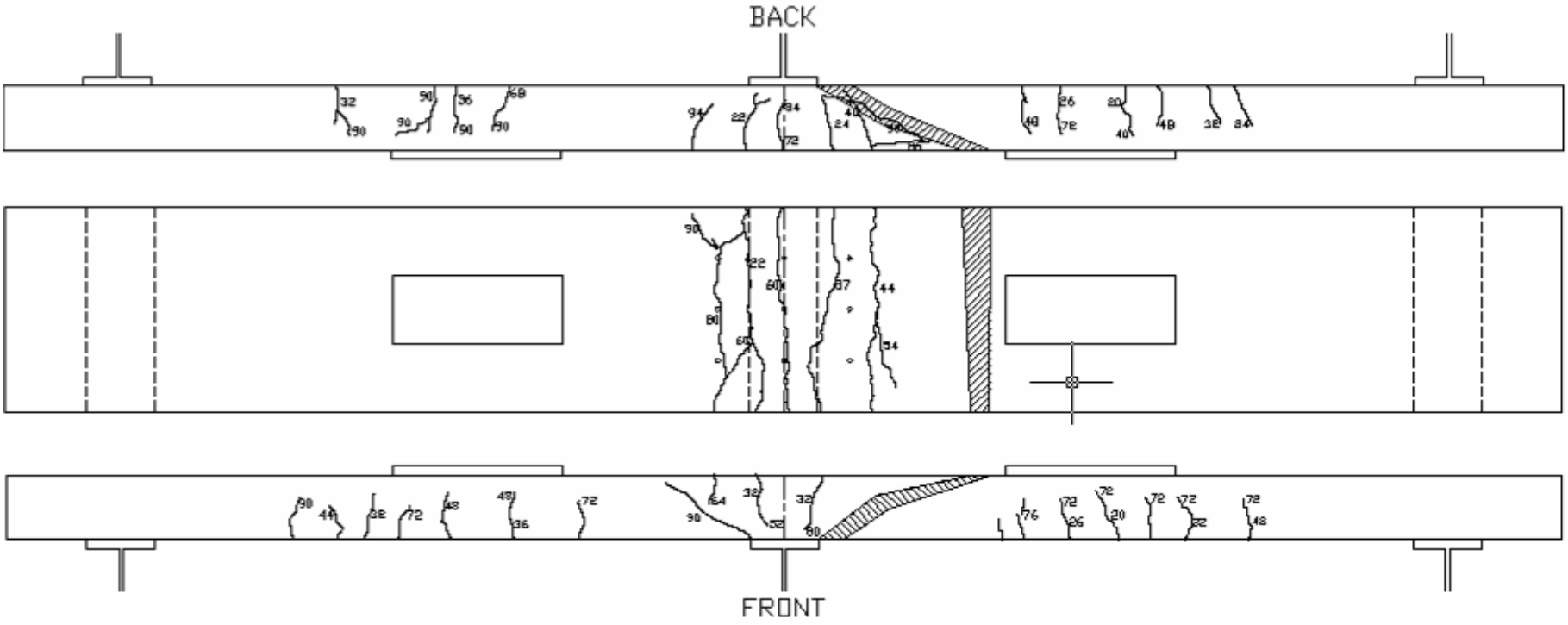


**Figure K.2 – Crack map for 2 ft Shear (hatched area represents shear failure zone; loads are total loads in kips)**

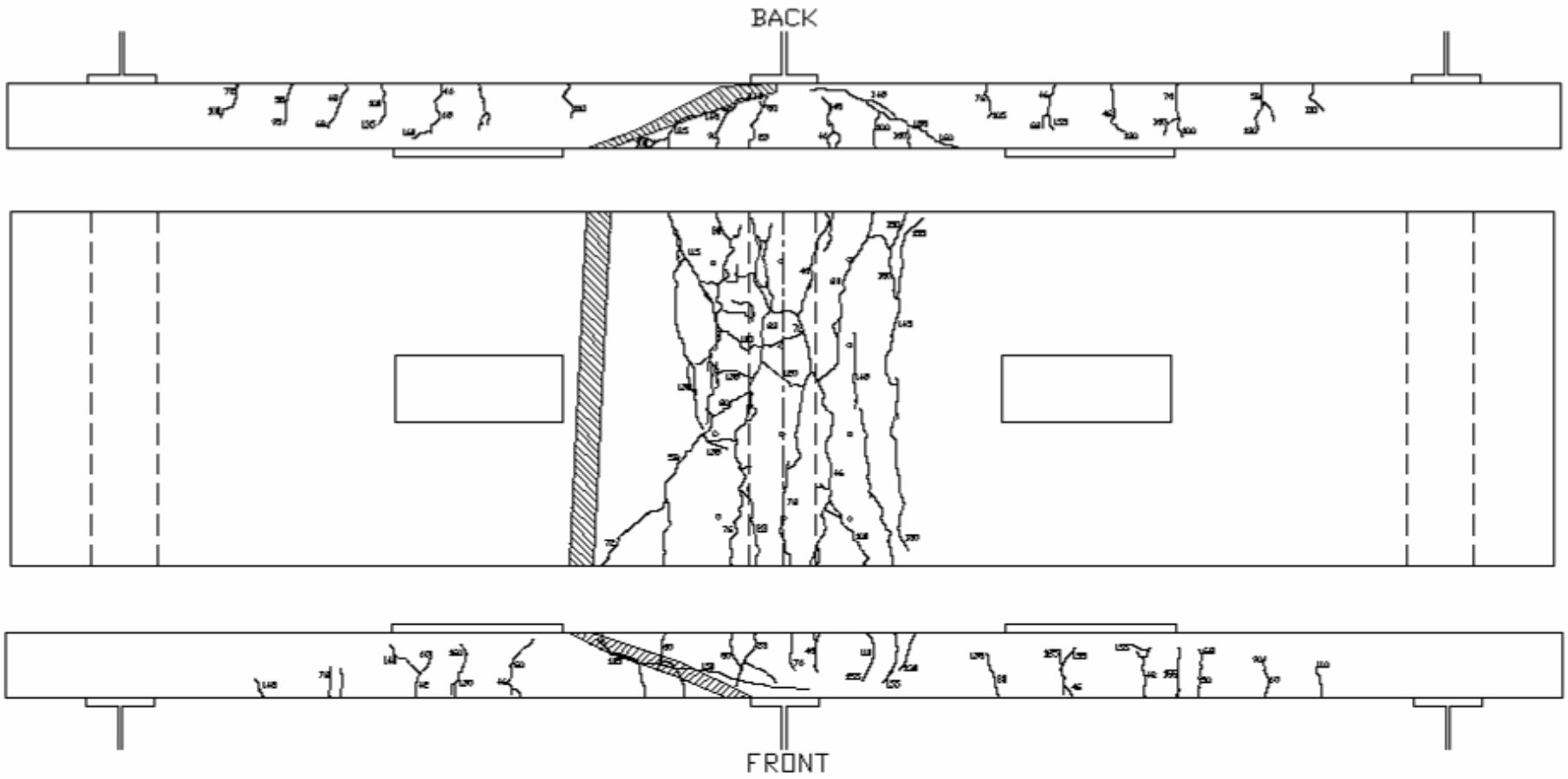


**Figure K.3 – Crack map for 3.5 ft Shear (hatched area represents shear failure zone; loads are total loads in kips)**

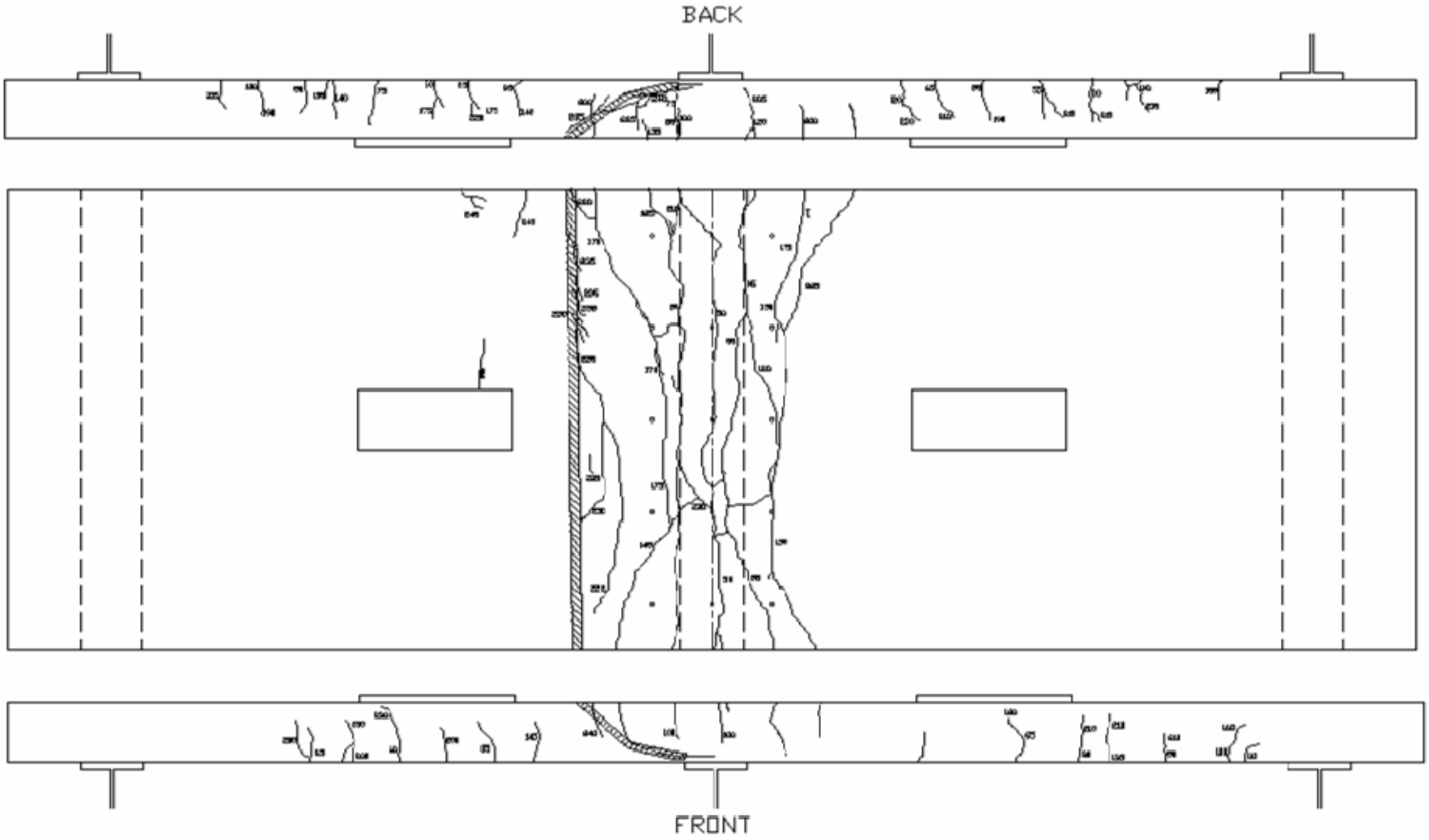


**Figure K.4 – Crack map for 5 ft Shear/Strength 1 (hatched area represents shear failure zone; loads are total loads in kips)**

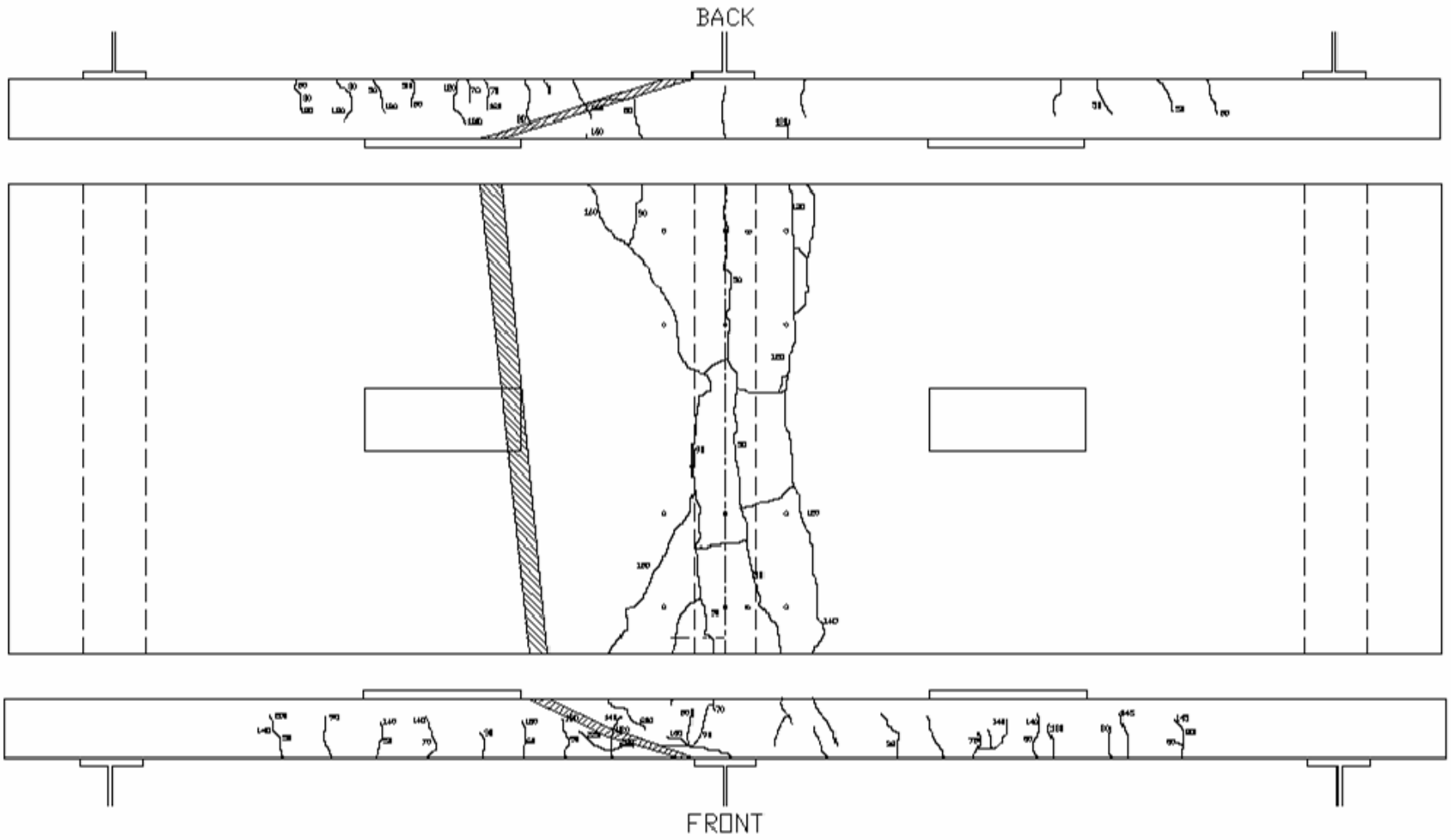


**Figure K.5 – Crack map for Strength 2 (hatched area represents shear failure zone; loads are total loads in kips)**

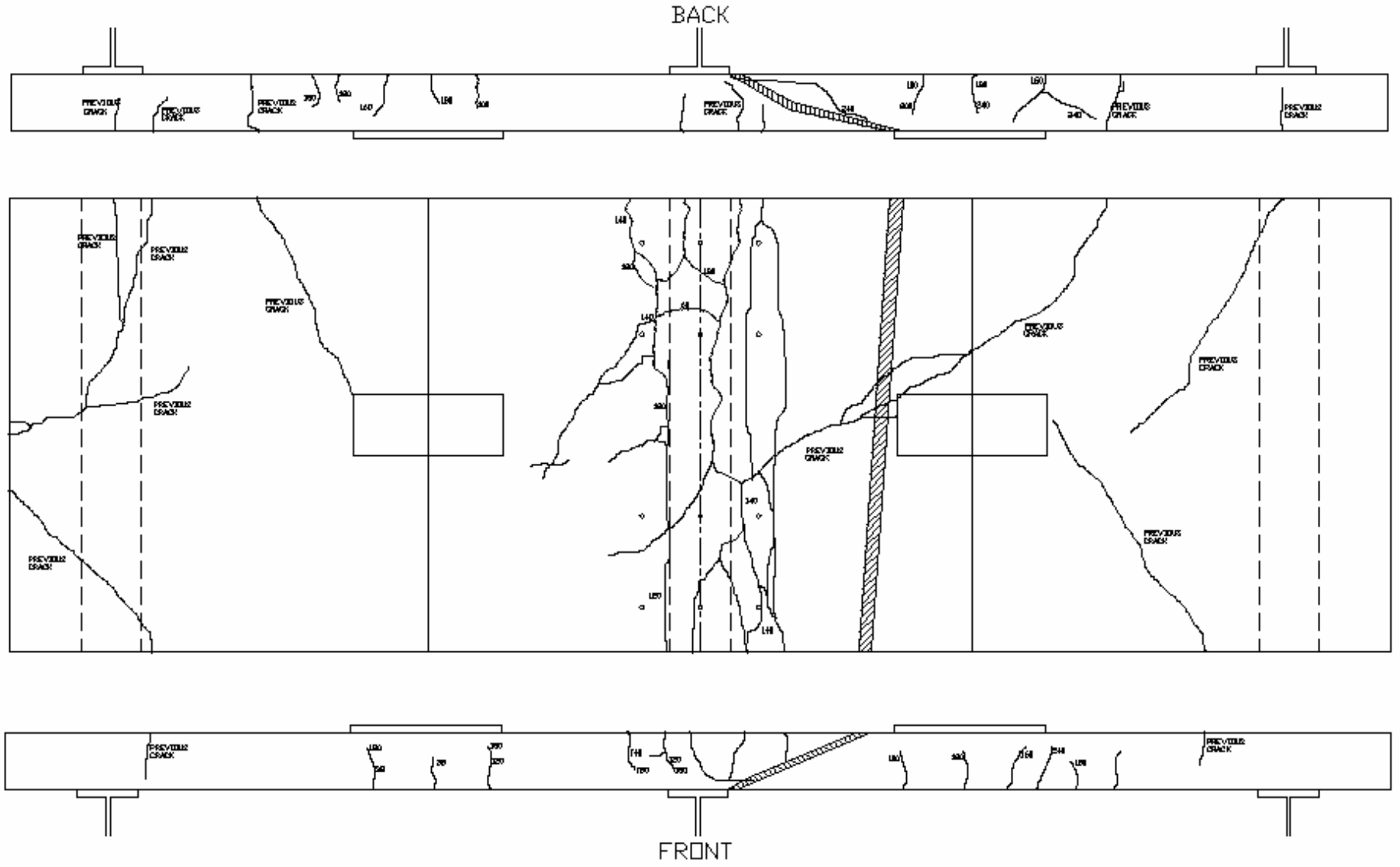


**Figure K.6 – Crack map for Strength 3 (hatched area represents shear failure zone; loads are total loads in kips)**

## *Vita*

Ross D. "Nick" Amico was born to Ross L. and Margaret E. Amico on January 15, 1978, in Columbia, South Carolina. As a youth, Nick was actively involved in the Boy Scouts of America and rowed for his high school crew. At 17 he enlisted in the US Army Reserve. He graduated from Robinson Secondary School in Fairfax, Virginia, in June 1996. He then studied at Virginia Polytechnic Institute and State University from 1997 to 2002, from which he received a Bachelor of Science degree in Civil Engineering, graduating *summa cum laude*. During his undergraduate period at Virginia Tech, Nick was active in the Student Government Association, the Student Engineers' Council, and the Corps of Cadets. He also participated in the co-op program with the Eastern Federal Lands Highway Division of the Federal Highway Administration. After completing his undergraduate study, he accepted a commission as a Medical Service Corps officer in the Army Reserve and stayed on at Virginia Tech for graduate school, receiving his Master of Science degree in Civil Engineering with an emphasis on Structural Engineering in 2005. Nick is licensed as an Engineer In Training in the Commonwealth of Virginia and works as a Bridge Designer with Figg Bridge Engineers in Tallahassee, Florida. At the time of this publishing, Nick is deployed in Afghanistan in support of Operation Enduring Freedom.